Sequestration of soil organic matter by nanominerals: experimental approach to the formation of organo-mineral complex from biotite alteration products

Wuhib Zewde Tamrat

AIX-MARSEILLE UNIVERSITE

PhD

To obtain the grade

Doctor of AIX-MARSEILLE UNIVERSITY

Discipline: Environmental Geosciences

Ecole doctorale: Science de l'Environnment

Mr. Wuhib Zewde TAMRAT

directed by Mrs. Isabelle BASILE-DOELSCH and Mr. Jérôme ROSE

Will support publicly his thesis work entitled

Sequestration of soil organic matter by nanominerals: experimental approach to the formation of organo-mineral complex from biotite alteration products

Defense schedule for Thursday, 14th of December 2017 at 2PM

Place: CEREGE, Europôle de l'Arbois, Avenue Louis Philibert,
13545 Aix-en-Provence Cedex 4
Salle Amphithéâtre du CEREGE

Composition of jury

Mrs. Cécile QUANTIN	**Université Paris-Sud/GEOPS**	**Reviewer**
Mr. Jean-Louis HAZEMANN	**CNRS/Institut Néel**	**Reviewer**
Mr. Pierre BARRE	**CNRS/Laboratoire de Géologie de l'Ecole normale supérieure**	**Examiner**
Mr. Jérôme BALESDENT	**INRA/CEREGE**	**Examiner**
Mrs. Isabelle BASILE-DOELSCH	**INRA/CEREGE**	**Supervisor of PhD**
Mr. Jérôme ROSE	**CNRS/CEREGE**	**Co-director of PhD**

Avis de Soutenance

Monsieur Wuhib Zewde TAMRAT

Géosciences de l'Environnement

Soutiendra publiquement ses travaux de thèse intitulés

Séquestration des matières organiques des sols par les nanominéraux : approche expérimentale de la formation de complexes organo-minéraux à partir des produits d'altération de la biotite

dirigés par Madame Isabelle BASILE-DOELSCH et Monsieur Jérôme ROSE

Soutenance prévue le **jeudi 14 décembre 2017 à 14h00**

Lieu: CEREGE, Europôle de l'Arbois, Avenue Louis Philibert, 13545 Aix-en-Provence Cedex 4
salle Amphithéâtre du CEREGE

Composition du jury

Mme Cécile QUANTIN	**Université Paris-Sud/GEOPS**	**Rapporteur**
M. Jean-Louis HAZEMANN	**CNRS/Institut Néel**	**Rapporteur**
M. Pierre BARRE	**CNRS/Laboratoire de Géologie de l'Ecole normale supérieure**	**Examinateur**
M. Jérôme BALESDENT	**INRA/CEREGE**	**Examinateur**
Mme Isabelle BASILE-DOELSCH	**INRA/CEREGE**	**Directeur de thèse**
M. Jérôme ROSE	**CNRS/CEREGE**	**Co-directeur de thèse**

Acknowledgements

First and for most, my deepest gratitude goes to my FAMILY (specially Tet) for standing by my side, for doing the impossible, for scarifying your time, energy and resources so that I am able to reach were I am today. Zediye (RIP), you gave us all, you made everything full and plenty. It is my deepest sorrow that you are unable to be here. I imagine and certainly know how happy and most of all, how proud you would have been if you saw my achievement at this moment and time. This one is for you too. Big and Lil bros, you guys are awesome and I appreciate the confidence that you put in my progress, especially in recent years. Victory is for one and for all, so we will move forward. This is for you guys too. We often take family for granted but not this time. So I would like to, collectively, say thank you to the four of you and know that this couldn't have been done with out your presence in my life.

And thank you for my little Tinchel. You were patient when it needed be, you were bossy when I was lazy, you were helpful when I needed aid and you were soft hearted when all seemed bleak. For all that, I am deeply indebted to you and I hope I will be able reciprocate.

Next comes FRIENDS. Wendeye, Dejene (Mule/Ermias), Debish, Abrish, and many more. You guys have been and still are a constant in my life and I am deeply happy that I get to change this chapter in my life with you guys.

Pierre (AKA-Bro), William, Xavier (Cecile and little Josephine), Hocine (AKA-two mountains ;)), you guys are my brothers from another mother. I will never forget the times we spent and the impact you had on my lives.

Julie (Pupier), I think I qualify to be better than a ladybug now. You are a true friend and my little sister. Nathan (AKA-BOSSA) and Nelly, you guys are super awesome. I will not forget how welcoming you were and how you opened your house to a strange guy from Africa when I didn't know anyone. Astrid, Eleonore, Manon, Maureen, Chloe, Celine, Danielle and Alexia and, you ladies were kind and compassionate when I needed true friends around me. Kiro (AKA Ricco), Valenti, Ross, Aladine, and Luaye you guys are the dudes. Thank you all of you. Life at CEREGE wouldn't have been easy with out the fun time we spent together.

I would also like to thank everyone that I had close contact with at CEREGE, everyone in our team (Interfast) who aided me with research and may the day-to-day office life smooth and easy. Perrine, thank you for the lessons and Clement thank you for being a good friend in the lab and at the pitch. Daniele, than you for your constant morning greetings, which showed if not anything, at least respect.

Specifically, I would like to clearly mention that Isabelle and Jerome that both of you are great human beings and that I deeply appreciate the collaboration we had for the past 4+ years. I was able to gain momentum and courage every time we had our update meetings and I was able to leave our meetings with a smile on my face. That is way more than I can say for most students in similar position. So, thank you.

Table of Content

Acknowledgements III
Table of Content IV
Abstract VIII
Summary (In French) 1
Introduction 1
État de l'art et objectifs 1
1.1. Altération des phases minérales 1
1.2. Synthèse de minéraux secondaires 2
1.3. Objectifs de la thèse 3
Composition et structure à l'échelle moléculaire de nanominéraux formés par précipitation de produits d'altération de la biotite 3
1.4. Matériaux et méthodes 3
1.5. Résultats 4
1.6. Discussion 7
Associations organo minérales (SroMOAs) formées par l'altération des minéraux primaires dans les sols: approche en laboratoire 9
1.7. Introduction 9
1.8. Matériaux et methods 10
1.9. Résultats 11
1.10. Discussion 14
1.11. Conclusion 16
Conclusions 16
Manuscript (In English) ..... A
1 Introduction 1
1.1 Carbon, a global context 1
1.2 Global Carbon 1
1.3 Soil Organic Carbon (SOC) 2
1.4 Organo-mineral interactions 5
1.5 Nanoscale Organo-Mineral Complexes (nCOMx) 7
1.6 General objectives 9
1.7 Structure of manuscript 10
2. State of the art and objectives 11
2.1 State of the art 11
2.1.1 Weathering of mineral phases 11

2.1.2 Alteration of organic matter 20
2.1.3 Synthesis of secondary minerals 21
2.1.4 Inorganic to organic matter interactions 27
2.1.5 Interest of EXAFS regarding SRO and sroMOAs 39
2.1.6 Why are natural systems difficult to study? 45
2.2 Objectives of the thesis 47
2.2.1 Objectives of the preliminary phase 48
2.2.2 Specific objectives 48
2. Preliminary experiments 50
Analytical methods 50
2.1.1. X-Ray Diffraction (XRD) 50
2.1.2. Micro X-ray fluorescence (μXRF) 50
2.1.3. Inductively coupled plasma atomic emission spectroscopy (ICP-AES) 51
Basalt dissolution/precipitation 51
2.1.4. Characterization of the basalt 51
2.1.5. Experimental setup 52
2.1.8. Results 54
2.1.11. Discussion 57
2.1.14. Synthesis of learning from the basalt experiment 58
Biotite dissolution and precipitation 59
2.1.15. Objective 59
2.1.16. Materials 60
3.1.1 Pre-experiment trials: methods, results and discussions 62
3.1.2 Conclusion of the preliminary experiments 65
3.1.3 Overview of main experiments 66
4 Composition and molecular scale structure of nanominerals formed by precipitation of biotite weathering products 68
4.1 Introduction 68
4.2 Materials and Methods 70
4.2.1 Experimental protocol 70
4.2.2 ICP-AES 71
4.2.3 TEM images and analyses 72
4.2.4 EXAFS at the Fe K edge 72
4.3 Results 75
4.3.1 Chemical composition of the leachate solution and conditions of

nanominerals formation 75
4.3.2 Dissolution rate calculations 75
4.3.3 TEM-EDX characterization of nanominerals 76
4.3.4 EXAFS at the Fe K-edge: iron atomic range structure 78
4.4 Discussion 82
4.4.1 Biotite dissolution rate and physical-chemical conditions of polymerization in batches 82
4.4.2 Local structure of nanominerals 82
4.4.3 Two stages of precipitation: growth and maturation 86
4.4.4 Synthetized nanominerals are representative of nanominerals formed in soils 87
4.5 Conclusion 88
4.6 Acknowledgements 89
5 Short range order mineral organic associations (sroMOAs) formed by weathering of primary minerals in soils: laboratory approach 90
5.1 Introduction 90
5.2 Materials and Methods 91
5.2.1 Material 91
5.2.2 Experimental protocol 92
5.2.3 Physico-chemical characterization (ICP-AES, EXAFS and TEM) 93
5.2.4 Reference standards selection for EXAFS analysis 93
5.3 Results 96
5.3.1 Titration experiment (co-precipitation stage) 96
5.3.2 EXAFS – Iron local range order and extent of polymerization 96
5.3.3 TEM – Image Analysis/EDX: morphology, sizes of particles, chemical composition and state of crystallinity 99
5.4 Discussion 102
5.4.1 Two stages of precipitation: growth and maturation 102
5.4.2 Two mechanisms of sroMOAs growth 104
5.4.3 Optimal conditions of sroMOAs coprecipitation 106
5.4.4 Comparison with batch sroMOAs reported in the literature 106
5.4.5 Are the sroMOAS produced representative of natural samples? 107
5.5 Conclusion 109
6 Metal salt experiments 110
6.1 Material and methods 110
6.1.1 Materials 110

6.1.2 Methods 111
6.2 Results 113
6.3 Discussion 115
6.4 Conclusion 116
7 Conclusions and perspectives 118
7.1 General conclusions 118
7.2 Perspectives and future work 119
APPENDICES 121
Appendix 1 121
Appendix 2 123
Appendix 3 126
Appendix 4 126
Appendix 5 126
Appendix 6 127
Appendix 7 131
Appendix 8 133
Appendix 9 134
Appendix 10 138
Appendix 11 139
Appendix 12 139
LIST OF REFERENCES 147

Abstract

Among soil organic matter (SOM) stabilization mechanisms, molecular scale organo-mineral interactions are thought to play a major role in stabilizing organic compounds. Because of their large surface area and reactivity, nanometric-size soil mineral phases have a high potential for SOM stabilization. In the literature, Fe and Al phases have been the main targets of batch-synthesized nanomineral studies while nano-aluminosilicates (phases in which Al is associated with Si) have been mainly studied in Andic soils. Whatever the phases concerned, the generic process that results in the formation of nanominerals results from (1) the continuous alteration of the primary minerals, which releases ionic species and (2), the polymerization through hydrolysis (i.e. precipitation) of these species that form nanominerals at the interface between the primary mineral and the soil solution. In the present work, we conducted laboratory simulations of the subsequent processes to biotite alteration in acidic conditions and the resulting neoformations, from an Al Si Fe Mg K and C system, of secondary nanominerals after hydrolysis of the dissolved species. Their morphology, size, crystallinity and chemistry were characterized by TEM-EDX on single particles and their local atomic structure by EXAFS (Extended X-ray Absorption Fine Structure) at the Fe absorption K-edge.

In the absence of C, the main nanominerals formed were amorphous particles 10 to 60 nm in size whose composition (dominated by Fe and Si) was strongly controlled by the pH conditions at the end of the hydrolysis. At pH 4.2 and pH 7, the structure of the nanominerals was dominated by the polymerization of Fe, which was hindered by Al, Si, Mg and K. Conversely, at pH 5, the polymerization of Fe was counteracted by precipitation of high amounts of Si. In comparison with previous alteration studies, the synthetized nanominerals were estimated to be rather analogous to nanominerals formed in natural biotite-bearing soils. Because of their small size and potential high surface reactivity, the adsorption capacities of these nanominerals with respect to the OM should be considered in the framework of soil C stabilization issues.

In the presence of C, precipitates were still amorphous ranging in size from 2 to 200 nm. This size increased with increasing C presence until a 'molar concentration ratio' value of Metal:Carbon=1 and showed a decline after. Precipitation resulted into two distinct size ranges. Composition of the smaller particles was closer to the leachate solution. While for the larger particles, composition (dominated by Fe and Si) was strongly controlled by the C concentration. At No C and M:C=10, the chemistry of the nanominerals was dominated by Si. While conversely, M:C=1,0.1 and 0.01, the nanominerals were mainly Fe based. Interesting in these findings is the change in composition between smaller and larger particles in addition to the significant role played by Si, which is often overlooked in previous mineral formation studies. Therefore, the results of this study give an important overlook of the affinity of different inorganic species to varying C concentrations in natural soil systems. And finally, the specifics of these same results have effectively replicated nanominerals and their formation processes found in some natural systems such as andosols and podzols, at least part of the system, where OM is efficiently stabilized.

Key words: Soil Organic Matter Stabilization, Organo-mineral Nanophases, Coprecipitation, EXAFS and Biotite weathering.

Summary (In French)

Introduction

Le carbone (C) se trouve dans différents réservoirs, dont une portion importante dans le réservoir de matière organique organique du sol (GIEC, 2001; Schmidt, et al., 2011). Les processus anthropiques récents, dont les changements d'usage des terres, contribuent au flux du carbone de ce réservoir vers l'atmosphère. Ces phénomènes méritent l'étude des processus de stabilization du C dans les sols. Parmi les différents mécanismes de stabilisation des MOS, on estime que les Associations Minérales Organiques Minérales (MOAs) à l'échelle moléculaire jouent un rôle majeur.

Interactions organo-minérales

Les phases minérales jouent un rôle majeur dans les MOAs, qui finissent par stabiliser la MOS (Basile-Doelsch, et al., 2007). Les expériences de synthèse en laboratoire permettent, entre autres, d'étudier ces interactions. Les phases Fe et Al ont été les principales cibles des études nanominérales synthétisées, tandis que les nano-aluminosilicates ont été principalement étudiés dans les sols andiques. De plus, les concepts qui sous-tendent la recherche récente sur les interactions organo-minérales considèrent que les surfaces minérales ne sont pas stables, mais qu'elles sont continuellement altérées, ce qui précipite en fin de compte les phases amorphes nanométriques de Si, le Fe et l'Al (Basile-Doelsch, et al., 2015). Par conséquent, les mécanismes de stabilisation de la MOS sont associés non seulement à la présence d'Al3+, de Fe3+ et d'argile (Sollins, et al., 1996; Baldock et Skjemstad, 2000; Wagai, et al., 2013), mais aussi de polymères nanométriques ordonnés à courte distances composés principalement d'espèces hydrolysées d'Al, de Si et de Fe (Masiello et al., 2004; Basile-Doelsch et al., 2004).

L'objectif général de cette étude est de mieux comprendre la dynamique naturelle des MOS. Comme il s'agit d'un processus complexe, cette étude vise à synthétiser des complexes organo-minéraux nanométriques et à étudier leur dynamique à l'échelle du laboratoire. Cela impliquera spécifiquement l'interaction de l'OM avec des phases mal cristallisées. L'attention de ce travail sera également concentrée sur les phases inorganiques et organiques du sol et sur l'interaction qui existe entre elles.

État de l'art et objectifs

1.1. Altération des phases minérales

L'altération des minéraux est un processus précurseur de la formation des MOA ou de la formation de phases inorganiques secondaires. Lors de l'altération minérale, dans la plupart des cas, les changements sont localisés à la surface des minéraux ou à de faibles profondeurs de la surface. Dans des conditions acides, les protons rompent les liaisons structurales facilitant la libération des espèces dissoutes en solution. Ce phénomène donne d'abondants précurseurs inorganiques pour la formation des MOA. Les précipitations abondantes (humidité) nécessaires à la production de biomasse végétale et les conditions d'altération physique, chimique et biologique qui favorisent la formation du sol constituent également une condition préalable.

En raison de l'interaction avec les minéraux, pour que l'OM soit à l'état physique et chimique réactif, il doit subir plusieurs processus. Ces processus, souvent affectés par les

communautés microbiennes, impliquent des processus d'oxydation et de dépolymérisation. Les composés de grande taille présents dans la MOS sont réduits en taille moléculaire par des microbes tout en effectuant une altération chimique (ajout d'oxygène) pour obtenir une solubilité aqueuse accrue (Piccolo, 2001; ten Have et Teunissen, 2001).

1.2. Synthèse de minéraux secondaires

L'immobilisation de la MO la preserve de la minéralisation (Scheel, et al., 2008). Pour soutenir la formation de SOM, en plus de l'OM, les espèces inorganiques doivent être présentes dans l'état de solubilité au pH du sol local spécifique (Kleber, et al., 2015).

1.2.1. Hydrolyse des métaux

L'hydrolyse des métaux se fait en plusieurs étapes. La première étape importante est la formation des premiers monomères. Les étapes subséquentes permettent à ces petits clusters de croître et de se polymériser en cristaux ordonnés ou en phases amorphes (Rose et al., 1997b).

Fe3+ et Al3+ (à l'inverse de Fe2+, Mg2+ et Ca2+) sont deux des cations les plus réactifs de la solution naturelle du sol. Ceci est dû à leur faible constante d'hydrolyse en dessous du pH du sol, ce qui leur permet d'interagir avec des composes organiques de petite taille (Kaiser et Guggenberger, 2007; Riedel et al., 2012). Par conséquent, dans les sols, le Fe3+ est en grande partie en competition avec l'Al3+ par rapport à tout autre cation. On a également observé que la présence variable de Si interfère à des degrés divers en limitant la polymérisation du Fe (Doelsch, et al., 2000; Pokrovski, et al., 2003).

1.2.2. Interactions de la matière inorganique à la matière organique

La formation des MOAs est souvent déclenchées par des changements dans l'environnement physique et chimique (p. ex. pH, état d'oxydoréduction, force ionique) (Weng, et al., 2007; Riedel, et al., 2013). Dans les études d'interactions organo minérales, le choix des composés organiques est très varié et dépend de divers facteurs liés aux objectifs des expériences. Pour étayer le compose organique choisi dans ce travail, diverses études ont été citées (Cornell et Schneider, 1989; Eusterhues, et al., 2008; O'Loughlin, et al., 2010; Eusterhues, et al., 2011; Henneberry, et al., 2012; Mikutta, et al., 2014).

Avec la formation des MOAs, Kleber et al. (2015) discutent des interactions à amorcer et à poursuivre en empêchant la liaison entre deux monomères d'oxydes métalliques en raison de l'interaction des sites inorganiques avec les ligands organiques. Ils soulignent en outre qu' à long terme, ce processus entraîne une perte de cristallinité et altère les propriétés telles que la taille des particules individuelles, la distorsion du réseau cristallin et l'état de coordination des métaux dans les phases nouvellement formées.

Pour le protocole expérimental, les hypothèses et simplifications suivantes ont été adoptées: étapes d'altération et de précipitation séparées, taille de filtration de 10kDalton pour récupérer les espèces réellement dissoutes au lieu des polymères/agrégats, les précipitations seront en solution (en l'absence de surfaces) et l'addition d'OH- sera à un taux constant et beaucoup plus rapide que dans des conditions naturelles.

1.3. Objectifs de la thèse

Les objectifs, subdivisés en deux parties (1) visent d'abord à recueillir les espèces réellement dissoutes lessivées et (2) à synthétiser les phases inorganiques amorphes (sans OC) ainsi que les complexes organo-minéraux en utilisant les espèces dissoutes issues des expériences d'altération. Ces processus visent à simuler des processus physico-chimiques semblables à ceux qui se produisent dans les systèmes naturels du sol (Chorover, 2011; Eusterhues et al., 2014a; Eusterhues et al., 2014b). Plus précisément, il s'agissait de caractériser la morphologie, la taille, la cristallinité et la chimie des nouvelles phases par TEM-EDX sur des particules individuelles et leur structure atomique locale par EXAFS (Extended X-ray Absorption Fine Structure) au seuil d'absorption du Fe. Ce dernier objectif a donc été divisé en deux séries d'expériences qui ont précipité de nouvelles phases (1) en l'absence de C et (2) en présence de C.

Composition et structure à l'échelle moléculaire de nanominéraux formés par précipitation de produits d'altération de la biotite

1.4. Matériaux et méthodes

La biotite étudiée provient de Bancroft, Ontario Canada (Ward Science) (Turpault et Trotignon, 1994).

$$K_{0.92}\left(Fe^{(2+)}_{1.06}Mg_{1.66}\right)\left(Fe^{(3+)}_{0.094}Ti_{0.12}Mn_{0.046}\right) \times [Si_{3.00}Al_{1.00}O_{10}](OH_{1.10}F_{0.90}) \ \ldots (1)$$

L'échantillon a été broyé mécaniquement (<50 µm) à l'aide d'un broyeur à billes en oxyde de zirconium, lavé, tamisé à l'eau ultra-pure et séché (40^0C).

Étape de dissolution: 33 g de particules de biotite < 50 µm ont été placées dans 1L de pH2 HNO3 (rapport solide/liquide de 1:30). Après 29 jours, les espèces dissoutes ont été récupérées à l'aide d'un système de filtration tangentiel (TFF) à une taille de coupure de 10 kD (pores d'environ 2 nm). La solution filtrée sera ci-après dénommée "solution de lixiviat". Les concentrations d'espèces dissoutes dans la solution de lixiviat ont été controlées à l'aide d'un ICP-AES, avec une incertitude de mesure inférieure à 10 %.

Étape de polymérisation: Les nanominéraux ont été précipités en augmentant le pH de 2 à trois pH finaux (soit 4.2, 5 et 7) à l'aide de 0,2N NaOH. Une titration préliminaire de la solution de lixiviat a été effectuée et un changement de pente de la courbe a permis d'identifier trois états de pH correspondants à des changements dans les phases polymérisées. Aux pH finaux, un échantillon d'aliquote de 1 ml a été prélevé pour le TEM-EDX et la solution restante a été ultra-centrifugée à 80 000 tr/min pendant 2 h pour séparer les nanominéraux précipités des espèces dissoutes. Les particules décantées ont été lyophilisées pour les analyses EXAFS.

Les données structurales ont été collectées par les sources synchrotron ESRF et ELETTRA à Grenoble (France) et Trieste (Italie). L'analyse quantitative des données du système EXAFS a suivi deux approches. La première approche consistait à étudier couche par couche l'environnement atomique du Fe (shell by shell fitting, SSF). La deuxième approche a utilisé l'ajustement de combinaison linéaire (linear combination fitting LCF) basé sur la structure connue de la bibliothèque des composés de référence.

Méthodologie Shell by shell fitting (SSF)

Shell by Shell Fitting (SSF) a été utilisé pour extraire des informations structurelles telles que le numéro de coordination (Nj) et les distances interatomiques (Rj) par rapport à l'atome d'absorbeur en utilisant le code logiciel Artemis (Ravel et Newville, 2005).

Les fonctions partielles EXAFS (momentum (q) space) étaient les moindres carrés ajustées par une fonction théorique (dans l'approximation à diffusion unique) afin de déterminer les paramètres structuraux et chimiques des voisins atomiques autour de Fe. La sortie de ces ajustements donne (1) la nature, (2) la distance radiale de l'atome central (R) et (3) le nombre (N) des atomes voisins avec (4) le facteur Debye-Waller (σ^2) correspondant aux désordres statiques et thermiques associés au fit. Les incertitudes pour les distances radiales demeurent dans une plage de ±0,02 Å typique des calculs de distance (Pokrovski, et al., 2002).

1.5. Résultats

1.5.1. Composition chimique de la solution de lixiviation et calculs du taux de dissolution

La composition chimique de la solution de lixiviat est présentée au tableau 1. Fe, Mg et Si ont principalement contribué à la solution de lixiviat, tandis que Al et K y ont contribué dans une moindre mesure. Le taux de dissolution élémentaire le plus élevé a été enregistré pour Mg, suivi de Si, Fe et K avec le taux de dissolution le plus lent attribué à Al (tableau 1). Mais pour les calculs basés sur l'ensemble de la biotite, le taux de dissolution minérale basé sur K a donné le taux le plus rapide suivi de Fe, Mg, Al et Si.

Table 1: Elemental release rates and biotite dissolution rates. Rates are calculated over the 29 days weathering experiment. Taux de dissolution élémentaire et taux de dissolution de la biotite. Les taux sont calculés sur une période de 29 jours.

	Fe	Si	Al	K	Mg
Concentration (µM)	937.2 ± 56.5	1006.1 ± 27.1	513.5 ± 30.5	383.1 ± 83.4	1246.7 ± 23.2
Elemental release rate (10^{-8} mole m^{-2} hr^{-1})	3.2 ± 0.2	3.4 ± 0.1	2.1 ± 0.1	3.0 ± 0.3	4.2 ± 0.1
Biotite dissolution rate (10^{-8} mole m^{-2} hr^{-1}) *	2.8 ± 0.2	1.1 ± 0.03	2.1 ± 0.1	3.3 ± 0.3	2.6 ± 0.05

* Stoichiometric composition calculated from the empirical formula Composition stœchiométriqu calculée à partir de la formule empirique => $K_{0.9}Mg_{1.7}Fe_{1.2}Al_{1.0}Si_{3.0}$

1.5.2. Formation de nanominéraux secondaires

En se basant sur l'expérience de titrage préliminaire, les expériences d'hydrolyse ont donné lieu à des phases qui se forment dans les plages de pH comprises entre 2 et 4,2, 2 à 5 et 2 à 7 respectivement.

Caractérisation MET-EDX

Quel que soit le pH, les particules ont été agrégées, formant des cluster distincts de petites et grandes particules (Figure 39) au-dessous et au-dessus de la taille de coupure

d'environ 15 nm. Les analyses par diffraction des électrons ont révélé un profil diffus dans toutes les tailles de pH et de particules (Figure 39).

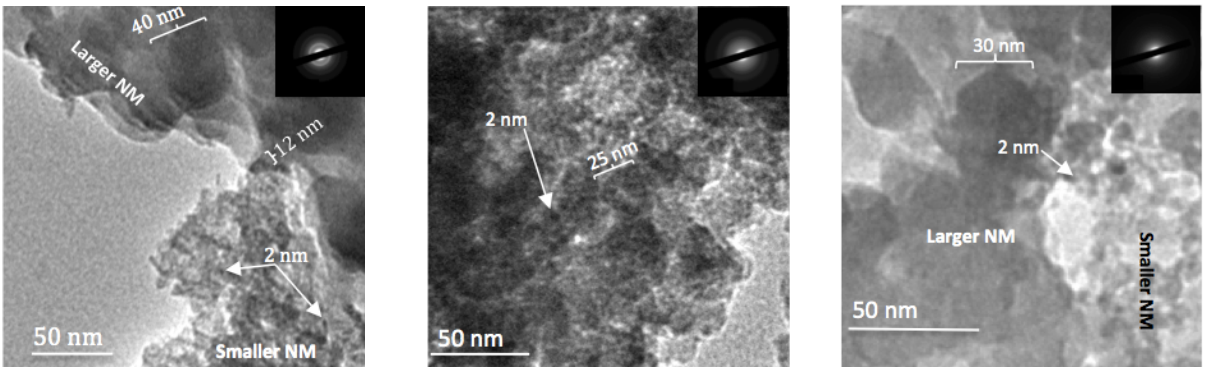

Figure 1: Micrographies MET des nanominéraux. pH 4,2 (gauche), pH 5 (au milieu) et pH 7 (droite). L'analyse par diffraction électronique est superposée aux images, révélant la structure amorphe des nanominéraux. SP: particules plus petites; LP: particules plus grosses.

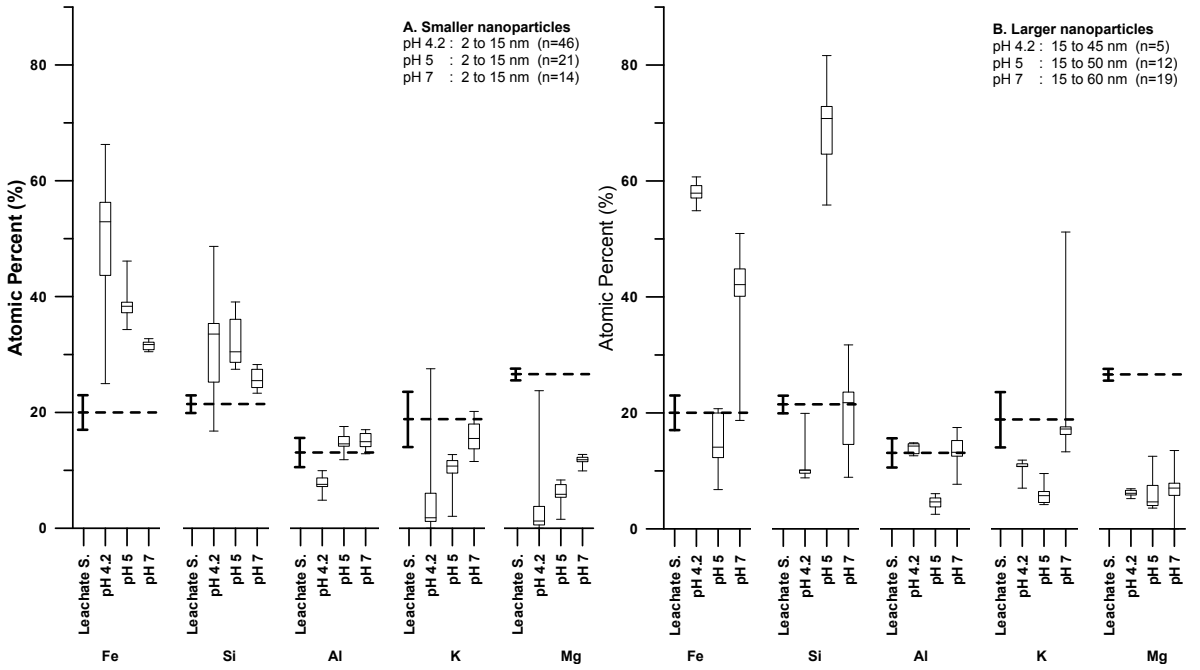

Figure 2: Analyse chimique TEM-EDX des particules polymérisées à trois pH, exprimée en % atomique. Les diagrammes de boîtes à moustaches représentent la valeur médiane, les quartiles supérieur et inférieur ainsi que les valeurs min et max des données. La composition chimique de la solution de lixiviation (Leachate S.) est également présentée à des fins de comparaison (ligne pointillée en gras, avec leurs valeurs d'erreur spécifiques à chaque élément). A: composition chimique des nanominéraux les plus petits; B: composition chimique des nanominéraux les plus grands. n: nombre de particules analysées.

Le Fe et le Si composent principalement les nanominéraux, quel que soit le pH et la taille (figure 3 A et B). Les proportions de Fe et Si sont plus élevées que dans la solution de lixiviat, ce qui indique une polymérisation préférentielle du Fe et du Si par rapport aux autres éléments. Les proportions d'Al dans les nanominéraux sont proches de celles de la solution de lixiviat. Les proportions de K et de Mg dans les nanominéraux sont dans la même gamme que celles d'Al. Cependant, ils sont significativement appauvris dans les nanominéraux par rapport à la solution de lixiviation. Enfin, en termes de tendances générales en fonction du pH, le pH 5 représente un cas singulier dans lequel les grosses particules sont extrêmement enrichies en Si et appauvires en Fe et Al.

1.5.3. EXAFS au seuil K du Fe: structure atomique des polymère de fer

A. Comparaison des données brutes

Les interactions structurales entre les octahedres de Fe sont représentées sous forme de signaux à ~5,2 Å-1 et ~7,5 Å-1 sur les spectres EXAFS, et sous forme de pics dans l'espace R à R~2,7 Å et ~3,2 Å correspondant respectivement aux interactions par arête et par double sommet (Figure 41).

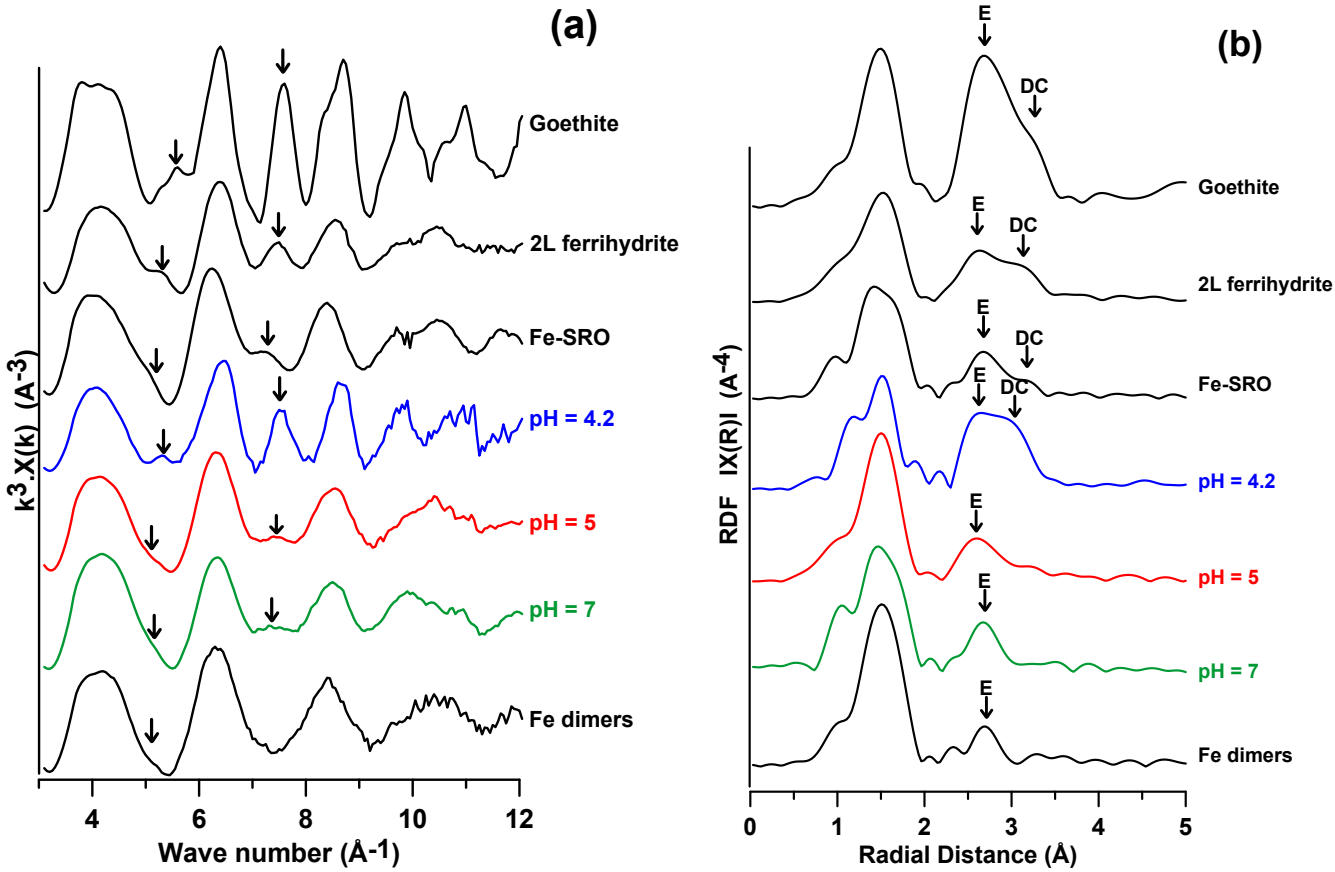

Figure 3: Graphiques de spectres EXAFS (a) et RDF (b). Les flèches indiquent les emplacements des signaux Fe-Fe. Les spectres en noir représentent les références. E et DC désignent respectivement les interactions par arête et par double sommet. Les distances sur le RDF ne sont pas corrigées des déphasages.

Les phases formées ià pH 4.2 montrent un spectre avec des marqueurs Fe-Fe dont l'intensité se situe entre la goethite et la ferrihydrite 2L. Pour les phases pH 5 et 7, la comparaison des spectres k et R donne une moyenne entre les références 2L ferrihydrite et Fe-SRO.

B. Analyse quantitative des données de l'EXAFS shell by shell fitting

Pour cet ensemble de résultats, le Shell by shell fitting a été jugé plus approprié pour extraire les informations structurales. L'analyse de la 1ère sphère de coordination a montré la formation d'octaèdres ferriques pour toutes les phases et éventuellement la coordination en tétraèdres pour les phases pH 5 (Table 18).

Table 2: Analyse SSF des pH 4,2,5 et 7 phases. N, R, σ et Eo représentent respectivement le nombre de coordination, la distance radiale, le désordre et la valeur énergétique de départ pour l'ajustement. Le facteur R est un paramètre de qualité d'ajustement. Fe-Fe2 correspond au interactions par arête, Fe-Fe3 correspond aux interactions par double sommet.

	R window Å	N ±20%	R (Å) ±0.02	σ (Å)	N ±20%	R (Å) ±0.02	σ (Å)	N ±20%	R (Å) ±0.02	σ (Å)	E_o (eV)	R-factor
pH 4.2	1.00-3.63		Fe-O			$Fe-Fe_2$			$Fe-Fe_3$		4.0	0.023
		6.3	1.97	0.12	1.5	3.01	0.08	1.9	3.38	0.08		
pH 5	1.00-3.09		Fe-O			$Fe-Fe_2$			Fe-Si		3.0	0.006
		4.9	1.96	0.09	1.1	3.01	0.09	3.9	3.18	0.09		
pH 7	1.00-3.24		Fe-O			$Fe-Fe_2$			$Fe-Fe_3$		4.0	0.011
		6.5	1.98	0.11	2.5	3.06	0.11	0.5	3.35	0.11		

Le SSF des deuxième et troisième sphères de coordination de tous les échantillons a été réalisé en testant successivement les paires atomiques Fe-Fe, Fe-Si et Fe-Al. Pour l'échantillon de pH 4.2, la meilleure solution a été obtenue avec du Fe dans les 2e et 3e enveloppes atomiques. Les distances interatomiques sont en accord avec des interactions par arêtes et par double sommet. Pour l'échantillon de pH 5, la solution obtenue montre des interactions par arete Fe-Fe2 dans la 2ème couche et par Fe-Si (ou Al) dans la 3ème couche. La distance Fe-Si (Al) correspond à un seul sommet entre l'octaèdre Fe et le tétraèdre Si (ou Al). Cependant, l'indice de coordination Fe-Fe (1,1-1,8±20 %) est beaucoup plus faible que pour l'échantillon de pH 4,2. Pour l'échantillon de pH 7, les ajustements ont donné 3 solutions pour décrire au mieux la structure. S'appuyant sur la composition dominante Fe de la meilleure solution des nanominéraux, les interactions Fe-Fe occupaient les 2e et 3e couches. Mais quelle que soit la solution, à pH 7, l'indice de coordination Fe-Fe (2,5-3±20%) est supérieur à pH 5 mais inférieur à pH 4,2.

1.6. Discussion

1.6.1. Taux de dissolution de la biotite et conditions physico-chimiques de polymérisation en lots

Les proportions de Fe, Si, Al, K et Mg dans la solution de lixiviat différent de celles de la stoechiométrie dans la biotite, ce qui signifie une dissolution incongruante. Au 29e jour, les taux de dissolution varient de 1,1 à 3,3 10-8 mol m-2 h-1 (calculés avec Si et K) respectivement (tableau 1). Toutefois, ces valeurs ont été plus lentes que celles données dans la littérature (voir Bonneville et al. (2011 pour une analyse) en raison de la taille de coupure d'environ 2 nm imposée pour les espèces véritablement dissoutes. Par comparaison, d'autres études utilisent des filtres à 200 nm (Bonneville, et al., 2011; Bray, et al., 2015) qui donnent des valeurs de taux de dissolution plus rapides.

1.6.2. Structure locale des nanominéraux

Le degré de la polymérisation du fer des nanominéraux (Ntot) synthétisés dans nos expériences était inférieure à 3,4 quel que soit le pH. Cette valeur est inférieure à celle des études portant sur les systèmes de Fe pur ainsi que sur les systèmes contenant du Si (Combes, et al., 1990; Doelsch, et al., 2000) en raison de la présence d'Al, Si, Mg et K dans la solution qui entrave clairement la polymérisation du Fe quel que soit le pH.

Le pH contrôle la structure locale des nanominéraux

À pH 4,2, le niveau de polymérisation des nanominéraux est le plus élevé de nos expériences et le Fe est l'élément principal des nanominéraux (figure 3). Dans ces phases, la spéciation du fer est similaire à celle que l'on trouve dans les systèmes Fe purs,

ressemblant à de la ferrihydrite De plus, les liaisons Fe-Fe avec des interactions à double sommet dominent la structure locale.

L'augmentation du pH dans le système Fe pur conduit généralement à une augmentation du degré de polymérisation du fer. Une telle tendance n' a pas été observée dans notre système lorsque le pH est passé à 5 et 7. Dans les systèmes non Fe purs, ligands complexants tels que Si (Doelsch, et al., 2000), P (Rose, et al., 1996; Rose, et al., 1997a), As (Waychunas, et al.., 1993; Manceau, 1995; Waychunas, et al., 1995), Se (Manceau et Charlet, 1994) polymérisation du Fe toxique lorsque l'hydrolyse est suffisamment avancée pour que ces espèces atteignent un état insoluble. Par conséquent, le nombre élevé de coordination Fe-Si pour les phases pH5 suggère que la structure locale ressemble à celle du groupe Fe3-Si2,3 proposée par Pokrovski et al. (2003) ou caractérisée par FTIR par Doelsch et al. (2001). Avec ces phases pH5, l'indice de coordination Fe-O (4.9) était beaucoup plus faible que les autres phases pH, ce qui suggère fortement la présence de Fe coordonné tétraèdrique (Pokrovski, et al., 2003). Le nombre d'interactions par arete est légèrement plus élevé que le nombre de doubles sommets, ce qui suggère également que la structure locale est un mélange de dimères et de trimères.

Néanmoins, dans notre étude, l'effet de compétition du Si sur le Fe à pH5 n' a pas été vérifié à pH7. Au cours de l'augmentation du pH, il semblait que l'obstacle dû au Si était plus faible et que la polymérisation du Fe recommençe mais à un degré inférieur à celui du pH 4.2. Cependant, à la différence du pH 4.2, les octaèdres sont pour la plupart lies par leurs arètes, formant des structures locales plutôt planes (régimes de croissance en 2D). Doelsch et coll. (2000) soutiennent que dans des conditions qui favorisent la formation d'espèces polymères de Si (c. -à-d. l'abondance relative de Si par rapport à Fe), Si est en concurrence avec ses propres espèces, laissant ainsi la polymérisation du Fe progresser mieux. Dans notre étude, on pourrait soutenir que des conditions favorables similaires se produisent à pH7 avec une solubilité plus élevée du Si (aussi les autres espèces cationiques, spécialement Al) augmentant l'interaction entre les espèces de Si et d'autres espèces cationiques, à l'exception du Fe (spécialement Al) réduisant l'effet de limitation de la polymérisation du Fe.

Cependant, les données de l'EXAFS qui ne sont pas complétées par des techniques donnant la taille des particules (p. ex. SAXS, TEM) n'ont pas pu confirmer sans équivoque l'étendue de la polymérisation des phases individuelles.

1.6.3. Deux stades de précipitation: croissance et maturation

Les différences de composition chimique en fonction de la taille sont illustrées dans le diagramme ternaire Fe, Si et Al de la figure 5. La chimie des particules plus petites est proche de celle de la solution de lixiviat initiale, tandis que celle des particules plus grosses est différente à la fois de la solution de lixiviat et des particules plus petites. Elles ont été enrichis en Fe à pH 4,2 et 7, et en Si à pH 5. La différence dans la composition des particules plus grandes et plus petites indique la présence d'une deuxième étape de maturation, ce qui ne peut pas être expliqué par une simple agrégation des particules plus petites. Cependant, l'analyse structurale et chimique couplée montre que les signaux EXAFS des phases polymérisées sont plutôt dominés par la structure des grosses particules.

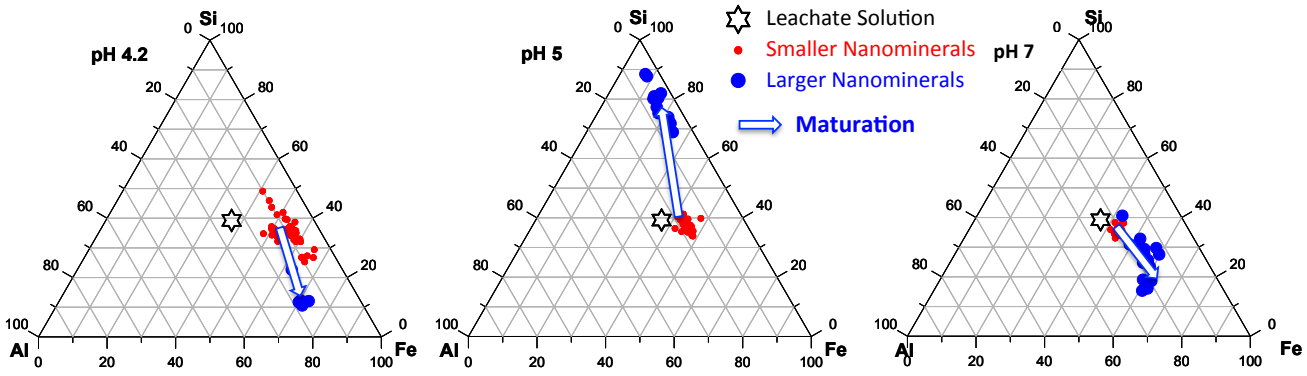

Figure 4: Diagrammes ternaires des proportions atomiques de Fe, Si et Al dans les nanominéraux formés à pH 4,2,5 et 7. L'étoile blanche représente la composition initiale de la solution de lixiviat, les petits points rouges représentent les petits nanominéraux et les grands points bleus les plus gros. La flèche blanche représente la maturation.

1.6.4. Les nanominéraux synthétisés sont représentatifs des nanominéraux formés dans les sols.

L'étude de Bonneville, et al. (2011) est particulièrement pertinente pour comparer nos résultats avec un système de résultats d'interface minérale-mycorhize moyennés sur la zone de biotite altérée de 20 nm d'épaisseur. La comparaison de leurs résultats (pH enregistré 4,6-5,8) montre des compositions similaires à nos nanominéraux formés à pH 5. Par conséquent, les phases de pH 5 pourraient être une bonne représentation des phases qui se forment au front d'altération de la biotite dans la plage de pH spécifiée.

Associations organo minérales (SroMOAs) formées par l'altération des minéraux primaires dans les sols: approche en laboratoire

1.7. Introduction

Les interactions organo-minérales sont reconnues comme un facteur clé de la stabilisation de la matière organique dans les sols (Kleber et al., 2015). Ils contribuent grandement au stock de C du sol (2400 Gt, Stockmann, et al. (2013)) et jouent ainsi un rôle clé dans la maîtrise du cycle biogéochimique de la surface C (Le Quéré, et al., 2015). Dans certains ouvrages, les interactions organo-minérales sont même considérées comme un levier d'augmentation du reservoir des MO en cas de changement d'affectation du sol (Wissing, et al., 2013). La compréhension des mécanismes qui régissent la formation des complexes organo-minéraux est donc un enjeu majeur en vue d'augmenter les stocks de C du sol de 4 pour 1000 (Paustian, et al., 2016; Minasny, et al., 2017).

Deux types de localisation des interactions organo-minérales peuvent être distingués dans la matrice du sol: les oxyhydroxydes pédogéniques et les surfaces minérales (voir l'étude exhaustive de Kleber et al. (2015). Dans le cas de l'adsorption sur des surfaces minérales, les modèles considèrent une structure minérale cristalline parfaite (Churchman, 2010). Mais les processus d'altération jouent un rôle majeur dans la perturbation des surfaces minérales. Un modèle conceptuel récent a proposé de prendre en compte ces processus d'altération des surfaces minérales dans les interactions organo-minérales (Basile-Doelsch, et al., 2015). Ce modèle suggère que des processus de coprécipitation se produisent entre les phases minérales formées pendant l'altération et les composés organiques du sol, ce qui contribue probablement à la stabilisation de la MOS.

De nombreuses expériences de synthèse ont été réalisées pour comprendre ces mécanismes de stabilisation de l'OM par coprécipitation avec des oxydes de Fe et d'Al (Masion et al., 1994; Masion et al., 2000; Jansen et al, 2003; Colombo, et coll., 2004; Xu, et coll., 2010; Eusterhues, et coll., 2011; Mikutta, et coll., 2011; Henneberry, et coll., 2012; Shimizu, et coll., 2013; Eusterhues, et coll., 2014b; Mikutta, et coll., 2014). Dans le présent travail, comme dans les études en laboratoire sur Al et Fe (Masion, et al., 2000; Colombo, et al., 2004; Eusterhues, et al., 2011; Mikutta, et al., 2011; Shimizu, et al.., 2013) notre but est de tester si des complexes organo-minéraux peuvent être formés par coprécipitation en présence non seulement de Al et Fe, mais aussi d'autres éléments résultant de l'altération des silicates. Dans le présent travail, nous caractérisons ces associations minéralo-organiques à courte distance (sroMOAs) formées à pH5 avec des concentrations croissantes d'OM (le rapport métal / C passant de l'état No C à 10,1,0,1 et 0,01). Le pH = 5 a été choisi pour représenter les états acides du pH du sol (Schwertmann et Murad, 1983; Voinot, et al., 2013) ainsi que l'altération fongique opérée au front des minéraux de biotite (Bonneville, et al., 2011).

1.8. Matériaux et methods

1.8.1. Matériaux

La 3,4-dihydroxy-L-phénylalanine a été utilisée comme modèle pour les petites molécules de MOS (Zimmerman et al., 2004). Elle a les principales fonctions que l'on retrouve dans les processus de stabilisation organo-minéraux: amine, carboxyle et un composant d'hydroquinone (Mikutta, 2011; Kleber et al., 2015) (Figure 6). A pH5, le groupe amine existe sous forme NH3+, le groupe carboxyle COO- et le groupe phénol OH.

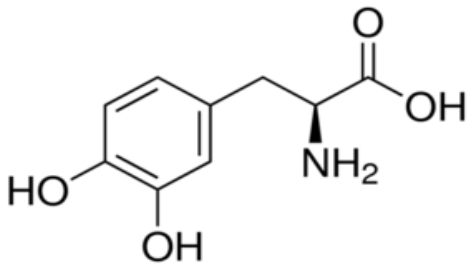

Figure 5: 3,4-Dihydroxy-L-phenylalanine

1.8.2. Protocole expérimental

Les étapes de dissolution de la biotite suivies dans cette étude sont semblables à celles décrites au chapitre 3. La précipitation des sroMOA a été effectuée en augmentant le pH d'une solution de lixiviat de 100 ml à partir d'un pH de 2 à 5 en présence de concentrations différentes de CO (c'est-à-dire des rapports molaires métal[Fe+Al]/ C (M: C) de'No C', 10,1,0,1 et 0,01). La caractérisation physico-chimique a été effectuée à l'aide d'outils similaires à ceux du chapitre 3.

Méthode de fit par combinaison linéaire (LCF)

Pour cet ensemble de spectres, la LCF a été utilisée avec le progiciel ATHENA sur l'espace d'ajustement de $\chi(k)$. La sensibilité du LCF se situe dans une fourchette de 5 à 20 % (O'Day et al., 2004). Pendant le montage, toutes les contributions devaient rester entre 0 et 1 sans forcer leur somme à 1. Les étalons de référence choisis (tableau 3 avec figure 7 en noir) ont montré des taux croissants de polymérisation du Fe octaèdre dans l'ordre du

citrate de fer, des colloïdes Fe-C, des dimères de Fe, du Fe-SRO et de la ferrihydrite 2L.

Table 3: Tableau récapitulatif des types et proportions de liaisons pour les references.

Reference Standards	Edge	Double Corner
Iron (III) Citrate	-	-
Fe-C Colloids	-	0.4
Fe Dimers	1	-
Fe-SRO	2.6	0.63
2L Ferrihydrite	2.1	5

1.9. Résultats

1.9.1. EXAFS structure locale et degree de ploymérsiation

A. Quantification de la polymérisation du fer: analyse des données brutes

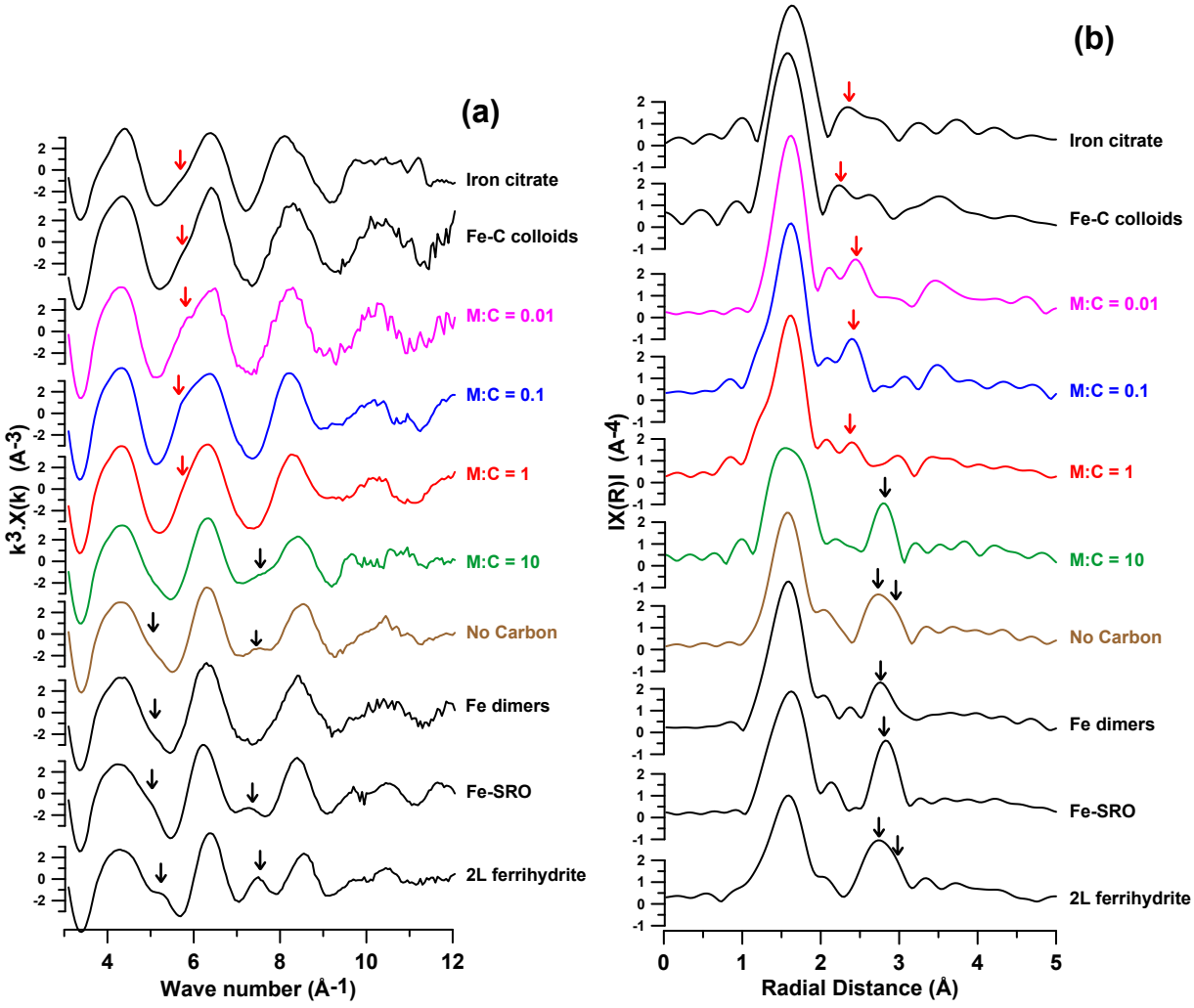

Figure 6:Graphes EXAFS et RDF. a) espace k et b) espace R série "pH=5". Les flèches noires et rouges sur les spectres de l'espace k indiquent des parties des oscillations spécifiquement produites par les interactions Fe-Fe

et Fe-C respectivement. Les mêmes flèches noires et rouges, dans l'espace R, indiquent les distances radiales correspondant aux interactions Fe-Fe et Fe-C respectivement.

Les spectres EXAFS et les fonctions de distribution radiale (RDF) pour les échantillons expérimentaux sont illustrés à la figure 7. Au-delà de la première région de la couche, on observe des marqueurs d'interactions octaèdres Fe-Fe (voir chapitre 3) avec des intensités différentes. Ces marqueurs de l'interaction Fe-Fe réduisent en intensité au fur et à mesure que nous passons des échantillons No C à l'échantillon avec une teneur en C progressivement plus élevée. Et finalement, ces marqueurs Fe-Fe sont remplacés par un signal d'interaction Fe-C avec plus de C dans le système.

B. Quantification de la polymérisation du Fe: LCF/comparaison avec les références

Les résultats du LCF pour tous les échantillons sont présentés dans le tableau 4 avec une marge d'erreur de ±15 % pour toutes les valeurs. La structure locale des phases formées avec No C présente une analogie significative avec "2L Ferrihydrite" et, dans une moindre mesure, avec "Fe-SRO" et "Fe Dimers". Dans le cas des phases M: C=10 (par rapport au No C) la contribution collective du Fe pur contenant est passée de 102% à 82%. Une augmentation de 10 fois plus importante en C (M: C=1) entraîne une ugmentation de la contribution des interactions Fe-O-C. Une nouvelle multiplication par 10 de la présence de C (M: C=0,1) entraine une diminution de la contribution de 35 % à 14 % de Fe-O-Fe. Alors que les contributions Fe-O-C ont augmenté collectivement de 72 % à 94 %. À la teneur maximale en C de M: C=0,01, on a noté de petits changements aux contributions d'ajustement qui sont bien en deçà de la marge d'erreur de 15 % pour LCF.

Table 4: Linear Combination Fitting numbers.

	Citrate	Colloi	Dime	SRferrihydrite		R-factor	
	Fe-O-C	Fe-O-C + Fe-O-Fe	Fe-O-Fe				
No C			0.33	0.25	0.44	1.02	0.015
M:C=10	0.30			0.45	0.37	1.12	0.010
M:C=1	0.27	0.45		0.35		1.06	0.038
M:C=0.1	0.41	0.53		0.14		1.08	0.059
M:C=0.01	0.58	0.39		0.12		1.10	0.053

1.9.2. MET - Analyse d'images/EDX: morphologie, taille des particules, composition chimique et état de cristallinité.

Les micrographies MET des séries d'échantillons aux cinq rapports M:C sont illustrées à la figure 8. Quel que soit le rapport molaire M: C, les particules forment des clusters distincts de particules de plus petite taille et de plus grande taille (tableau 5), avec des signatures chimiques distinctes. Indépendamment de la présence de carbone et de la taille des phases, les analyses par diffraction d'électrons ont montré un motif diffus pour tous les échantillons.

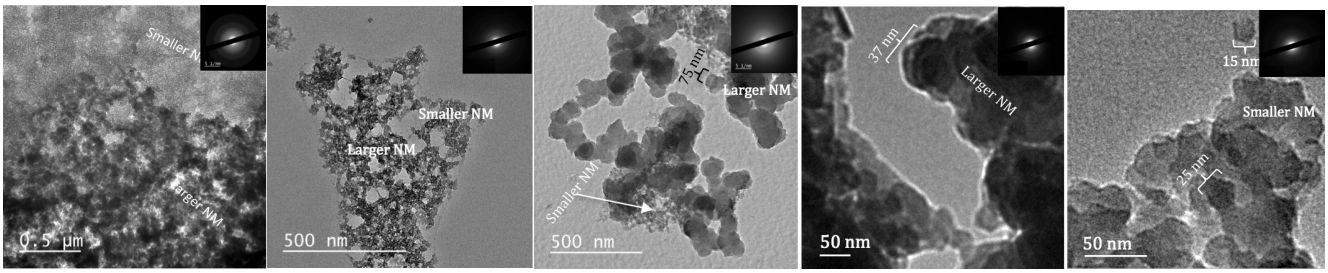

Figure 7: Micrographes électroniques MET des sroMOAs - série à pH=5: (de gauche à droite):' No C', M: C=10, M: C=1, M: C=0,1 et M: C=0,01. Et des modèles de diffraction d'électrons diffusés pour toutes les phases. Les sroMOA LP et les sroMOA SP désignent respectivement les sroMOA des particules plus grosses et des particules plus petites.

Les analyses MET-EDX des particules sont présentées sous forme de diagrammes à la figure 9 pour Fe, Si, Al, K et Mg pour chaque rapport M: C. Les compositions chimiques des petites phases nanoparticulaires (figure 9A) se trouvent à proximité immédiate de la concentration de la solution de lixiviat avec un léger enrichissement en Fe, Si et Al et un appauvrissement important en K et Mg.

Table 5: Analyse de la taille des images MET.

Size (nm)	No C	M:C=10	M:C=1	M:C=0.1	M:C=0.01
Smaller Particles	2 to 15	2 to 20	5 to 35	-	15 to 60
Larger Particles	10 to 50	10 to 40	55 to 200	10 to 90	35 to 72

Les nanoparticules les plus grosses, au contraire, ont montré un profil dépendant de la teneur en C pour tous les éléments sauf K et Mg. Si s'est avéré important à de faibles teneurs en C (No C et M: C=10) en montrant un enrichissement par rapport aux faibles concentrations de Fe et Al appauvries.

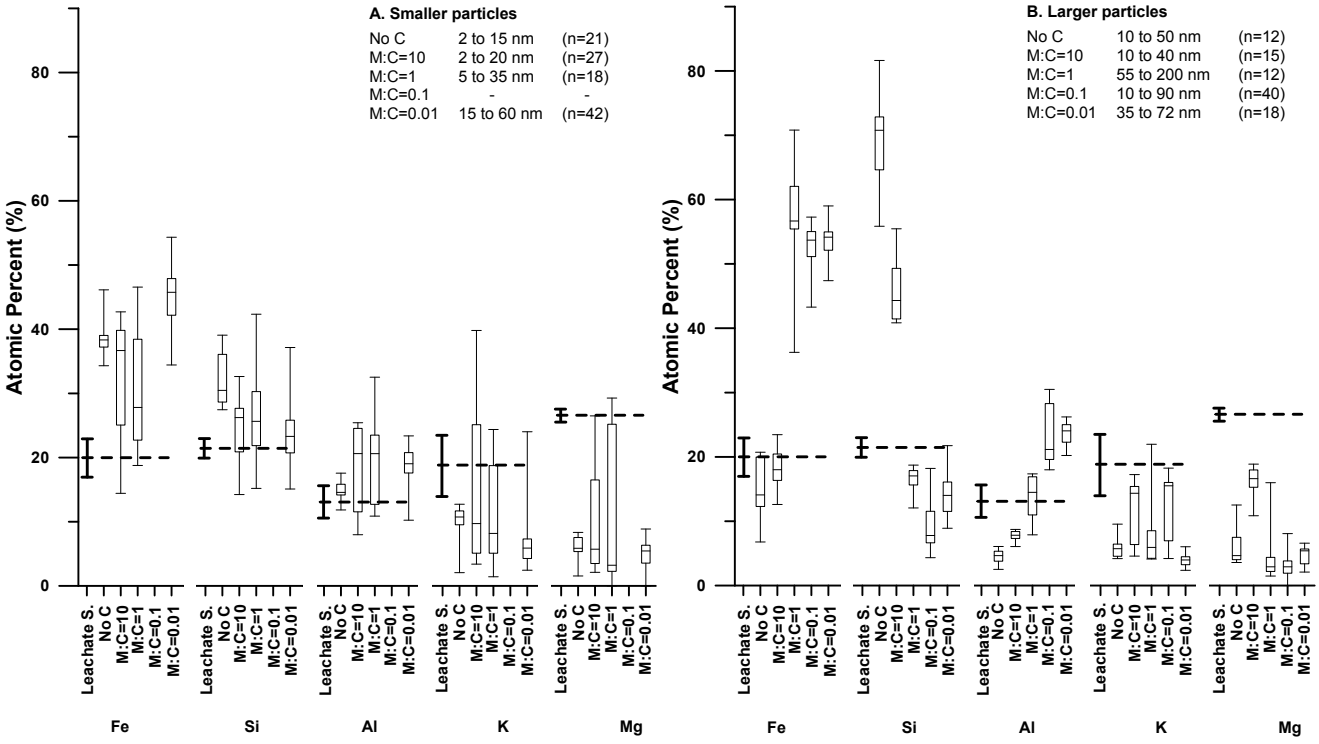

Figure 8: Analyse chimique MET-EDX des particules polymérisées aux cinq rapports molaires M: C sous la forme d'un "box-and-whisker". A: nanoparticules de plus petite taille; B: nanoparticules de plus grande taille. n:

nombre de particules analysées. La composition chimique de la solution de lixiviat (Leachate S.) est également présentée à des fins de comparaison.

A une charge C plus élevée (M: C=1,0,1 et 0,01) au contraire, la contribution du Fe est importante (et dans une moindre mesure aussi de l'Al) et le Si contribute dans une moindre mesure. En ce qui concerne le K et le Mg, les nanoparticules plus petites et plus grosses ont montré un appauvrissement par rapport à la solution de lixiviat. Généralement, nous observons la concentration d'OC à M: C=1 comme un point de bascule où les écarts par rapport à cette concentration de C se traduisent pour les nano phases par des caractéristiques opposées.

1.10. Discussion

1.10.1. Deux stades de précipitation: croissance et maturation

La formation des sroMOA prend différentes voies en présence d'une quantité significative de C (c. -à-d. M:C≤1) par rapport à des échantillons faibles ou dépourvus de C (chapitre 3). Cette interference avec le C se manifeste directement sur la taille, la composition chimique et la structure des phases formées (Kleber, et al., 2015). Les différences de composition chimique en fonction de la taille sont illustrées sous forme d'un diagramme ternaire pour Fe, Si et Al à la figure 10.

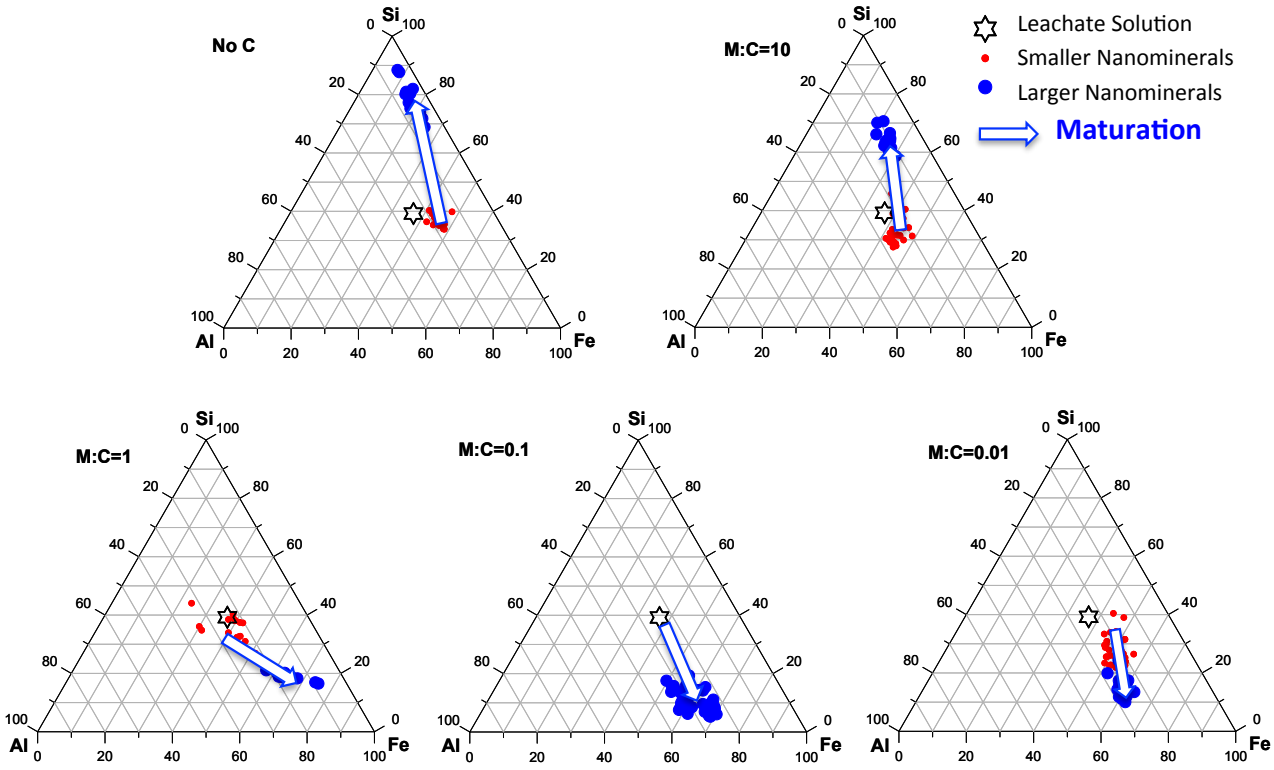

Figure 9: Diagrammes ternaires des proportions atomiques de Fe, Si et Al dans les nanophases. L'étoile noire représente la composition initiale de la solution de lixiviat, les petits points rouges représentent la composition de nanominéraux plus petits et les plus grands points bleus la composition de nanominéraux plus gros. La flèche blanche représente le processus de maturation.

En plus de la différence dans la taille des particules, ces deux ensembles de clusters montrent un contraste dans la composition chimique et dans la façon dont elles interagissent avec C. Les particules plus petites, quelle que soit la teneur en C ajoutée, ont une composition chimique proche de la solution de lixiviat initiale, avec un faible

enrichissement en Fe qui signale un processus de précipitation presque congruant. Cette similarité propose que ces particules plus petites soient probablement les produits initiaux de nucléation et de croissance. Les matières organiques ne semblent pas avoir d'effet sur le processus de nucléation en termes de composition chimique.

Les particules plus grosses présentent des coprécipitations en différentes phases dont la composition chimique diffère de celle des particules plus petites, de la solution de lixiviat et aussi les unes des autres à des concentrations de C variables. La différence de chimie entre ces deux tailles dans un même échantillon exclut toute possibilité d'agrégation. Il est plutôt possible que ces particules plus grosses se forment pendant qu'on modifie chimiquement la phase de croissance (c. -à-d. après l'étape d'hydrolyse), qui est fortement affectée par l'abondance de C (An, et al., 2010).

La figure 9b illustre deux régimes de composition chimique. La première comprend les phases No C et M: C=10 tandis que la deuxième comprend les trois phases restantes. Le changement observé lors du passage de M: C=10 à 1 est la preuve d'un déplacement du schéma de croissance des nanophases lorsque la proportion de C augmente et atteint l'égalité avec celle des métaux (Fe et Al).

1.10.2. Deux mécanismes de croissance des sroMOAs

Dans les batches de précipitation, en se basant sur nos données LCF, deux mécanismes de croissance ont été observés. Sur addition de OH- nous avons d'une part la neutralisation des espèces dissoutes cationiques/métalliques en solution où par hydrolyse inorganique des métaux et polymérisation des minéraux est favorisée. Le deuxième mécanisme porte sur la complexation de Fe avec OC. Cette dernière interaction augmente avec l'augmentation de la concentration en C. Par conséquent, les données de la LCF montrent que nous avons un changement entre deux mécanismes concurrents. Cette transition est controlée par la proportion de C dans le système à une valeur de transition M: C de ∼1. Conditions optimales de coprécipitation des sroMOAs.

1.10.3. Comparaison avec les sroMOA de batchs étudiés dans les travaux antérieurs dans la littérature

Ce qui distingue nos constatations, c'est que toutes les phases formées sont ordonnées à courte portée. La présence d'autres cations inorganiques (tels que Si, Al, etc.) et C contribue à l'absence de cristallinité dans nos polymères Fe.

Pour les phases formées en conditions M: C=10 &' No C', les complexes n'étaient pas plus avancés que les polymères Fe par arete. Cela ne prend pas en compte la teneur en C, ce qui s'est finalement traduit par un enrichissement en Si et un appauvrissement en Fe (figure 9B). Dans les phases formées à M: C=1,0,1 et 0,01, contrairement à l'enrichissement significatif en Fe, aucune preuve des interactions Fe-O-Fe attendues n' a été observée en raison de la teneur élevée en C. Ceci prouve l'affinité préférentielle de "C en abondance" pour Fe mais en même temps son caractère perturbateur pour la polymérisation des phases inorganiques (Vilgé-Ritter, et al., 1999). Ce phénomène dans les coprécipités a été examiné par Kleber et al. (2015) comme étant la tendance des oxydes métalliques à s'enfoncer dans une matrice organique (Pédrot et al., 2011; Mikutta et al., 2014) en présence élevée de C, ce qui se traduit par des sous-unités plus petites de MOA (Vilgé-Ritter et al., 1999). Les résultats de cette étude ont montré que cette forte présence de C a entraîné l'inhibition de la coordination Fe - Fe fortement favorisée.

1.11. Conclusion

La formation des particules plus petites n' a pas été affectée par la présence variable de C dans le système. Mais avec les particules plus grosses, une faible présence de C (No C et M: C=10) s'est traduite par une contribution majeure de Si dans les MOA, alors qu'une présence de C élevée (M: C=1,0,1,0,01) s'est traduite par une contribution majeure de Fe (et Al mineur) dans les MOA. Lors de l'étude du rôle que jouent les espèces inorganiques dans la stabilisation de l'OM, le Si est fortement sous-estimé, tandis que l'accent est davantage mis sur le Fe et l'Al. nos résultats démontrent l'importance du Si, en particulier dans des conditions de faible présence de C.

Les précipités subissent des stades de croissance et de maturation beaucoup plus avancés en présence de C plus élevés. L'augmentation de la concentration en C par rapport au rapport M: C=1 a donné les conditions optimales de maturation qui ont entraîné la formation de grosses particules (200 nm). Même augmentation à M: C=1 définit les conditions dans lesquelles la préférence du carbone pour le complexation est passée de Si à Fe.

Conclusions

Au cours de cette étude, l'objectif général était de mieux comprendre la dynamique naturelle des MOS. Comme on l' a étudié dans les différents chapitres, les sous-objectifs comprenaient (1) répondre à des questions liées à la compréhension de la synthèse de nCOMx dans un système contrôlé à l'échelle du laboratoire et (2) étudier leur dynamique. Une autre question était également de savoir si le protocole des expériences permettait d'obtenir des nanominéraux représentatifs des systèmes naturels.

La première étape importante a été de simuler l'altération d'un minéral primaire, la biotite. Indépendamment de l'incongruité de la dissolution, l'objectif principal a été atteint en produisant une solution d'espèces véritablement dissoutes, qui ont constitué les principaux éléments constitutifs de la synthèse de nos nouveaux nanominéraux.

Dans la précipitation de nanominéraux inorganiques, l'objectif était d'étudier l'effet du pH sur la formation et la structure des phases synthétisées. La taille des particules inférieure à 60 nm à tous les pH signifie que nos expériences étudient les stades initiaux de la formation. Spécifiquement, les compositions élémentaires des précipités étant uniquement dominées par le Fe à pH 4,2 et 7 et par le Si à pH 5, l'interaction complexe qui résulte de notre choix d'une solution de lixiviat qui a au moins cinq éléments principaaux.

Avec la deuxième série d'expériences de synthèse, les résultats ont montré que le protocole conçu était efficace, non seulement avec les espèces inorganiques mais aussi en présence de carbone organique. Cette étude a également démontré que l'OM pouvait être coprécipité non seulement par les espèces Fe et Al mais aussi par les produits d'altération des minéraux silicatés. Ce cheminement dans les systèmes naturels aboutit en fin de compte à des phases amorphes, ce qui était également évident dans nos expériences en laboratoire en raison de l'interaction principalement entre les espèces C, Fe et Si. Cette étude a également démontré l'importance qu'il faut accorder au Si dans les études de coprécipitation, en particulier en présence de MO..

La conclusion de cette étude est que les protocoles suivis pour la production de ces phases synthétiques ont été efficaces pour répliquer dans une gamme plus large de

phases amorphes naturelles ainsi que les processus de précipitation. Par conséquent, cette gamme plus large nous permet d'affirmer que notre étude représente effectivement un éventail plus large de systèmes de sols naturels (p. ex. andosols, podzols, etc.).

Manuscript (In English)

1 Introduction

1.1 Carbon, a global context

Our planet soils, the very top layer of the crust, are geo/bio-chemically different from the section just below them. In this top layer we find rocks, minerals, organisms, water, etc. interacting differently and to a varying extents depending on their geographical location. These components are ever changing by the continuous processes that are alive within this layer. Precipitation, ground water, erosion, change in temperature, change in chemical state, agriculture, global warming, etc. all contribute to giving it life and making it one of the most dynamic sections of our planet, which allows it to sustain life. For the soil to remain in such equilibrium, each components and processes has to play their parts in sustaining the stability of their system.

1.2 Global Carbon

Carbon (C) has been and is an essential component in biotic and abiotic processes on our planet for millennia. It is found in the different pools located in deep underground (rock), soil, ocean, atmosphere, etc. in different physical and chemical forms. Carbon takes 100-200 millions of years to move between the different pools through geochemical and climatic processes such as tectonics, erosion, rain, mineralization (U.S.DOE., 2008). The rather slower transfer processes involving the stable and less accessible C pools contributed to an annual 0.01–0.1Gt of carbon movement through the "Slow Carbon Cycle", while the quicker processes attributed to the "Fast Carbon Cycle" (i.e. the biosphere and life forms) contributed 10–100Gt of carbon movement annually (U.S.DOE., 2008) (Figure 10). Therefore, these numbers give a perspective to imagine the alarmingly increasing recent carbon emission into the atmosphere by human beings (9Gt/year) that is with in the global context that had harmonically long existed.

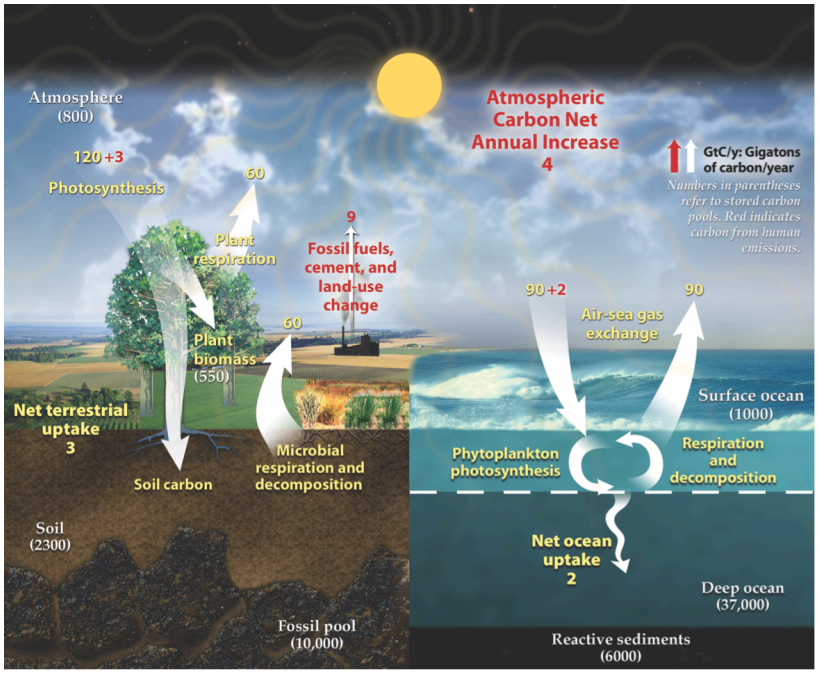

Figure 10: Carbon cycle showing the storage and movement of carbon between land, atmosphere, and oceans in billions of tons (Gt) of carbon per year. White numbers indicate C stock in the various pools, yellow numbers indicate natural fluxes and red numbers indicate human contributions. Diagram adapted from U.S.DOE. (2008).

1.3 Soil Organic Carbon (SOC)

A good part of the soil carbon pool is derived from a biotic origin, thus giving soil organic matter (SOM). Organic matter (OM), in addition to playing a key role in soil system performance, offers crucial control over ecosystem services such as soil fertility, water quality, resistance to erosion, and more (Millennium Ecosystem Assessment, 2005).

One reason, amongst many, that derives soil organic matter research is its contribution to the global carbon pool. SOM globally contributes to more than three times carbon in amount as compared to carbon in terrestrial vegetation or carbon in the atmosphere (Schmidt, et al., 2011). Organic matter (OM) approximately comprises 1% to 6% of top soil mass for majority of upland soils (Troeh and Thompson, 2005). Soil organic carbon in the top 1m depth is estimated to contribute between 1500 to 1600 Gt to the global SOC stock (Batjes, 1996; Monger and Gallegos, 2000; Lal, 2004; Shi, et al., 2012). Going deeper to the top 2m depth these SOC stock estimate increases to 2400Gt (Batjes, 1996; Stockmann, et al., 2013; Minasny, et al., 2017). For these reasons, the risk of release of large amount of greenhouse gases (such as carbon dioxide and methane) into the atmosphere is higher with slight fluctuations or disturbance of this vast C pool as compared to threat from the terrestrial and/or atmospheric carbon pools (Lehmann and Kleber, 2015).

In order to answer the question 'why is SOM important?' one needs to clarify this broader view and justify this SOM importance in spite of the relatively smaller portion it contributes in the global carbon context (Figure 11). According to the report by the U.S.DOE. (2008), the soil carbon pool covers ~4% of the global carbon stock (Figure 11). The relatively larger global carbon pools in fossil deposits, the deep ocean and the reactive (marine) sediments contribute 4, 16 and 2 times more carbon respectively than SOM. But soil carbon pool stores more carbon than plants and the atmosphere combined. Irrespective of all of that, change in land use (more so with abusive human activities such as poor land management) is leading to the untimely cycling or perturbation of this vast reservoir, making it a major carbon contributor to the atmosphere. These phenomena, therefore, left us with the much discussed and debated 'global warming' present day issues; which by themselves have a 'chain reaction' of more global carbon destabilization due to rise in temperature.

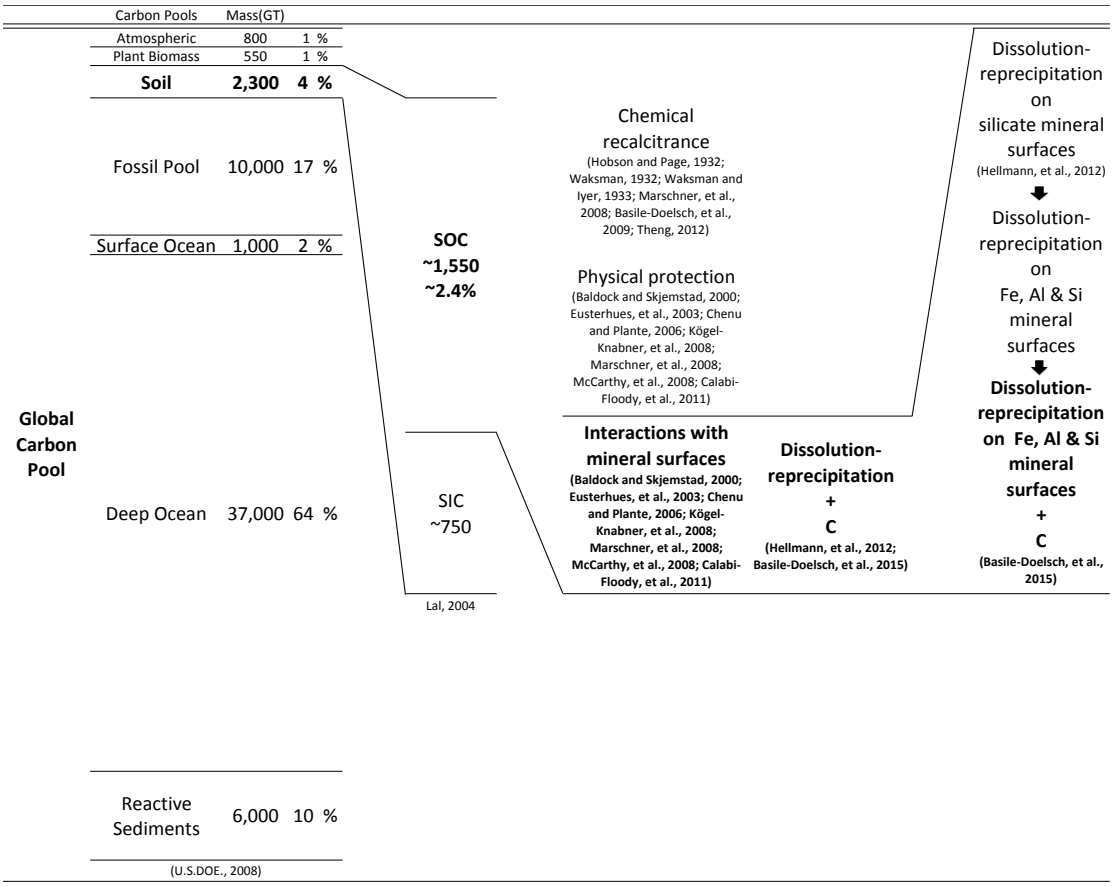

Figure 11: The different carbon pools, C stabilization mechanism in soil and emerging weathering thoughts (Global to nano scale). SOC stand for Soil Organic Carbon and SIC stands for Soil Inorganic Carbon. Areas of study of interest to this PhD are highlighted in bold. (Hobson and Page, 1932; Waksman, 1932; Waksman and Iyer, 1933; Baldock and Skjemstad, 2000; Eusterhues, et al., 2003; Lal, 2004; Chenu and Plante, 2006; Kögel-Knabner, et al., 2008; Marschner, et al., 2008; McCarthy, et al., 2008; U.S.DOE., 2008; Basile-Doelsch, et al., 2009; Calabi-Floody, et al., 2011; Hellmann, et al., 2012; Theng, 2012; Basile-Doelsch, et al., 2015)

Relying on recent global C cycle data compiled from the years 2005 to 2014 a recent global carbon budget report estimates C emission to the atmosphere due to land use to be close to 0.9±0.5 Gt C/year (Le Quéré, et al., 2015) (Figure 12). This contribution ten times less than data recorded for fossil fuels and industries may seem comparatively negligible, but given time even these releases accumulate to a significant contribution. In the years between 1850 to 1998, as a result of change in land use, a collective 136±55Gt of C has been released into the atmosphere (IPCC, 2001) (156 Gt of C for between 1850 to 2000 (Houghton, 2003) for the same reason). ~57% of that is estimated to be contributed by anthropogenic related depletion of SOC (Lal, 1999; Lal, 2004). A more recent report by FAO (2014) and IPCC (2014) of two (1990-2011) and four decades (1970-2010) of study puts this contribution specifically from agriculture, forestry, and other land use (excluding sequestered carbon) at 24% of global greenhouse gas emissions. And these reports also confirm these specific emissions to have doubled since the 1950s, and that they are expected to increase by 30% by 2050.

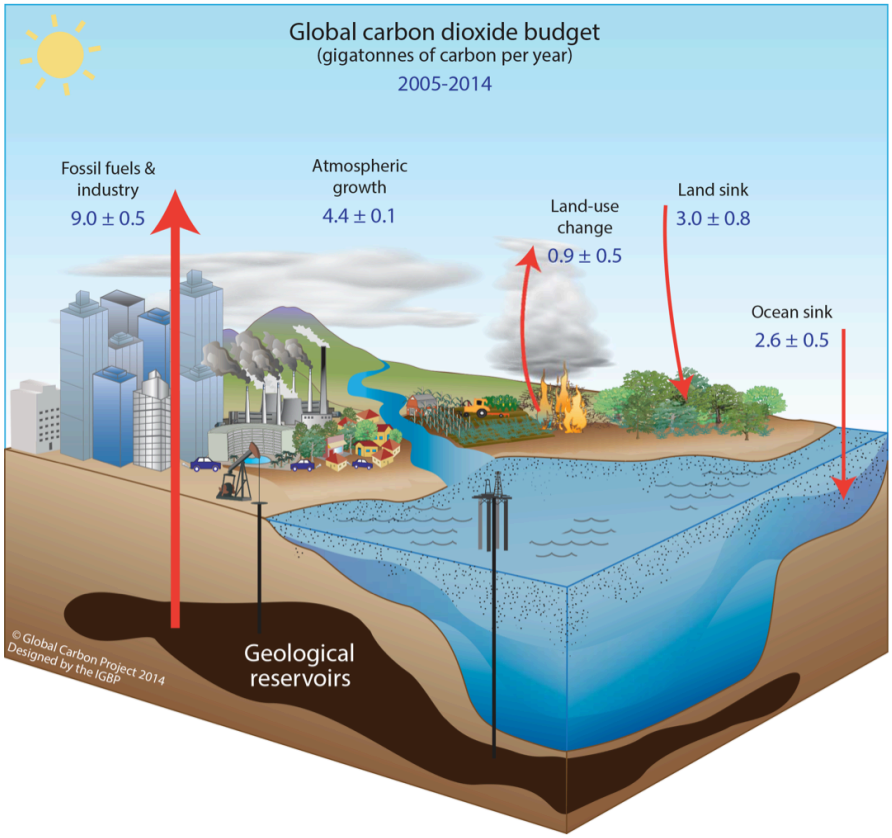

Figure 12: Schematic depiction shows the five most active major categories that are swaying the global C cycle/stock. Adopted from Le Quéré, et al. (2015).

Moreover, soil carbon stock merits more attention due to the crucial role it plays in keeping up the soil quality and its structural integrity intact. This intertwines SOM to soil fertility and ability to produce life giving and supporting processes, upon which human life sustainability is critically dependent on (Figure 13).

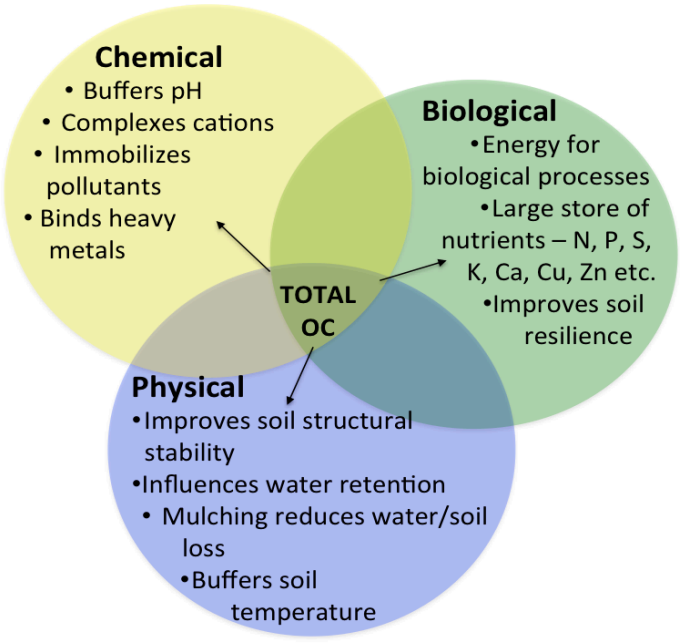

Figure 13: Chemical, physical and biological benefits of SOM from FAO (2005).

Therefore, the questions that we need to ultimately ask and to a certain degree have been asked by some (Kleber, et al., 2007) are 'why is SOM important?', 'how does SOM interact with minerals and mineral surfaces?', 'how strong are these interactions?', 'what affects the sustainability/stability of these interactions?', 'how do these interactions eventually break?' and 'how all these affect SOM residence time in the soil matrix?'.

OM associations to minerals contribute greatly to the biogeochemical cycle of surface carbon (Lagzi, et al., 2013). If applied properly processes such as sustainable agricultural practices could off-set this C emission to the atmosphere to the positive and insure future food, water, energy security (Jain, et al., 2005). Recent global and regional projects such as '4 per mille initiative' to increase soil C stock are good examples of these initiatives that are aiming to tip the balance against global emissions of greenhouse gases due to anthropogenic sources (Minasny, et al., 2017). Studies are also pointing out to the additional benefit of improved soil structure and conditions that come along with increasing the SOC stock (Lal, 2016). Improvements due to change in soil management are also vastly reported (Chen, et al., 2015).

1.4 Organo-mineral interactions

Carbon in soils is mostly found interacting with inorganic soil components thus giving rise to organo-mineral interactions. Mineral phases play a major role in this interaction, which ultimately stabilizes SOM (Basile-Doelsch, et al., 2005; Basile-Doelsch, et al., 2007; Basile-Doelsch, et al., 2009). This strong association is exhibited inmost soils except in soils in water logged and high altitude areas (Christensen, 1992; Sollins, et al., 2009; Wagai, et al., 2013). It is crucial for the preservation and cycling of organic carbon (OC) as well as for the dynamics of the minerals themselves (Jones and Singh, 2014). The importance of this relationship arises from the essential transfer of OC from the quick atmosphere-biosphere carbon cycle to the slower cycling stable soil carbon pool (Masiello, et al., 2004). And this crucial role minerals play in protecting OM from microbial mineralization was acknowledged as far back as six decades ago (Jung, 1943; Allison, et al., 1949).
Understanding organo-mineral interaction would require understanding the molecular structure of SOM (Kleber, et al., 2007). Most studies argue good organo-mineral interactions occur with finer mineral particles (Kleber, et al., 2007). In soils suitable for cultivation in temperate regions, clay-sized fractions hold 50-75% of the OM with the proportion declining to 20-40% in the silt fraction and <10% in the sand fraction (Christensen, 2001). With up to 40% of the OM in the sand fraction existing in an uncomplexed state (Christensen, 2001).

Additionally, concepts that are driving recent organo-mineral interactions research is considering mineral surfaces as not stable but as continuously subjected to weathering which ultimately generates Si, Fe and Al based nanometric amorphous phases (Basile-Doelsch, et al., 2015). At first glance this could be understood as weathered minerals having increased surface area thus increasing C sorption sites (Mayer, 1994; Masiello, et al., 2004). Understandably so, relatively large amount of OM is present in soils such as Andosols and Oxisols due to its stabilization by allophane and iron oxides respectively where both have large specific surface and small particle size (Martin and Haider, 1986; Oades, et al., 1989; Oades, 1995; Parfitt, et al., 1997). However, C sorption on mineral surfaces does not adequately justify SOM stabilization in most soil systems (Mayer, 1999; Mayer and Xing, 2001; Masiello, et al., 2004). This implies the effect of weathering on SOM stabilization to be more complex and strongly affected by surface chemistry and

mineralogy of secondary phases (Guggenberger and Kaiser, 2003; Chorover, et al., 2004).

Moreover, in humid areas where most soil systems lack exchangeable calcium, SOM abundance can be associated with Al and Fe presence as intermediate metastable Al and Fe products of weathering processes (Kaiser and Zech, 1996; Torn, et al., 1997; Percival, et al., 2000; Kleber, et al., 2015). For instance Fe and Al as cations can inner-sphere complex with oganic ligands such as carboxylic functional groups (Higashi, 1983; Boudot, et al., 1989) and as minerals, their oxides, hydroxides, and oxyhydroxides are effective sorbents of dissolved OM (Kaiser, et al., 1997; Wagai, et al., 2013). Therefore, in these cases which are strongly associated with mineral surface dissolution, SOM stabilization mechanisms are associated not only with the presence of Al^{3+}, Fe^{3+} and clay minerals (Sollins, et al., 1996; Baldock and Skjemstad, 2000; Wagai, et al., 2013) but also nanometric short-range ordered polymers mainly consisting of hydrolyzed Al, Si, and Fe species (Masiello, et al., 2004; Basile-Doelsch, et al., 2015).

In a SOM model, Kleber, et al. (2007) assume SOM to be a heterogeneous mixture of compounds capable of self-organizational behavior in aqueous solution which means it's interaction with mineral surfaces occurs in distinct zones (Figure 14).

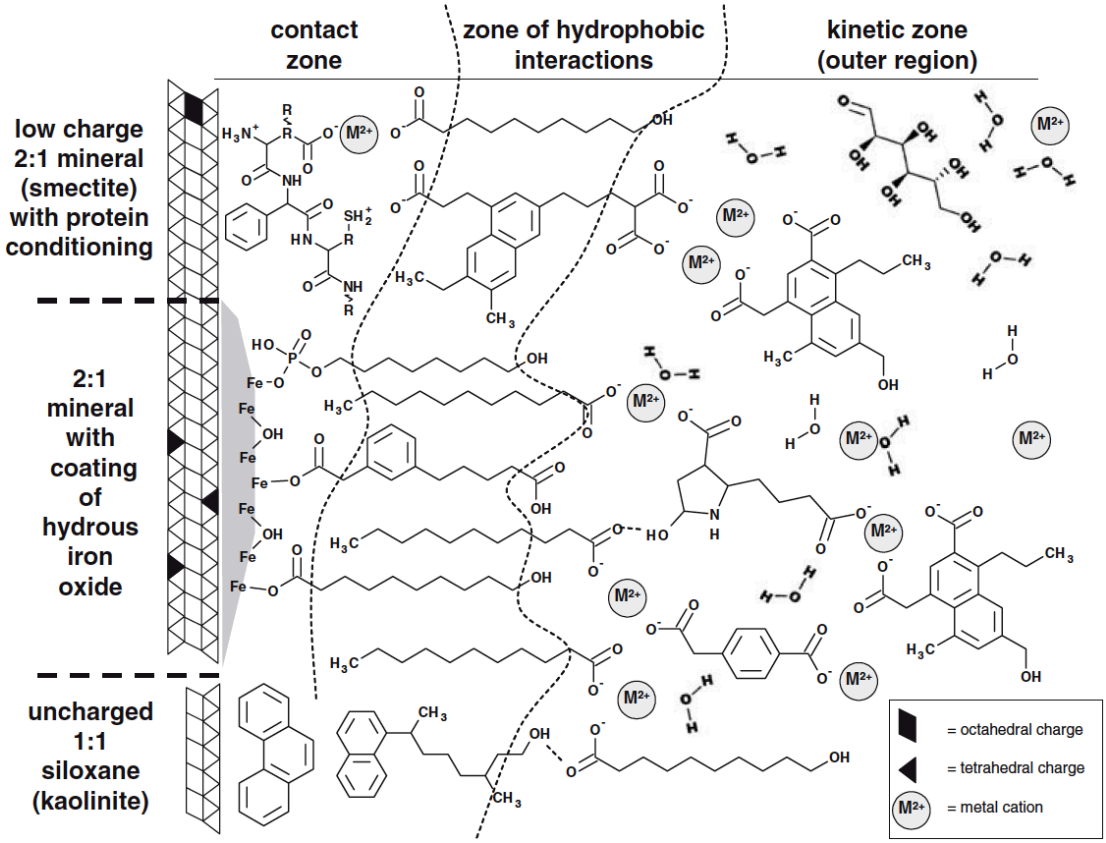

Figure 14: Model description of an assumed heterogeneous SOM content and it's zonal interaction with heterogeneous mineral surfaces. Figure from Kleber, et al. (2007)

In their zonal model of organo-mineral interactions they summarize the near surface interactions in the vicinity of various minerals surface types. The model does not indeed exemplify the full range of mineral surface types but it illustrates major bonding mechanisms and areal partitions with regard to bonding near surfaces. The presence of

compounds in the 'contact zone' is influenced through charge interactions with the mineral surfaces. Charged surfaces in this zone accumulate amphiphilic compounds via electrostatic interactions. According to their model, siloxane surfaces with low-charge also get additionally polarity functionality through proteins. The same interaction that attracts the amphiphilic compounds to the surface pushes away hydrophobic compounds into the polar aqueous zone thus resulting in 'zone of hydrophobic interactions'. Accumulation of organic molecular fragments in the outer region probably due to the presence of multivalent cations creates the 'kinetic zone', whose thickness is probably to be influenced by the addition of organic compound and thus to be principally be controlled by exchange kinetics.

1.5 Nanoscale Organo-Mineral Complexes (nCOMx)

nCOMx is a generic name applied to organo-mineral complexes when they are viewed at the nanoscale. These nanoparticles are known to be abundantly found in soils such as andosols of volcanic rock origins as minerals such as imogolites and allophane (Tonneijck, et al., 2010) also as an even smaller particles called proto-imogolites (Levard, et al., 2012; Basile-Doelsch, et al., 2014).

Even though OM is historically quantified to be exceedingly more stabilized in soils such as andosols, nCOMx are evidenced to exist in other soils types too. That is in soils, which do not tie their origin to the weathering of volcanic glass.

Kawano and Tomita (2001) studied a crystal of bytownite (feldspar plagioclase) that was altered in a natural environment. Their image analysis showed a 100nm altered layer that spanned the entire mineral surface, which was composed of nCOMx of a C complexed amorphous phase. Also a study by Chenu and Plante (2006) could be considered a second example where nCOMx are found as C embedded between stacks of clay platelets in an acrisol from Touyas, France. The chemical analysis of the nCOMx in this soil showed evidence of OM association with abundant Si, Al and to a lesser extent Fe. Other soils such as Andosols, Cambisols, Phaeozems, Umbrisols and Podzols studied from Italian soils are also good examples of presence of properties related to nCOMx in soils irrespective of difference in taxonomic Iamarino and Terribile (2008).

When mineral surface are exposed to weathering (physical/chemical) their compositions get leached from the surface down leaving behind zones of varying alteration (Figure 15). These zones advance deeper with more weathering that the surface is exposed to. Eventually, at zones close to the mineral-solution interface enough dissolved material will be present to give rise to re-precipitates often of an amorphous nature. These re-precipitates as well as the abundant presence of dissolved inorganic and OM will give rise give the perfect reaction partners in the formation of nCOMx.

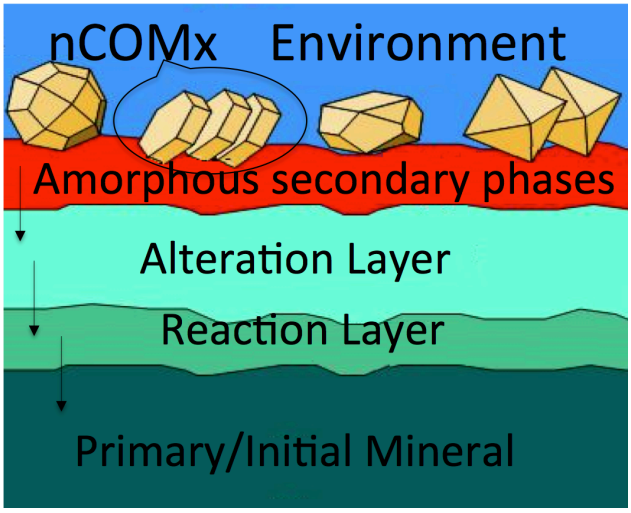

Figure 15: Illustration of different zones along an alteration path from the surface of primary minerals.

Therefore, there is plenty of proof for the existence of organo-mineral associations but the emerging technique of viewing these interactions on a nanometric scale is only recently being carried out (Chenu and Plante, 2006; Lehmann, et al., 2007; Levard, et al., 2012).

On a slightly larger scale, organo-mineral interaction nanometric scale was numerically best demonstrated by Leinweber and Schulten (1999) (Figure 16). Their model of a mineral-bound heavy organic particle illustrates the interaction between silicate layers, humic acids, labile carbohydrates and peptides, pedogenic Fe oxides, and alkali and alkaline earth cations. This model is at the limit to 3D-molecular mechanics calculations, which is approximating molecular structures at the soil surfaces. This effective approximation of organo-mineral interactions thus allows better visualization of nCOMx and also advances SOM research with such representative simulations of chemical reactions in soil systems.

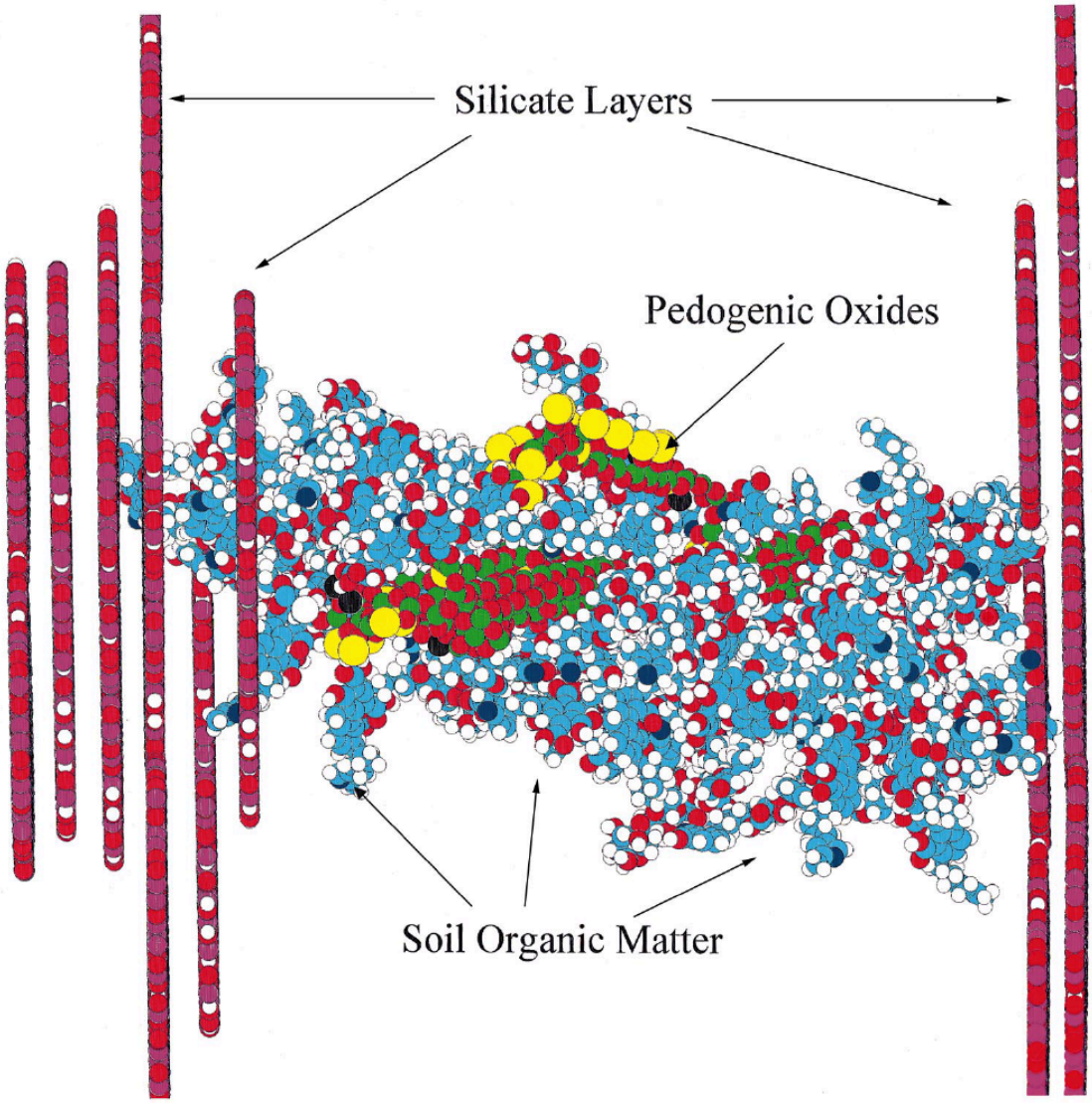

Figure 16: Model of a heavy, mineral-bound organic particle with 30837 atoms with: (1) 16 subunits (1068 atoms each) of mineral matrix of silicate layers, (2) bonded to 13749 atoms of SOM (complex of humic acids) (3) trapped labile carbohydrates and peptides, (4) pedogenic Fe oxides, and (5) alkali and earth alkali cations. Colors: white=hydrogen, sodium and potassium; cyan=carbon; red=oxygen; blue=nitrogen; violet=silicon; green=iron; yellow=calcium; and black=magnesium. Figure from Leinweber and Schulten (1999). (Chen, et al., 2015)

1.6 General objectives

General aim is to better understand natural SOM dynamics. That will entail understanding the soil mass with regard to better preserving its OM content. SOM dynamic is a complex process. Therefore, this study aims at synthesizing nCOMx and studying their dynamics at a laboratory scale. In doing so it will assess mechanisms of nCOMx formation and synthesis in a controlled system. It will also demonstrate the changes in the precipitation steps in the presence of OM (Crystal growth/ structural order hindrance). Knowledge gained from these studies will therefore help understand the mechanisms of stabilization/ destabilization of SOM using laboratory based synthesis approach. Therefore, focus will be on an emerging view involving the stabilization of SOM by means of physiochemical interactions with inorganic soil phases and altered surfaces. That specifically will involve interacting OM with poorly crystalline phases. The attention of this work will also be focused on the inorganic and organic soil

components individually and the interaction that exists between them.

1.7 Structure of manuscript

After this introduction section the following 'State of the Art' chapter will summarize in detail weathering and mineral synthesis processes as well as studies on organo-mineral interactions. Following that, results will be presented in four consecutive chapters. First of those, chapter 3, will detail preliminary experiments carried out on basalt and biotite minerals which finally aided in the design of protocols for three main sets of experiments (chapters 4 to 6). Next two major chapters will present the steps taken (weathering + precipitation) that led up to the formation of inorganic nanominerals and nano organo-minerals. That is, chapter 4 will discuss the formation of inorganic nanominerals (no C) as affected by variations of soil pH conditions. This chapter is presented as a paper. It was submitted to GCA the 5th of September. While chapter 5 will discuss the formation of nano organo-minerals as affected by variations of soil C concentrations. This chapter is also presented in a paper format but still in preparation. A last and smaller chapter (chapter 6) will make a comparable study on nanomineral formation and their structure when they are precipitated from an artificial metal salt mix instead of natural mineral weathering product. Note: Samples synthesized in this chapter 6 were not entirely characterized and analysis was also not carried out to the full extent. Therefore, reader should take information therein as a perspective work that will be finalized afterward. Final chapter (chapter 7) will summarize the entire work and make conclusions according to results obtained as well as analysis and discussions carried out.

2. State of the art and objectives

2.1 State of the art

According to a review by Kleber, et al. (2015) the most active mineral components in Mineral Organic Associations (MOAs) in nature are metal oxy-hydr-oxides, short-range ordered aluminosilicates and phyllosilicates. They further specify the reactivity of these inorganic phases to be dependent on size, shape, surface topography and degree of aggregation; as well as the properties of their surface functional groups such as type, charge and abundance. Some of these poorly crystalline aluminosilicates include phases of Al and Si layers such as proto-imogolites and proto-imogolite allophanes often found in volcanic soils (Basile-Doelsch, et al., 2005; Levard, et al., 2012). Among the above mentioned mineral components in MOAs studies specify that poorly crystalline minerals, principally the very low polymerized aluminosilicates, play the major role in controlling C sequestration (Dahlgren, et al., 1993; Nanzyo, et al., 1993; Basile-Doelsch, et al., 2007). Nevertheless, due to their equally important contribution to C stabilization, Fe based phases also merit equal attention. Therefore, formation of MOAs is a complicated process. In consequence, this review will summarize studies done on MOAs in order to give fundamental understanding.

2.1.1 Weathering of mineral phases

A precursor process to formation of MOAs or formation of inorganic secondary phases is weathering of minerals. This process in nature is an important geo-physical/chemical processes mostly localized to the shallow depths of our crust. Certain changes to minerals occur due to changes in the chemical state of their environment in their immediate vicinity (Weissbart and Rimstidt, 2000; Oelkers and Gislason, 2001). Such changes as weathering of minerals and precipitation play a key part in element transport and cycles at the Earth's surface, because these processes redistribute and exchange materials between the solid and solution (Murakami, et al., 2003).

2.1.1.1 Mineral Dissolution Kinetics/Surface reactions

During mineral weathering, in most cases than not, the changes are localized to the surface of the minerals or to only shallow depths from the surface. Studies demonstrate these processes with simplified models as in Weissbart and Rimstidt (2000) of wollastonite dissolution (Figure 17 left), by Oelkers and Gislason (2001) of basaltic glass dissolution (Figure 17 middle) and by Schott, et al. (2009) of quartz hydrolysis using water (Figure 17 right).

Figure 17 (left) shows the weathering of the surface of the silica based wollastonite mineral through a simplified proton exchange processes. The scheme shows a two stages process where early stages break and release bridging cations leaving behind an altered layer; and a second stage characterized by advanced loss of structural integrity of the leached surface where monomers and polymers get released into the medium (Weissbart and Rimstidt, 2000).

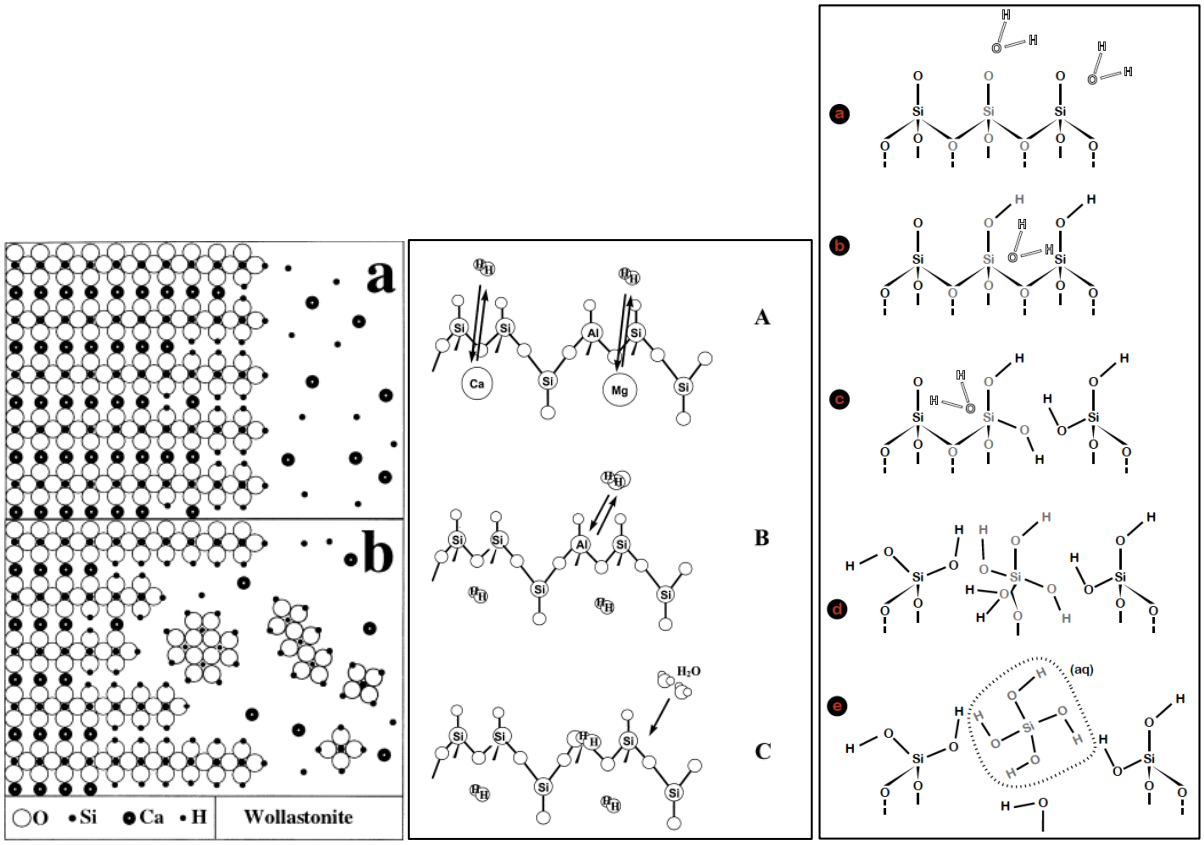

Figure 17: "Left" A conceptual model portraying two crude steps that are involved in the leaching of cations in silica-rich wollastonite. a) Ca released from structure into solution by hydrogen ions due to proton exchanged mechanism leaving behind a silica-rich leached layer of the approximate composition (H_2SiO_3). b) Release into solution of silica monomers and polymers from the leached layer due to the loss of structural integrity due to step 'a'. From Weissbart and Rimstidt (2000). "Middle" Illustration of dissolution mechanism of basaltic glass A) proton exchange reactions resulting in the removal of monovalent and divalent cations, B) proton exchange reactions resulting in partial removal of Al from the glass framework and C) again proton exchange leading to the final liberation of Si. From Oelkers and Gislason (2001). "Right" a model showing steps in water molecules successively hydrolyzing quartz by breaking individual Si-O bonds resulting in monomeric $Si(OH)_4$.From (Lasaga, 1995) and (Schott, et al., 2009).

Oelkers and Gislason (2001) describe the same process on basaltic glass but on a more intricate level using mathematical equations (Figure 17 middle). They discuss that initial stages involve removal of non-framework cations (e.g. Mg, Ca, etc.) through metal-proton exchange processes. Then advanced level of dissolution lead to the removal of framework cations beginning with Al and then finally reaching to Si. That last process effects loss of structural integrity by liberating Si tetrahedra. Both Figure 17 (left), (Figure 17 middle) and discussions there in deduce that in most cases than not, changes due to weathering are localized to the surface of the minerals or to only shallow depths from the surface. And depending on the strength of the factors impacting the chemical change and also duration of exposure to these changes, the alteration is proposed to proceed to the inner structure (Basile-Doelsch, et al., 2015).

Depending on the strength of the factors impacting the chemical changes and also duration of exposure to these changes, the alteration may proceed to the inner structural regions. In the case of a porous medium, Schott, et al. (2009) emphasizes on the extent of the porosity and pore connectivity influencing dissolved species transport thus ultimately influencing the dissolution surface reaction.

But often a natural weathering process is not as simple as demonstrated in above models. Various physical and chemical factors (grain size, ionic strength, pH, redox state, etc.) play a role that complicates the task of understanding the processes more. One environmental control that plays an essential role in mineral dissolution mechanics is the chemistry of the medium; a major component to that being the pH state. Protons break structural bonds. Acidic conditions therefore facilitate the weathering of minerals increasing the release of dissolved species into solution. This phenomenon gives abundant precursors for mineral-organic associations (MOAs) thereby favoring their formation in the long run.

Another parameter contributing to the chemical alteration of the soil environment is the redox state. Effect of redox state in most natural conditions is observed in non-aerated (oxygen deficient) environments such as gelisols, gleysols, peatlands, as well as in grounds contaminated by drainage from acid mines which often experience Fe(II) build up (Kleber, et al., 2015). In minerals this same effect observed in iron and sulfur bearing phases with reduced oxidative state such as pyroxene containing Fe2+. In locations where these changes in redox state are seasonal, the oxidation-reduction cycles often leave minerals with highly weathered structures (Brinkman, 1970; van Breemen, et al., 1983).

In a microbially controlled system, Bennett, et al. (2001) argues these organisms to aggressively alter weathering patterns. They reported olivine to be more stable than microcline (contrary to pattern expected from goldich dissolution series) due to the nutrient oriented and selective weathering of minerals in these anaerobic environments. Additional factor could be minerals are most stable in environmental settings closest to the conditions of their formation (Goldich, 1938). Therefore, soil chemistry and mineral surface alteration are controlled by kinetic, which remains very difficult to address. In addition, surface alteration form very reactive transient species that are difficult to characterize due to their unstable and amorphous nature (Kawano and Tomita, 1995).

2.1.1.2 Rate and mechanisms of surface alteration

The rate of dissolution of silicate minerals is a function of the abundance in solution of H^+ and OH^- ions (Blum and Stillings, 1995; Berner and Berner, 1996; Murakami, et al., 1998). Therefore, surface reactions involving these ions play a key role in controlling dissolution of minerals and eventually or simultaneously precipitation on to them

At the solid-liquid interface dissolution rate is usually controlled by the slower of two processes, namely 'diffusion controlled reaction' and 'surface controlled reaction'. These two mechanisms take control depending on various factors such as pH, pressure, temperature, mineral structure, surface defects, the reactive surface area, adsorbed ligands, ΔG of the mineral and connectivity of the system; thus resulting in a dissolution rate highly lacking pattern and uniformity for different minerals (Figure 18) (Lüttge, et al., 1999; Brantley, 2008; Schott, et al., 2009).

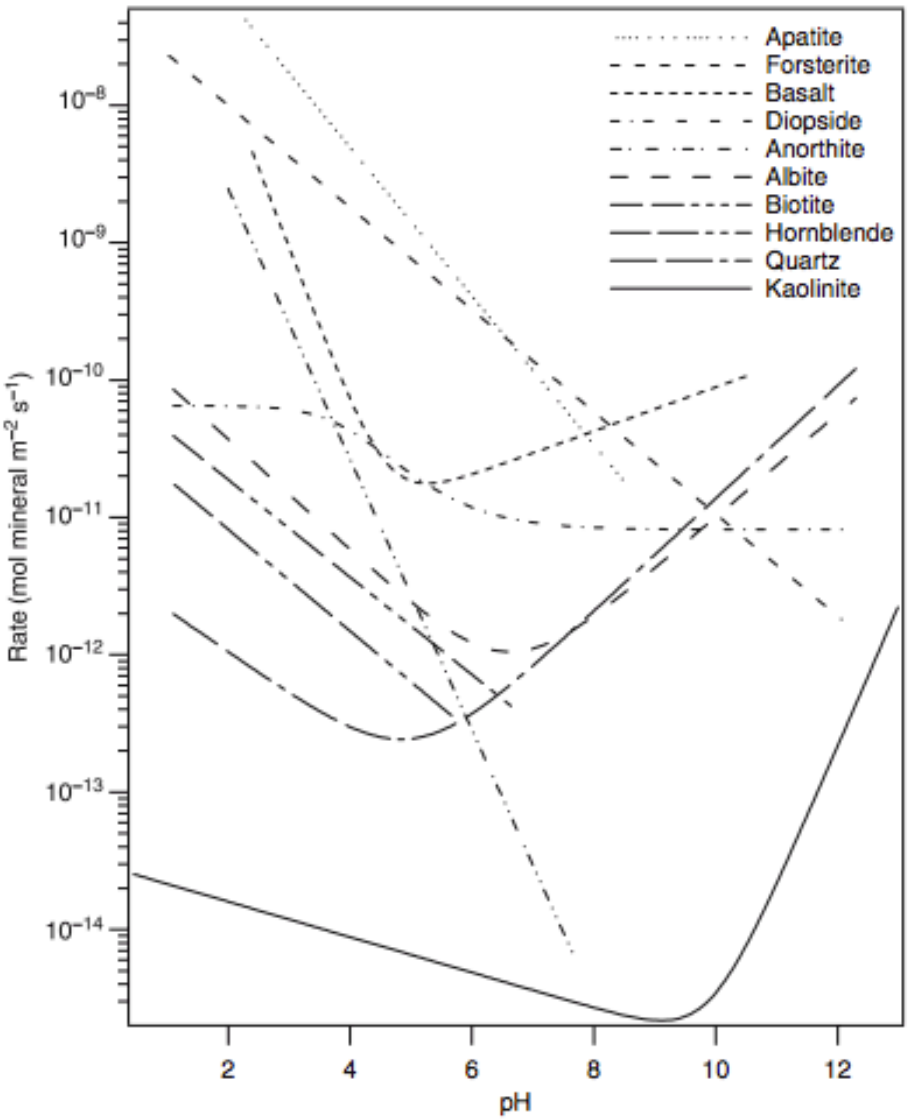

Figure 18: Dissolution rates predicted as a function of pH. Figure from Brantley (2008).

'Diffusion controlled reaction' for minerals such as silicates refers to slow transport through an alteration layer on the mineral surface due to non-stoichiometric release of cations more than silicon (Schweda, 1990; Stillings and Brantley, 1995; Taylor, et al., 2000; Brantley, 2008; Schott, et al., 2009). But given time, stoichiometric release of cations will be attained for many silicates.

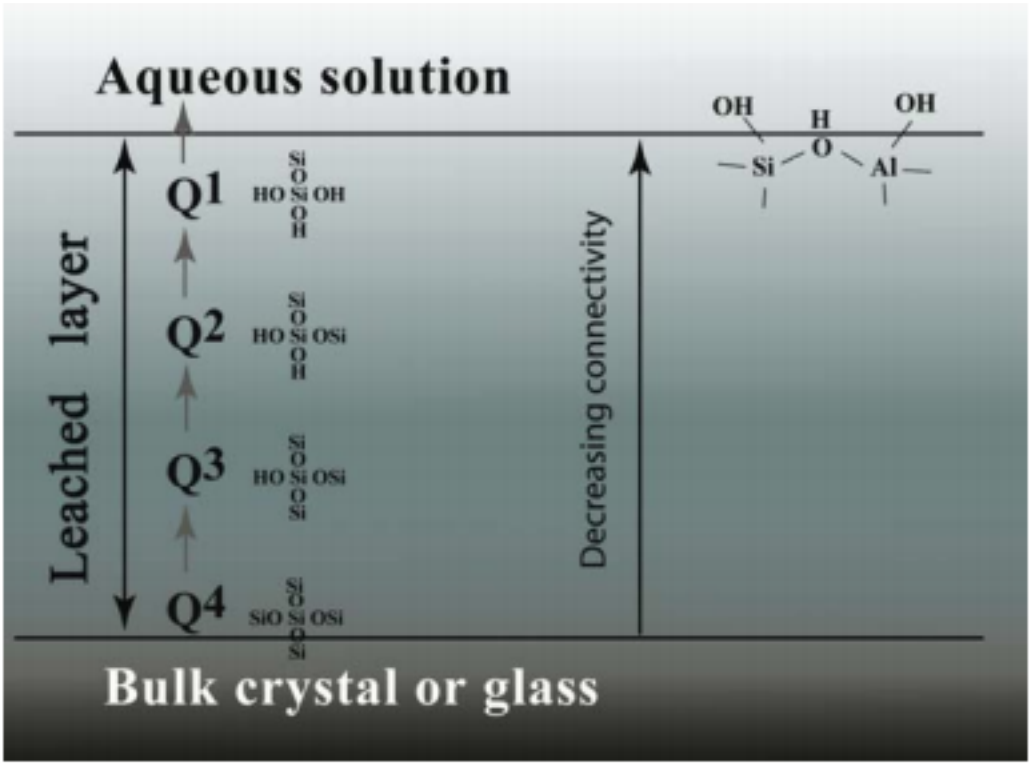

Figure 19: Silicate surface dissolution. Figure from Tsomaia, et al. (2003).

For silicate minerals, these processes are best portrayed with a simplified model as in Figure 19 where the dissolution process leads to protonation of species departing from the surface with the help of bridging oxygen (Q4 -> Q3 -> Q2 -> Q1). This process begins with Si tetrahedron surrounded by four other Si tetrahedra in the bulk crystal (Q4 state). With protons starting to take effect in the system, the bridging oxygen between two tetrahedra moves to one central Si atom. The charge deficiency gets neutralized with a proton on one side and an OH^- on the other, thus advancing the stage to the Q3 state. This process continues until all four coordinations are severed resulting in a Q0 state with an isolated Si tetrahedron ($Si(OH)_4$). This Si local coordination in the model transiting in the other direction (Q1 -> Q2 -> Q3 -> Q4) can also be a model for a precipitation processes (Tsomaia, et al., 2003; Brantley, 2008).

Dissolution pattern becomes slightly more complex with minerals with more complex structures such as clay minerals. Specific to these minerals with flat morphology dissolution proceeds by an edge attack mechanism resulting in an altered silica-enriched rim that is produced by leaching of interlayer (K^+, Na^+) and octahedral (Mg^{2+}, Fe^{2+}, Fe^{3+}, Al^{3+}) cations selectively through the (hk0) surfaces (Acker and Bricker, 1992; Kaviratna and Pinnavaia, 1994; Turpault and Trotignon, 1994; Rufe and Hochella, 1999; Aldushin, et al., 2006; Cappelli, et al., 2013). Their data implies that edge sites dissolve quicker than the basal surface sites and often edge sites primarily influence the overall dissolution rate especially under acidic conditions.

Nevertheless, at localized positions on the basal surface (00l) preferential dissolution (and also precipitation) occurs at locations of high energy surface defects (Rickman and Srolovitz, 1993; Whitehouse, 2011). These reasons make clay minerals one of the most efficient acceptors of functional groups of organic compounds in the crystalline minerals domain.

2.1.1.3 Conditions/parameters in protocols for weathering experiments

Environmental factors such as temperature and pH strongly affect the weathering reactions. For effective weathering experiments the studies usually need to be carried out at low pH conditions. Temperature is also a crucial parameter that will determine experimental duration. Elevating this parameter thus results in rapid and more dynamic dissolution of minerals (Aldushin, et al., 2006; Pachana, et al., 2012; Cappelli, et al., 2013). Ambient temperatures were also adopted by other researchers at 25°C (White, 1983; Oelkers and Gislason, 2001), at 24°C (Turpault and Trotignon, 1994), and at 22 ± 2°C (Kalinowski and Schweda, 1996).

Recent studies also observe these surface alteration processes in in-situ conditions using scanning microscopy techniques. Hu and Jun (2012) studied biotite dissolution at high temperatures and pressures in 1M brine NaCl solution and utilized AFM in contact mode to study the reacted basal surfaces. Same tool operated in contact mode was used on muscovite and biotite hydrothermal (200°C) alteration products in acidic solutions (at pH 3.3) by Pachana, et al. (2012). Aldushin, et al. (2006) also used hydrothermal atomic force microscopy (HAFM) to observe the basal plane reactivity of apophyllite and phlogopite at pH 4 to 5.6 (T = 20–100 ^{0}C). Rufe and Hochella (1999) quantitatively assessed the reactive surface area of phlogopite in the fluid cell of an AFM at room temperature and pHs 2 and 5.7 using HF and HCl. Therefore, above summary indicate AFM to be a highly valuable tool in studying surface alteration of flat surfaces.

pH, temperature and studying in-situ conditions are just three of the many experimental settings manipulated by studies. Therefore, a more inclusive summary of what has been done so far in close proximity to the outline/objective of this work is briefly summarized in Table 6. And information therein was used to design the main experimental together with new additions to the protocol.

Table 6: Weathering experiments carried out in other studies to summarize experimental conditions and set-up often adopted in similar studies.

	Description of experiment	Experimental setup	Equipment (analysis/ characterization	Solid to Liquid ratio (S:L)	Reference
1	In situ biotite basal surface dissolution using long-term flow-through experiments at pH 1 (T = 11.5−70 °C). Flakes with (001) cleavage surfaces of ~2 × 8 mm^2 and thickness 0.08-0.15 mm were used in the experiments.	Custom-made Teflon flow-through reactor cell	LCM-DIM	-	(Cappelli, et al., 2013)
2	Evaluation of changes in the biotite and muscovite (1 X 1 X 0.1 cm^3 monocrystal) basal surface nano-morphology at different pHs (pH = 1.1, 3.3 and 5.7) and at different temperatures (T= 25, 120 and 200°C).	PTFE tube cell	AFM	-	(Pachana, et al., 2012)
3	Quantifying basaltic glass dissolution rates as controlled by surface reactions far from equilibrium conditions. In attaining their objectives, basaltic glass dissolution rates at steady-state were measured as a function of pH from 2 to 11 at temperatures from 6° to 50°C and at near neutral pH conditions at temperatures from 6° to 150°C.	Open system titanium mixed flow reactors	SEM	-	(Gislason and Oelkers, 2003)
4	Some concepts of the weathering processes were tied to be clarified by examining and comparing biotite dissolution in the laboratory and in nature. For the batch dissolution experiments, fresh biotite was weathered at 150°C for durations spanning from 1 to 56 days.	Batch dissolution in Teflon vessels	SEM (with EDS), HRTEM	1:2000	(Murakami, et al., 2003)
5	Steady state basaltic glass dissolution rates were measured at 25°C and pH 3 and 11. Rates were measured as a function of concentration variations of aqueous aluminum, silica, and oxalic acid.	Mixed flow reactors continuously stirred with floating Teflon bars	-	Single basaltic glass powder	(Oelkers and Gislason, 2001)

7	δ-Al_2O_3 dissolution kinetics was examined over the pH range 3-9 as is affected by the presence of salicylate and 8-hydroxyquinoline-5-sulfonate (HQS). Study attempted to determined dissolution rate constants' dependency on Al coordination and pH.	Continuous-Flow Stirred-Tank Reactor	Adsorption and florescence measurements	-	(Kraemer, et al., 1998)
8	Biotite dissolution rate and stoichiometry were studied in the at pH 2-10. Attempt was made to determine release rate of interlayer and framework cations and the corresponding weathering controlling mechanisms.	Thin-film continuous flow-through reactors	XPD, SEM (EDS), FTIR and BET	-	(Malmström and Banwart, 1997)
9	Biotite, trioctahedral phlogopite and dioctahedral muscovite reaction kinetics during weathering experiments was studied in aqueous solutions at room temperature in the pH range 1-4. Preferential release of interlayer or octahedral or tetrahedral cations relative to each other and the resulting alteration products were studied. Change in specific and total surface areas and weather or not they are correlated to changes of dissolution rates were also studied.	Dialysis-Cell Reactor based on the principle of a continuously eluted dialysis cell built in polyacrylic plastic	XRD, ICP, SEM, Ar BET surface area analysis	1 g of mineral, recirculated mineral suspension ~10 mL	(Kalinowski and Schweda, 1996)
10	Phlogopite weathering using HCl was studied in the presence of NaCl at 50°, 80° and 120°C. Objective of study was to understand the dissolution process in micas and formation of secondary or altered interstratified phases, and specifically the relative release rates of the interlayer and framework cations.	Hydrothermal runs in sealed Teflon vessels	XRD, TEM and AEM (Analytical Electron Microscopic)	1:1000 or 1:5000	(Kuwahara and Aoki, 1995)
11	Batch experiments made use of sized biotite single crystals at 24°C and in 0.1 N $HN0_3$ to determine respective contributions from the two geometric interfaces (external (00l) planes of the crystal and (hk0) lateral surface) between the biotite crystal and solution.	Leaching in PFA vials with moderate agitation, grid separating stirring rod from the sample	SEM, XRD, FTIR	1:125 & 1:100	(Turpault and Trotignon, 1994)
12	Biotite dissolution was investigated in acidic solutions in the pH range 3-7. Study attempted to determine weathering rates as dependent on pH. Also studied were weathering congruency and preferential release of cations interlayer compared to framework or octahedral compared to tetrahedral.	Fluidized-bed reactors and flow-through columns	XRD, BET	~ 1:10	(Acker and Bricker, 1992)

13	Effect of organic acids and fluoride on the dissolution kinetics of hydrous alumina was investigated at pH 3-6 and in the presence of organic ligands. Study investigated the control surface processes and concentrations of fluoride ions have over the dissolution process and rate. It also investigated the relative affinity of various organic ligands for the Al_2O_3 surface sites.	The dissolution experiments were performed in 1L thermostated glass vessel electrochemical cell.	ESM (electron scanning micrograph) and XRD	-	(Žutić and Stumm, 1984)
14	Three types of glassy rocks were weathered at 25°C and pH 1.0 to 6.2 for a reaction duration as much as 3 months. The weathering mechanisms and rates were investigated as well as the suitable conditions suitable for steady state under the different weathering combinations.	Dissolution was carried out in three-neck, Pyrex distillation flasks at 25±0.1 ^{o}C. Batch was continuously stirred and purged of CO_2 by N_2.	XRD	~ 1:92	(White, 1983)
15	Albite, oligoclase, labradorite, bytownite, anorthite, and a high-K variety of plagioclase were weathered at room temperature in deionized water, with four organic acids at 0.01 M concentrations. Dissolution was carried out at room temperature on particle sizes between 44 µm and 150 µm for 1, 6, 12, and 24 days in closed system. Study attempted to determine the relative weathering susceptibility of the different minerals and also the relative complexing capacities (thus their dissolution abilities) of different organic ligands to the surfaces of these silicate minerals.	Crushed specimen were mixed with 0.01M organic acids in polyethylene bottles and shaken slowly.	Spectrophotometer (Si), atomic absorption spectrophotometer (Al, Mg, Ca, Na and K)	~ 1:83	(Huang and Kiang, 1972)

*S:L values are given corresponding to g/ml solid to liquid ratios.

Table 6 summarizes that for half the studies that utilized different static setups the solid to liquid ratios ranged between 1:5000 to 1:10. The use of dialysis membrane as demonstrated in Kalinowski and Schweda (1996), was also an important and better alternative to using syringe filters (cut off size often in the microscopic range) utilized when sampling eluates. Dialysis membrane or similar filtering mechanisms with nano metric cutoff sizes are the better options for allowing the passage of only truly dissolved species into solution.

2.1.2 Alteration of organic matter

Formation of the different soil components is also a complex process in itself with its own constrictions or preconditions. A major prerequisite for the formation of organo-mineral complexes is ample precipitation (moisture) for plant biomass production and sufficiently suited conditions for physical, chemical and biological weathering that leads to soil formation.

In view of interacting with minerals, for OM to generally be able to reach a physical and chemical state (i.e. from its crude forms of dead plant and faunal debris) capable of reacting with minerals and their surfaces, it needs to undergo several processes. These processes, often affected by microbial communities, facilitate transport (i.e. faster diffusion) of OM through an aqueous phase (i.e. polar medium/H2O) through processes involving oxidation and depolymerization. These processes are nowadays being formulated into a theory that replaced the concept 'fresh synthesis of unique humic OCs by soil' by an "oxidative depolymerization" process (Sutton and Sposito, 2005; Kleber, et al., 2015). In the latter process, the large compounds in OM are reduced in molecular size by microbes at the same time while effecting chemical alteration (adding oxygen-containing ionizable functional groups) to result in enhanced aqueous solubility (Piccolo, 2001; ten Have and Teunissen, 2001). For abiotic oxidative depolymerization options reference can be made to Sunda and Kieber (1994) and literature there in.

These alteration schemes, in addition to the oxidative chemical alterations that also increase reactivity toward mineral surfaces and metal cations, have been proposed as the "partitioning model" in earlier works by (Hedges and Keil) as far back as 1999 (Kleber, et al., 2015). Figure 20 demonstrates the scheme as the 'partitioning model' that is broad and well descriptive of geochemical processes. These processes are inclusive of the constraining/controlling effect the aqueous medium has in the transition stage from the time OM is in its crude and non-reactive state until it ends up adsorbed or coprecipitated on to minerals surfaces.

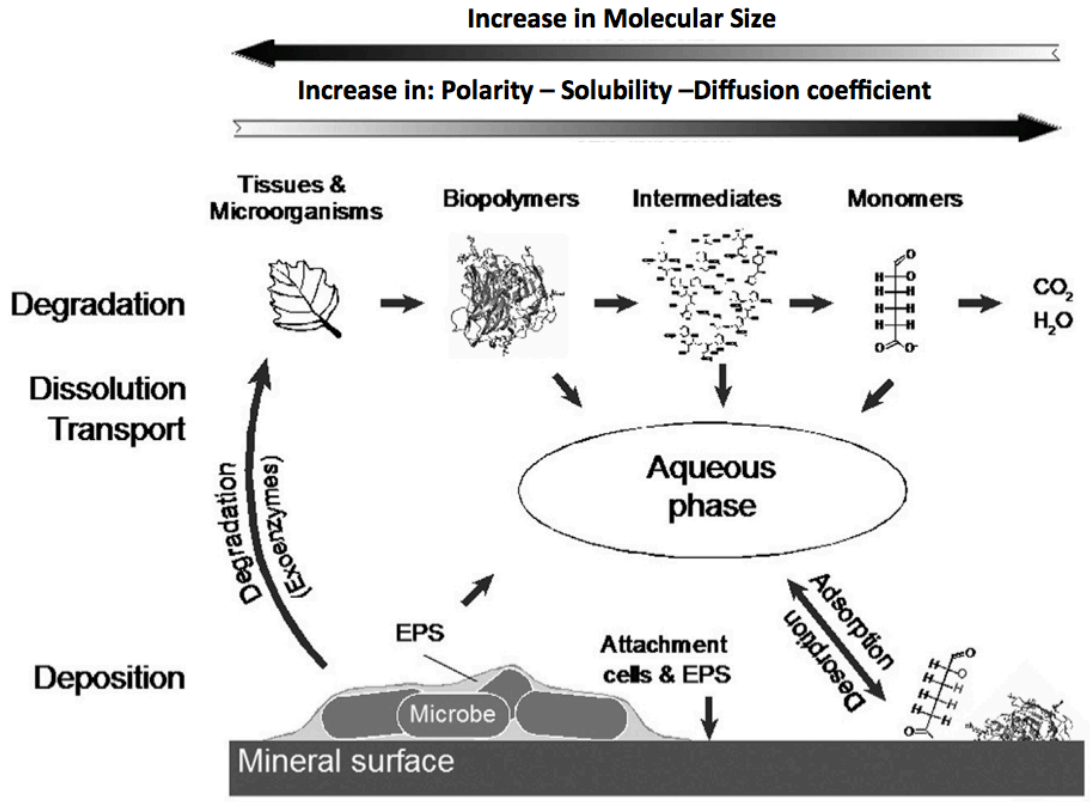

Figure 20: Partitioning Model, initially proposed by Hedges and Keil (1999) and presentation slightly adjusted and adopted from Kleber, et al. (2015). EPS: extracellular polymeric substances, are high-molecular weight compounds secreted by microorganism into their environment that establish the functional and structural integrity of biofilms (Staudt, et al., 2004).

2.1.3 Synthesis of secondary minerals

Immobilization of OM aids in protecting it against decay (Scheel, et al., 2008). To support the formation of SOM, in addition to the OM, inorganic species need to be present in their active state of solubility at the specific local soil pH (Kleber, et al., 2015). A good example that demonstrates this critical dependency is seen in natural soils highly deficient in oxygen. These soils (e.g. gleysols, stagnosols, etc.) that are enriched in Fe^{2+}, upon aeration, oxidize their abundant Fe^{2+} to Fe^{3+} resulting in a rapid coprecipitation of Fe phases with the OM (Cismasu, et al., 2011; Kleber, et al., 2015).

2.1.3.1 Metal hydrolysis

Organic matter interacts with mineral surfaces by ways of coprecipitation and adsorption. Various papers detail these processes especially in relation to synthesis of metal oxides (e.g. ferrihydrites which are one of the most interactive mineral groups in natural MOAs) (Schwertmann and Cornell, 2000; Eusterhues, et al., 2008; Eusterhues, et al., 2011; Henneberry, et al., 2012; Eusterhues, et al., 2014a; Eusterhues, et al., 2014b; Mikutta, et al., 2014). Kleber, et al. (2015) give a compilation of studies carrying out Al and Fe coprecipitation by complexing with OM.

Metal polymerization through hydrolysis reactions has been a major area of research in various research domains (Brinker and Scherer, 1990; Buffle and Van Leeuwen, 1993; Bottero, et al., 1994; Rose, et al., 1997b). In following this process, one important parameter to consider is the Hydrolysis Ratio (R). This parameter is defined as the ratio between OH to metal concentrations in the system at a given time. Metal hydrolysis

occurs in various steps. First major step involves the formation of the first few monomers. Subsequent stages allow these small clusters to grow/polymerize into ordered crystals or amorphous phases (Rose, et al., 1997b).

A. Al hydrolysis

In Al speciation studies as well, the hydrolysis ratio R remains one of the most important factors to consider. For concentrations exceeding 0.1mM (Bottero, et al., 1980; Bottero, et al., 1987), Al hydrolysis undergoes two major stages (Bottero, et al., 1994). Figure 21 from Bottero, et al. (1987) gives a representation of these stages from analytically and numerically complementary sources. The first stage (R range between 0.5 to 2.5) involves various processes that lead to the formation of Al_{l3} polycation from monomers, dimers (Akitt, et al., 1972; Bottero, et al., 1980), and trimers (Henry, et al., 1992). The hydrolysis products often encountered in this R range and consistently cited in literatures are $Al(H_20)_6^{3+}$, $Al_2(OH)_2^{4+}$ and $Al_{13}O_4(OH)_x(H_2O)_{36-x}^{(31-x)+}$ (Bottero, et al., 1980; Bottero, et al., 1987). This trivalent state of the monomeric molecule allows it to neutralize OM ligands at a higher efficiency at acidic conditions (Nierop, et al., 2002; Zhao, et al., 2009). Not restricted to monomeric Al states, a recent study of aluminum trichloride hydrolysis by Zhao, et al. (2009) also found that acidic states were dominated by monomeric and dimeric Al species. The latter of the three species is the Keggin ion of 12 Al octahedra surrounding one central Al tetrahedron, where this species is observed to be dominant in the R range 2 to 2.5 (Bottero, et al., 1987).

In the second stage (R>2.5), according to infrared and neutron scattering studies, Al hydrolysis follows two sub-stages of polymerization (Elderfield and Hem, 1973; Christensen, et al., 1982). The first sub-stage, in the R range >2.5, follows the formation of an amorphous Al gel with an open fractal structure (Schaefer, et al., 1986; Bottero, et al., 1987). R approximately around 2.3 is marked as the onset of polymerization with progressive removal of Cl^- (i.e. where the hydrolysis was started from $AlCl_3.6H_2O$ salts)(Bottero, et al., 1982; Axelos, et al., 1985). As the hydrolysis ratio increases (until R=2.8) hydroxyls from adjacent octahedra condense making oxo-bridges resulting in the aggregation of octahedral Al species. This stage squeezes, while at the same time protecting, the central Al tetrahedron from further hydrolysis. More and faster hydrolysis beyond this R value would force the tetrahedron to partially re-arrange into an octahedron giving much improvement for the overall octahedral symmetry. The second sub-stage, if the gel is allowed to age and dehydrate it would undergo structural re-arrangement and result into crystalline Al species (Christensen, et al., 1982; Bradley, et al., 1993; Gebauer, et al., 2014). This re-arrangement is a solid-state transformation of the Al_{13} polycations (Bottero, et al., 1987). This last sub-stage between R=3-4, long-range order crystallized trihydroxides as in bayerite, gibbsite, or norstandite minerals start to form (Bradley, et al., 1993).

Note: Care needs to be given with NMR analysis around R=2.8 and above due to the quadrupolar nature of ^{27}Al; which gives an erroneous data of complete replacement of Al tetrahedra by Al octahedra.

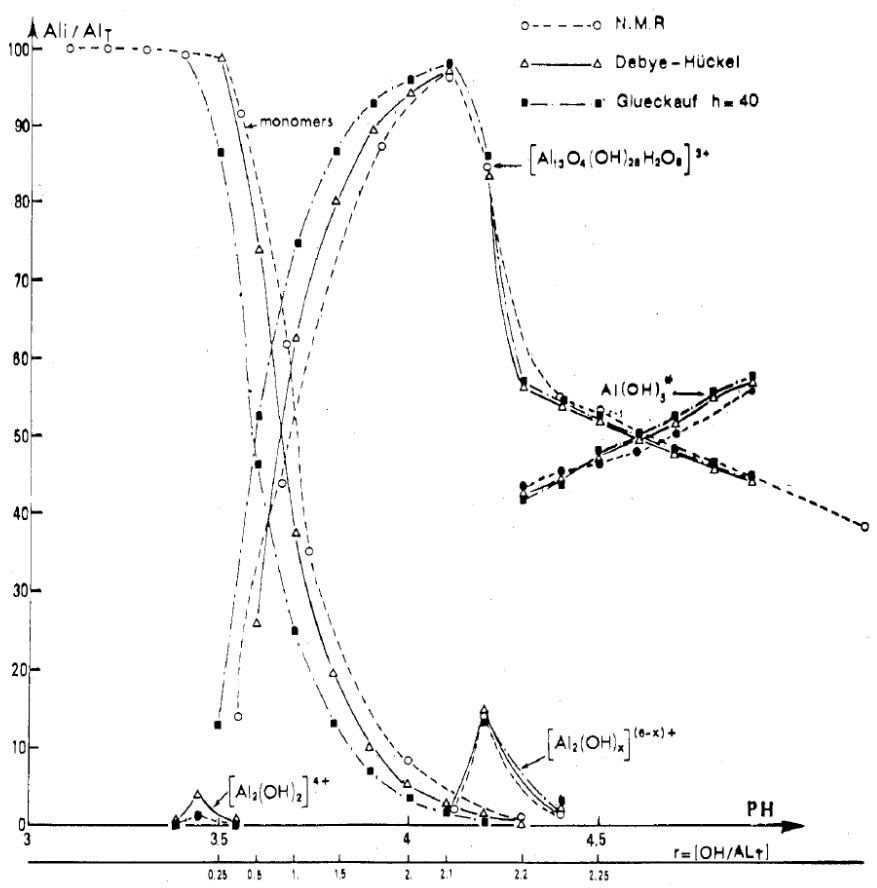

Figure 21: Al speciation in proportion to total Al vs. pH and R values. Data represented from (o) NMR; (△) Debye-Huckel law; (■) Glueckauf formula; (●) 100 NMR quantitative results. From Bottero, et al. (1987).

B. Fe hydrolysis

When clusters form, 3D or branched out local structures (as opposed to 2D which are more of linear) are more strongly preferred when their octahedron is composed of more of OH or O than other anions such as Cl (Combes, et al., 1989; Manceau and Drits, 1993; Bottero, et al., 1994). This is due to the ability of O or OH anions to form bridging ligands. Therefore, extent of structural order and type of metal-to-metal linkages in Fe hydrolysis partly depends on the ingredient material and the hydrolysis ratio (R). Primarily, R is important because it controls directly the extent of polymerization. And in the case where Cl^- is present it controls the fate of this anion as it is pushed out/replaced from the system with hydroxyl ions.

i. Ferric nitrate hydrolysis

At the very initial stages of Fe (Nitrate) hydrolysis and polymerization (R<1) Fe species occur in their monomeric state (Combes, et al., 1989; Bottero, et al., 1994; Senesi and Wilkinson, 2008). At these initial stages distinct EXAFS peaks in real space are absent in the range between 2.85-3.5 Å (Combes, et al., 1989; Rose, et al., 1997b). That is to mean if peaks are present in that range, they would unequivocally represent dimers and/or trimers.

Further addition of OH^- allows the formation of the first dimers through face and/or edge sharing linkages. Face sharing linkages are a possibility in the radial distance range

mentioned above but occurring at a reduced frequency (Manceau and Drits, 1993). These Fe-Fe_1 face interactions (~2.89Å) often found in hematite occur at prolonged hydrolysis or aging of ferric gels at conditions that favor dehydration (e.g. elevated temperature) (Combes, et al., 1990; Manceau and Drits, 1993; Pokrovski, et al., 2003). Cases have been cited where structural rearrangements due to dehydration and further dehydroxylation of Fe-OH-Fe linkages favored the increase in the number of face sharing associations (Manceau and Drits, 1993).

Fe-Fe_2 edge sharing interactions, compared to face sharing interactions, have a higher rate of occurrence around radial distance of 3±0.15 Å. That together with lack of enough EXAFS resolution to unambiguously differentiate the two, face sharing bonds are often included with in the edge sharing domain (Rose, et al., 1997b). Often, when face and edge interactions can not be differentiated, an average radial distance is detected (i.e. R~2.95Å, which is shorter than a pure edge sharing interaction and longer than pure face sharing interaction) (Combes, et al., 1990). Next nearest iron to iron interactions (i.e. Double Corner (Fe-Fe_3) and Single Corner (Fe-Fe_4)) are also observed in ferric nitrate hydrolysis (Combes, et al., 1989; Bottero, et al., 1994; Doelsch, et al., 2000). These longer Fe-Fe interactions aid in growth and polymerization of crystals and other phases depending on aging time, temperature and solution composition (Pokrovski, et al., 2003).

All these polymerization steps start from elementary monomeric building blocks such as $[Fe(H_2O)_6]^{3+}$ and are followed by intramolecular condensation which involves deprotonation at every step (Combes, et al., 1989; Rose, et al., 1997b). Formation of the small clusters (using edge and double corner sharing interactions) is all included in the initial stage of "nucleation" which is followed by latter stages of growth and aggregation (via corner sharing interactions) (Wells, 1984; Rose, et al., 1997b).

In ferric nitrate hydrolysis Rose, et al. (1997b) mentioned to have found local structures resembling well crystalized Fe oxides only at high hydrolysis ratios (R=2.5) and aging times (t=20 days). At low R values produced oligomers have local structure far from the conventional Fe crystalline minerals such as goethite and lepidocrocite (Rose, et al., 1997b). Same study was unable to model these phases synthesized at lower R values and shorter edging times using crystalline minerals.

ii. Ferric chloride hydrolysis

In ferric chloride hydrolysis, one distinct difference from their nitrate counterparts is the presence of chloride in the octahedron at low R values. At the very beginning of $FeCl_3.6H_2O$ hydrolysis (i.e. R=0) Bottero, et al. (1994) state Fe octahedra to have 4 '$O/OH/OH_2$' occupancy at radial distances of 2.01Å and 2 'Cl' occupancy at radial distances of 2.31Å. Combes, et al. (1989) have found this '4 to 2' 'oxygen to chloride' ratio to persist until hydrolysis ratio of 0.3. And this local structure was found to be still similar to structures found in crystalline $FeCl_3.6H_2O$ (Lind, 1967). Bottero, et al. (1994) affirm the absolute necessity of replacement of Cl^- ions for nucleation and coalescence to occur. Increasing the hydrolysis ratio up to 2.0-2.2 gradually expels Cl from the octahedron. This results in Fe 6 fold '$O/OH/OH_2$' coordination at an average R_{Fe-O}=2Å (Combes, et al., 1989).

Presence of chloride in polymers formed below R=2.2 renders the aggregates to be very linear. While its absence in aggregates formed above this value has a more branched out

(3D) arrangement (Bottero, et al., 1994). Edge and double corner interactions contribute to the 2D growth scheme at radial distance ranges of 3.01-3.05Å and 3.44-3.47Å respectively (e.g. (Combes, et al., 1989; Bottero, et al., 1994)). An observed difference in the absence of Cl ion (e.g. ferric nitrate hydrolysis) is that same interactions are found at slightly longer radial distance ranges of 3.06-3.14Å and 3.42-3.52Å respectively. Also an additional face sharing interactions can be found between 2.88 to 3.05 Å (e.g. (Rose, et al., 1997b)) with Fe nitrate hydrolysis, at a hydrolysis ration of 1.5 (Pokrovski, et al., 2003). Manceau and Drits (1993) summarized local structures of the formed phases to resemble of β-FeOOH (Schneider, 1984; Bottero, et al., 1994) and 6L-ferrihydrite (Combes, et al., 1989; Combes, et al., 1990) like local structures at partial and full hydrolysis stages respectively. At final stages of hydrolysis particles are observed to reach a maximum cluster size of 30 Å with both Fe chloride and nitrate precursors (Combes, et al., 1989).

Advanced stages of polymerization lead to either the extension of the local order further out into well crystalized Fe (hydr)oxides; or lead to structural poisoning which results in amorphous phases. This phenomenon of structural poisoning which has a negative connotation, in the context of Fe polymerization losing its ordered growth, changes to a positive in the context of carbon stabilization. The positive connotation arises from embedding of carbon with in the structures of Fe and aluminosilicate phases resulting in its physical and chemical protection from mineralization of various origins.

2.1.3.2 Fe hydrolysis in the presence of other inorganic elements

However, in dilute solutions, the role of Cl^- in Fe hydrolysis is far less evident and restricted to octahedral distortion as compared to structural alterations imposed due to the presence of other compositions such as silica that extend beyond the first shell (Pokrovski, et al., 2003).

A. Fe hydrolysis in the presence of Si

Fe hydrolysis in the presence of varying Si concentrations was studied by Pokrovski, et al. (2003) in dilute aqueous solutions of 0.01m iron concentration (i.e. molar Fe/Si=0.2). In acidic states (2.7 < pH < 3), they found Fe-O bonds in small Si presence (0.05m) (2.00 Å) to be distinctly longer than Si free Fe hydrolysis cases (1.97Å). This could be attributed to the formation of the longer Fe-O-Si and/or Fe-OH linkages instead of the shorter Fe-O-Fe interactions. In similar Si concentration (0.05m) but above a pH state of 2.8, they found Si to have removed Fe-Fe corner linkages that would otherwise have formed in its absence. And the Fe-Fe distances corresponding to the edge linkages show slight increase (3.12–3.14 Å) with also Si entering in the second coordination shell of Fe (Pokrovski, et al., 2003). At higher Si concentration (0.16m) they reported presence of ~20% short Fe-O distances at ~1.84Å possibly 'Si by Fe substituted' tetrahedral coordination. This high Si concentration of 0.16m also showed complete absence of any Fe-Fe interactions. This indicates the destruction of the Fe-Fe bonds and the formation of different Fe-Si linkages (Doelsch, et al., 2000).

Using FTIR and ^{29}Si NMR, Doelsch, et al. (2001) made a clear demonstration that the abundance of Si atoms hinders Fe-Fe interactions. At pH=3, Si molar concentrations needed to equal twice as much as Fe's for Si-Si interactions to manifest. At pH=5, same proportions were required to be four times as much to see the Si-Si interactions. With these observations, which were also dependent on pH state; they were able to conclude,

equal Si to Fe molar concentrations to be the crossover proportions from 'a dominantly Si-Fe precipitates' to 'the formation of Si rich pockets (i.e. Si-Si bonding)'. Complementary EXAFS analysis on same samples showed the increase in molar Si/Fe concentration from <1 to >1 (i.e. Si/Fe from 0 to 4) also dictates a transition in the formed Fe-Fe polymers from a 3D to 2D structures (Doelsch, et al., 2000).

Not much literature exists with direct EXAFS evidence of Fe to Si interactions. But correlations can also be done by relying on similar interactions with tetrahedrally coordinated anions analogues to Si such as phosphorous (P), arsenic (As), selenite/selenate (Se), etc. With regard to P, corner interactions were recorded at radial distances from Fe in the range between 3.2-3.58Å, for numerous naturally occurring minerals; and a singular example of edge Fe to P interaction at a shorter distance of 2.75Å in $Fe_3(H_2O)(PO_4)_2$ (Rose, et al., 1996; Rose, et al., 1997a). With As(V) and Se(VI and IV) double corner interactions to Fe are observed with in a radial distance range of 3.25-3.38 Å (Waychunas, et al., 1993; Manceau and Charlet, 1994; Manceau, 1995). Similar study also reported a distance of 2.80-2.85 Å for a shorter edge sharing interaction of an Fe octahedra with As or Se tetrahedra.

Pokrovski, et al. (2003) made following suggestion as to these possible Fe to Si complexes by making similar analogy with above detailed tetrahedral anions arsenate, selenate, selenite and phosphate. They propose a possible Fe octahedra to Si tetrahedra edge sharing interaction at $R_{Fe\text{-}Si}$~2.8-2.9 Å and single-corner sharing at $R_{Fe\text{-}Si}$~3.4-3.6 Å. However, they deduce the unlikeliness of the former interaction at acidic (pH<3) and basic (pH>12.7) conditions specific to their study. While they also mention difficulty to detect the latter Fe to Si linkage due to the high degree of freedom associated with single corner sharing interactions; and related to that the high sensitivity to disorder of EXAFS. Pokrovski, et al. (2003) also limit Fe interaction to monomer silicic acid $Si(OH)_4$ forming $FeSiO(OH)_3^{2+}$ complex in acidic solutions (Weber and Stumm, 1965; Olson and O'Melia, 1973; Reardon, 1979) as opposed to less possible interactions with larger silicate polymers attributed to steric constraints and slow kinetics (Swaddle, 2001).

B. Fe hydrolysis in the presence of Al

Fe^{3+} and Al^{3+} (not Fe^{2+}, Mg^{2+}, and Ca^{2+}) are two of the most reactive cations in natural soil solution. That is due to their low hydrolysis constant below soils pH, which allows them to interact with small sized organic molecules (<100 nm) at the onset of metal hydrolysis (Kaiser and Guggenberger, 2007; Riedel, et al., 2012). Therefore, in a soil solution Fe^{3+} receives much of its competition from Al^{3+} when interacting with NOM than any other cation.

In a study comparing the mobility of Fe^{2+}, Fe^{3+} and Al^{3+} in acidic soils at three pHs (3.5, 4.0 and 4.5) Jansen, et al. (2003) observed results for Al at pH 4.5 resembling state of insolubility for Fe at all three pH values. Al starts to get hydrolyzed close to pH 4.5 while Fe already has started at a slightly more acidic state. This is a good observation indicating that in this 3.5-4.5 pH range Fe and Al speciations are different. Therefore, the competition between these two metals and their ability to complex with and subsequently precipitate OM depends on the metals' state of solubility (thus the pH) and the abundance of C present (i.e. M:C molar ratio), which will be discussed in latter sections of this chapter (Jansen, et al., 2003). These phenomena obey the individual hydrolysis behavior of Al and Fe species as discussed in detail in section 2.1.3.1.

2.1.4 Inorganic to organic matter interactions

Irrespective of the quantified proof of long term stability of OM in soils, from thermodynamic point of view it is viewed to be unstable (Schmidt, et al., 2011). Inquiry about this basic puzzle and as to why and how it behaves in this manner, in the broader carbon scheme, has been voiced a decade and a half ago by Hedges, et al. (2000). But the ability of minerals to protect SOM has been recognized by earth scientists as far back as six to seven decades ago (Jung, 1943; Allison, et al., 1949).

Few of the widely argued on and still investigated long term SOM stabilization techniques are chemical recalcitrance of the organic compounds, isolation from micro-organisms by physical protection, and interaction with minerals by physiochemical processes (Oades, 1988; Chenu and Plante, 2006; Theng, 2012; Lehmann and Kleber, 2015).

1st mechanism: 'chemical recalcitrance' was found and accepted quite early on to be a stabilization inherent characteristic for humic substances (Hobson and Page, 1932; Waksman, 1932; Waksman and Iyer, 1933; Marschner, et al., 2008; Basile-Doelsch, et al., 2009; Theng, 2012). This mechanism represents the ability of some natural organic molecules (humic substances and similar others) to withstand microbial decomposition purely because of their intrinsic molecular properties; such as larger and complex to decompose, and non-repeating structural units (Theng, 2012). Studies contributing in support of this mechanism and structural existence of OM in the form of large, complex and recalcitrant compounds (such as the much disputed fulvic acid, humic acid, etc.) include old works by (Swaby and Ladd, 1962; Turchenek and Oades, 1979; Anderson, et al., 1981; Anderson and Paul, 1984; Catroux and Schnitzer, 1987) and new ones by (Galeska, et al., 2001; MacCarthy, 2001; Rice, 2001; Krull, et al., 2003).

However, numerous recent researches and reports give more support and evidence to the remaining OM stabilization mechanisms (i.e. physical protection and interactions with mineral surfaces) and/or against chemical recalcitrance (Baldock and Skjemstad, 2000; Eusterhues, et al., 2003; Chenu and Plante, 2006; Kögel-Knabner, et al., 2008; Marschner, et al., 2008; McCarthy, et al., 2008; Calabi-Floody, et al., 2011). But a study by Amelung, et al. (2008) can be considered as one of the pioneer studies that clearly demonstrated that chemical recalcitrance is not a valid stabilization process.

One of the latter three mentioned mechanisms include, the 2nd mechanism: organic carbon stabilization by 'physical entrapment and protection' with in minerals and their aggregates (Hedges and Oades, 1997; Baldock and Skjemstad, 2000; Calabi-Floody, et al., 2011). This interaction, as clearly implied by its name, gives protection to OM by physically shielding it against both physical and chemical attacks inherent to its environment. Examples could be physical and chemical erosion from temperature and precipitation and also enzymatic attacks from microbial communities. The role of soil structure in the protection of OM and associations with microbial populations is well detailed and can be inferred from publications by Van Veen and Kuikman (1990), Baldock and Skjemstad (2000) and Fazle Rabbi, et al. (2010) and reference therein.

3rd mechanism: organic carbon stabilization via its 'interaction with crystalline minerals' implies dependence on specific mineral properties such as specific surface area, charge characteristics and porosity inherent to most clay minerals and oxides of iron (Parfitt, et al., 1997; Krull, et al., 2003). Moreover, numerous more recent publications are proof of

increased research interests concerning the stabilization of SOM. Studies by Kaiser, et al. (2002) and Kaiser and Guggenberger (2003) give good analysis to that regard on the role mineral surfaces play in the stabilization process.

Therefore, due to the relevance OM has on the global carbon cycle and the necessity of an in depth study of the latter mentioned two stabilization processes, taking OM research to an even higher and more complex levels is a necessity and was an understood consensus in the scientific community (von Lützow, et al., 2006). That required studies to be extended into the nano metric scale for better understanding and viewing of OM interactions with its surrounding. These led to an emerging view, where state of the art analytical tools are revealing the more intricate interaction and stabilization of organic carbon through 'interaction with mineral surfaces and newly formed amorphous entities on these surfaces' (Jahn, et al., 1992; Schnitzer and Kodama, 1992; Torn, et al., 1997; Eusterhues, et al., 2003; Kleber, et al., 2005; Chenu and Plante, 2006; Putnis and Putnis, 2007; Hellmann, et al., 2012; Mikutta, et al., 2014; Basile-Doelsch, et al., 2015; Hellmann, et al., 2015; Kleber, et al., 2015).

Figure 22 demonstrates this later mechanism where by the altered-unaltered mineral surface front progressively deepens with time where by the newly forming low crystalline nanoparticles in the altered layer simultaneously complex with readily available organic compounds.

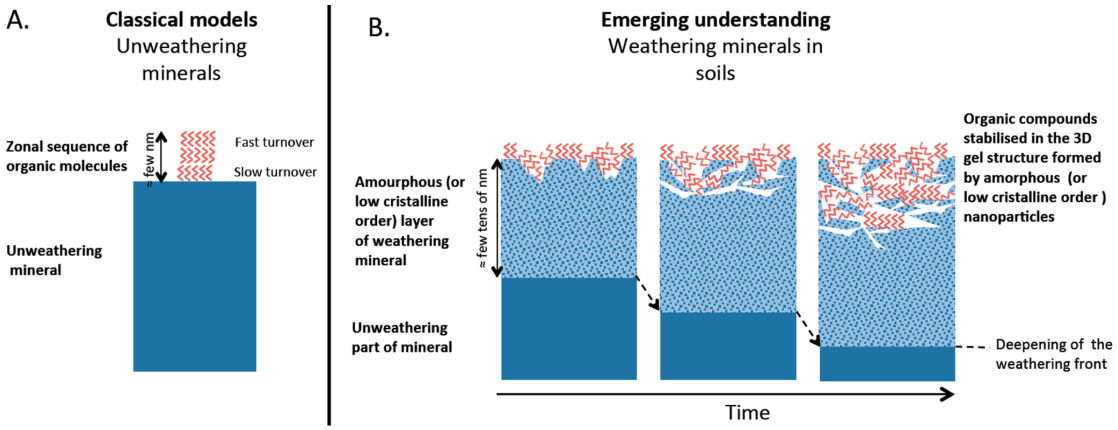

Figure 22: A comparison between classical and emerging views of weathering of minerals in soils and interaction with OM. Image from Basile-Doelsch, et al. (2015)

A review by Kleber, et al. (2015) discusses that areas of the world where we find active interaction of OM with these surfaces of clays, oxides and amorphous phases are supported by sufficient soil moisture for continued and elevated plant biomass production by rigorous weathering. They further discuss that these weathering soil forming processes simultaneously result in the acidification of the soil and release of multivalent metals and lead to the creation of secondary minerals that will eventually interact with OM.

At the end of the chemical and physical changes (as discussed in detail in sections 2.1.1 and 2.1.2), the low molecular weight inorganic and organic compounds obtained are the two reaction partners needed for the formation of MOAs. The main reason we study this intricate association is because of the role these inorganic entities play in the long-term stabilization of OM (Kleber, et al., 2015). These interactions have been found to be effective with certain minerals such as clays (Bishop and Philp, 1994; Calabi-Floody, et al., 2011), iron oxides (Mikutta, et al., 2010; Eusterhues, et al., 2011; Eusterhues, et al.,

2014b; Mikutta, et al., 2014) and long-range ordered amorphous minerals (Levard, et al., 2012; Basile-Doelsch, et al., 2015); which are capable of providing high surface area and abundant reactive sites for complexation with organic compounds.

Often MOAs are triggered by changes in the physical and chemical environment (e.g. pH, redox state, ionic strength) where these two reaction components are abundantly available (Weng, et al., 2007; Riedel, et al., 2012; Riedel, et al., 2013). The MOAs themselves are also exceedingly more important in stabilizing and preserving SOM (Schmidt, et al., 2011; Kleber, et al., 2015).

2.1.4.1 Summary of OCs utilized in SOM studies

In organo mineral interaction studies, choice of organic compounds is quite varied and depends on various factors related to the objectives of the experiments. Table 7 gives a summary of organic compounds or OM used in various experiments to give base to the OC selected for this work.

Table 7: Summary of organic matter used in various SOM studies. FFE and EPS stand for Forest Floor Extract and microbial Extracellular Polymeric Substances.

	OM used	Experiment description	Reference
1	FFE from a litter Oi and Oa forest floor horizons	Study of the properties and reactivity of Fe MOAs formed by coprecipitation vs. adsorption.	Mikutta, et al. (2014)
2	DOM (from an agricultural drainage water)	Structural stability of coprecipitated natural organic matter and ferric iron under reducing conditions.	(Henneberry, et al., 2012)
3	FFE (Oi and Oa horizons of a Podzol) and sulfonated lignin	Fractionation of organic matter due to reaction with ferrihydrite by making comparison between coprecipitation and adsorption.	(Eusterhues, et al., 2011)
4	NOM (citrate, oxalate, EPS, and humic substances).	Bioreduction of lepidocrocite (gamma-FeOOH) and the formation of secondary minerals as affected by oxyanions, NOM and bacterial cell numbers.	(O'Loughlin, et al., 2010)
5	Water extractable OM from a forest topsoil	Characterization of ferrihydrite-SOM coprecipitates by X-ray diffraction and Mössbauer spectroscopy.	(Eusterhues, et al., 2008)
6	L-cysteine	The effect of OM (L-cysteine) on directly promoting the formation of goethite from ferrihydrite as opposed to previous studies with other OM ligands that argue to the contrary.	(Cornell and Schneider, 1989)

7	3,4-L-dihydroxyphenylalanine (L-DOPA)	The role of mineral mesopores in OM protection against enzymatic degradation by using synthetic mesoporous alumina and silica minerals and their nonporous analogues.	(Zimmerman, et al., 2004a)
8	Lactic, meso tartaric, L-tartaric, citric, oxalic, succinic, malonic, maleic, or malic (=cis butenedioic) acid	Influence of organic anions in inhibiting crystallization of ferrihydrite and also preference of hematite formation relative to goethite.	(Cornell and Schwertmann, 1979)
9	Acetic acid, alanine, citric acid, caffeic acid, glucose amine and glucosonic	Research trial to study organic matter-imogolite interaction.	Clement Levard (Unpublished)

2.1.4.2 Fe and Al precipitating in the presence of OC

MOA in nature and in controlled laboratory settings are not the same. In natural systems OC precipitation is accompanied by fractionation in which the precipitated organic component does not exhibit same properties as the original OM (Omoike and Chorover, 2006; Scheel, et al., 2008; Eusterhues, et al., 2011; Riedel, et al., 2012; Kleber, et al., 2015). Mineral components in coprecipitates are also not the same with regard to increasing structural strain and/or disorder in comparison to their counterparts precipitated in the absence of OM (Rancourt, et al., 2005; Eusterhues, et al., 2008; Mikutta, et al., 2010).

When MOAs form, crucial elements that influence this process are the proportion of the reaction partners (i.e. M:C), the pH state, type of metal cation (e.g. Fe^{3+} and Al^{3+} as opposed to Mg^{2+} and Fe^{2+}) and the affinity of the organic ligand to the metal species involved (Kleber, et al., 2015). pH is an influencing factor because it affects the ionic state in most organic compounds and also the stage of hydrolysis in most metals. Different metals occur also in different states of solubility at different pH states. That gives different metals competing at varying efficiency to complex with OM.

Change in M:C is a good technique to directly study changes in the soil solution. Studies argue the relevance of change in this ratio to represent (im)mobilization of nutrients (e.g. Fe, Al, …) that lead to major changes in soils such as podsolization (Jansen, et al., 2003). M:C is also decisive in a way that abundance and/or scarcity of one component affects the availability or scarcity of reactive sites. When reactive sites are abundant strong inner-sphere complexes form, where as when there is competition for reactive sites weaker outer-sphere complexes form that are highly dependent on pH (Persson and Axe, 2005).

As is the case for all metals, formation of Al crystalline phases is also affected by the presence of carbon (Kleber, et al. (2015). For Al phases formed in the presence of OM (e.g. low-molecular weight organic acids) their formation is restricted to lower polymerization stages of Al (i.e. monomers and oligomers) (Masion, et al., 1994; Masion,

et al., 2000). Depending on the type of OM, precipitates may also include poorly crystalline $Al(OH)_3$ phases (Scheel, et al., 2007; Xu, et al., 2010).This happens due to the blockage of inorganic coordination sites by the organic ligands (Ng Kee Kwong and Huang, 1981; Colombo, et al., 2004).

Jansen, et al. (2003) in a precipitation experiment using only Al studied its compositions in the form of Al-DOM precipitates, soluble Al-DOM form and as Free Al at pH 3.5, 4.0 and 4.5. They showed that proportion of Al complexed with DOM in precipitates (as compared to Al in soluble Al-DOM complexes and 'Free' Al) increases with increasing Al/C ratio, at all the three pHs they used. But also showed a pH dependence where this increase in Al in the precipitates was nearly negligible at pH 3.5 and clearly visible at pH 4.5. That is to mean the higher the pH the quicker the increase of Al in precipitates with increasing Al:C ratio. They explain that with higher availability of deprotonated functional groups with increasing pH. But with similar protocol followed, Fe^{3+} attained a rapid increase in Fe content in Fe-DOM precipitates at pH 3.5 with increasing Fe:C ratio. But contrary to Al, Fe showed almost negligible change in this trend when the pH state was increased from 3.5 to 4.5. That is because Fe^{3+} hydrolysis begins at more acidic pH and lower M:C ratio than Al^{3+} that makes much of the difference in how these metals act in the presence of OM (Nierop, et al., 2002).

Studies by Xu, et al. (2010) report other forms of structural perturbation in the form of increasing tetrahedrally coordinated Al co-precipitates correlated to increasing carbon presence. They also compared three OCs and observed increasing structural perturbation changing from salicylate to citrate to malate (Xu, et al., 2010). In similar studies with Al precipitating in the presence of tanic acid, analogous results were observed where Al coordination decreased from '6' to 'mixed 6 with 5 or 4' (Hu, et al., 2008).

Competition between different metal species could ultimately depend on the proportion of soluble and insoluble states of each metal competing. With systems having Fe(III) and Al competing, the difference will be more evident at acidic pH states. At initial low metal concentrations (be it Fe(III) or Al), regardless of the titration pH (3.5, 4.0 or 4.5) similar levels of M-OM precipitation occurs with strong inner sphere complexation (Nierop, et al., 2002). This pH independence stems from the relatively small available active sites present with the small M:C. At higher metal concentrations (or M:C ratios) the effect of pH on metal speciation as well as the efficiency and therefore the competition of these metals to complex with OM becomes evident.

In the pH range studied by Nierop, et al. (2002), often appropriate for Al to Fe competition experiments, they showed higher pH to result in higher fraction of the metal coprecipitating with C. They recorded minimal difference of <20% with Fe(III) while significant difference of ~55% with Al in the precipitated metal fractions between the pH states 3.5 and 4.5. The relatively more significant increase in the state of hydrolysis of Al in the pH range studied explains this pH dependency (Ares and Ziechman, 1988; Duan and Gregory, 2003).

In the same pH range both metals give more soluble phases at pH 3.5 than 4.5. But that is less so in amount (proportion to total metal) for Fe(III) than Al. Therefore, in this system, Al would be more successful in precipitating OM at lower M:C ratios owing to three to four fold active Al presence than Fe(III) (Nierop, et al., 2002). At higher M:C ratio there will be abundance of active soluble Fe(III) species to compete with Al thus

making Fe(III) more effective than Al at higher M:C ratios. This latter outcome is in favor of Fe(III) (1) regardless of its reduced solubility compared to Al at more acidic states (e.g. pH 3.5); and (2) even also with the potential for it to be reduced to the less effectively binding oxidation state Fe(II) (Nierop, et al., 2002).

Fe and Al could also occupy different sites during precipitation (Cabaniss, 1992). This would explain the above observation by Nierop, et al. (2002) even though Fe achieves insolubility before Al at these earlier stages of hydrolysis (pH≤3.5). The studies argue this different OM active sites occupancy, at least partially, due to an increased Al and Fe(III) complexation with OM in the studies where the metals were made to compete than when they were studied individually (Cabaniss, 1992; Nierop, et al., 2002). In the pH 3.5-4.5 range, relationship between pH and 'Al to Fe' competition studies also gave Al precipitation dependence on pH to solely depend on Al. While with Fe, OM precipitation was more related to pH in the presence of Al than in its absence (Nierop, et al., 2002).

Variations in abundance of the organic and inorganic reaction partners in MOAs also determine the kind of coprecipitates formed. With high Al presence, sites involved in stronger chelation reactions get occupied leaving space for weaker cation exchange reactions (Nierop, et al., 2002). Cation exchange interactions are highly pH dependent therefore in these circumstances resulting in more Al-OM precipitates at higher pH values due to the reduced competition from protons. In MOAs during the initial stages of hydrolysis, oligomeric Fe and Al phases likely adsorb to OM due to the obvious exceedingly larger size of the organic phase (Mikutta, et al., 2014). In later stages of hydrolysis, same study demonstrates that the organic components rather interact with larger inorganic Fe and Al phases. This shows the influence M:C has on the modes of formation of coprecipitates.

The surface area of MOAs is also affected by the presence of OM. Yu, et al. (2006), in a study for short-range-ordered (SRO) Al precipitates formed under the influence of tannate, recorded a 10 fold increase in SSA with an increase in Tannate presence from non to Tannate/Al molar ratio of 0.1. They attributed the increase to the high number of newly formed micro pores and gradual decrease of pore diameter from 6.6 to 2.4 nm.

Most studies conclude that presence of OCs inhibits formation of inorganic crystals. This is achieved by inhibiting the growth process specific to the specific minerals. With enough concentrations of OC this inhibition process alters the morphology of the newly forming crystals and in very high OC concentrations inhibit the whole crystal formation process (Gautier, et al., 2015). Therefore, it is important to study the nature of metal to OM interactions as well as the individual components when various cations are simultaneously considered. Studies carried out in this manner give complex results as compared to simplified studies where individual cations are reacted with OM. But ultimately these complex results will end up representing natural systems more than the simplified ones.

In sections of the soil horizons high in particulate organic matter (and permanent negative charge sites) and low in amorphous phases, these stronger direct sorption mechanisms through coordination bonding leading to the immobilization of DOM become less apparent (McBride, 1994; Jansen, et al., 2003). And often are replaced by cation bridging and in some cases by weaker interactions such as Van der Waals forces or hydrophilic/hydrophobic interactions (Tipping, 1990; Jansen, et al., 2003). But these kind of weaker interactions are expected less due the control over experimental

parameters in laboratory experiments, therefore they will not be discussed further.

2.1.4.3 OM interaction with crystalline minerals

Active parts of the inorganic soil component are found either in the form of active site on mineral surfaces or as dissolved species in solution (pedogenic oxides) in their monomeric, dimeric, ... state. Often, OM found in soil accumulates in the interface between mineral surfaces and in the immediate vicinity of these surfaces resulting in the process of adsorption on to the mineral surfaces (Essington, 2004). Crystalline minerals such as metal oxides and phyllosilicates (e.g. clays) sometimes play a crucial role as bearers of the surface hydroxyl groups of the minerals in these interactions with the ligands of the OCs (Arnarson and Keil, 2000; Yoon, et al., 2004; Borer, et al., 2009; Lagaly, et al., 2013).

Efficiency of organo-mineral association in stabilizing OM in soil also depends on the extent of the association (inner/outer-sphere), the nature of the minerals and proportion of the reaction partners (Basile-Doelsch, et al., 2009). Generally, SOM is stabilized most efficiently in close proximity to fine soil components. According to Christensen (2001) 50-75% of SOM in temperate cultivated soils is know to exist in less than 2 microns mineral fractions. This soil fraction is mainly composed of clay minerals and iron oxides (Fontes, 1992; Urushadze, et al., 2006; Vogel, et al., 2015) with higher porosity and larger specific surface area, thus resulting in more abundant reactive sites (Parfitt, et al., 1997; Krull, et al., 2003).

These studies, therefore, support clay minerals and iron (hydr)oxides as one of the most capable sequestration agents for carbon. But regardless, presence of crystalline minerals is now being associated with having a reduced capacity to store OM in soil profiles compared to soils with higher poorly crystalline material presence than clay minerals (Jahn, et al., 1992; Parfitt, et al., 1997; Torn, et al., 1997; Basile-Doelsch, et al., 2005). With regard to phosphates adsorption, comparison of short range ordered aluminosilicates against crystalline minerals (e.g. phyllosilicates) as receivers of the organic ligands gave two orders of magnitude difference in favor of the non-crystalline phases (Hesterberg, 2010; Huang, et al., 2016).

But the MOAs are not limited to surface sorption processes only. And in the presence of dissolved inorganic species (such as Al, Fe, Si, etc.), interaction with OM often proceeds in favor of coprecipitating new secondary phases that only exhibit short range order (Masion, et al., 2000; Schwertmann and Cornell, 2000; Mikutta, 2011).

2.1.4.4 OM interaction with non-crystalline minerals: Emerging views

Andosols are a good example of where these MOAs are the most efficient for C sequestration. Fairly recent OM stabilization studies discuss that these soils, which are mostly the weathering products of volcanic rocks, are able to store organic carbon at a considerably high proportion compared to other types of soils (Basile-Doelsch, et al., 2015). Andosols contribute to only ~0.8% of the ice-free surface on our planet (Staff, 1999; McDaniel, et al., 2012). Yet, due to their average ~8–12% OC content (McDaniel, et al., 2012) they are able to sequester more than ~1.8% of the soil carbon stock globally (Matus, et al., 2014; Huang, et al., 2016; Takahashi and Dahlgren, 2016). These soils have also proved exceedingly effective in protecting the OM content against turnover (Dahlgren, et al., 2004; Goh, 2004; Calabi-Floody, et al., 2014; Huang, et al., 2016). And

this nature of volcanic soils is well documented and is associated with their relatively higher content of poorly crystalline minerals (Jahn, et al., 1992; Torn, et al., 1997; Percival, et al., 2000). Allophanes are nano allumino-silicates with Al to Si ratio ~2 (Levard, et al., 2012) and SSA as high as ~900 m^2/g (Iyoda, et al., 2012), and these minerals are known to be the main constituents of many Andosols (Levard, et al., 2012; McDaniel, et al., 2012).

A study by de Junet, et al. (2013) of the 23-35 cm depth of an Andosol layer puts 70% of OM to be bound to minerals while in a study by Basile-Doelsch, et al. (2007) of another Andosol sampled at deeper 75-85 cm depth puts the number at 83%. Moreover, Parfitt, et al. (1997) made a comparison of the nature of the minerals in the MOAs in Inceptisols (main composition: mica) and Andosols (main composition: allophane and ferrihydrite). Their observations showed stronger OM stabilization and more resistance to organic carbon turnover (due to change in land use) with Andosols than Inceptisols.

In these soils under acid conditions, studies suggests ligand exchange between hydroxyl groups on mineral surfaces and carboxyl functional groups of OM to be a key controlling factor on the formation of stable mineral-organic complexes (Kaiser and Guggenberger, 2000). In the presence of OM, nucleation and growth of alumino-silicate precursors into well formed imogolite tubes and allophanes is stopped at the early development stage and resulting in proto-imogolites with only short range local order (Al/Si~2: alumino-silicates) (Figure 23) (Levard, et al., 2012). These phenomena hinder crystal growth but facilitate strong complexation of OM with inorganic matter thus aiding in the protection of the former.

In conclusion the high SSA contributes to the high organic compound complexing ability of allophanes (Chevallier, et al., 2010; Parfitt and Yuan, 2012) and similar minerals such as imogolites (Parfitt, 2009). And that in turn contributes to the high carbon sequestering and slower carbon turnover nature of Andosols (Torn, et al., 1997; Parfitt, 2009). Therefore, ultimately studies involved with these kinds of soils and their non-crystalline mineral content proves the ability of such soils to better protect organic carbon (Dahlgren, et al., 2004; Goh, 2004; Calabi-Floody, et al., 2014; Huang, et al., 2016).

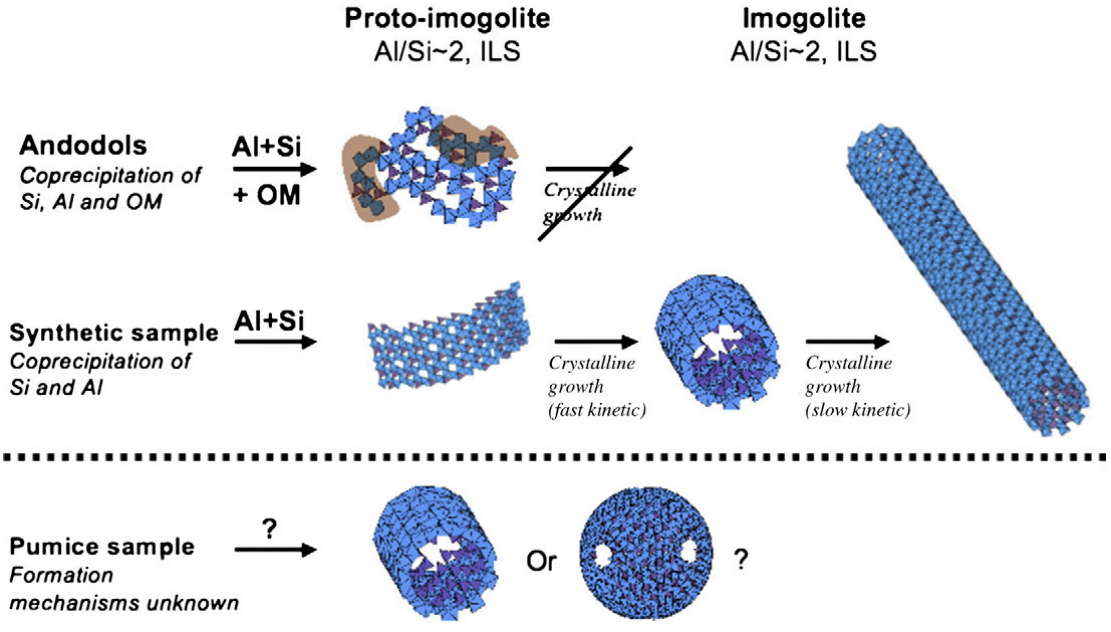

Figure 23: Demonstration of imogolite and allophane growth with and without OM presence. Figure from Levard, et al. (2012)

Moreover, other major factors that affect MOAs include the kind of cations and organic compounds involved in the complexation, the inorganic to organic proportion (i.e. metal to carbon molar ratio) during the interaction and chemical state of the medium (pH, redox state, etc.) (Nierop, et al., 2002; Mikutta and Kretzschmar, 2008; Mikutta, 2011; Kleber, et al., 2015). OM complexation to inorganic cations starts to be favored at as low molar metal to carbon ratios as 0.03; with trivalent cationic species being more favorable than divalent cationic species at conditions lower than soil pH (Thieme and Niemeyer, 1998; Kaiser and Guggenberger, 2007; Siéliéchi, et al., 2008; Kleber, et al., 2015). Due to their pH dependent state of dissolution, Fe^{3+} ions are more favored than Al^{3+} ions when considering more acidic condition (Holt, 2002; Salgado, et al., 2013). But studies have also shown preferential affinity of either Fe^{3+} or Al^{3+} to different organic compounds relative to each other and depending on the nature of the OC (Vilgé-Ritter, et al., 1999a; Mason, et al., 2000).

Kleber, et al. (2015) discuss these interactions to commence and proceed by hindering linkage between two metal oxide monomers due to the presence and interaction of the active inorganic sites with organic ligands (such as carboxylates). They further point out that in the long run this process results in loss of crystallinity/order and alters properties such as individual particle size, distortion of lattice and metal coordination state in the newly formed phases (Figure 24).

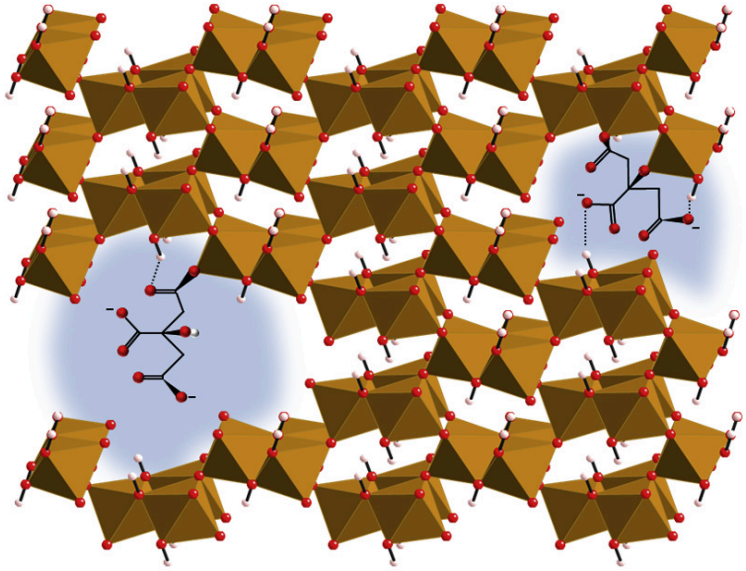

Figure 24: Model demonstrating the perturbation effect of organic ligands on the structure of Fe oxide (α-FeOOH) by preventing linkage between individual $Fe(O,OH)_6$ octahedra. Figure from Kleber, et al. (2015).

2.1.4.5 Factors affecting MOAs

C. Type of OCs: effect on MOAs

In studies that used extracellular polymeric substances (EPS) complexing with inorganic minerals, MOAs were forming via Fe-O-P linkages instead of Fe-O-C linkages. In this coprecipitation experiment, Fang, et al. (2012) showed that no Fe-O-C interactions were detected. Similar experiments by Cao, et al. (2011) of goethite interacting with EPS were

characterized by FTIR. They recorded shift in the bands that were originally of EPS indicating that PO_2^- is interacting with the goethite and no conclusive signals were observed for Fe-O-C interactions, irrespective of the overwhelming polysaccharide presence (21.5 and 437.6 mg/g of total phosphorus and polysaccharide concentrations respectively).

In a coprecipitation study, Mikutta, et al. (2008) made use of:

- polygalacturonic acid (PGA) (1 carboxylic+2 phenol groups /6C repeat unit),
- alginate (1 carboxylic+2 phenol group /6C repeat unit) and
- xanthan (1 carboxylic+11 phenol group/35C repeat unit)

to demonstrate the effect structural and molecular weight variations of organic compounds have on precipitates. This study discusses different C:Fe ratios resulting in varying leftovers or inclusion of the OM in the precipitates. PGA incorporates fully when the carbon presence is at C/Fe of 0.37 (M:C=2.7). Higher carbon concentrations showed reduced total inclusion of the OM in the solids. Alginate coprecipitation showed almost full inclusion into the solids at C/Fe of 1.21 (M:C=0.83). Where as for xanthan, an increase in the proportion of carbon in the solid was recorded that was more than the original proportion. Observation made from these data was that the OC was less efficient at complexing with the Fe phases in the case where the 'proportion of carboxylic functional group per C in a repeat unit' was very low (e.g. xanthan) (Mikutta, et al., 2008). Meaning a carboxylic group in a 35C repeat unit was less efficient in interacting with the Fe phases than the other two cases of a carboxylic group in a 6C repeat unit. An observation from this study is that, if biological extracts are used phosphorous could ultimately dominate over carbon in interacting with inorganic active bonding sites (Cao, et al., 2011; Fang, et al., 2012).

D. Steric effect

Most studies that use low molecular weight OC often utilize compounds with only carboxylic acid as a functional group (Yoon, et al., 2004; Persson and Axe, 2005). But other studies make use of OCs with additional functional groups (even multiple repeats of the same functional group) and often underestimate the additional level of complication in MOAs. One such complication is steric ligand effect. This steric effect on the MOAs was demonstrated by Mikutta (2011) by using hydroxybenzoic acids with varying structural isomorphs (Figure 25). He tested the relative position of carboxylic and phenol functional groups in affecting ferrihydrite coprecipitates and ferrihydrite local structure. They used 4-hydroxybenzoic acid, 2,4-hydroxybenzoic acid and 3,4-hydroxybenzoic acid at ligand/Fe ratios increasing in the order 0, 0.1, 0.2, 0.4 and 0.6 (i.e. M:C=Fe:C= 'No C', 1.4, 0.7, 0.36 and 0.24).

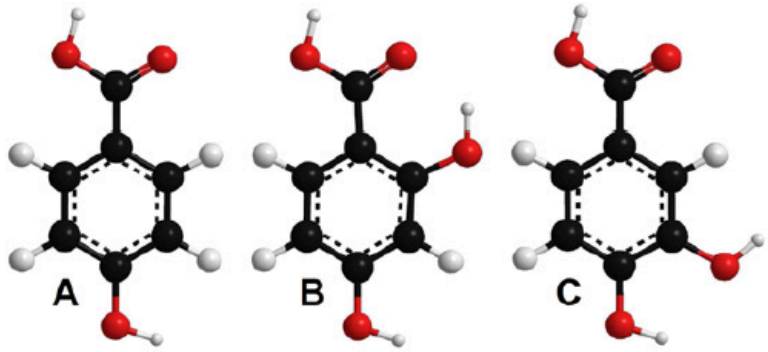

Figure 25: Schematic isomorphs of Hydroxybenzoic acid. (A) 4-hydroxybenzoic acid, (B) 2,4-hydroxybenzoic acid and (C) 3,4-hydroxybenzoic acid. Red, black, and white spheres represent O, C and H atoms, respectively. Figure from Mikutta (2011).

3,4DHB was found to hinder ferrihydrite formation the most followed by equal complexing capacity of 2,4DHB and 4HB. 3,4DHB was able to make bidentate mononulclear interaction using two phenol groups (Figure 26E). 2,4DHB also made bidentate mononulclear linkage but using one OH and one COOH ligands (Figure 26D). This latter interaction compared to the former may be more difficult to achieve due to the very large pH gap between the pKa values of the two functional groups (i.e. 9.24 and 2.58 respectively). 4HB, due to the physical gap between the two functional groups, it was only able to make weaker monodentate mononuclear interactions. In conclusion Mikutta (2011) showed position of phenol groups relative to each other and also relative to other functional groups to have higher importance instead of the mere number of the phenol groups.

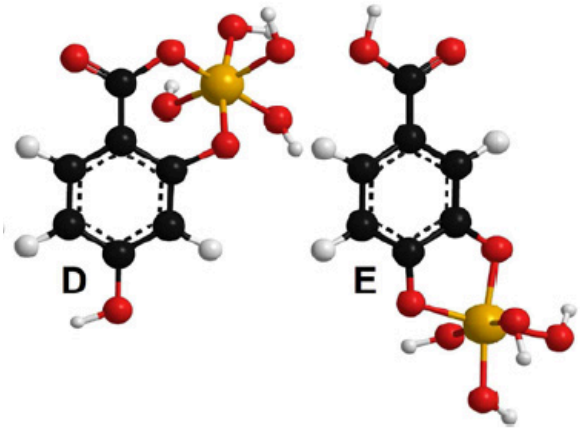

Figure 26: Hydroxybenzoic acid-Ferrihydrite principal complexes. (D) salicylate-type Fe(III) binding by 2,4- dihydroxybenzoic acid, (E) catecholate-type Fe(III) binding by 3,4-dihydroxybenzoic acid. Charges of the complexes are omitted for clarity. Red, black, orange, and white spheres represent O, C, Fe, and H atoms, respectively. Figure from Mikutta (2011).

With ferrihydrite to 4HB and 2,4DHB complexes, no significant changes in structure (e.g. improvement in disorder) were observed in the Fe octahedra by EXAFS. But with 3,4DHB at Fe:C ratio<0.7 a strong increase in amplitude from the first shell Fe-O peak was observed allowing Mikutta (2011) to concluded a reduced octahedral distortion compared to pure ferrihydrite. His conclusion goes parallel to an observation and

conclusion drawn in a previous study by Mikutta, et al. (2010).

At these high carbon concentrations the ordinary ferrihydrite bond distances (for edge and double corner sharing) were observed to have considerably increased in the presence of 3,4DHB. In parallel to that, much decrease in Fe coordinations were recorded with specifically for the Fe:C=0.36 coordination number falling by as much as 2/3 for edge and 3/4 for double corner interactions relative to pure ferrihydrite. This advanced stage of Fe-3,4DHB complex was also accompanied by a consistently lower double corner coordination number compared to number for edge interactions in the co-precipitation series with the other two OCs. The author believes these low numbers (especially for the longer Fe-Fe interactions) suggest dominant two-dimensional crystal morphology. At the highest 3,4DHB concentrations (Fe:C=0.24), the coprecipitates were not able to be modeled by any Fe-Fe contributions. This suggests complete poisoning of possible crystalline ferrihydrite framework; or if any Fe-Fe interactions exist (SRO), they are not coherently scattering enough to give EXAFS detectable signals.

Mikutta (2011) finally concludes that these hydroquinone moieties of NOM effectively suppress MOA coprecipitation by kinetically controlling the availability of inorganic Fe(III) species. And also he proposes that these findings explain the reported Fe(III) mononuclear coordination found in humic acid and organic soils as reported by Karlsson, et al. (2008) and Karlsson and Persson (2010).

E. External influencing factors and processes

The interactions in MOAs are also significantly affected by some abiotic factors. For instance, acidic pH generally promotes protonation of most functional groups in organic compound (often carboxylic groups) making them less soluble and less favorable to interaction with inorganic species (Nierop, et al., 2002; Mikutta, 2011). Additionally, the resulting increase in proton concentration in the system poses competition to cations for reaction sites on organic compounds (Mikutta, et al., 2011; Kleber, et al., 2015). At the same time lower pH conditions dissolve minerals by releasing dissolved metal species into solution that, in contrary to above argument, favors the formation of nCOMx.

Kleber, et al. (2015) discusses the chain reaction that follows an active biotic metabolism in soils. These processes result in biomass degradation (oxidative depolymerization), and one of the effects of that being lowering of soil pH. Soil pH lowering in turn promotes further biomass degradation. And with the inorganic soil components it also promotes release of dissolved cationic species and/or alteration of mineral surfaces. These phenomena ultimately give reactive species and/or reactive secondary minerals with the potential to complex to OM (Basile-Doelsch, et al., 2015).. This natural chain of reactions validates the need to study soil transformation in the context of nCOMx formation at acidic yet humid conditions. In microbial hot spots (areas of elevated microbial activity), one should also expect high MOAs turnover rates due to the active, abundant and continuous supply of reactive OM by the microbial community and subsequent degradation of OM and MOAs by similar or other microbial community (Kleber, et al., 2015).

The geochemical processes affected by MOAs are known to influence other critical anthropogenic processes such as crop growth, immobilization of contaminants, production of green house gasses, etc. thus demanding the much needed attention to

this area of research (Kleber, et al., 2015).

F. Common steps in protocols in laboratory based MOA synthesis experiments

Most MOA studies in a laboratory context often follow similar steps in their protocols. Below is a summary of experiments whose protocols made much of the contribution to design the main experimental protocol for this study.

In a simplistic synthesis experiment, Mikutta, et al. (2010) mixed iron nitrate nonahydrate, anhydrous citric acid and disodium arsenate heptahydrate in HDPE bottles and raised the pH from starting values between 0.5-1.4 to a final pH value of 6.5. They achieved this by adding 1M KOH at a rate of 300 µmol/min using a computer controlled titrator under vigorous stirring. They then centrifuged their post precipitation solution at 5000g for 1 hour at 20^0C. Finally supernatants were stored for further analysis (if needed) and settled portions were freeze dried and stored in a desiccator.

A similarly relevant study by Fang, et al. (2012) utilized 40mg of goethite mixed with 8ml of EPS salt solution containing 0, 0.8, 1.6, 3.2, 4.8, 6.4, 8, 9.6, 12, 16 mg of EPS at pH 5. Gentle shaking was applied for 2 hours at 25^0C. They then centrifuged their post adsorption mix at 20, 000g for 30 minutes.

To insure maximal integration of the organic compound with the inorganic components, researchers employ various techniques. In some works agitation or stirring were found to be a necessary step. In a study that involved organic matter adsorption and coprecipitation with ferrihydrite, techniques such as vigorous stirring (Eusterhues, et al., 2014a; Mikutta, et al., 2014) and 12 hours of continuous stirring (Eusterhues, et al., 2011) were employed to bring about the desired exposure of the reaction components to each other. Also, Turpault and Trotignon (1994) carried out static leaching test on blocks of biotite with mild agitation using a stirring mechanism where the sample and stirring rod were separated by a grid. And to avoid precipitation of OM at the low initial pH other techniques by Mikutta, et al. (2014) involved immediate titration of the solution with freshly prepared 1 M NaOH at a rate of 97 mmol min^{-1} until the desired pH was reached.

When briefly summarizing above discussed experiments, they demonstrate that the type, abundance and position of functional groups in an OC could alter expected experimental outcomes. Also, environmental factors such as pH, redox state and ionic strength, and components of our laboratory protocol (e.g. mixing, centrifugation, filtration, etc.) if not properly selected and implemented in our experiments, they would easily divert studies from their target objectives. Therefore, the lesson learnt is the need for carefully selecting the OC as well as the experimental parameters in our studies.

2.1.5 Interest of EXAFS regarding SRO and sroMOAs

EXAFS is a powerful tool that allows us to probe the atomic environments of a selected X-ray absorbing core element in our samples (Gaur and Shrivastava, 2015). And this tool is becoming an increasingly common practice to use for the analysis of element speciation especially where a non destructive tool with high sensitivity to low concentration is needed (O'Day, et al., 2004). Often used and easily available spectroscopic techniques (e.g. ICP-MS, XRF, etc.) give chemical qualitative and quantitative data on analyzed samples but not structural information. Other analysis techniques such as X-ray diffraction are rendered inadequate due to the absence of long-

range order (crystallinity) in SRO and sroMOAs that have central presence in this PhD and similar other amorphous phases in other studies.

Data retrieved from EXAFS analysis is structural information in the angstrom range away the central atom and the limit for good quality signal (with regard to structural distance) may extend as far as ~4Å from this absorber atom (O'Day, et al., 1994). Variations to this distance limit depend on quality of signal acquired. That in turn depends on factors such as the nature of the core element being probed, the quality of sample prepared (i.e. availability of enough of the core element to give adequate signal or not), etc. For this reasons EXAFS becomes a powerful tool in probing the short range order which is often the extent of order available in non-crystalline minerals.

There are also major cons that are characteristic to the nature of this tool, especially in fitting steps to determine the nature of the backscattering atoms. For instance, backscattering atoms with nearly same atomic numbers (e.g. Si, P, Al, etc.) are difficult to differentiate one from the other since they backscatter from almost identical radial distances (Rose, et al., 1996). Moreover, signals from light (low atomic number) elements (C, Si, Al, etc.) could easily be overshadowed by much stronger signals from heavier elements (for example Fe) (Rose, et al., 1997a). Additionally, EXAFS for most of its data analysis methods (e.g. Shell by Shell Fitting, Linear Combination Fitting, Principal Component Analysis, Target Transformation, etc.) it relies on standards or reference data which need to have their own prior proof of validity (Gaur and Shrivastava, 2015).

Regardless, the targeted phases in this PhD fall with in above mentioned category of non crystalline minerals. And irrespective of this technique's shortcomings this section of the state of the art will demonstrate the importance and the validity in using EXAFS by exemplifying results in other studies that analyzed SRO and sroMOAs phases.

2.1.5.1 EXAFS for studying non-crystalline SRO phases

With regard to SRO phases, studies use EXAFS to study a very wide range of properties and were able to compare atomic environments of phases:

- with different elemental compositions (e.g. Fe vs. Mn oxides) or multi element compositions with in the same sample,
- with same core elements but with varying stage of hydrolysis (e.g. oxides vs. hydroxides vs. oxyhydroxides),
- with varying polyhedral coordination (e.g. tetrahedrally vs. octahedrally coordinated Fe phases),
- with 2D or 3D growth frameworks. That is by quantifying the presence or absence of short range (e.g. face and edge sharing) and long range (corner sharing) interactions,
- formed from similar initial starting materials but at different temperatures by identifying the thermal disorders (Manceau and Combes, 1988), etc.

Around 3 decades ago, EXAFS was used quite frequently to lay the foundation to concept behind the hydrolysis and then subsequent polymerization stages of ferric gel formations by basing analysis on the polyhedral approach (Combes, et al., 1989; Bottero, et al., 1994). Using this approach these researchers managed to show the evolution of Fe local structures as a function of hydrolysis ratio. Relying on EXAFS, Combes, et al. (1989)

additionally observed that crystalline minerals often form from their amorphous precursors by attaining long-range order with out compromising their initially achieved short-range order. Using EXAFS Bottero, et al. (1994) gave a direct experimental evidence for the first time for dimers and trimers occurrence in inorganic Fe (III) solutions. Coupling their EXAFS results with particle size data from SAXS experiments, Bottero, et al. (1994) were able to propose a 24 Fe polycation linked as in β–FeOOH for hydrolysis ratio >1.5.

In the same manner Combes, et al. (1990) showed similar local short range order similarities as solutions containing ferric hydrous oxide gels aged into hematite. Fe-Fe face sharing interactions are rarely detected separate from edge sharing interactions. That is mostly due to their small coordination number thus leading to their RDF (Radial Distribution Function) signal (~0.1Å shorter than distance for Fe-Fe edge sharing) to be masked by peak from Fe-Fe edge sharing interaction (Rose, et al., 1997b). But with EXAFS, Combes, et al. (1990) were able show the formation of this nearest possible Fe-Fe interaction in a transient phase at quite an early stage during the aging process. They were additionally able to trace this face Fe-Fe interaction all the way to the formation of the initial hematite crystals. Therefore, this technique (also applied with other minerals) allowed the identification of the amorphous origin of crystalline minerals; which was otherwise impossible to correlate using other less refined techniques such as X-ray diffraction.

Additionally, these aging studies show shortening or elongation of some of the interatomic distances with time. This change in radial distance is caused due to changes in the inter-octahedral angles. That in turn is caused by rearrangement of the various interatomic interactions (e.g. edge sharing interaction being replaced by corner sharing interaction). For example Combes, et al. (1990) showed the shortening of double corner Fe-Fe bonds from 3.43Å to 3.38Å in transiting from the initial non-aged ferric gel to hematite. This was due to the disappearing of edge interactions from N=3.5 to 0 while face and double corner interactions increased from N=0 to 3.9 and 1.5 to 2.8 respectively, with 200 hours of aging. This last observation also demonstrates the power of EXAFS in showing the structural arrangements that favor more order, or vise versa. It is also evidence of the changes in structure that occur as phases mature from amorphous to crystalline in natural environments.

In most naturally occurring minerals, Fe frequents octahedral coordination. And rarely enough, when the right conditions are met we get tetrahedrally coordinated Fe, which has various implications. With Fe K-edge EXAFS shell-by-shell fits and distance distribution analyses Maillot, et al. (2011) were able to determine ~20-30±5% of tetrahedral Fe coordination in their five ferrihydrite samples. The authors state that it is possible to discriminate between these two Fe coordinations by other techniques such as Mössbauer spectroscopy and electron energy loss spectroscopy (EELS). But they additionally state, that with Mössbauer spectroscopy it will be difficult to separate signals from the two contributions (Da Costa, et al., 1994; da Costa, et al., 1995; da Costa, et al., 1998). While with EELS they mention confirmed ferrihydrite beam damage effecting an octahedral to tetrahedral Fe transformation and also reduction of Fe^{3+} to Fe^{2+} (Pan, et al., 2010). These results will allow design of better formulated models with regard to Fe octahedral coordinations, vacancies and defects. This will ultimately aid in understanding how these ferrihydrite phases interact in their environment with other species such as silicates, OM, etc.

As far back as three decades ago Manceau and Combes (1988) also utilized EXAFS to study the poorly ordered structures of Mn and Fe oxides. As far as Fe interacting with other species goes, they were able to give topological data for these oxides and oxyhydroxides including their hydrous states, at an early time in the development of EXAFS tool when diffraction analyses mostly failed.

At a latter time, in a more natural context, Manceau, et al. (1995) studied Fe-Si natural geothermal system that created deposits resembling hisingerite local structure from dissolved ferrous iron and silicic acid. By using Fe and Si K-edge EXAFS (supplemented by other tools) they compared hisingerite structure to standards such as nontronite. And they were able to tell the extent of hisingerite polymerization by simply comparing the difference in signal amplitude and determine the extent of structural disorder to which EXAFS is extremely sensitive to. As such, they were able to differentiate a 2D growth scheme with the hisingerite like coprecipitates in the presence of silicic acid as compared to 3D growth scheme of 2L-ferrihydrite in its absence. Also due to EXAFS's ability to acquire signal from various absorption edges, they were able to more accurately predict for the first time the local structures of hisingerite from the point of view of both Fe and Si as central atoms. They were also able to assert that the local structure of hisingerite resembles that of poorly crystallized, non-stoichiometric nontronite.

Where as, when moving to laboratory settings, a study by Doelsch, et al. (2000) showed the effect of varying Si concentrations on Fe polymerization using EXAFS analysis. They were able to demonstrate increasing Si/Fe ratio resulting in a shift from 3D to 2D growth schemes of Fe colloids, where the shift occurred at an equivalent Si to Fe molar concentrations.

SRO phases are not only composed of Fe but also Si, Al, K, Mg, P, etc. In considering these compositions as factors, some studies demonstrate how other species are also able to modify the hydrolysis path of Fe (Manceau, et al., 1995; Doelsch, et al., 2000). The preferential affinity of P over other species (such as C) by Fe octahedra is well exemplified by Fe containing mineral surface alteration studies in the presence of EPS (extracellular polymeric substances) (Cao, et al., 2011; Fang, et al., 2012). Laying the foundation for these studies were experiments that were employing both P and Fe K-edge EXAFS by analyzing Fe(III) chloride hydrolysis in the presence of phosphate ions (Rose, et al., 1996; Rose, et al., 1997a). Using EXAFS these earlier studies were able to show the first steps during the nucleation and growth process around Fe and P local structures, and how presence of chloride and phosphorus atoms in the first and second coordination shells of Fe inhibits Fe-Fe polymerization.

Levard, et al. (2009) studied Ni reactivity with aluminosilicate nanoparticles in natural and synthetic soil settings. Their Ni K-edge EXAFS results (coupled with XANES and XRD data) identified the Ni-bearing mineral phases and they showed Ni to have the same local structure in both settings. Their results also confirmed earlier findings on sewage spreading processes not affecting Ni mobility in agricultural practices (Doelsch, et al., 2006; Doelsch, et al., 2008).

The study of heavy metal speciation in soils and sediments has also received additional attention for reasons related to remediation attempts in heavy metal contaminated grounds. Often these heavy metal contamination studies include the domains of metalloids such as As and minerals often observed syncing As are iron (oxy)hydroxides.

Waychunas, et al. (1993) studied the surface chemistry of ferrihydrite and crystalline FeOOH phases after As adsorption and coprecipitation. With EXAFS, specifically replying on Fe-Fe coordination numbers, they were able to tell the higher the concentration of the foreign material (As in this case) the more the Fe-Fe polymerization was progressively disrupted. But it should be noted (though not discussed by Waychunas, et al. (1993)) that there is a limit to the increase in Fe polymerization poisoning associated with the increase in the concentration of the non-Fe species (Doelsch, et al., 2000). Therefor, these combinations of conditions in natural environmental settings will lead to the formation of amorphous phases that, in the presence of OM, are known to be good for sequestrating C.

On a more crude level, the 'take away' from these studies would be the need to use EXAFS to also study the role these species (Si, P, Mn, Al, Ni, Fe, etc.) play in mineral formation, which would eventually affect other geochemical processes in soils.

Above studies summarize well the argument that EXAFS has major utility as a tool in mineral identification and to follow elemental speciation. But O'Day, et al. (2004) demonstrate that this tool is not yet perfected and that work still needs to be done. O'Day, et al. (2004) employed a set of 27 Fe containing reference compounds (such as sulfides, phosphates, oxides, carbonates, phyllosilicates, etc.) to make an empirical assessment as to the usefulness of EXAFS (also XANES) in making Fe mineral identifications in sediment and soil matrixes. At the same time they reviewed the shortcomings and irregularities that arise from the need to compare data acquired at various facilities (e.g. synchrotron) and components with in those facilities. Good examples would be spectral incoherence and thus the need for calibration due scans on different beam-lines, monochromator crystal resolutions, entrance slit sizes, and sample-detector geometries. Finally the authors suggested employing similar specifications for example on components at two different synchrotron facilities or beam-lines. The also made high emphasis on the importance and the need for a superior quality, experimentally coherent reference compound database and reference standard mixtures for spectral calibration to aid in identifying complex mixtures using this tool.

2.1.5.2 EXAFS for studying non-crystalline SRO mineral-organic associations (sroMOAs)

Considering the studies reviewed in the previous section, it is worth noting that EXAFS utility does not rest just with in the boundaries of inorganic minerals, but also beyond. In the presence of OM, this tool aids in understanding how minerals sink and sequester C by effectively revealing the interatomic interactions between inorganic species such as Fe, Al, Si, etc. (M) with C (also N). These organo-mineral interactions are often studied from the perspective of formation of stronger Metal-C interactions or weaker Metal-Metal interactions eventually resulting in suppressed polymerization/crystallization of the inorganic phases.

Oxides and hydroxides precipitated in the vicinity of extracellular biosurfaces or polymeric substances of biotic origin give structural and physical characteristics that are quite different from precipitates formed in the absence of these OCs (SRO phases)(Mikutta, et al., 2008). With EXAFS, Mikutta, et al. (2008) observed the abundance of carboxylic groups to have a major role in precipitating ferrihydrite. They point out the minimal change in ferrihydrite local order detected in the presence and

absence of polysaccharides as compared to the significant change detected in the presence and absence of low molecular weight OCs such as citrate (Liu and Huang, 1999, 2003). Mikutta, et al. (2008), with this comparison of polysaccharides with other OCs (Liu and Huang, 2003; Rancourt, et al., 2005) gave an idea on the effect the nature of the OCs (e.g. molecular weight/size) has on the complexing efficiency when forming MOAs. Mikutta (2011) was also able to show, not only variations in molecular weight but also steric effect from different isomers results in significant difference in suppressing ferrihydrite formation (see section 2.1.4.5). This means in MOAs, not all OCs are the same and behave the same, even those OCs that are close to identical to each other as isomers. And these studies demonstrate the efficacy of EXAFS's characterizing resolution of these different effects.

By coupling Fe-EXAFS with ATR-FTIR Persson and Axe (2005) were able to investigate the molecular surface alteration caused by the interaction of low molecular weight OCs (oxalate and malonate) with goethite surfaces. In doing so, they were able to show the impact of OC binding on mineral surfaces and the resulting changes in the surface atomic environment of inorganic species (e.g. Fe). Additionally this example was able to show that during MOAs both reaction partners get altered. And their suggestion was when modeling these interactions using inputs from tools such as EXAFS it is important to weigh in both reaction partners into the equation appropriately.

Often MOAs do not give absolute and mutual protection to their reaction components. Shimizu, et al. (2013) were able to show ferrihydrite stability against Fe(III) reducing bacteria. Their results showed that the bioreduction reduced in the presence of low C concentrations (C/Fe≤0.8) while it was enhanced in C abundance (C/Fe≥1.8), all compared to pure ferrihydrite. They also observed coprecipitation to have resulted in reduced surface area ultimately altering the bioreduction rate while also resulting in total obstruction of goethite and partial obstruction of magnetite formations. The study, using EXAFS, aided in understanding processes in a not well-aerated environments (e.g. anaerobic Fe respiration) with in the soil matrix and also processes involved in biogeochemical Fe-cycling.

pH often plays a major role in most environmental/geochemical processes. Fang, et al. (2012) demonstrated this effect by studying the adsorption on to goethite of extracellular polymeric substances (EPS), extracted from soil bacteria. Using EXAFS and various other techniques, they were able to show the MOAs (Fe-O-P) were formed at pH 3 via monodentate innersphere complexes and at pH 9 via bidentate innersphere complexes. Subsequent fitting steps showed longer octahedral Fe-O distances with higher pH. That was possibly due to the smaller Fe-O-P angle by the bidentate complex compared to a monodentate complex. Their results dictate on the varying nature of the innersphere complexes formed in the MOAs that are dependent on the pH of the environment. On a more general note, the authors were able to conclude that their study gives important insight on how minerals interact with bacteria be it in aquatic or soil settings.

Mikutta, et al. (2010) studied the effect citrate has on precipitating ferrihydrite and thus consequently affecting the speciation of As(V) in contaminated oxic environments. Their EXAFS analysis showed increasing citrate presence to have favored (1) monodentate binuclear to monodentate mononuclear complexes, (2) much reduced outer sphere As(V) complex formations and (3) higher stability of Fe(III)-citrate complexes. They

point out that, in all three above stated effects the presence of these OCs may lessen the potential toxic harm. That means their observations showed the citrate presence increased the strong adsorption of As(V) on ferrihydrite while decreasing the proportion of 'weakly' sorbed As(V). These studies and tools ultimately aid in the understanding of As(V) sequestration attempts in man made "catastrophic systems" such as acid mine drainage.

EXAFS still remains one of the most important tools capable of uniquely probing the local structure of most amorphous/non-crystalline minerals in the angstrom range. But that does not mean it is the only tool suited for this objective. Other techniques such as NEXAFS (Lehmann, et al., 2007; Wan, et al., 2007; Henneberry, et al., 2012), Mössbauer spectroscopy (Johnston and Lewis, 1983; Eusterhues, et al., 2008), SANS (small angle neutron scattering) (Christensen, et al., 1983), FTIR (Doelsch, et al., 2001; Lehmann, et al., 2007), TEM (Levard, et al., 2012), NMR (Doelsch, et al., 2001; Eusterhues, et al., 2007; Levard, et al., 2012; Rennert, et al., 2014), etc. have also given considerable aid in understanding these MOAs.

In conclusion, EXAFS results from the above summarized studies are important since they aid in understanding surface alteration behavior of minerals, speciation during hydrolysis of dissolved species. Same tool will also help comprehend how all these inorganic soil components react with OM in forming MOAs. Therefore, EXAFS coupled with other state of the art characterization instruments is one of the best tools to analyze these interactions and will aid in ultimately finding ways to stabilize these interactions better and sequester C more efficiently.

2.1.6 Why are natural systems difficult to study?

This obstacle stems from the very inherent complexity of all natural systems and also the complex interactions between their components. The soil matrix is an ensemble of living soil populations, and mineral and organic particles with varying chemical characteristics, shapes and sizes in different stages of chemical/physical alteration. This makes the soil matrix an inherently complex system. These complex interactions therefore give insight to the question why these natural systems are difficult to study.

2.1.6.1 Methods to studying complex systems

The complexity and difficulty of studying these natural processes therefore brings much emphasis on the need to simplify. With regard to MOAs, scientists often carry out research by studying actual samples from locations where these processes are the most active (e.g. Andosols in volcanic locations) (Nichols, 1984; Burke, et al., 1989; Basile-Doelsch, et al., 2007; Levard, et al., 2012; Cappelli, et al., 2013; Eusterhues, et al., 2014a; Kleber, et al., 2015). Other techniques still valid but less pursued devise laboratory based experiments to study natural MOAs under simplified and controlled conditions (Schmidt, et al., 1990; Galeska, et al., 2001; Murakami, et al., 2003; White and Brantley, 2003). Or studies also create models to replicate as much the inputs as possible for the various physical and chemical components involved in these processes so as to have much representative outputs (Krull, et al., 2003; Rytwo, 2004; van der Lee, 2005; Kleber, et al., 2007; Frugier, et al., 2008; Aradóttir, et al., 2013; Bonan, 2013).

2.1.6.2 The difference between laboratory based and natural weathering of minerals

The difference between studying MOAs in a natural context and within a laboratory is the relative simplicity of the method in favor of the latter. Often, to effect this simplicity of method various assumptions need to be considered (Huang and Kiang, 1972; Van Veen and Kuikman, 1990; Schwertmann and Cornell, 2000; Dai, et al., 2014) include:

- assuming singular shape of particles (e.g. spherical) in modeling or particle analysis studies,
- fixing a constant pore size and diffusion rate in fluid-rock interface studies
- limiting environmental factors to either only pH or temperature or redox state,
- limiting environmental conditions within either biotic or abiotic domains
- separating natural processes (i.e. either weathering or precipitation experiments),
- considering only one or two minerals and only one weathering agent in weathering experiments.

Some researchers summarize the difference between laboratory weathering experiments and natural weathering of minerals to be in the state of congruency of the dissolution and the presence of simultaneously forming secondary minerals or lack thereof (Hochella and Banfield, 1995; Hellmann, et al., 2012). On the other hand White and Brantley (2003) report discrepancy between the two systems where even the rates of dissolution differ with orders of magnitude. And often, in laboratory precipitation experiments, secondary mineral formation mechanisms involve direct precipitation from saturated bulk solution without nucleation surfaces (Hellmann, et al., 2012). This precipitation process is highly unlikely in natural systems and complicated due to the abundantly available surfaces.

Some studies have tried to bridge or explain this gap between the two approaches (Murakami, et al., 2003; Hellmann, et al., 2012). But often these simplifications and assumptions are there for a reason; and are often used since their presence makes analysis and data interpretation necessarily easier. But these simplifying conditions should be constrained enough so that the experiments remain representative of natural processes and the results obtained are good enough to be extrapolated to the natural processes they were designed to represent.

Other pressing questions

With laboratory based experiments representing natural systems, there are crucial questions to ask.

> How are weathering and mineral formation natural systems different from laboratory based experiments?
>
> Is there a relation between the characteristic of mineral organic associations and the mode of complexation of organic carbon to minerals and/or their secondary surface alteration products?
>
> Specifically, does residence time and stabilization of OM differ when phases are formed by adsorption as compared to coprecipitated phases?

Do other processes such as the mineral degradation activity induced by roots or exchange reactions between new/undecomposed OM inputs and an already mineral-associated OM affect residence time and stabilization of OM?

Some of these questions have been answered adequately for the good part of the last century and some, are not. Kleber, et al. (2015) argues that they are yet to be addressed in depth, specifically with simplified laboratory studies and state of the art and advanced characterization techniques.

In literatures, the precipitates that are being proposed to form with the various formation mechanisms, their occurrence in nature need to be quantified with reliable technics; and analysis should not only be restricted to characterization but also to their reactivity in relation to their chemical and morphological composition (Kleber, et al., 2015). Moreover, more study is merited with regard to the subsequent destabilization of carbon from these organo-mineral complexes. Points such as factors involved in the mineralization and/or initial formation mechanism relating to mineralization extent and rate need more research emphasis.

2.1.6.3 Assumptions and simplifications

This PhD work will be carried out in laboratory based above ground synthesis experiments to study the interaction of OM with inorganic soil components, under varying conditions of formation. In light of the complex nature of natural systems that this work is trying to duplicate, above arguments validated the need to accept certain levels of simplification and assumptions. This will allow the experiments to be carried out in simplified and rapid manner and the results to give basic insights into the intricacies of natural MOAs.

Synthesizing materials that are replica of natural compounds poses a challenge. Factors involved in the formation of these particles are abundant thus making this process complicated. Therefore, the following experimental steps and the much necessary major simplifications will be adopted in the protocol with regard to the dissolution and precipitation processes.

1. Both the weathering and precipitation setups and stages of the experiment will be carried out separately.
2. Dissolution products will be filtered at a cutoff size of 10kDalton to limit precipitation only from truly dissolved species (i.e. basic precursors, e.g. monomers and dimers) instead of polymers/aggregates.
3. Precipitation setups will be void of the weathered biotite thereby omitting provision of nucleation surfaces that are otherwise present in natural systems.
4. OH^- addition to invoke precipitation of new phases will be done at a constant and much faster rate than the conditions and rate it occurs in nature. This will reduce the duration of formation in this work by orders of magnitude compared to natural systems.

2.2 Objectives of the thesis

The crude objectives briefly described in Chapter 1 are here subdivided into two parts. First part is to proceed following the weathering of primary minerals with the aim of collecting leached truly dissolved species that are the raw material in the formation of

new phases. In doing so the work will also take into effect the background contributions from minor mineralogical compositions (e.g. Mg, K, etc.) and their effect in the precipitation of secondary minerals or how the major species (e.g. Fe, Al, Si, etc.) polymerize and how their surrounding is affected. It will also give more emphasis to Si than previous studies, especially in the presence of more than one metal species. Second part is to synthesize amorphous inorganic phases (without OC) and also organo-mineral complexes using the dissolved species from the weathering experiments. These processes are aimed at simulating similar physicochemical processes that occur in natural soil systems; processes such as the co-precipitation (nucleation, growth and maturation), adsorption and hetero-aggregation of inorganic and organic phases (Chorover, 2011; Eusterhues, et al., 2014a; Eusterhues, et al., 2014b). Specifically, task involved observing and studying the interaction of the different reaction partners and the structure during and after the formation of MOAs.

2.2.1 Objectives of the preliminary phase

The objectives of the initial steps will exclusively be involved in gathering theoretical information from literatures and carrying out preliminary laboratory experiments to aid in the design of the main experimental protocol. Tasks will involve setting up proper weathering batches and selecting proper primary minerals to weather. These tasks will help to find materials and processes that would give a compromise between efficient total consumed experimental time and ability for the batch experiments to be representative of a natural soil processes.

2.2.2 Specific objectives

In specific areas of study dealing with mineral surface alterations, various research directions have been pursued. Work by Hellmann, et al. (2015) on secondary mineral precipitates on silicate glass surfaces follows new and state of the art characterization techniques such as EFTEM (Energy Filtered TEM), APT (Atom Probe Tomography) and ToF-SIMS (Time of Flight-SIMS). Their work, though new and advanced in its kind, was specific to silicates and was restricted to inorganic soil components only. Also nanometric secondary precipitates will be studied not only from the perspective of silicate glass but also from phyllosilicate minerals that have abundant Si, Al and also Fe. More over, this work also will incorporate studies of the formation of these nanometric secondary precipitates in the presence of carbon.

Therefore, studies such as Hellmann, et al. (2015) and similar others (e.g. (Kleber, et al., 2015)) grossly argue that what has not been done so far is actually studying these MOAs at a greater depth using reliable quantitative measures and state of the art characterization tools, tools that are continuously being optimized with regard to their resolution and detection limits. Therefore, these following attempts will be included in the objectives.

1. Since minerals in soils are not only composed of only Si or Fe or Al, the newly synthesized phases in this work will try to allow a more diverse and representative composition.
2. Additionally, since OM is also a major constituent in the soil matrix, this study will try to test whether organo-mineral complexes can be formed by precipitating C in the presence of Fe, Al, Si and also other elements resulting from the alteration of silicates, phyllosilicates and iron oxides. This will go parallel to the

theory of dissolution and simultaneous reprecipitation of secondary minerals by Hellmann, et al. (2015). The concept of dissolution-reprecipitation of mineral surfaces will be tested on a geologically representative phyllosilicate, biotite.

3. And effect of abundance and/or deficiency of either of the reaction partners will be determined by varying concentration of carbon.
4. Since pH is also a major environmental factor, this work will attempt to show variation in pH as having an effect on the structure of the newly forming phases.
5. The work will also attempt to chemically and structurally characterize the newly formed phases with state of the art characterization tools such as EXAFS and TEM.

2. Preliminary experiments

The preliminary experiments were composed of a number of trial experiments. Their collectively objective was to give insight and valuable information that allowed the selection of best combinations of minerals and experimental setups for the main weathering experiments (Chapters 4 and 5). Basalt and biotite were used in these weathering experiments at varying levels of dissolution scales (different volumes of batches), which will be discussed in their individual sub-sections.

The preliminary experiments that are presented in this chapter:

- Basalt dissolution/weathering followed by precipitation of new phases
- Biotite dissolution

The results of these experiments allowed us to design the optimized conditions of the experiments presented in chapters 4 and 5.

Analytical methods

A set of analytical methods was used in these preliminary experiments to quantify release of ions at equilibrium conditions and to characterize basalt and biotite alteration: they are presented in a single section below to avoid repetitions.

2.1.1. X-Ray Diffraction (XRD)

X-Ray diffraction analysis (XRD) is a crystallography technique used to determine the atomic long-range order of a crystal. XRD in our study was carried out with X'Pert PRO differactometer using CuKα radiation (40 kV, 40 mA) in the 2θ range of 4^0-70^0 at a step size of 0.03^0 and time per step of 600 sec. Following data retrieval and analysis were done using X'Pert PRO and X'Pert HighScore Plus (a complete full powder pattern analysis tool) software respectively. During the sample preparation stage, same finely ground mass was used in most of the cases for the purpose of obtaining comparative analytical conditions between samples. Additionally, all diffractograms, for purposes of obtaining comparable data, intensity values were normalized by their respective sample masses to give intensity values equivalent to 1g of sample.

2.1.2. Micro X-ray fluorescence (μXRF)

Micro X-ray fluorescence (μXRF) is a non-destructive elemental micro-analysis technique. Compared to conventional XRF, μXRF provides spatially resolved information. This is achieved by using X-ray optics to restrict the incident beam spot size(diameter of 100 μm in this study)(XOS, 2017). This technique gives qualitative and semi-quantitative chemical results for various type of samples (solid, solution, biological, natural samples, etc.) and is complementary to other quantitative techniques such as ICP-AES for subsequent studies. It should be noted that the lateral resolution of such micro-analysis is smaller (compared for e.g. to SEM-EDS analysis) and varies in function of the nature of the detected element and of the probed matrix. Indeed, the X-ray beam penetrates through the sample and interacts with the matrix.

μ-XRF analyses were done using a HORIBA XGT-7000 microscope equipped with an X-

ray guide tube producing a finely focused and high intensity beam with a 100 µm spot size. The X-ray beam was generated with a Rh X-ray tube at an accelerating voltage of 30 kV with a current of 1 mA. X-ray emission from the excited atoms was detected with an Energy-Dispersive X-ray (EDX) spectrometer equipped with a liquid nitrogen-cooled high purity Si detector. The resolution of the detector was 145 eV at the Mn Kα emission line. µ-XRF analyses provided a detection limit (≈ 100 mg/kg). The counting time for each micro-analysis was 500 seconds.

µ-XRF analyses provided a detection limit between ≈100mg/kg and 1000mg/kg depending on element and sample matrix. Elements from Na (Z=11) to U (Z=92) can be detected.

2.1.3. Inductively coupled plasma atomic emission spectroscopy (ICP-AES)

ICP-AES is a technique used for analyzing the concentration of elements in solid and liquid samples. This technique uses the optical emission principles of excited atoms to determine the elemental concentrations. All analysis are done on dissolved samples. As a result, solid samples are required to be dissolved into a solution form, in an appropriate solvent (preferably an acid) (MEE, 2009).

In this study quantitative solution chemistry was done using an ULTIMA C spectrometer from HORIBA Jobin Yvon. Its double fixed polychromator allows simultaneous fourteen major and minor elements analysis (Si, Al, Ca, Na, K, Mg, Fe and Ti species were analyzed in our case) and its high-resolution monochromator adjustable stepwise allowed the sequential multi-elemental (but one by one) analysis of trace elements (Mn and P species were analyzed in our case).

Basalt dissolution/precipitation

Basalt is a microlitic rock with a glass phases that weathers at a fast rate (Aradóttir, et al., 2013). Andosols, which trace their origin to mainly basaltic rocks and volcanic ash are mineralogically composed of short-range ordered aluminosilicates which play a great role in OM stabilization (Levard, et al., 2012; Basile-Doelsch, et al., 2015). The objectives were to develop a laboratory experimental protocol that simulates (1) a natural weathering process (dissolution step) and (2) a subsequent precipitation step from the released dissolved species of stage (1).

2.1.4. Characterization of the basalt

The basalt (Piton de la Fournaise, Réunion Island) had major mineral composition of Andesine, Diopside, Olivine and Ilmenite, as well as a glass phase (not detected by XRD). Its chemical composition, determined by ICP-AES after total digestion is given in Table 8.

Table 8: Chemical composition of the basalt sample obtained by ICP-AES. Results are arbitrarily expressed as oxides.

	ICP-AES
Oxides	**Mass %**
Al_2O_3	15.2
CaO	10.6
Fe_2O_3	13.5
K_2O	0.8
MgO	8.9
MnO	0.2
Na_2O	2.5
P_2O_5	0.3
SiO_2	48.9
TiO_2	2.6
SO_3	0
SrO	0
V_2O_5	0
Ba (mg/Kg)	157.2
Sr (mg/Kg)	363.2
Sum of Oxides	**103.6**

2.1.5. Experimental setup

2.1.6. Dissolution step

The solid samples were contained within a 10 kDa dialysis membranes (~2.8nm equivalent size) to achieve the migration of only dissolved species through the membrane out into solution. The membrane had a 29 mm diameter and 35 mm clip closures were used to clamp the ends.

The dry basalt powder in its dialysis membrane was immersed in an acid solution (HNO_3 solution, at pH2) contained within PFA containers (Perfluoroalkoxy alkane) with volumetric capacity of 60 ml (120 & 1000 ml were used at a latter stage) (Figure 27). Different solid (basalt) to liquid (HNO_3) ratios (S:L) were used at 6g, 2g, 1.2g and 0.6 g of solid samples with a constant total solution volume of 60 ml to obtain 1:10, 1:30, 1:50 and 1:100 S:L ratios respectively.

Entire setup was put in a water bath at a fixed temperature of 25^0C (Figure 27). To monitor pH and conductivity during the test, an automatic titration/dosage setup (785 DMP Titrino with separate 856 conductivity module) from Metrohm was used.

There were specific reasons for selecting nitrate-based compounds. These compounds were used because other acids contain elements of interest (e.g. chlorine in HCl) that have influence on our experiments. With regard to their ligands, the way they will interact with the electron donor metals (e.g. Fe) depends on electronegativity and Pauling rules. For example chloride ion has much more affinity and the possibility to

interact a metal ion than a nitrate ion. Therefore, nitric acid was a good choice for weathering our minerals. For comparison of similar weathering/dissolution experiments using different solutions (water and other acids) reference can be made in Huang and Kiang (1972).

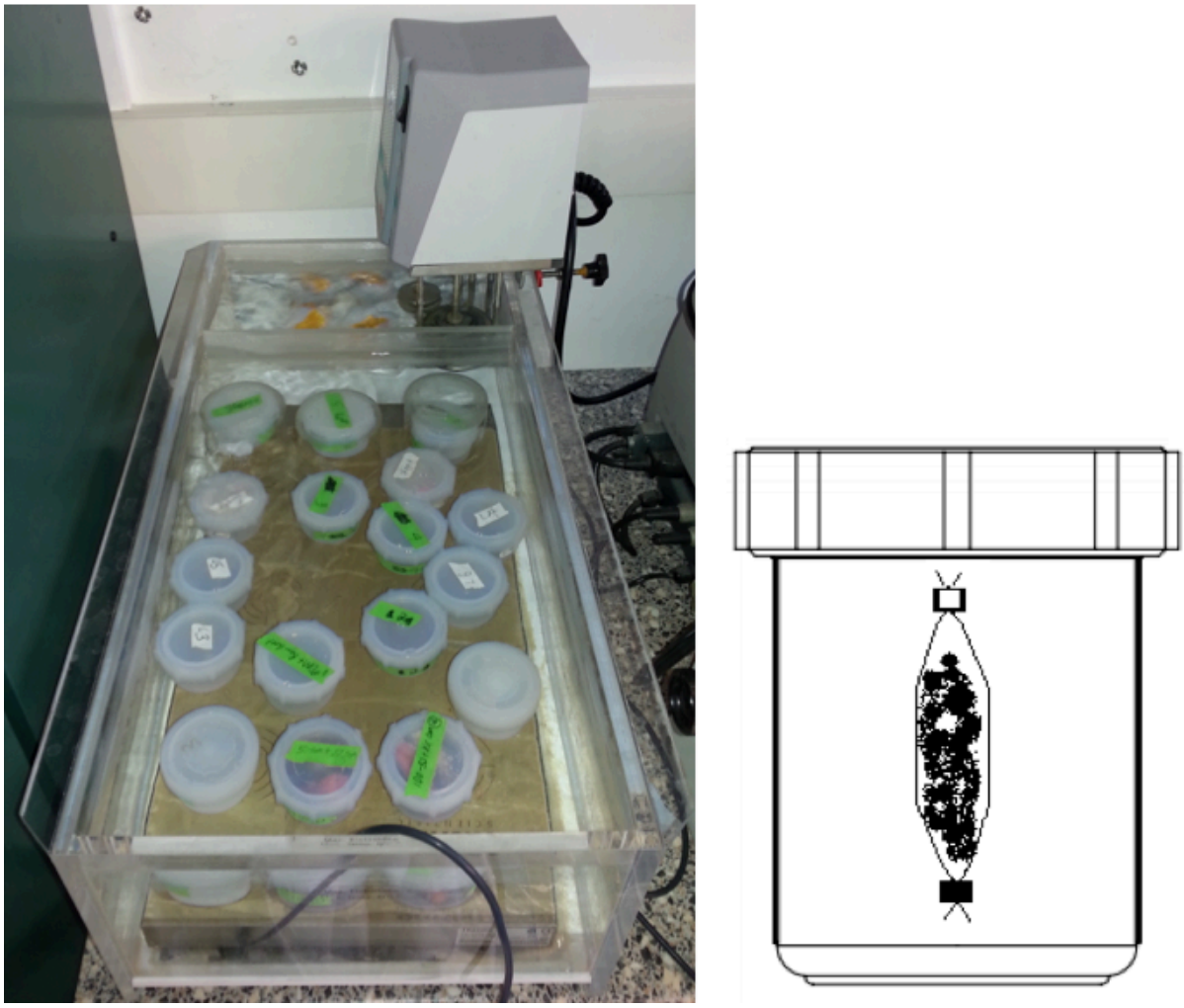

Figure 27: Experimental setup in temperature regulated water bath (left) and sample inside a dialysis membrane with in a PFA container (right)

During the 28 days of the dissolution step, 5 ml solution samples were taken whenever the PFA vessels were opened for pH and conductivity measurements. Solution samples were collected 8 times during the duration of the experiment from outside the dialysis membrane, just before pH adjustment. These samples were analyzed using ICP-AES to obtain concentration of ions released from basalt dissolution. Batch total volume was kept constant by replacing volume of liquid (0.1M HNO_3 solutions for pH adjustment) equal in amount as the volume sampled each time. These steps were repeated until the system needed no more HNO_3 for pH adjustment.

2.1.7. Precipitation step

Second stage of the experiment required the pH to be rapidly elevated to a value suitable for precipitation of secondary minerals from ions released in step 1 (dissolution step). Prior to pH elevation, the weathered basalt and the dialysis membrane were removed from the 1:10 batch to get only the leachate solution with released ions from step 1 for

precipitation. To achieve precipitation, 33.5 ml of 0.1N NaOH solution was used to elevate the pH to a value of 5. Small subsequent volumes of the same solution were added to keep pH stat conditions during the entire precipitation step (32 hours). Solution was manually dosed and was kept continuously stirred using magnetic stirrer. pH and electrical conductivity measurements were done using an automatic titration apparatus (785 DMP Titrino). After approximately 31 hours at pH 5, solution was ultra-centrifuged at 10,000 rpm for 10 minutes using Heraeus Magfuge 40 centrifuge from Thermo Scientific, to isolate secondary precipitates. Titration set up shown in Figure **28** was used which included a flask for storing in the titration solution, a dosage unit (5ml capacity) for adding the titration solution at a constant controlled rate, a Teflon vessel to in-house all the titration mix and, a pH and conductivity electrodes attached to their own separate modules to control their measurements. At the end, samples precipitated in solution were retrieved and freeze dried separately for further characterization.

Figure 28**: Titration setup for the precipitation stages of the experiment**

2.1.8. Results

2.1.9. Weathering/dissolution step

Cations concentrations accompanied by solution pH at the time of sample collection are as given in the four plots of Figure 29. Figure shows release kinetics of ions/cations from basalt dissolution at pH 2. Concentration values were normalized by initial sample mass to give values corresponding to a unit mass.

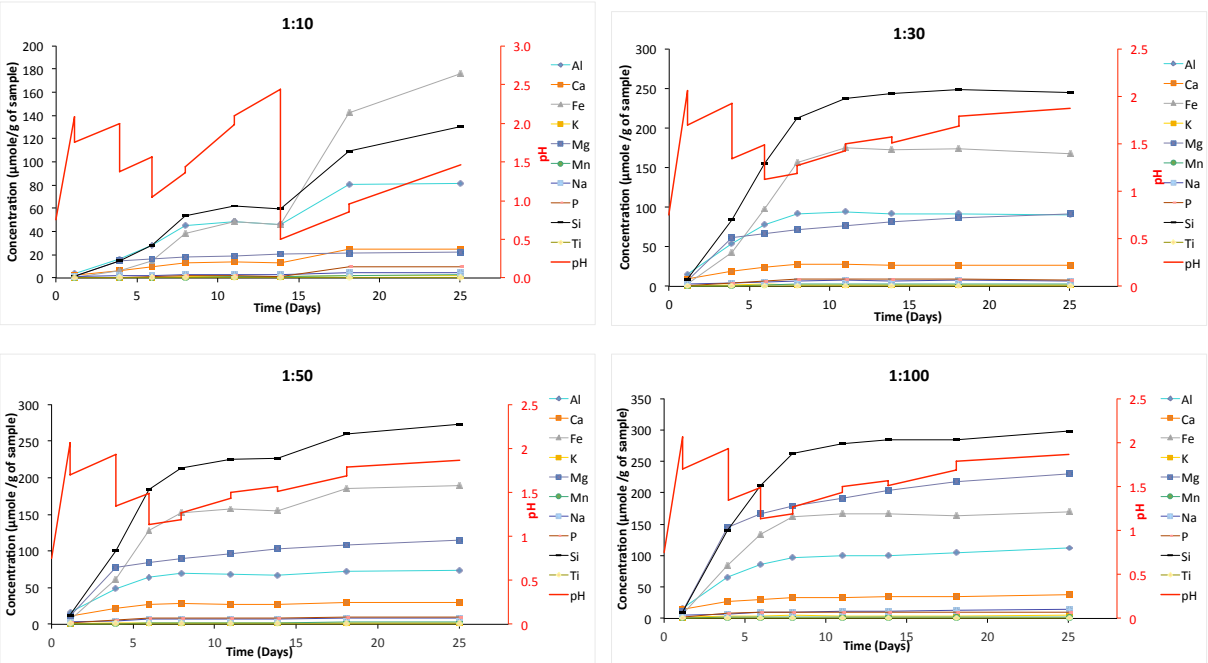

Figure 29: The evolution in time of the concentration of dissolved species in solution of four S:L ratios against pH . Dissolution for 28 days. Final sampling at the 25th day.

Since the 1:10 batch was assumed to have the most dissolved species in solution (before ICP-AES results), it was selected for the precipitation experiment. But with in 28 days of dissolution time, a plateau was reached in all the three cases with regard to release of dissolved species into solution, except for the 1:10 sample (Figure 29). Additionally, in the remaining three samples the plateau was reached in <10 days thus making 1:30 batch setup the most suitable and efficient for subsequent experiments, i.e. post the preliminary stages. The suitability and efficiency refers to the optimal combination of the most reduced experimental time and the most availability of material to weather.

2.1.10. Precipitation of secondary phases

During the initial quick raise to a pH value of 5, conductivity value showed an equally quick drop from a value of 29.9 mS/cm to 15.9 mS/cm (Figure 30). This leachate conductivity decrease reveals the precipitation of secondary minerals for the 1:10 batch.

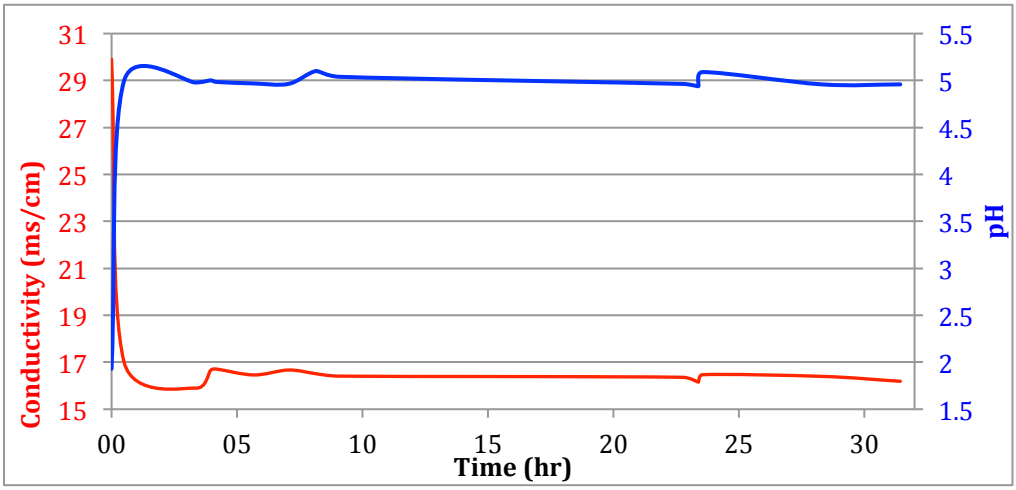

Figure 30: Evolution of conductivity against pH of the final precipitation stage of the experiment (batch 1:10)

During this pH raise, the initial 60ml solution with a conductivity state of 29.9 ms/cm and pH = 1.93 was transformed to a final volume of 93.5ml at a final conductivity state of 16.36 ms/cm at pH =4.98.

A. Structural analysis of secondary precipitates outside dialysis membrane

This sample component was centrifuged and as a result two portions were retrieved. A much coarser yellowish red solid portion (0.4 g, Figure 31) and close to transparent aqueous solution portion.

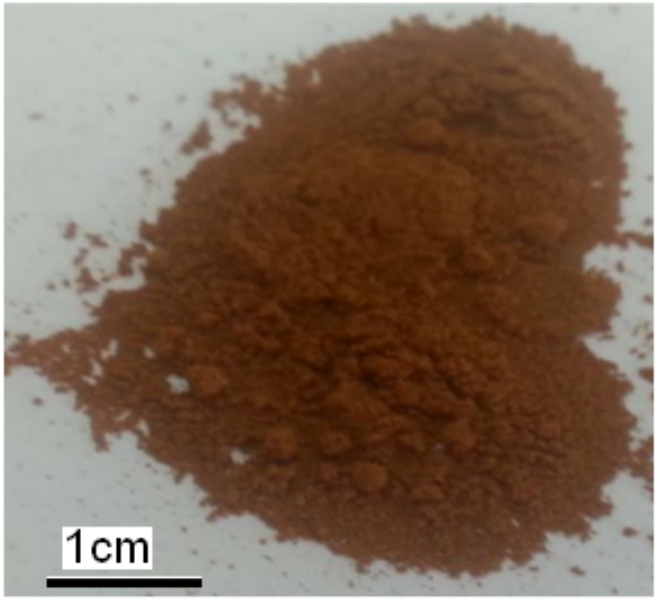

Figure 31: 0.4g nanominerals precipitated outside dialysis membrane.

X-ray diffractogram of this solid portion showed obvious Na-based salt plus feldspar (anorthite and orthoclase) presence. An extended hump from $2\theta=20^0$-50^0 was also evident.

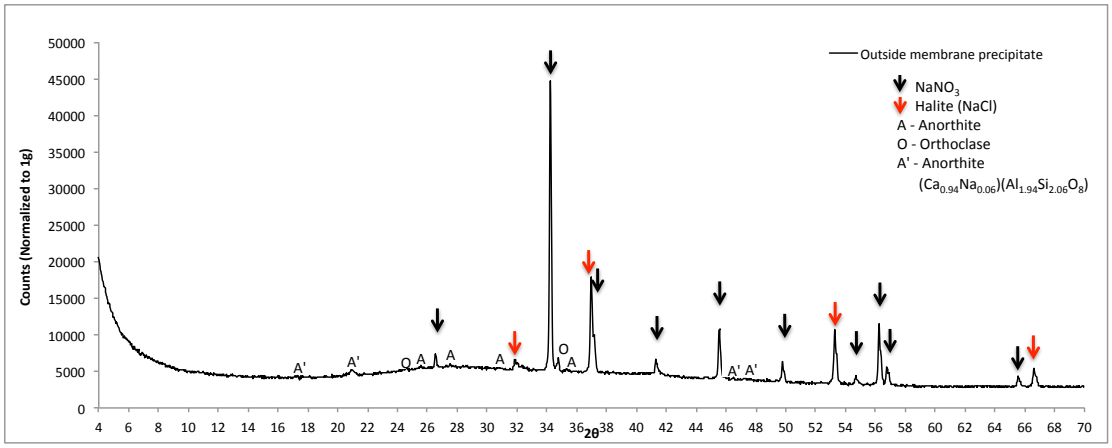

Figure 32: X-ray diffractogram of precipitate obtained in step 2 from outside dialysis membrane and isolated by centrifugation (settled portion after 10,000 rmp for 10 minutes)

B. Micro X-Ray fluorescence (µXRF)

µXRF analysis was carried out on the following three solid samples:

- basalt (initial unaltered material),
- altered basalt (inside the dialysis membrane) and after 28 days of batch leaching at pH 2 (dissolution step 1)
- secondary mineral precipitates from released ions (outside the dialysis membrane) at pH 5 in step 2 (precipitation step).

Since these solid samples are heterogeneous samples, five micro-analyses with an incident X-ray beam spot size of 100 µm were performed at five different locations. These analyses provide semi-quantitative data on chemical composition.(Table 9).

Table 9: µXRF results (average 5 spots of 100 µm) (batch 1:10). Semi-quantitative results are arbitrarilyy expressed as oxides.

	Basalt		Basalt Inside Membrane		Nanominerals Outside Membrane	
Oxides	**Mass %**	**Deviation**	**Mass %**	**Deviation**	**Mass %**	**Deviation**
SiO_2	45	1.2	47.4	0.6	20.9	1.6
Al_2O_3	14.8	0.3	14.7	1.2	10.3	0.5
Fe_2O_3	16.7	2.8	14.1	1.3	32.2	1.4
MgO	5.3	0.7	4.3	0.9	6.7	0.4
CaO	11.3	1.1	11	0.7	0.5	0.1
Na_2O	1.4	3.1	3.3	2	21.2	2.6
K_2O	1.1	0.1	0.9	0.1	0.1	0
TiO_2	3.2	0.2	3.2	0.2	0.1	0
P_2O_5	0.5	0	0.4	0.1	2.3	0.2
MnO	0.3	0	0.2	0	0	0
SO_3	0.1	0	0.1	0	0.5	0.1
SrO	0.1	0	0.1	0	-	-
V_2O_5	0.1	0	0.2	0.1	5	0.4
Cr_2O_3	-	-	0.1	0	0	0
CuO	-	-	0	0	0	0
ZnO	-	-	0	0	0	0
NiO	-	-	0.1	0	0	0
Sum of Oxides	**99.9**		**100**		**100**	

2.1.11. Discussion

2.1.12. Weathering/ dissolution of basalt at pH 2

Equilibrium with regard to dissolution was reached in 25 days for 1:30, 1:50 and 1:100 batches and was not for the 1:10 batch. Therefore, reactions in batches 1:30, 1:50 and 1:100 were 'diffusion controlled reactions' while for batch 1:10 it was 'surface controlled reaction'.

Comparison of the altered basalt with the pristine basalt shows preferential dissolution of olivine (Figure 33). Semi-quantitative micro-XRF analysis of initial and altered basalt (Table 9) additionally demonstrates this selective leaching of mineral compositions Fe_2O_3 and MgO show a slight decrease from 16.7 to 14.1% and 5.3 to 4.3% respectively. While for SiO_2 a small increase was recorded from 45 to 47.4%. These data goes parallel to the observed almost disappeared diffraction peak intensity of olivine [$(Mg,Fe)_2SiO_4$]

and small increase in intensity of andesine [$Na_{0.75-0.5}(Al,Si)_4O_8$] peaks (Figure 33). This can be explained by the theory of Goldich stability/dissolution series (Goldich, 1938).

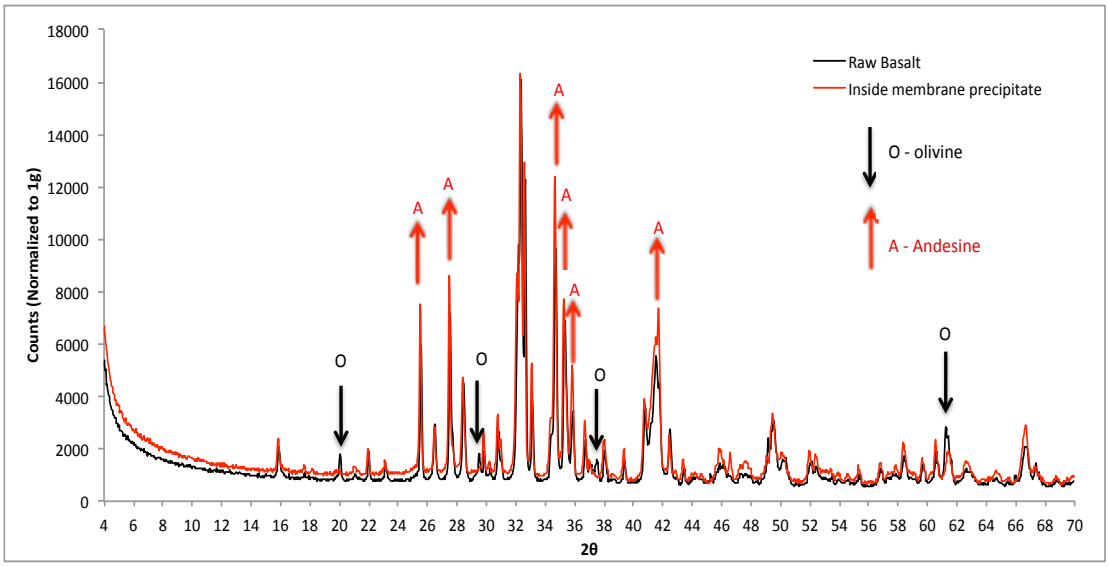

Figure 33: X-ray diffractograms of initial basalt specimen and the weathered/altered basalt from inside the dialysis membrane after 28 days of weathering/batch leaching at pH 2, S:L=1:10. Black arrows (O) indicate the locations where olivine peaks have lost intensity partially or completely. Red arrows (A) show locations where andesine peaks have gained intensity.

Geochemical modelling with CHESS code predicted complete dissolution of andesine for batch leaching at pH 2 with S:L of 1:10 (Appendix 1), which was not recorded in above analysis. But CHESS calculations are based only on equilibrium constants, and do not consider kinetic constants of dissolution/precipitation reactions. With basalt the interpretation of the result of dissolution steps will therefore be complex due to the need to consider simultaneous dissolution of the minerals and glass also at varied dissolution rates.

2.1.13. Secondary precipitation of released ions at pH 5

Mineralogy (**Figure 32**) and chemical analysis (Table 9) of the precipitate obtained at the end of step 2 revealed that this precipitate is mainly composed of: (i) Na-based salts due to NaOH addition for pH regulation and (ii) amorphous phases (as indicated by the presence of a bump between 20 and 50° on X-ray diffractogram) rich in Fe, Al, Si and Mg. The few residual peaks in Figure 6 corresponding to the original basalt mineralogy are likely due to cross contamination during the experiment.

2.1.14. Synthesis of learning from the basalt experiment

The lessons learnt from the weathering step were, good/optimized conditions for dissolution would dictate the use of 60ml HNO_3 solution (concentration ~0.2N) at pH ~2 for weathering at 25°C. A dialysis membrane would be required to isolate the truly dissolved species. A 1:30 S:L ratio would give optimal dissolution in a duration of 28 days to reach equilibrium. Finally a single mineral with pure composition (contrary to basalt with 5 dominating compositions) is highly recommended to better control the dissolution process.

Where as lessons learnt from the precipitation step include the need to use 0.2N NaOH solution to raise the pH to a state of pH=5. And the precipitates are expected to be of an

amorphous nature composed of not only Fe and Al but also Si, Mg and potentially, to a lesser extent, all the elements present in the leachate solution.

Biotite dissolution and precipitation

2.1.15. Objective

Objectives at this stage included a weathering stage adapted for retrieving truly dissolved species from an Fe, Al and Si bearing mineral and re-precipitation into nanominerals with and without OM via two mechanisms: coprecipitation versus adsorption. Biotite is an Fe, Al and Si bearing mineral, common in the critical zone (Nesbitt and Young, 1984; Bonneville, et al., 2011). It functions as a primary mineral in the formation of various endogenous rocks (Kuwahara and Aoki, 1995). It is characterized as having an intermediate relative weathering potential according to the Goldich dissolution series. It forms as highly smooth sheets/lamellae that are suitable for surface alteration studies using AFM.

Laboratory based MOA studies are carried out in various ways. Significant portion of the studies use actual natural OM such as soil floor extracts (Eusterhues, et al., 2014b; Mikutta, et al., 2014), EPS (extracellular polymeric substances) (Norén and Persson, 2007; Cao, et al., 2011; Fang, et al., 2012) and various more heavy/large molecular weight compounds. Utilizing these organic materials is quite representative of the medium they are selected for but makes analysis quite complicated.

However, similarly significant portion of studies use a more simplistic approach to study MOAs. These approaches utilize low molecular weight organic compounds to represent at least the most active functional groups associated with SOM. Some of such materials utilized in studies include OCs contributing multiple carboxylic groups such as oxalate and malonate (Yoon, et al., 2004; Persson and Axe, 2005); and carboxylic + phenol groups such as citrate, hydroxybenzoic acids, polygalacturonic acid (PGA), alginate and xanthan (Mikutta, et al., 2008; Mikutta, et al., 2010; Mikutta, 2011). Therefore, the choice for OM in this study was required to fulfill the following criteria. (1) The compound is to be a model for SOM. That means it should have the major functional groups in most soil organic compounds. That required the OC to include mostly carboxylic functional group and to a lesser extent amine and hydroxyl groups (Kleber, et al., 2015). (2) The compound should have simplicity in its structure meaning it should have low molecular weight.

90% of the dissolved OM is proposed to be equipped with carboxyl functional groups (Sigg and Stumm, 1991). A compilation of pK_a values for extracted or in soil organic materials suggests carboxyl functional groups to be the only functional groups (i.e. among the major ones in soil) reactive at low pH (refer to Kleber, et al. (2015) table 2). Same review mentions polycarboxylates and hydroxybenzoic acids to be one of the most effective groups of ligands in natural OM with the ability to efficiently hinder Fe octahedra polymerization. Additionally, some marine researches studying mussels have repeatedly argued the importance and presence of Catecholate-type Fe(III) complex which is a key component that allows this organism to bind to marine surfaces (Taylor, et al., 1996; Lee, et al., 2006; Hwang, et al., 2010; Holten-Andersen, et al., 2011; Kim, et al., 2015; Rodriguez, et al., 2015). This interaction utilizes a complex formation between double hydroxyls (adhesive protein secretion) and Fe(III) active surface sites at marine pH (~8.2) that effects the binding to the marine surface (Sever, et al., 2004; Hwang, et

al., 2010).

To that end, as in other similar studies (Zimmerman, et al., 2004a) two organic compounds, namely L-phenylalanine and 3-4 Dihydroxy-L-phenylalanine (DOPA), were selected because they represent the OM domain as model low molecular weight OCs. These compounds were also good choices as model OCs because they contain moieties (specially amine, hydroxyl and carboxyl) usually located in complex natural OM such as lignins and humic materials; and also have similar pK_a values (Schnitzer and Khan, 1972; Zimmerman, et al., 2004a; Zimmerman, et al., 2004b; Mikutta, 2011).

Using this simple low-molecular weight organic molecules in organo-mineral interaction studies follow a rationale that they posses similar functional groups as natural OM, resulting in similar reaction mechanisms with mineral surfaces. Kleber, et al. (2015) justify above mentioned rationale with a list of numerous studies (Table 4 in aforementioned review) that used low-molecular weight organic compounds (such as aliphatic and aromatic carboxylates, amino acids, hydroxamate ligands, or phospholipids) interacting with variable-charge metal oxide surfaces. These reasonings, therefore, make above choices as model OC legitimate. These OCs contribute the main functional groups known in organo-mineral stabilization processes: aromatic ring (with two hydroxyl functions for the latter OC), amine and carboxyl functional groups (Kleber et al. 2015).

2.1.16. Materials

2.1.17. Biotite

The biotite studied comes from Bancroft, Ontario Canada (Ward Science). Biotite from similar source was used by Turpault and Trotignon (1994) in an experiment to determine the varied influence of different reactive surfaces (basal and edge) of biotite single crystals. The following structural formula will in this study be adopted as calculated by Turpault and Trotignon (1994) on a basis of twenty-two charges from a wet chemical analysis:

$$K_{0.92}\left(Fe^{(2+)}_{1.06}Mg_{1.66}\right)\left(Fe^{(3+)}_{0.094}Ti_{0.12}Mn_{0.046}\right) \times [Si_{3.00}Al_{1.00}O_{10}](OH_{1.10}F_{0.90}) \ \ldots (1)$$

From a crystallographic point of view, biotite is a TOT phyllosilicate (Tetrahedral Octahedral Tetrahedral). Tetrahedral sheets are formed with three Si and one Al atoms and octahedral sheet with Mg and Fe. The negative tetrahedral charge deficiency (i.e. due to Si by Al substitution) is balanced by K^+ in the interlayers. Biotite is a solid solution with annite and phlogopite as the Fe and Mg end members respectively.

First step in the weathering process was making the mineral more susceptible to leaching by increasing the edge to basal surface area proportion. This was achieved by reducing the biotite to smaller sizes. In this context various particle size ranges (<50, 50-100, 100-160 and 160-200 μm) were tried. Size reduction was achieved using a zirconium oxide ball and bowl grinder.

The mineralogy and effect the size reduction has on the structure of the mineral are shown on the diffraction data given in Figure 34. The biotite mineral used is close to 100% pure. That is evidenced by all the visibly significant peaks in the diffractogram being from phlogopite, in addition to the peaks being significantly sharp.

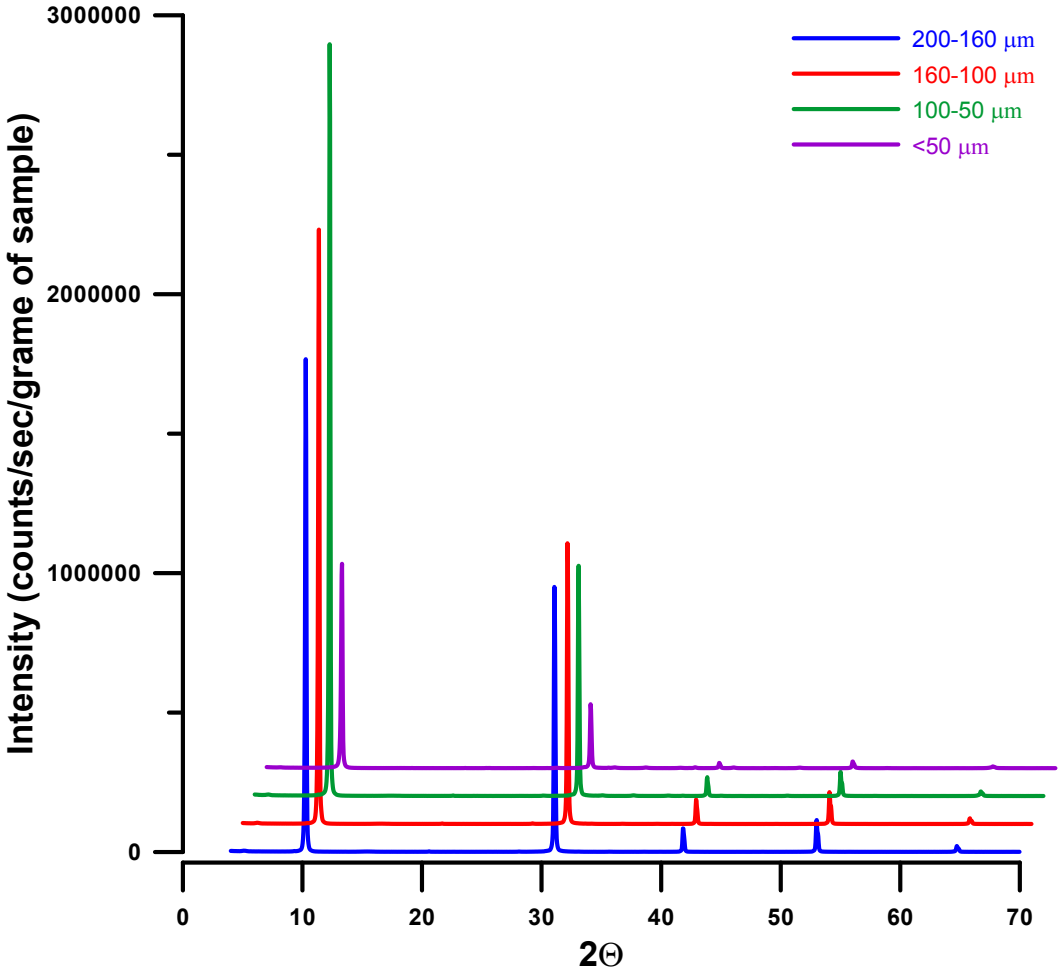

Figure 34: Diffraction data of four size fractions of the biotite sample. Diffractograms are plotted with 1^0 offset for x-axis 2θ values and 10 000 cps/g offset for y-axis intensity values for purposes of comparison.

In Figure 34 we observe peak intensity for phlogopite varying between the four size fraction ranges. Excessive grinding is known to cause damage to structure of minerals on a nano-metric scale. This phenomenon is described as an inverse relationship between intensity (and/or duration) of grinding vs. crystal size (Gonzalez Garcia, et al., 1991). It can be deduced from the peak intensities in the diffractograms that 50-100μm size range is the best option for structural characterization techniques (e.g. XRD). The finest size fraction of <50μm would give faster dissolution rates and was utilized in stages of the project where structural information was not a necessity. But particles in this size range have undesirably reduced crystal sizes thus reducing the coherent scattering domains. That in turn resulted in relatively less intense diffraction signal compared to the other larger size ranges.

2.1.18. Organic Matter

A. L-phenylalanine

L-phenylalanine (Sigma Aldrich) is an α-amino acid with the linear formula $[C_6H_3CH_2CH(NH_2)CO_2H]$; and functional phenyl, amine (pK_a=9.24) and carboxyl (pK_a=2.58) groups (Figure 35). Its L-stereoisomer is the precursor isomer dominantly contributing as a building block to proteins (Lindemann and Hoener, 2005; Broadley, 2010). Because of the hydrophobic nature of the benzyl side chain, this organic

compound is classified as nonpolar or neutral. It has a molecular weight of 165.16 g/mol and was used in only the initial preliminary experiments that will be discussed briefly in following sections.

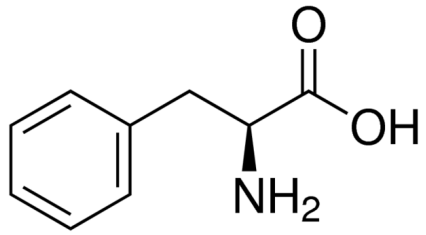

Figure 35: L-phenylalanine

In light of above discussed general requirements, L-phenylalanine was selected because of few important reasons. It has an aromatic ring and two functional groups. The pK_a values of these groups indicate that the organic compound will be in its least reactive state thus interfering minimally in the dissolution process at pH values around 2. That is theoretically valid since both functional groups exist dominantly in their conjugate acid form (HA) at these pH values. And at pH levels greater than the pK_a value of 2.58, during the targeted precipitation pH in our study, the carboxylic functional groups will dominantly lose their proton (thus existing in their conjugate base form, A^-). That allows the organic compound to interact more in the higher pH range suitable for the formation of secondary minerals. Aromatic ring is also expected to give additional reactivity to the organic compound due to its polar nature.

B. 3-4 Dihydroxy-L-phenylalanine

3-4 Dihydroxy-L-phenylalanine (DOPA, Sigma Aldrich) is also an amino acid with the linear formula $[(HO)_2C_6H_3CH_2CH(NH_2)CO_2H]$. It is structurally similar to L-phenylalanine but with two additional hydroxyl groups attached to the 3rd and 4th carbons of the benzyl ring (Figure 36).

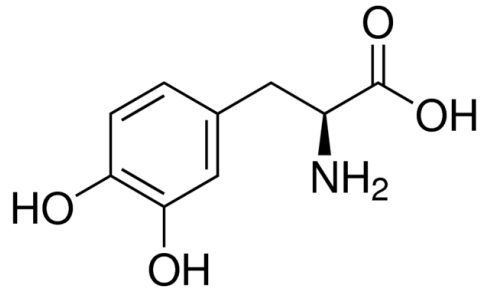

Figure 36: 3-4 Dihydroxy-L-phenylalanine

3-4 Dihydroxy-L-phenylalanine replaced L-phenylalanine due to the additional di-hydroxyl groups and the important abundance of hydroxyl groups in natural OM. Regardless of the phenol and amino groups existing in their conjugate acid state (OH and NH_3^+) at pH5, latter sections will propose more effective complex formation via these groups. While the carboxyl group is dominantly in its most reactive conjugate base state (COO^-) at pH5 state.

3.1.1 Pre-experiment trials: methods, results and discussions

In these preliminary experiments, biotite was weathered at different conditions. When

pH is raised in the precipitation stages, the system was to proceed in three directions depending on at what stage in time the OM is added and if at all it is added. That is coprecipitation of the organic and inorganic reaction partners or adsorption of OM on already formed inorganic phases or precipitation of inorganic phases with out the interference of OM. In doing so, various pre-experimental trials were carried out and the relevant lessons learnt from each are discussed briefly below. Scheme of experiments is given in Table 10 while detailed information on the experiments can be found on Table 26 in Appendix 2.

Table 10: Descriptions of the batch preliminary experiments. Information in this table should be used as an initial data for detailed information in Table 26.

				OM (L-Phenylalanine)	S:L	Description
1st round experiments	Batch 1	1.5g <200µm powder	45 ml pH2 HNO_3		1:30	
2nd round experiments	Batch 1	1.5g 100-200µm powder	45 ml pH2 HNO_3		1:30	Acid washed
	Batch 2	1.5g 20-100µm powder	45 ml pH2 HNO_3		1:30	Acid washed
3rd round experiments	Set 1 & Set 2	1.5g 50-100µm powder	45 ml pH2 HNO_3	0.12g (8%)	1:30	Duplicate experiments in a dialysis membrane

		pH=2			pH=5		Description
4th round experiments	Batch 1	1.5g 50-100µm powdered particles	+ 45ml HNO_3		+ 0.2N NaOH		Dissolution followed by precipitation with out OM
	Batch 2		+ 45ml HNO_3		+ 0.2N NaOH	+ OM	Adsorption
	Batch 3		+ 45ml HNO_3	8% OM	+ 0.2N NaOH		Co-precipitation
	Batch 4		+ 45ml HNO_3+ 8%OM		+ 0.2N NaOH		Effect of OM on dissolution, followed by precipitation

1st round experiments weathered 1.5g of <200µm powdered biotite (not washed) in 45ml HNO_3 at pH 2. That gave a S:L ratio of 1:30. Rapid dissolution of the very fine particles resulted in random rises and drops of pH and conductivity readings. At this stage washing the ground biotite to remove the very fine fractions (e.g. <50µm) was recommended. That would give better control and a steady evolution of dissolution.

2nd round experiments employed similar experimental conditions but divided the size range into two size fractions of 20-100µm and 100-200µm. Of the two size ranges, particles only in the 20-100µm batch were fine enough to effect significant dissolution with in the allotted time window. Lesson learnt was the narrower and smaller size fraction range was better. Recommendations for further experiments were to try an

even narrower size range of 50-100µm.

3rd round experiments employed, again, similar experimental conditions but with the new size range of 50-100µm plus 0.12g of L-phenylalanine. 0.12g OC will represent 8% OM close to the 8-10% Andosols' OC content (McDaniel, et al., 2012). The objective of this round was to check OM effect on weathering and probable simultaneous re-precipitation processes. OM addition gave an initial instantaneous drop in conductivity (Figure 60), which was followed by slower dissolution trends as observed in previous trial experiments. Batches with OM reached stable state faster than batches with out. The initial drop in conductivity was due to the instantaneous mass consumption of H^+ by the $-COO^-$ groups of the OC. Due to absence of change after the initial instantaneous drop in conductivity, L-phenylalanine in this case may not aid therefore be redundant factor in the weathering process. Analysis did not detect any simultaneous re-precipitation.

4th round experiments followed similar protocol but with 4 batches to study formation of nanominerals 1st in the absence of OM, 2nd with OM adsorbed, 3rd with OM coprecipitated and 4th with OM added at the start of weathering.

Congruency of dissolution: difference in the concentrations vs. time values (Figure 64 and Figure 65) were barely above the error margins (especially to wards the end of weathering). But they are enough differentiated to indicate shift in composition of the leachate solution with time. Data shows until a ~11days cations follow Fe > Mg > Si > K > Al > Mn > Ti release pattern while shifting to Si > Fe > Mg > K > Al > Mn > Ti release pattern after ~11days.

According to the empirical formula in section 2.1.16 (assuming congruent dissolution) cation release pattern would follow Fe (0.38), Mg (0.55), Si (1), K (0.31), Al (0.33), Mn (0.02) and Ti (0.04). Values in brackets are molar ratios: [Cation]/ [Si]. An incongruent dissolution being the unambiguous conclusion here, the following additional observations and conclusions were also made. (1) Si, Fe and Mg get leached the most, with K and Al getting leached moderately and Ti and Mn getting leached the least (Figure 65).

The precipitated nanominerals from the 1st, 2nd and 3rd batches respectively yielded phases with no C, adsorbed phases and coprecipitated phases, all of which lacked crystalline order. Analysis of batch 4 showed no significant change when weathering in the presence of L-phenylalanine compared to with out it. Meaning, this L-phenylalanine does not affect the weathering of biotite contrary to observations with other OCs such as oxalate (Olsen and Donald Rimstidt, 2008).

In some of the batches due to prolonged exposure to acidity, the dialysis membrane lost much flexibility and broke towards the end of the weathering process. Therefore, it was not used further in both main and preliminary experiments that followed.

Dissolution rate calculations

With the 4th round experiments, after state of congruency of the dissolution experiments was determined further calculations were made to determine the involved rates of dissolution. Dissolution rates ($m_{i,t}$) were calculated from the monitoring using the modified equation of Bray, et al. (2015):

$$\boldsymbol{m_{i,t} = \frac{c_{i,t} \cdot V_t}{s \cdot M \cdot n_i}} \qquad \textbf{Eq. (1)}$$

where $c_{i,t}$ (moles L^{-1}) gives the concentration of element i at time t, V_t the aqueous volume (L) at t, s the initial specific surface area (m^2 g^{-1}, SSA_{BET}), M the mass of biotite (g) and n_i the stoichiometry of element i in the biotite formula.

The BET specific surface area (Brunauer, et al., 1938) of the 50-100 µm size fraction of initial biotite was measured via a N_2 adsorption (micromeritics 3Flex). Triplicate measurements gave SSA_{BET} of 1.27±0.11 m^2/g. The biotite dissolution rates (Table 11) varied from 1.7 10^{-8} mol m^{-2} h^{-1} (calculated with Si) to 5.8 10^{-8} mol m^{-2} h^{-1} (calculated with Fe) over the first 2.8 days. Over the 14 days of experiment, dissolution rates varied from 1.1 10^{-8} mol m^{-2} h^{-1} (calculated with Si) to 2.8 10^{-8} mol m^{-2} h^{-1} (calculated with Fe).

Table 11: Elemental release rates and biotite dissolution rates.

		Mg	Al	Si	K	Fe
Concentration (µM)	2.8 days	193.8 ± 7.0	72.6 ± 2.2	145.5 ± 15.6	130.4 ± 6.8	190.1 ± 3.4
	14 days	429.9 ± 12.5	220.80 ± 2.6	487.5 ± 81.9	252.4 ± 7.1	463.5 ± 5.1
Elemental release rate (10^{-8} mole m^{-2} hr^{-1})	2.8 days	6.9 ± 0.2	2.6 ± 0.1	5.2 ± 0.6	4.6 ± 0.2	6.7 ± 0.1
	14 days	3.0 ± 0.1	1.6 ± 0.02	3.4 ± 0.6	1.8 ± 0.05	3.3 ± 0.04
Biotite dissolution rate (10^{-8} mole m^{-2} hr^{-1}) *	2.8 days	4.1 ± 0.1	2.6 ± 0.1	1.7 ± 0.2	5.0 ± 0.3	5.8 ± 0.1
	14 days	1.8 ± 0.1	1.6 ± 0.02	1.1 ± 0.2	1.9 ± 0.1	2.8 ± 0.03

* Stoichiometric composition calculated from the empirical formula => $K_{0.9}Mg_{1.7}Fe_{1.2}Al_{1.0}Si_{3.0}$

However, the calculated dissolution rates (Table 11) were slower than the values reported in the literature (see Bonneville, et al. (2011) for a review). A 10 kD filtration was applied in our protocol. This ~2 nm cutoff allowed the truly dissolved components to be retreived separately from the undissolved colloidal particules (McCarthy and Zachara, 1989; Buffle and van Leeuwen, 1992). By comparison, the most frequently used filtration protocols in other studies utilized filters with a cutoff size of 200 nm (Bonneville, et al., 2011; Bray, et al., 2015) to define the threshold for dissolved species. This difference may explain the observed slower dissolution rates in our experiments. For detail calculations of the rates, refer to Table 31 in Appendix 7.

3.1.2 Conclusion of the preliminary experiments

As described above, the purpose of these preliminary experiments were to aid in designing the master experimental protocol. Some of the important points learnt from these experiments include that:

- dialysis membranes are not adopted for use at pH2 conditions due to the effect of prolonged exposure to acidity, despite information to the contrary in the material specifications. Therefore, Tangential Flow Filtration (TFF) mechanism replaces the dialysis membranes in the main experimental protocol. This method of filtration will be more effective since the membrane will be exposed to acidity for much less time compared to dialysis membranes in the trial experiments. We

believe this will not affect the dissolution rate calculations since the cutoff size will be the same.

- with regard to the very fine fractions, there is a grave necessity in washing the powdered specimen so that all the narrow size fractions strictly represent their specified size ranges.
- and larger size ranges made controlling the progression difficult. Therefore it was necessary to divide the powdered biotite into narrower size ranges to have more control over the weathering process. Also, these trials runs gave 50-100 μm to be best size range for weathering biotite to be used in following batches.
- the OCs selected for this study do not aid in the dissolution process. In the contrary their addition consumes protons thus reducing the weathering potential. Therefore, they will not be added until the weathering stage is concluded in the main experimental protocol.
- these experiments showed 45ml dissolution batches to be too small. Therefore, following main experimental batches are designed with bigger volumes with TFF to be applied at the end.
- chemical analysis proved incongruent dissolutions. Therefore, in the batches that will follow, we should expect dominant Si, Fe and Mg and intermediate Al and K presence in the leachate solution.

3.1.3 Overview of main experiments

All stapes followed until this point and taking into account above conclusions and recommendations, we were able to reach experimental protocols fully described in following chapters. These following weathering + precipitation analyses were divided into three major experimental sections that yielded a total of 27 samples.

- First set of experiments dealt with weathering and following precipitation of only inorganic nanominerals (Chapter 4). Column of three samples in Table 12 gives conditions of precipitation which were with No C but final pHs were set at 4.2, 5 and 7 to simulate variable natural pH states for the precipitation of nanominerals.
- Second set of experiments dealt with similar weathering stages. But during the precipitation stage, C was added to precipitate nano organo-minerals (Chapter 5). Row of five samples in Table 12 gives these conditions of precipitation which were all set at pH 5 for all samples but C concentrations varied from No C to M:C=10, 1, 0.1 and 0.01 to simulate OM fluctuations or special differences.

Table 12: Chart demonstrating combinations of OC to pH utilized to produce nanominerals from biotite weathering product.

M:C ->	No C	10	1	0.1	0.01
pH 4.2	X				
pH 5	X	X	X	X	X
pH 7	X				

- Third set of experiments (Table 13) was done in a similar manner but without the weathering of a natural biotite mineral. Instead major compositions of the

biotite leachate solution were duplicated using commercially bought metal salts (e.g. $FeNO_3$, etc.). This mix was applied as a starting material for the precipitation of nanominerals both in the presence and absence of C (Chapter 6). This last set of experiments (Table 13) used varying combinations of final pH of precipitation and C concentration. Therefore, this section was able to make comparison between nanominerals produced from natural biotite weathering as opposed to from a laboratory mix of metal salts.

Table 13: Chart demonstrating combinations of OC to pH utilized to produce nanominerals from metal salts.

	No C	M:C=10				M:C=1				M:C=0.1				M:C=0.01			
		DOPA		L-Ph		DOPA		L-Ph		DOPA		L-Ph		DOPA		L-Ph	
		Coprecipitation	Adsorption	Coprecipitation	Adsorption	Coprecipitation	Adsorption	Coprecipitation	Adsorption	Coprecipitation	Adsorption	Coprecipitation	Adsorption	Coprecipitation	Adsorption	Coprecipitation	Adsorption
pH 3										x							
pH 4.2	x	x				x				x							
pH 5	x	x				x				x				x			
pH 7	x	x				x				x							

	Samples that were precipitated in the laboratory
x	Samples that were analysed by EXAFS but not discussed in this section of the report
x	Samples that were analysed by EXAFS and also discussed in this section of the report

4 Composition and molecular scale structure of nanominerals formed by precipitation of biotite weathering products

Abstract

Among soil organic matter (SOM) stabilization mechanisms, organomineral interactions at the molecular scale are suspected to play a main role in stabilizing organic compounds. Nanometric-sized soil mineral phases, because of their large surface area and reactivity, have a high potential for SOM stabilization. In the literature, Fe and Al phases have been main targets of batch-synthetized nanominerals studies while nano-aluminosilicates (phases in which Al is associated with Si) have been mainly studied in Andic soils. Whatever the phases, the generic process forming nanominerals results from (1) the continuous alteration of the primary minerals that releases ionic species and (2), the polymerization through hydrolysis (i.e. precipitation) of these species that form nanominerals at the interface between the primary mineral and the soil solution. The present work simulated, in laboratory, the subsequent processes of biotite alteration in acidic conditions and the following neoformation, in an Al Si Fe Mg K system, of secondary nanominerals after hydrolysis of the dissolved species. Their morphology, size, crystallinity and chemistry were characterized by TEM-EDX on single particles and their local atomic structure by EXAFS at Fe absorption K-edge. The main nanominerals formed were amorphous particles of 10 to 60 nm whose composition (dominated by Fe and Si) was strongly controlled by the pH conditions at the end of the hydrolysis. At pH 4.2 and pH 7, the structure of the nanomimerals was dominated by Fe polymerization, which was hindered by Al, Si, Mg and K. Conversely, at pH 5, the polymerization of Fe was counteracted by the polymerization of high amounts of silica. By comparison with previous alteration studies, the synthetized nanominerals were estimated to be rather analogous to nanominerals formed in natural biotite-bearing soils. Because of their small size and potential high surface reactivity, the adsorption capacities of these nanominerals with respect to the OM have to be considered in the framework of soil C stabilization issues.

4.1 Introduction

The global soil carbon (C) stock is estimated to be 2344 Gt (excluding permafrost) (Stockmann, et al., 2013). The soil C stock is significantly higher than the C stock in biomass (350 to 550 Gt) and in the atmosphere (825 Gt) (IPCC 2013). The soil C stock therefore plays a key role in global C cycle. This role of soil organic matter (SOM), especially since COP21, is particularly highlighted by policy makers for its dual potential both for mitigation of climate change and food security (cop21, 2015; Paustian, et al., 2016; Dignac, et al., 2017). However, it remains largely unknown why some soil organic matter (SOM) persists for millennia whereas other SOM readily decomposes (Schmidt, et al., 2011). Among organic matter (OM) stabilization mechanisms, organo-mineral interactions at the molecular scale are suspected to play a main role (Kögel-Knabner, et al., 2008).

Nanometric-sized soil mineral phases, because of their large surface area, with their large percentage of surface atoms with unbalanced charge and large number of surface functional groups per unit of mass, have a high potential for SOM stabilization (Levard, et al., 2009; Qafoku, 2010; Levard, et al., 2012). These natural nanoparticles (NPs) may occur either as « mineral NPs » (which are defined as minerals that can also exist in larger sizes) or as « nanominerals » (which are defined as minerals that only exist in

nanometric scale) (Hochella, et al., 2008). Most of the laboratory work on the interactions between soils-nanominerals and OMs focused on the Fe-OM and Al-OM systems (Kleber, et al., 2015). They show that OM interaction with hydrolysable metals results in insoluble metal–organic complexes and structures. OM impairs the formation of Fe and Al oxy-hydroxides with higher crystalline order and strongly alters their properties, including primary particle size, metal coordination, and symmetry of Fe and Al octahedra (Kleber, et al., 2015). On the other hand, SRO (short range order) minerals strongly stabilize OM against enzymatic and microbial degradation (e.g. Eusterhues, et al. (2014a) and reference therein).

Fe and Al systems have been the main subjects of previous studies due to soil observations (Kaiser and Guggenberger, 2000) as well as due to the poor solubility of Fe and Al species in most soil pH and redox conditions (pH above ≈2 for Fe in oxidative conditions and pH above ≈5 for Al). However nanominerals other than Al and Fe oxy-hydroxides are known to complex or sorb OM, the best known examples being the Al and Si imogolite/allophane phases in andosols (Torn, et al., 1997; Basile-Doelsch, et al., 2005; Basile-Doelsch, et al., 2007; de Junet, et al., 2013; Basile-Doelsch, et al., 2015). Levard, et al. (2012) showed that the presence of OM impairs the mineral growth and stops the polymerization at a precursor (proto-imogolite) stage. On the other hand, Torn, et al. (1997) and Basile-Doelsch, et al. (2005) showed that OM has been stabilized by these nanominerals for several tens of thousands years.

Thus nanominerals formed with Al and Si can also have interactions with OM, as the Fe and Al mineral phases: released by the continuous alteration of the primary minerals, they can form nanominerals at the interface between the primary mineral and the soil solution. Direct nanominerals formation by the weathering of rock material has been described in oxic waters (Faimon, 2003; Zänker, et al., 2006). These newly formed nanominerals can complex the organic compounds and stabilize them for extended periods of time. This mechanism represents a conceptual model proposed by Basile-Doelsch, et al. (2015). To validate this model, it is necessary (1) to show that the products of the alteration of primary minerals are likely to form nanominerals and (2) to show that these nanominerals complex and stabilize the OM durably. In this paper, we focus on step (1). We propose to characterize the chemical nature and the structure of the nanominerals formed from the elements resulting from the alteration of a primary mineral in the absence of OM. For this, we considered biotite as a common soil primary mineral able to provide, by weathering, a complex combination of elements (Fe, Al, Si, Mg and K).

The formation of nanominerals from a solution requires a polymerizing step by hydrolysis of metallic cations like Fe or Al (Manceau and Drits, 1993; Rose, et al., 1997b; Doelsch, et al., 2000). In oxic conditions and at pH higher than 3-4, Fe^{3+} for instance, is known to be insoluble and reactive (Dousma and Debruyn, 1976; Byrne, et al., 2000; Rose and Waite, 2003). Polymerization steps start from elementary monomeric building blocks such as $[Fe(H_2O)_6]^{3+}$ octahedron and are accomplished via intramolecular condensation which first involves deprotonation (Combes, et al., 1989; Rose, et al., 1997b). Formation of the small clusters via edge and double corner sharing between Fe octahedra is all included in the initial stage of “nucleation” which is followed by latter stages of growth and aggregation (Wells, 1984; Rose, et al., 1997b). Polymerization routes were found for Al too, with the formation of a transient Al_{13} polymer (Bottero et al., 1980). It has been shown that Si can strongly impair the polymerization stages in both elements (Lartiges, et al., 1997; Doelsch, et al., 2000).

Our experimental protocol combined both a weathering step which provided a complex solution of Fe, Si, Al, K and Mg cations, followed by the polymerization of nanominerals in a range of pH corresponding to soil conditions (pH 4.2, 5 and 7). Atomic structures of nanominerals were determined by Fe k-edge EXAFS (Extended X-ray Absorption Fine Structure) spectroscopy and size, shape, crystallinity and chemical composition by TEM-EDX. Three main questions are raised in this paper: (1) Does the proposed experimental protocol make it possible to obtain nanominerals? (2) Are the polymerized nanominerals homogeneous or of variable chemical composition? (3) Are the obtained nanominerals representative of phases that can form in soils?

4.2 Materials and Methods

4.2.1 Experimental protocol

Biotite is a TOT phyllosilicate. The tetrahedral sheets are inherently formed with three Si and one Al atoms and octahedral sheet with Mg and Fe. The negative tetrahedral charge is balanced by K^+ in the interlayers. The biotite in our study comes from Bancroft, Ontario Canada (Ward Science) (Turpault and Trotignon (1994)):

$$K_{0.92}\left(Fe^{(2+)}_{1.06}Mg_{1.66}\right)\left(Fe^{(3+)}_{0.094}Ti_{0.12}Mn_{0.046}\right)\ [Si_3AlO_{10}](OH_{1.1}F_{0.9}) \qquad \text{Eq. (1)}$$

The sample was mechanically ground (<50 µm) by zirconium oxide 'ball mill' setup, washed, sieved with ultra pure water and dried (40^0C).

Dissolution step: Post the preliminary stage biotite experiments, this larger-scale experiment that increased the amount of dissolved species production was designed. 33 g of < 50 µm biotite particles were placed in 1L of pH2 HNO_3 solution (solid:liquid ratio of 1:30). After 29 days, dissolved species were separated from non-weathered biotite particles using tangential filtration flow (TFF) (Spectrum Labs model) at a cut-off size of 10kD (pore size of ~2 nm). The filtered solution will hereafter be referred as 'leachate solution'. Concentrations of dissolved species in the leachate solution were monitored with an inductively coupled plasma atomic emission spectrophotometer (ICP-AES, Horiba Jobin-Yvon "Ultima C", Longjumeau, France). The measurement uncertainty was below 10%. The results of the preliminary experiments that contributed to the design of the above dissolution protocol are detailed in Figure 64 and Figure 65 of Appendix 6.

Polymerization step: the precipitation of nanominerals was performed by increasing pH of the leachate solution. Initial pH 2 was raised by adding 0.2N NaOH (Sigma Aldrich) at a constant rate of 70 µL/min (785 DMP Titrino). Pyrex beakers and stir bars were used. Three final pHs were targeted: 4.2, 5 and 7. To determine the target pH values, a preliminary titration curve of the leachate solution was preliminary performed (Figure 37). The slope of this curve changed at pH 4.2 and 5. The slope variations indicated changes in the nature of the hydrolyzing system, inferring correlative changes in the nature and / or structure of the polymerized phases. These conditions represented end of precipitation and also pH state as in mineral precipitation in natural soils (Schwertmann and Murad, 1983; Yong and Phadungchewit, 1993).

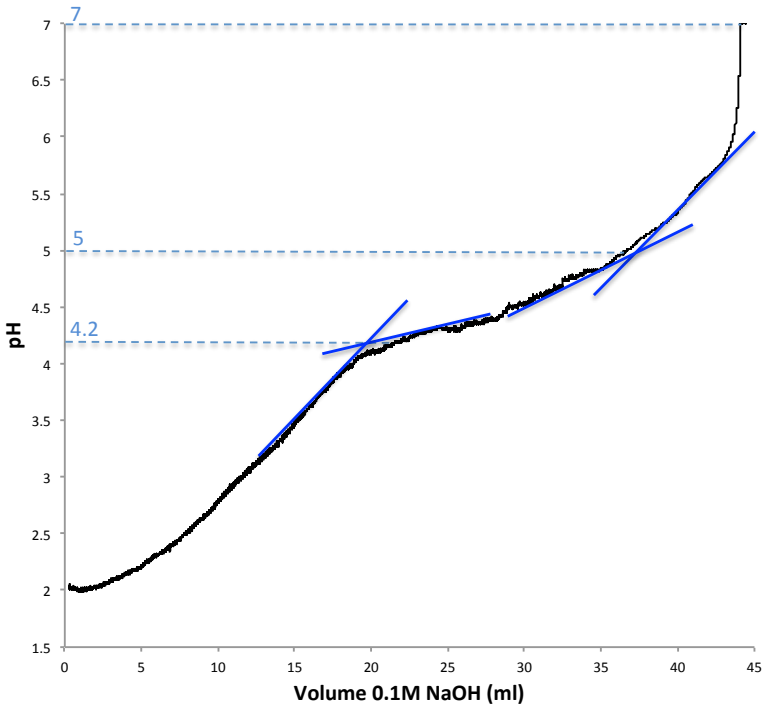

Figure 37: Preliminary titration curve with 0.1M NaOH of a solution with concentration in Si, Al, Fe, Mg and K given in Table 1. Slope changing points at pH 4.2 and 5 indicate changes in the nature of the hydrolyzing system, inferring correlative changes in the nature and / or structure of the polymerized phases. pH 7 represents a pH at which the addition of NaOH no longer has an effect on the polymerized phases.

pH 7 represented a pH at which the addition of NaOH no longer had an effect on the hydrolysis. Durations of hydrolysis and polymerization were 1.4, 1.5 and 1.67 hours for pH 4.2, 5 and 7 respectively. When the target pH was reached, a 1ml aliquot sample was collected for TEM-EDX analyses and the remaining solution was ultra-centrifuged at 80 000 rpm for 2h to separate precipitated nanominerals from the dissolved species. The settled particles were freeze-dried for EXAFS analyses. The whole experimental protocol is summarized in Figure 38.

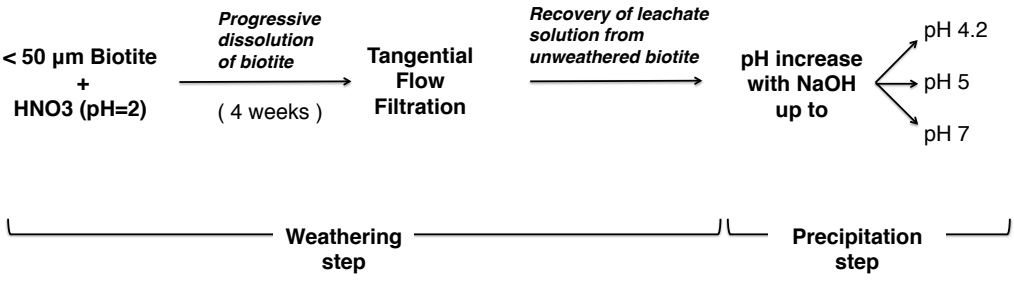

Figure 38: Experimental protocol for biotite weathering and precipitation of nanominerals

4.2.2 ICP-AES

Concentrations of dissolved species in the leachate solution were monitored with an inductively coupled plasma atomic emission spectrophotometer (ICP-AES, Horiba Jobin-Yvon "Ultima C", Longjumeau, France). A six points calibration curve was made with standard solutions in 5% HNO_3 containing varying proportions of cations. The measurement uncertainty was below 10%.

4.2.3 TEM images and analyses

Images and chemical analysis of nanominerals were obtained using a transmission electronic microscope coupled with an EDX analyzer (JEOL JEM 2011 TEM). For each sample, EDX analyses were performed on a set of around 40 nanominerals of different sizes. Parameters were: magnification of 50 000X, angular tilt of 20^0 toward the detector, energy range of 40keV, and corrected counting time of 30 s. A constant beam density was set at ~63.5 $pA.cm^{-2}$. Fe, Si, Al, K, and Mg were quantified by applying the Bruker AXS MET line mark data quantification procedure (Property of Bruker) inherited from the original Cliff and Lorimer method (Cliff and Lorimer, 1975; Lorimer and Cliff, 1976; Mellini and Menichini, 1985). This technique allows the EDX spectra to be treated by applying background subtraction (Bremsstrahlung calculation), Gaussian deconvolution, and k factors corrections by utilizing pre-calculated data for layer silicate standards with known homogeneous compositions (Berthonneau, et al., 2014). Each EDX-analyzed nanoparticle was subsequently size-measured on the corresponding micrograph. Between 30 to 60 micrographs were taken for individual samples. Size analyses were done by measuring the size of a minimum of 10 data points (homogeneous clusters) per individual micrographs.

4.2.4 EXAFS at the Fe K edge

Extended X-ray absorption fine structure (EXAFS) spectroscopy at the Fe K-edge data was collected at ESRF synchrotron source on the FAME beam line (Grenoble, France) and on beam line 11.1 at the ELETTRA synchrotron (Trieste, Italy). Spectra were acquired using Si(220) and Si(111) double crystal monochromators at the ESRF and ELETTRA for the samples and the references respectively. Analyzes were done at ambient conditions in both transmission and fluorescence modes (30-element solid-state Ge detector (Canberra, France)). All samples were pressed into 5mm diameter pellets mixed with boron nitride as a dilution agent. Each spectrum is an average of 3 to 5 individual spectra taken 107 eV below and 849 eV (14.75 $Å^{-1}$) above the absorption edge of Fe (7112 eV) at a counting rate of 2-9 seconds until 14.75 $Å^{-1}$. To get representative spectra and minimize the risk of beam damage, each spectrum was collected on a different pellet location. The data treatment was done using Athena software (Ravel and Newville, 2005). All radial distances in the RDF (Radial Distribution Function) in were uncorrected for phase shift. According to the relation $\Delta R = \pi/2k$, the minimum distance resolution of 0.11 Å was achieved.

The quantitative analysis of EXAFS data followed a two stages approach. The first stage consisted of using linear combination fitting (LCF) based on EXAFS spectra library of reference compounds. The second stage consisted of shell by shell fitting (SSF) to investigate the atomic environment of Fe. The two quantitative methods were performed for all three pHs. They give concordant results.

4.2.4.1 Linear combination fitting (LCF) methodology

The Fe polymerization degree of the different compounds was assessed by LCF using the ATHENA software package (Ravel and Newville, 2005). 'Fitting space' of $\chi(k)$ was selected for analysis. This software uses the Reciprocal (k-space) spectra in its entirety. Varying the k weight magnifies or suppresses different sections of the EXAFS signal. Increasing the k values multiplies the signal intensities by their respective wavenumber values for an amount of times equivalent to the k value. For example, k=2 allows

individual intensity values (from the k=0 EXAFS spectra) to be multiplied by their respective wavenumber values twice. This process allows weak or noisy signals at higher wavenumber values to be magnified and gain significance in fitting or other analysis steps. Experimental spectra in this set of samples were noisy towards higher wavenumber range at k weight of 3. Accordingly, due to the need for clarity of the data by suppressing noise, k weight of 2 was utilized for LCF.

LCF is meant to quantitatively reproduce EXAFS spectra features by using the smallest number of reference compounds. The LCF fit procedure commences with the Athena minimum of 2 reference compounds. Out of the possibilities given by Athena, one with the best fit will be selected. If the sum equals to 1±0.2 then fit and assumptions behind the fit are deemed acceptable. Fitting progresses by adding more reference compounds, one at a time. As a rule of thumb, adding any additional reference compound requires giving an improvement to the fit in comparison to the noise level. More precisely the comparison between two fits (fit A and fit B) was based on the comparison of the difference of the two residues (residue from fit A minus residue from fit B) with the noise level (back-Fourier transform of radial distribution function (RDF) from 15 to 20Å). If the sum of all reference compounds used in the fit equaled to 1±0.2, then fit and assumptions behind the fit were deemed acceptable (Manceau, et al., 2002). The relative goodness-of-fit between data and model was described by the residual factor (R-factor). R-factor is a measure of how well the fit predicts the experimental data (Morris, et al., 1992). Mathematically it is defined as in where 'i' stands for the i^{th} data point. A value below 0.05 generally can pass for a very good fit (Ravel, 2010).

$$R - factor = \frac{\sum_i (data_i - fit_i)^2}{\sum_i data_i^2} \qquad \textbf{Eq. (2)}$$

The sensitivity of LCF is within a 5-20% range (O'Day, et al., 2004), and no more than 3 reference components were used. During fitting all weights were restricted to remain between 0 and 1 without forcing their sum to equal to 1 (or 100%). The suite of reference materials was selected for their known extent of Fe polymerization: Fe dimers (Rose, et al., 1996), Fe-SRO (Doelsch, et al., 2000), 2L-ferrihydrite and goethite have gradually increasing level of Fe-Fe polymerization (Table 32)

Goethite, Ferrihydrite, Fe short range order (Fe-SRO) phase and Fe dimers were used as references. Goethite provides the highest Fe polymerization level of all reference compounds with 4 Fe-Fe octahedra edge-sharing and 4 double corner-sharing interactions. Ferrihydrite is characterized by reduced number of edge interactions (2 to 2.5) and double corners interactions (~3-5) as compared with goethite (Michel, et al., 2007; Maillot, et al., 2011). Fe-SRO is an Fe polymer embedded in silica. It is characterized by 2 edge-sharing but only 0.6 double corner interactions. It was synthetized at pH5 in the presence of Si (Si/Fe=4), conditions were there was no Si-O-Fe interactions (Doelsch, et al., 2000; Doelsch, et al., 2001). For Fe dimers only 1 edge sharing coordination was described (Rose, et al., 1996)). Further detail about these reference standards and their EXAFS spectra can be found in Table 32, Table 33 and Figure 66 (Appendix 8).

Note: Bonding between Fe and other species (e.g. Si, C, etc.) that would mean an iron from within an octahedron creating an Fe-O-Si, Fe-O-C, etc. interactions respectively would, hereafter, be designated as Fe-Si, Fe-C, etc. for simplification purposes. Same usage will apply for other coordinations.

4.2.4.2 Shell by shell fitting (SSF) methodology

Shell by Shell Fitting (SSF) was used to extract structural information such as the coordination number (N_j) and interatomic distances (R_j) relative to the absorber atom using the software code Artemis (Ravel and Newville, 2005). The χ(k) (k-space) signal is an ensemble of sinusoidal contributions from numerous interatomic interactions with the central atom and is empirically represented by the following formula.

$$\chi(k) = S_o^2 \sum_j \frac{N_j f_j(k) e^{-2k^2\sigma_j^2}}{kR_j^2} \sin\left[2kR_j + \delta_j(k)\right] \qquad \textbf{Eq. (3)}$$

where variables corresponding to structural parameters include:

- R_j = distance between central and neighboring atom-
- N_j - number of neighboring atoms
- σ^2 - disorder in the neighboring distance (Debye–Waller factor) which is a composite of the static and thermal disorder in the system

and variables corresponding to EXAFS/Atomic parameters include:

- $f_j(k)$ - amplitude function,
- $\delta_j(k)$ - phase shift function, both of which are the scattering properties of neighbouring atom j, and
- S_0^2 - variable that quantifies the relaxation of electrons in the system at the time of creation of the photoelectron relative to the initial state

This structural information from the experimental spectra was Fourier transformed to real (R) space where the resulting peaks represented distances traveled by scattered electrons from the central absorber atom to the neighboring atoms and back.

Note: When referring to R-space signals as Radial Distribution Function (RDF), as is erroneously done by many studies in the past, caution should be taken since these structural signals, especially at higher R values, are composed of signals from electrons that have followed multiple scattering paths. Therefore, this renders the term RDF inaccurate since its accuracy is valid for only scattered electrons that have followed a single scattering path from an absorber atom to a neighboring atom and back.

The contributions of the various atomic shells were determined using back-Fourier transform of the pseudo-radial distribution function into momentum (q) space. These partial EXAFS functions were then least-squares fitted by a theoretical function (in the single-scattering approximation) in order to determine the structural and chemical parameters of the atomic neighbors in the atomic shells around Fe. Output of these fits will give (1) the identity, (2) the radial distance from the central atom (R) and (3) the coordination number (N) of the neighboring atoms for a scattering path under consideration; with (4) the Debye-Waller factor (σ^2) corresponding to the static and temperature disorders associated with the fit. Uncertainties for radial distances remain with in a conservative ±0.02 Å range typical in the determination of this parameter (Pokrovski, et al., 2002). Since noise levels were not posing problem, k weight of 3 was utilized in these SSF stages.

A lepidocrocite spectrum with pre-confirmed Fe-O and Fe-Fe_2 structural information (coordination numbers and interatomic distances) was used to fix E_o and S_0^2 values to 2eV (±2eV) and 0.75 respectively (Johansson, 1992; Persson and Axe, 2005) . Allowing ±

2eV uncertainty, an E_o range of 0–4 eV was imposed for subsequent analysis of the experimental samples. Steps taken in attaining these values is given in supplementary information, Table 14. It is worth noting that in complex media, various fits may be obtained with similar quality. It is therefore important to remember that structural result may not be univocal.

Table 14: Output for lepidocrocite shell by shell fitting

		Fe-O_1 shell			Fe-Fe_1 shell			Fit Parameters		R-factor
	R-range (Å)	R (Å)	N	σ	R (Å)	N	σ	S_o^2	E_o (eV)	
Fit 1	1 to 2	2.01	5.8	0.08				0.75	2.8	0.015
Fit 2	1 to 3.2	2.01	6.3	0.09	3.07	6.1	0.08	0.75	2.0	0.024

4.3 Results

4.3.1 Chemical composition of the leachate solution and conditions of nanominerals formation

The chemical composition of the leachate solution is presented in Table 15. Fe, Mg and Si mainly contributed to the leachate solution, while Al and K contributed to a lesser extent. Mn and Ti had negligible concentrations (similar to data in Figure 44) and were not considered in the atomic proportions.

Table 15: Chemical composition of the leachate solution provided by the dissolution experiment. [M]/[Si] corresponds to ratio between molar metal to Si concentrations.

	Fe	Si	Al	K	Mg
Concentration (µM)	937	1006	614	883	1247
[M]/[Si]	0.93	1.00	0.61	0.88	1.24
Atomic Proportion (%)	20.0	21.5	13.1	18.8	26.6

The preliminary titration experiment of the leachate solution (Figure 37) showed that pH 4.2, pH 5 and pH 7 were expected as values indicating changes in the polymerization regime. Nanominerals formed at these three different pHs should thus theoretically show differences in chemical composition and/or atomic structure. Therefore, these hydrolysis experiments resulted in nanominerals representing phases that form in the pH ranges between 2 to 4.2, 2 to 5 and 2 to 7 respectively. Collected masses ranged between 11 to 15 mg. The chemical and structural characteristics of polymerized nanominerals are presented below.

4.3.2 Dissolution rate calculations

These rate calculations (Table 16) were done in similar manner as in the preliminary experiments in section 3.1.1. Similar to the total concentration values, highest elemental release rate was recorded for Mg followed by Si, Fe and K with the slowest release rate attributed to Al. But for the calculations based on the entire biotite, mineral dissolution rate based on K gave the fastest rate followed by Fe, Mg and Al with rate calculated based on Si recording the slowest.

Table 16: Elemental release rates and biotite dissolution rates. Rates are calculated over the 29 days weathering experiment.

	Fe	Si	Al	K	Mg
Concentration (µM)	937.2 ± 56.5	1006.1 ± 27.1	613.5 ± 30.5	883.1 ± 83.4	246.7 ± 23.2
Elemental release rate (10^{-8} mole m^{-2} hr^{-1})	3.2 ± 0.2	3.4 ± 0.1	2.1 ± 0.1	3.0 ± 0.3	4.2 ± 0.1
Biotite dissolution rate (10^{-8} mole m^{-2} hr^{-1}) *	2.8 ± 0.2	1.1 ± 0.03	2.1 ± 0.1	3.3 ± 0.3	2.6 ± 0.05

* Stoichiometric composition calculated from the empirical formula => $K_{0.9}Mg_{1.7}Fe_{1.2}Al_{1.0}Si_{3.0}$

4.3.3 TEM-EDX characterization of nanominerals

Hydrolysis experiments resulted in nanominerals obtained at three final pH 4.2, 5 and 7. Collected masses of nanominerals ranged between 11 to 15 mg. Regardless of the pH, particles were aggregated, forming distinct clusters of small and large particles (Figure 39). The size distribution showed a bimodal Gaussian fit with maxima at 6 (±3.7) nm and 30 (±15) nm. ~15 nm was the cut-off size between smaller and larger particles. Electron diffraction analyses revealed a diffuse pattern across all pH and particle sizes (Figure 39).

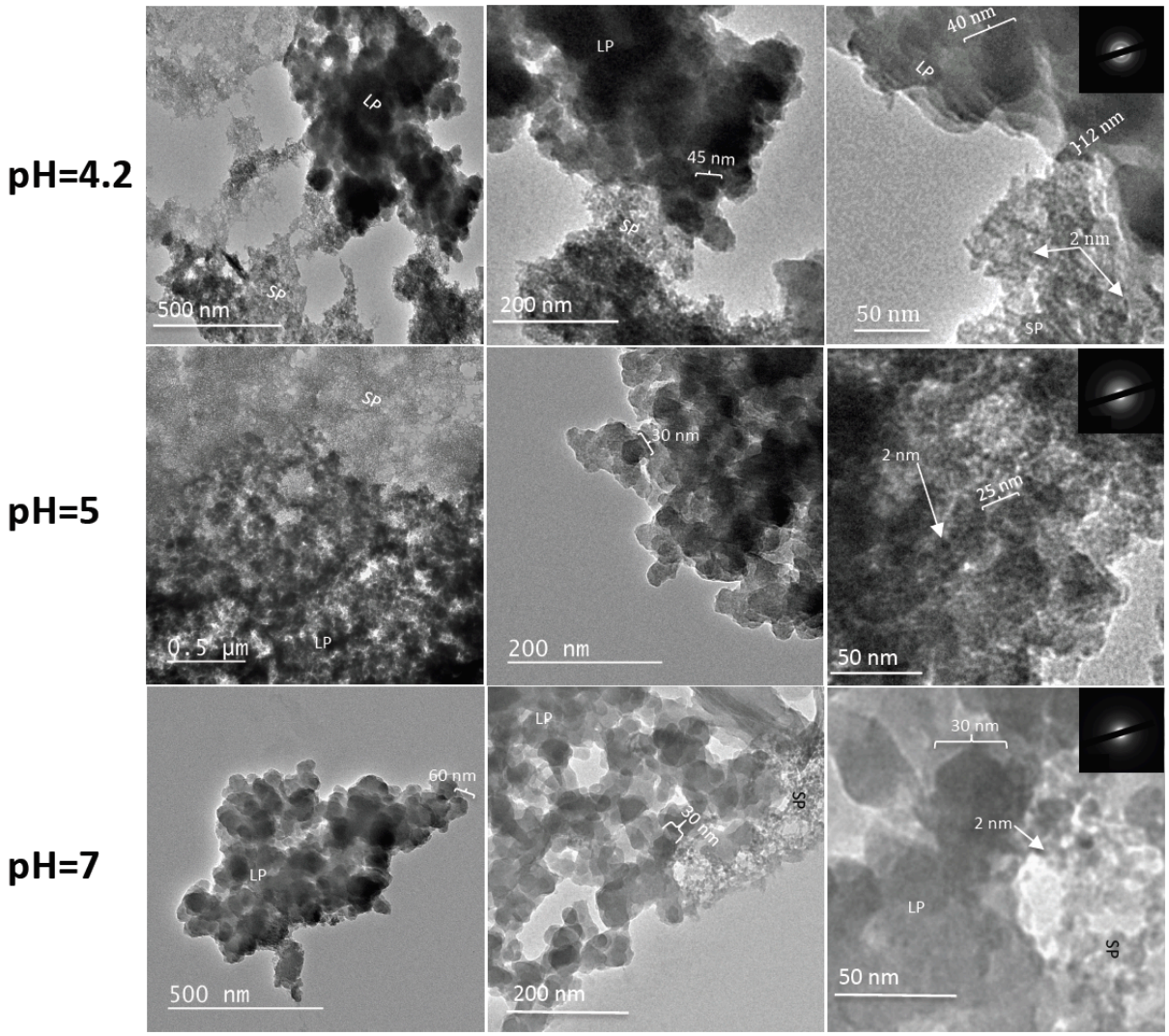

Figure 39: TEM micrographs of nanominerals. For each pH, magnification increases from left to right. On 50 nm scale images, electronic diffraction is superimposed, revealing the amorphous structure of the nanominerals. SP: smaller particles; LP: larger particles.

Fe and Si mainly composed the nanominerals regardless of the pH and size range (Figure 40 A and B). The proportions of Fe and Si were higher than in the leachate solution, indicating preferential polymerization of Fe and Si compared with the other elements. The proportions of Al in the nanominerals were close to those in the leachate solution. The contribution of Al was limited, even at pH ≥ 5 when polymerization of Al was theoretically expected. The proportions of K and Mg in the nanominerals were in the same range as that of Al. However, they were significantly depleted in the nanominerals compared to in the leachate solution. Finally, in terms of general trends as a function of pH, pH 5 represented a singular case in which the large particles were extremely Si enriched and Fe and Al depleted.

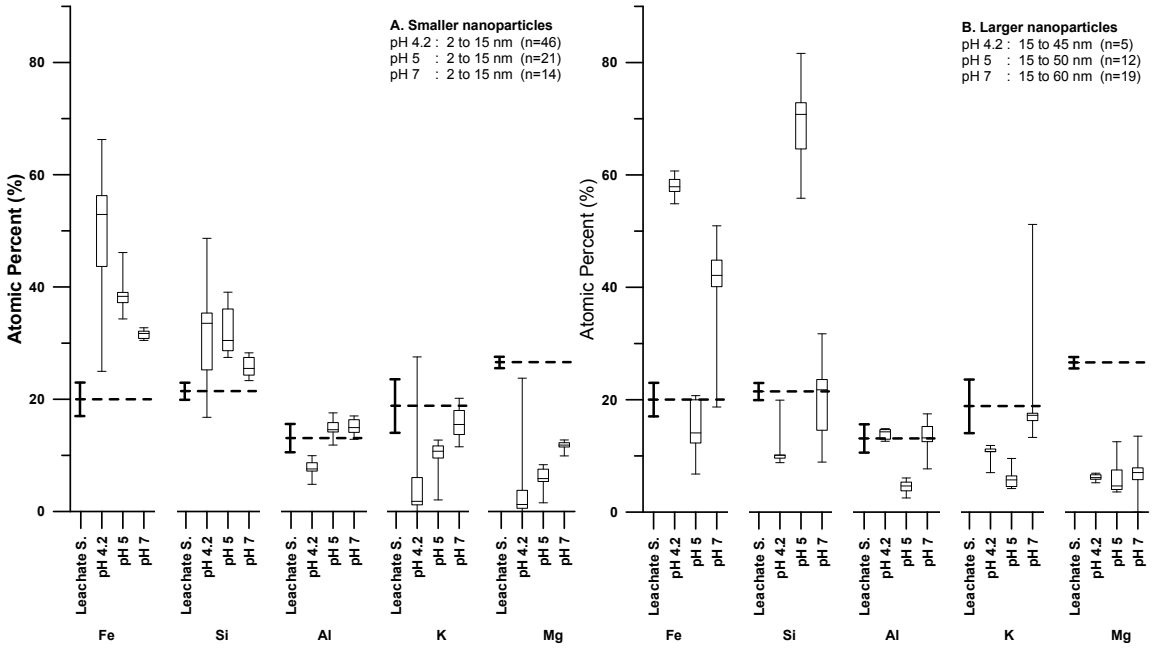

Figure 40: TEM-EDX chemical analysis of polymerized particles at three pH expressed in stoichiometric atomic %. The box-and-whisker plots represent the median value, the upper and lower quartiles, as well as the min and max of the data. The chemical composition of the leachate solution (Leachate S.) is also shown for the sake of comparison (bold dashed line, with their respective element specific error values). A: chemical composition of the smaller nanominerals; B: chemical composition of the larger nanominerals. n: number of particles analyzed.

4.3.4 EXAFS at the Fe K-edge: iron atomic range structure

4.3.4.1 Comparison of raw data

The structural interactions between Fe octahedra are represented as signals at ~5.2 $Å^{-1}$ and ~7.5 $Å^{-1}$ on the EXAFS spectra on Figure 41a (also on Figure 66 in Appendix 8) (Pokrovski, et al., 2003; Mikutta, et al., 2010; Mikutta, 2011). These interactions were also observed as peaks in R-space at radial distances of ~2.7 Å and ~3.2 Å corresponding to edge and double corner sharing interactions respectively (Figure 41b) (Rose, et al., 1997b). In transiting from the 'goethite and 2L ferrihydrite' to 'Fe-SRO and Fe dimers' references, i.e. with decreasing Fe octahedra polymerization, the weak intensity in k-space at ~5.2 $Å^{-1}$ converted into a faint shoulder and the intensity of the ~7.5 $Å^{-1}$ feature decreased. The above change in crystalline order was also seen in R-space with the double corner peak at ~3.2 Å disappearing and peak at ~2.7 Å decreasing in intensity.

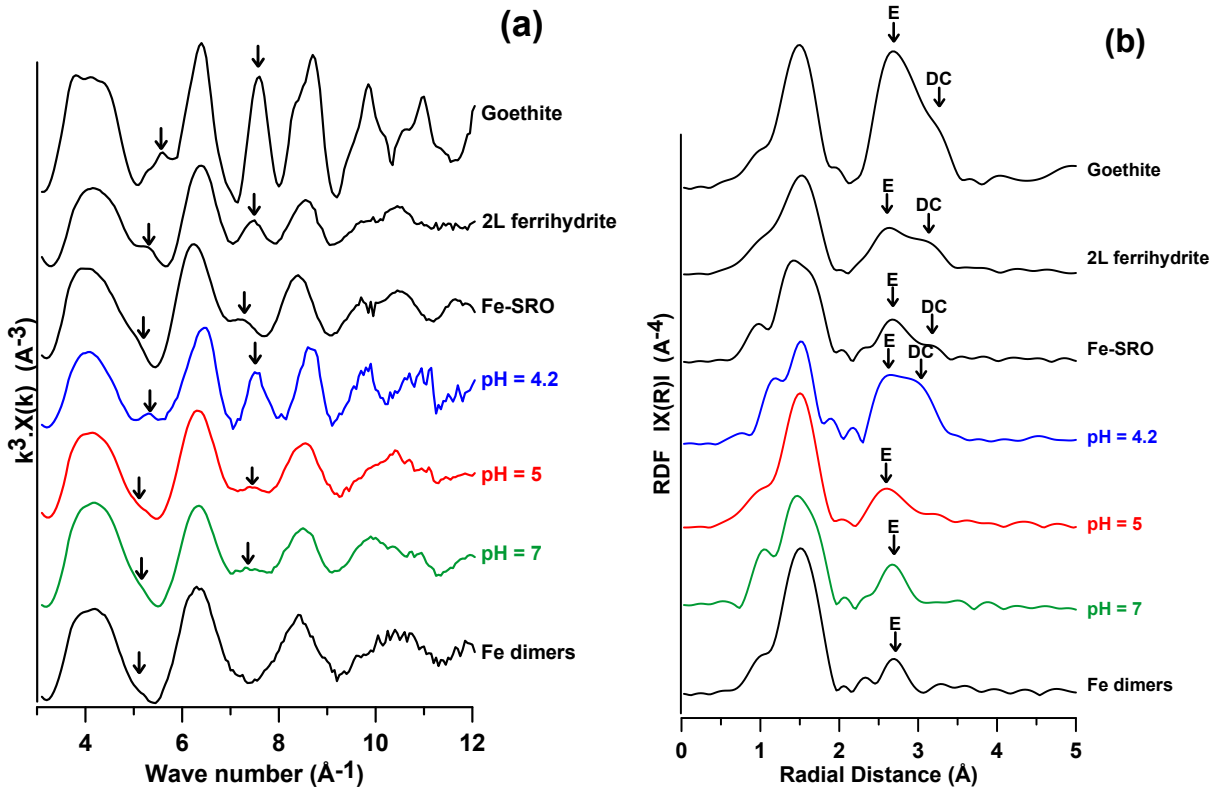

Figure 41: EXAFS (a) and RDF (b) plots. Arrows indicate locations of confirmed Fe-Fe signals. Spectra in black represent references. E and DC stand for edge-sharing and double corner sharing interactions respectively. Distances on the RDF are not corrected for phase shifts.

Features at ~5.2 $Å^{-1}$ and ~7.5 $Å^{-1}$ on the experimental EXAFS spectra showed that iron polymers larger than dimers were formed during the precipitation steps at each pH (Figure 41). Phases formed at the pH 4.2 produced a spectrum for Fe-Fe markers (section 2.1.3.1) whose intensity was between that for goethite and 2L ferrihydrite. These phases produced distinct structural signals with the highest intensity of all the samples (Figure 41). For pH 5 and 7 phases, collective comparison of k and R-space spectra gave an average between 2L ferrihydrite and Fe-SRO references. The intensities of the spectra for these two samples were even weaker than that of the pH 4.2 sample.

4.3.4.2 Quantitative analysis of EXAFS data using linear combination fitting

The best pH 4.2 fit indicated that the pH 4.2 sample corresponded to a mixture between moderately polymerized '2L-ferrihydrite' at ~40% and to the well-crystalized Fe standard of 'goethite' at ~27% (Table 17). 3 standards fits were also attempted but no improvement was observed due to an addition of a 3rd standard (difference of residues lower than noise, Figure 67A). The sum of these contributions reached 67%. This low value indicated the non-uniqueness of the fitting procedure (O'Day, et al., 2004). In the case of the pH 5 sample, addition of a 3rd reference standard improved the fit (difference of residues larger than noise, Figure 67B). It showed high proportion of poorly polymerized reference compounds (Fe dimers + Fe-SRO = 73%) and less than 20% of 2L ferrihydrite (Table 17). In the case of the pH 7 sample, the proportion of poorly polymerized compounds decreased from 73% to 63% while the proportion of 2L ferrihydrite increased to 32% (Table 17). This showed that the iron polymerization degree re-increased from pH 5 to pH 7.

Table 17: Steps in LCF analysis for pH 4.2, 5 and 7 phases. Values are proportions of the reference standards as output by the fit. All values have a ±20% uncertainty range. Fit numbers refer to the graph presented in Figure 67.

		Fe dimers	Fe-SRO	2L ferrihydrite	Goethite	Sum	R-factor
pH 4.2	1 Standards Fit	**-**	**-**	**0.40**	**0.27**	**0.67**	**0.122**
	2 Standards Fit	-	0.02	0.38	0.27	0.67	0.122
		0.06	-	0.34	0.27	0.67	0.121
pH 5		-	0.61	0.31	-	0.93	0.037
	1 Standards Fit	0.61	0.29	-	-	0.90	0.030
		0.70	-	0.21	-	0.91	0.027
	2 Standards Fit	**0.48**	**0.25**	**0.18**	**-**	**0.91**	**0.025**
pH 7		0.81	-	-	0.07	0.88	0.074
		-	0.76	-	0.12	0.88	0.063
	1 Standards Fit	0.58	-	0.36	-	0.94	0.062
		0.54	0.37	-	-	0.91	0.058
		-	0.55	0.41	-	0.96	0.052
	2 Standards Fit	0.01	0.55	0.40	-	0.96	0.052
		0.33	**0.30**	**0.32**	**-**	**0.95**	**0.047**

4.3.4.3 Quantitative analysis of EXAFS data using shell by shell fitting

In all samples, the first coordination sphere around iron was composed of oxygen atoms at a distance of 1.96±0.02 Å (Table 18). The coordination number varied from 6.3-6.5±1.3 for pH 4.2 and pH 7. This result showed the formation of iron octahedra as the main iron species. However, at pH 5, the coordination number was significantly lower (4.9±1.0). This number was either related to iron octahedra considering the 15-25% range error (O'Day, et al., 1994; 2000) or to the presence of a proportion of tetrahedral coordinated iron like in ferrihydrite due to a Keggin-like motif (Michel, et al., 2007; Maillot, et al., 2011).

Table 18: SSF analysis of pH 4.2, 5 and 7 phases. The R window is the radial distance range over which the fit is carried out. N, R and σ represent the coordination number, radial distance and disorder, respectively. E_o is the starting energy value for the fit and R-factor is a parameter for fit quality. Fe-Fe_2 corresponds to edge sharing, Fe-Fe_3 corresponds to double corner sharing. Fit numbers refer to the graph presented in Figure 68.

	R window Å	N ±20%	R (Å) ±0.02	σ (Å)	N ±20%	R (Å) ±0.02	σ (Å)	N ±20%	R (Å) ±0.02	σ (Å)	E_o(eV)	R-factor	Fit No
			Fe-O			Fe-Si			Fe-Fe_3		0,0	0,128	2
		6.8	1.95	0.12	3.5	3.25	0.05	2.2	3.42	0.06			
pH 4.2	1.00-3.63		Fe-O			Fe-Al			Fe-Fe_3		0.0	0.040	3
		6.6	1.94	0.12	3.5	3.02	0.04	1.6	3.40	0.03			
			Fe-O			**Fe-Fe_2**			**Fe-Fe_3**		**4.0**	**0.023**	4
		6.3	**1.97**	**0.12**	**1.5**	**3.01**	**0.08**	**1.9**	**3.38**	**0.08**			
			Fe-O			Fe-Fe_2			Fe-Fe_3		3.0	0.010	3
		4.7	1.96	0.09	1.2	2.99	0.07	0.6	3.13	0.05			
pH 5	1.00-3.09		**Fe-O**			**Fe-Fe_2**			**Fe-Si**		**3.0**	**0.006**	**4**
		4.9	**1.96**	**0.09**	**1.1**	**3.01**	**0.09**	**3.9**	**3.18**	**0.09**			
			Fe-O			Fe-Fe_2			Fe-Al		3.0	0.006	5
		4.9	1.96	0.09	1.0	3.00	0.08	4.9	3.21	0.08			
			Fe-O			**Fe-Fe_2**			**Fe-Fe_3**		**4.0**	**0.011**	**5**
		6.5	**1.98**	**0.11**	**2.5**	**3.06**	**0.11**	**0.5**	**3.35**	**0.11**			
			Fe-O			Fe-Fe_2			Fe-Al		4.0	0.011	6
pH 7	1.00-3.24	6.5	1.98	0.11	2.5	3.06	0.11	2.1	3.45	0.08			
			Fe-O			Fe-Fe_2			Fe-Si		4.0	0.011	7
		6.5	1.98	0.11	2.6	3.06	0.11	1.6	3.42	0.08			

The SSF of the second and third coordination spheres of all samples was performed by successively testing Fe-Fe, Fe-Si and Fe-Al atomic pairs. R-factors of all three atomic shell fits were systematically better than two atomic shell fits. Therefore, only three shell fits are selected to be presented in Table 18. Detailed steps in the SSF for all three phases are given in Figure 68 in Appendix 9. For the pH 4.2 sample, the best solution was obtained with Fe in the 2nd atomic shell with N_{Fe2}=1.5±0.3 at $R_{Fe\text{-}Fe2}$=3.01±0.02 Å and Fe in the 3rd atomic shell with N_{Fe3}=1.9±0.4 at a distance of $R_{Fe\text{-}Fe3}$=3.38±0.02 Å. The interatomic distances were in agreement with Fe-Fe octahedra edge and double corners sharing. The total Fe-Fe coordination number (N=3.4±20%) indicates a low level of polymerization (Table 18). For the pH 5 sample, two solutions had almost equal quality of fit (only differing in the path used for the 3rd atomic shell). The first solution used Fe-Fe_2 edge sharing interaction at R=3.01±0.02 Å with N_{Fe2}=1.1±0.2 and Fe-Si (or Al) path at R=3.18±0.02 Å with N_{Si}=3.9±0.8. The Fe-Si (Al) distance corresponded to a single corner sharing between the Fe octahedron and the Si (or Al) tetrahedron. The second solution only used Fe-Fe octahedra edge sharing with Fe-Fe_2 at R=2.99±0.02 Å with N_{Fe2}=1.2±0.2 and Fe-Fe_3 path at R=3.13±0.02 Å with N_{Fe3}=0.6±0.1. However, in both cases, the Fe-Fe coordination number (1.1-1.8±20%) was much smaller than for the pH 4.2 sample. For the pH 7 sample, the best fits showed 3 solutions. The fit with the Fe-Fe_2 edge sharing path at R=3.07±0.02 Å with N_{Fe2}=3.4±0.7 and the Fe-Fe_3 double corner sharing path at R=3.36±0.02 Å with N_{Fe3}=0.5±0.1 could be the most reliable solution, according to the Fe dominant composition of the nanominerals. Whatever the solution, at pH 7, the total Fe-Fe coordination number (2.5-3±20%) was higher than at pH 5 but lower than at pH 4.2. Detailed shell by shell fitting steps are well demonstrated in Figure 68 in Appendix 9.

4.4 Discussion

4.4.1 Biotite dissolution rate and physical-chemical conditions of polymerization in batches

The proportions of Fe, Si, Al, K and Mg in the leachate solution (Table 15, row for [M]/[Si]) differed from those in stoichiometry in biotite (Figure 65 in Appendix 6) at t=0. These proportions showed, as expected, that the dissolution of biotite is incongruent (Kalinowski and Schweda (1996); Turpault and Trotignon (1994); Bonneville, et al., 2009;Bonneville, et al. (2011)). At the 29th day, dissolution rates ranged from 1.1 10^{-8} mol m^{-2} h^{-1} (calculated with Si) to 3.3 10^{-8} mol m^{-2} h^{-1} (calculated with K) (Table 16). Higher rates in this large-scale experiment (compared to the small scale experiments in the preliminary biotite weathering section 3.3.3) could be related to the absence of dialysis membrane during the weathering step.

However, in a similar manner as the rates for the smaller preliminary weathering batches, the calculated dissolution rates in these batches (Table 15), were also slower than the values reported in the literature (see Bonneville, et al. (2011) for a review). The TFF 10 kD filtration that applied in our protocol post dissolution imposed an approximate 2 nm cutoff with regard the truly dissolved components being retreived separately from the undissolved colloidal particules (McCarthy and Zachara, 1989; Buffle and van Leeuwen, 1992). By comparison, the most frequently used filtration protocols in other studies utilized filters with a cutoff size of 200 nm (Bonneville, et al., 2011; Bray, et al., 2015) to define the threshold for dissolved species. This difference may explain the observed slower dissolution rates in our experiments due to the much reduced total concentration of the dissolved species as specified in Table 15 in comparison to those studies that impose a much larger cutoff size. Nevertheless, we obtained a solution with elemental proportions that are representative of the weathering of a mineral. This composition is therefore more representative of soil solutions than solutions produced by commercial metal salts (e.g. studies that precipitate iron (oxy)hydroxide minerals by hydrolyzing $FeNO_3$ salt) as well as solutions that consider only Fe and Al ions in the formation of nanominerals (Kleber, et al. (2015) and references therein).

As revealed by TEM, the polymerization step enabled the formation of nanominerals at pH 4.2, 5 and 7. These values correspond to realistic pH values in soils (Schwertmann and Murad, 1983; Yong and Phadungchewit, 1993). Moreover, experimental hydrolysis involves rapid changes in pH. Such abrupt variations have also been observed at very small spatial scales (Bonneville, et al., 2011) on biotite surfaces. Consequently, the batch approach used in our protocol, although greatly simplified compared to a soil system, made it possible to reproduce physical-chemical conditions that realistically mimic soil processes.

4.4.2 Local structure of nanominerals

4.4.2.1 The presence of Al, Si, Mg and K in the system limits Fe polymerization

The extent of iron polymerization of the nanominerals (N_{tot}) synthesized in our experiments were less than 3.4 whatever the pH. This value is lower than the number of Fe-Fe bonds in polymers synthesized in pure Fe systems (Combes, et al., 1989; Combes, et al., 1990; Doelsch, et al., 2000) (Figure 42). The same difference in values was also observed in systems in which Fe is hydrolyzed in presence of Si (Doelsch, et al., 2000;

Doelsch, et al., 2001; Doelsch, et al., 2002; Doelsch, et al., 2003; Pokrovski, et al., 2003). In our case, the presence of Al, Si, Mg and K in the solution clearly hinders the polymerization of Fe regardless of pH.

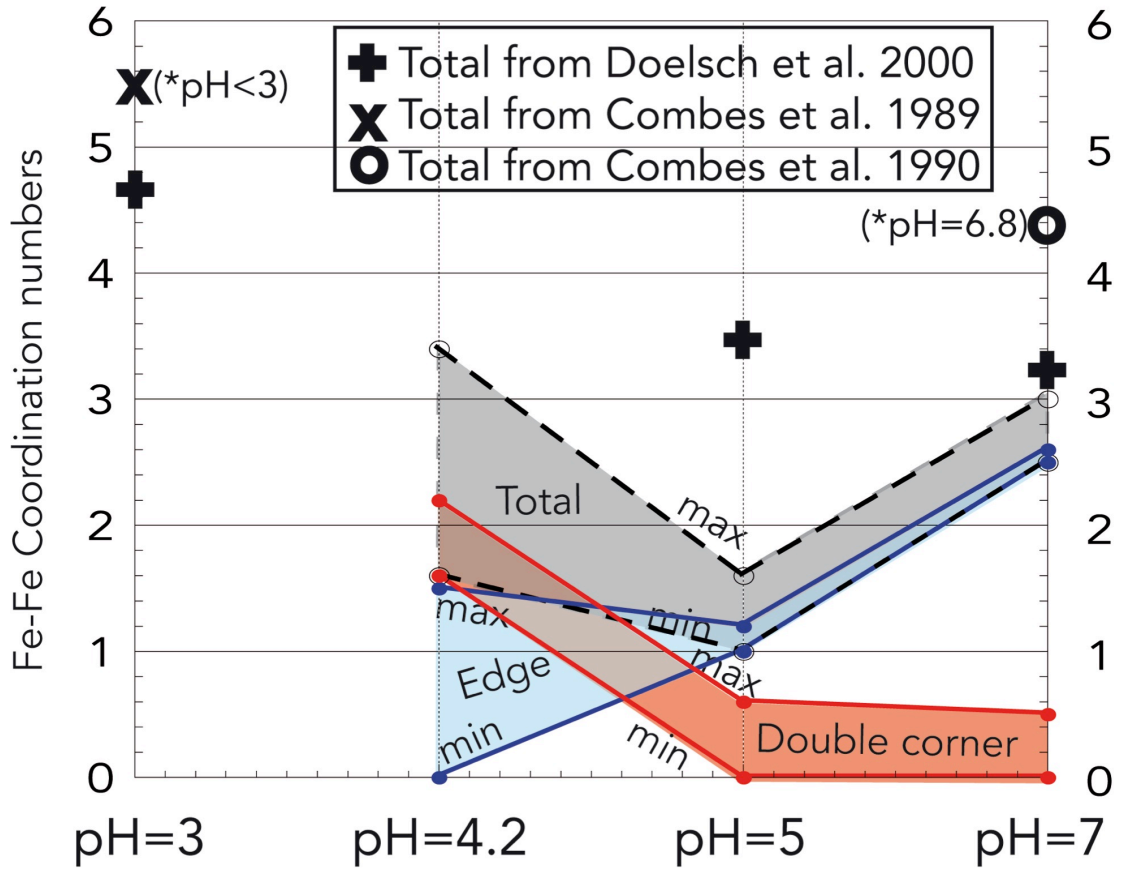

Figure 42: Changes in the coordination numbers for all Fe-Fe atomic pairs in the SSF analysis (Table 18) with the lowest R factors, leading to minimum (min) and maximum values (max) for each type of interaction and for each pH. Total represents the addition of coordination numbers by edge and double corner interactions. Total coordination numbers from pure Fe system from the literature are also shown for the sake of comparison.

4.4.2.2 The pH controls the local structure of nanominerals

For our current study the calculated hydrolysis ratio was higher than 3 for all samples. Under such condition the formation of oxy-hydroxide whether amorphous (Ferrihydrite) or well crystalized (Goethite) is highly favored. At pH 4.2, the level of polymerization of the nanominerals was the highest of our experiments (Figure 42) and Fe was the main element in the nanominerals (Figure 40). This phenomena was similarly demonstrated by the equilibrium calculations of Pokrovski, et al. (2003) for pH>3-4 hydrolysis which resulted in tetrameric or bigger polymers. By correlation, in our study given the coordination number (i.e. N_{Fe}=3.4) it is possible that similar clusters could form as a mix between tetramers and hexamers. In this pH 4.2 sample, the iron speciation is similar to that found in pure Fe systems, with a polymerization level close to Ferrihydrite minerals. Moreover, Fe-Fe bonds with double corner interactions dominated the local structure. The number of edge interactions was lower than double corners interactions (Figure 42). These polymers are therefore structured in three dimensions, coincidentally resembling the local structure of the polymers described in systems where Fe polymerizes in the presence of Si at a pH close to 3 (Doelsch, et al.,

2000; Pokrovski, et al., 2003). The occurrence of Fe-O-Si bonds between Fe octahedra and Si-tetrahedra was not observed (Table 18), which is consistent with the Fourier transformed infrared (FTIR) results obtained in conditions similar to our study (Si/Fe = 1, pH 3) (Doelsch, et al., 2001).

Increasing pH in pure Fe system generally leads to an increase in iron polymerization degree. Such trend was not observed in our system when pH increased to 5 and 7. In not Fe pure systems, complexing ligands such as Si (Doelsch, et al., 2000), P (Rose, et al., 1996; Rose, et al., 1997a), As (Waychunas, et al., 1993; Manceau, 1995; Waychunas, et al., 1995), Se (Manceau and Charlet, 1994) poison Fe polymerization when the hydrolysis is advanced enough for these species to reach insoluble state.

Pokrovski, et al. (2003) were able to detect Si presence in the neighbourhood of Fe by direct EXAFS fitting techniques with experimental conditions set to pH2.8 at 0.01m and 0.05m Fe and Si concentrations respectively. These results were obtained against great odds where by Si signal, in most cases than not, gets masked over by heavier elements such as Fe. Silica is known to lose its soluble form ($Si(OH)_4$) and turn into its amorphous state after circumneutral pH states (i.e. 7-9) (Ning, 2003; Icopini, et al., 2005; Belton, et al., 2012). Accordingly, an advantage in our system (compared to Pokrovski, et al. (2003)) for Fe-O-Si interactions to manifest in EXAFS, the one advantage was that precipitates were forming at latter hydrolysis stages (pH4.2, 5 and 7) closer to the insoluble pH states of Si. Disadvantages on the other hand include X5 reduced Si to Fe proportion in our system (i.e. [Fe]/[Si]= 1:1) and 50 times less over all Si concentration. Regardless, at pH5 in our study, the presence of Si was detected directly using Shell by Shell fitting techniques compared to other studies who argued that adding Si shells in their 2nd and 3rd shells fits were not a necessary step (Manceau, et al., 1995; Doelsch, et al., 2000). In these latter mentioned studies, they were only able to confirm Fe-O-Si presence indirectly regardless of higher Si to Fe proportions (Si/Fe=0-4 in (Doelsch, et al., 2000)) but higher overall Fe presence (0.2M Fe compared to 0.001M Fe in our case).

Doelsch, et al. (Doelsch, et al., 2000; Doelsch, et al., 2003) already mentioned that the presence of Si can affect the atomic structure of the Fe polymers. Indeed it was found that "the polymerization of Fe is very sensitive to the Si concentration but does not follow a linear trend". In their study the number of Fe-Fe linkages strongly decrease at [Si]/[Fe] ratio from 0.25 to 1. They also demonstrate in (Doelsch, et al., 2000) favorable akaganeite formation at acidic pHs until pH 5 at Si/Fe ratio of 1, which is similar to experimental conditions in our study. But at higher pH (>5) no crystalline Fe minerals were observed. The authors explain this loss of crystallinity by the replacement of structure stabilizing Cl ions by OH ions that do so less. But additionally, though not discussed therein, the presence and insolubility of Si at this close to neutral pHs enables it to start complexing with Fe.

Pokrovski, et al. (Pokrovski, et al., 2003) found that Fe-Si atomic pairs at a distance of 3.18 Å can be detected for [Si]/[Fe] ratio >1 and at pH3. Their result strongly suggested that aqueous silica hindered iron polymerization via corner sharing between iron octahedra and Si tetrahedra. According to Pokrovski, et al. (2003), the Fe-Si distance of 3.18 Å can be associated to the linkage of iron octahedra with silicate tetrahedra. The remaining Fe-Fe edge sharing confirmed that Si did not seem to be capable of blocking the very first stage of Fe polymerization (Jolivet, 2000), i.e. the formation of Fe dimers sharing edges (Pokrovski, et al., 2003). The $R_{Fe\text{-}O\text{-}Si}$=3.18 Å observed in our pH5 samples are in perfect agreement with values in Pokrovski, et al. (2003) and with slightly longer distances obtained with Fe to As (Waychunas, et al., 1993; Manceau, 1995; Waychunas,

et al., 1995), Se (Manceau and Charlet, 1994) and P (Rose, et al., 1996; Rose, et al., 1997a) interactions. Similar to above mentioned studies, the edge sharing interaction in our study showed a slight decrease from N=1.5 to 1.1 in transiting from pH4.2 to 5 while the double corner interactions of N=1.9 were totally lost. As in a similar argument by (Doelsch, et al., 2000) the over all effect of above discussed Si effect would be a 3D growth scheme at pH4.2 reduced to 2D at pH5.

The high Fe-Si coordination number (i.e. for pH5 phases) suggests that the local structure of our sample can look like the Fe_3-$Si_{2,3}$ cluster proposed by Pokrovski, et al. (2003). It is also worth noting that at pH5 the coordination number of the Fe-O atomic pair was much smaller than at the two other pHs. Even if the uncertainty on $N_{Fe\text{-}O}$ can reach 20%, the value of 4.9 strongly suggest the presence of tetrahedrally coordinated Fe. In the case of pure Fe-Si system, Pokrovski, et al. (2003) also found the presence of significant amount of Fe tetrahedra but only for very high Si/Fe ratio (>50). These structures may form by Fe to Si substitution of SiO_4 tetrahedra due to the relative abundance of Si in the system. In our case the Si/Fe of 1 seems much lower than in the case of Pokrovski, et al. (2003). However, our initial Fe concentration is 100 times smaller, which may explain the relative discrepancy.

To locally summarize this discussion, at pH 5, the level of polymerization of Fe was significantly lower than that of the structures observed at pH 4.2 and 7 (Figure 42). The number of edge interactions was slightly greater than the number of double corners. This local structure is therefore quite close to a mixture of dimers and trimers. Quantification by SSF suggests the potential presence of Fe in tetrahedral form in the local structure as observed by Pokrovski, et al. (2003), but it was not clearly demonstrated. On the other hand, as will be discussed below for pH 7 phases, SSF analysis (Table 18) suggests the existence of Fe-O-Si bonds that correspond to the FTIR results obtained at pH 5 for Si/Fe = 1 (Doelsch, et al., 2001). Thus, unlike the nanominerals discussed for pH 4.2 and will be discussed for pH 7, the composition of the nanominerals formed at pH 5 is largely dominated by Si (Figure 40). Fe is present only as dimers and trimers, probably isolated in an amorphous silica matrix.

Nevertheless, in our study, the competing effect of Si for Fe at pH5 was not verified at pH7. During the pH increase, it seemed that the hindrance certainly due to Si was weaker and that Fe polymerization re-started. Such transient effect of Si as function of pH was not reported in previous studies. Therefore, at pH 7, Fe was back to be the main element (Figure 40) but its degree of polymerization was slightly lower than that at pH 4.2. However, unlike pH 4.2, the octahedra were mostly bounded by their edges (Figure 42), forming rather planar local structures (2D growth schemes). Again, the system we studied behaved in a quite similar way to the Fe polymerization systems in the presence of Si (Doelsch, et al., 2000; Doelsch, et al., 2001). Moreover, these authors showed by FTIR the existence of Fe-O-Si bonds at pH 7, in agreement with the second alternative fit in our study (Table 18, fit 7).

Doelsch, et al. (2000) reports similar discrepancy in Si behavior but as a function of Si:Fe proportions. They showed increase in Si presence having a negative effect on Fe polymerization goes as high as Si:Fe=1 and the hindering effect reduces at higher Si proportions. They argue that in conditions that favor polymeric Si species formation (i.e. relative abundance of Si over Fe), Si competes with it own species leaving Fe polymerization to progress better. In our studies, it could be argued that similar favorable conditions occur at pH7 with higher solubility of Si (also the other cationic species, specially Al) increasing interaction between Si species and other cationic

species except Fe (specially Al) reducing the poisoning effect on Fe polymerization.

However, the extents of Fe polymerization given by EXAFS quantitative analysis are close estimation of the local structure of these phases. Indeed EXAFS signal only correspond to average information and can not take into account minerals heterogeneity. EXAFS data, therefore, not complemented by techniques that give particles sizes (e.g. SAXS, TEM) could not unequivocally confirm the extent of polymerization of individual phases.

4.4.3 Two stages of precipitation: growth and maturation

The individual nanominerals had two particle size ranges (Figure 39) regardless of the pH considered. The differences in chemical composition as a function of size are better illustrated in the Fe, Si and Al ternary diagram in Figure 43. Regardless of pH, the chemical composition of the smaller particles was close to that of the initial leachate solution, with a slight enrichment in Fe. These small particles are probably the first nanometric phases that polymerize during hydrolysis. They probably derive from the rapid growth of the initial nuclei. The chemical compositions of the larger particles differed from those of the smaller particles at the same pH. They were enriched in Fe at pH 4.2 and pH 7, and even more enriched in Si at pH 5. The difference in the composition of the larger and smaller particles means simple aggregation of the smaller particles cannot explain the formation of the larger particles. Instead, we propose that these particles are formed after the hydrolysis step, when the pH is stable, by a stage of maturation. Maturation is a stage of dissolution/precipitation: the unstable small particles are dissolved and reprecipitation occurs on the surface of the others growing. The composition and structure of the nanominerals formed during the stage of maturation appeared to be strongly controlled by the pH conditions.

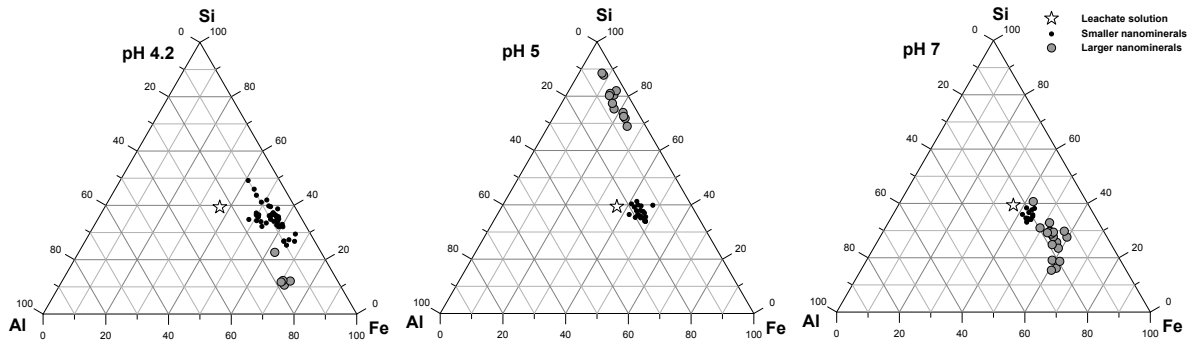

Figure 43: Ternary diagrams of Fe, Si and Al atomic proportions in the nanominerals formed at pH 4.2, 5 and 7. The white star represents the initial composition of the leachate solution, the small black dots represent the composition of smaller nanominerals and the larger grey dots the composition of larger nanominerals.

The TEM results thus revealed two polymerization steps in the formation of nanominerals: first initial growth, and second maturation. It is important to note that data from EXAFS were unable to distinguish between the two stages of hydrolysis. EXAFS information is still an average signal over all particle size ranges within a given sample. However, the observed structural differences, in particular the contribution of Si to the structure of the particles at pH 5 (Table 18 and Figure 42) tends to show that the EXAFS signal of the polymerized phases was rather dominated by the structure of the larger particles.

4.4.4 Synthetized nanominerals are representative of nanominerals formed in soils

In order to test the representativeness of the products formed in our experiment as analogues to nanominerals formed in soils, we compared the particles synthesized with two types of nanominerals in soils: the altered layer formed at the surface of biotite and the nanominerals formed at a distance from the initial altered surfaces.

The study of Bonneville, et al. (2011) is particularly relevant to compare our results with a layer of biotite alteration, since these authors reproduced the chemical alteration processes at mineral-mycorrhiza interface, representing the hotspot of the weathering engine at work in soils. The composition of the nanominerals formed in our pH 5 experiments are reported in Figure 44 together with their results averaged over the 20 nm thick altered-biotite zone. The comparison shows very similar compositions between nanominerals formed in batch at pH 5 and the products of the surface layer altered biotite. Moreover, these authors also measured pHs at the mineral-mycorrhiza interfaces, varying from values below 4.6 up to 5.8. The nanominerals formed in our pH 5 experiments can therefore be considered to be formed under rather similar conditions.

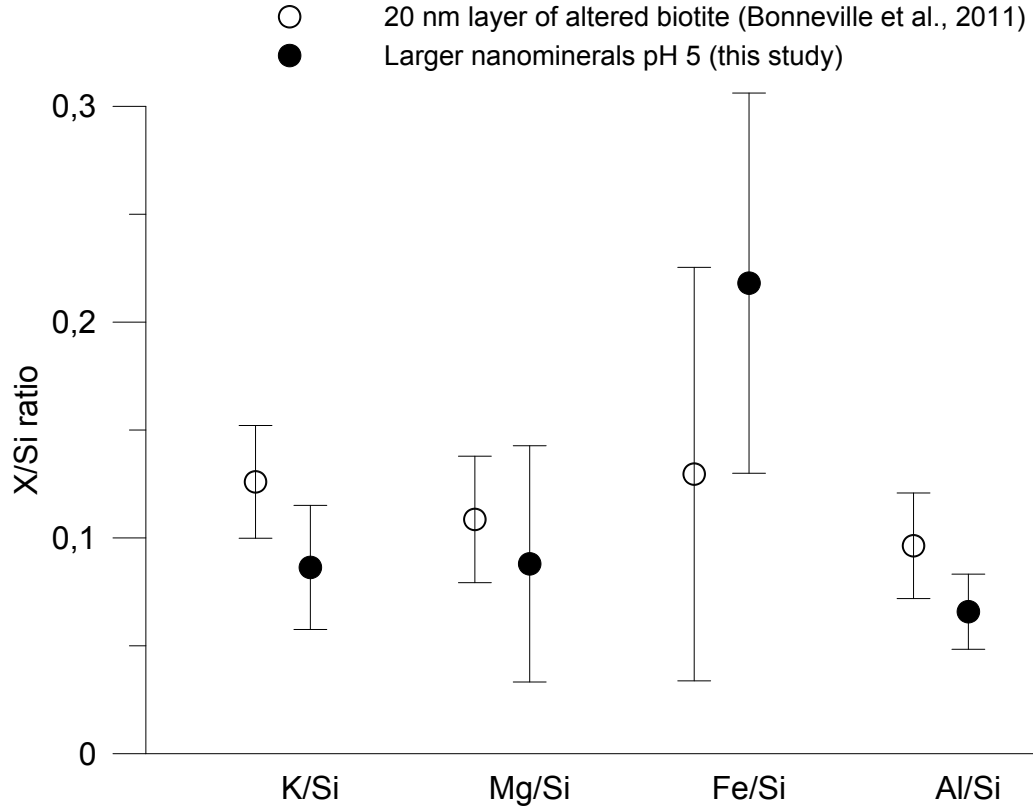

Figure 44: Chemical compositions expressed as K:Si, Mg:Si, Fe:Si and Al:Si ratios measured by TEM-EDX. Empty circles represent the chemical composition of the surface layer of an altered biotite (Bonneville et al., 2011) averaged over its 20 nm thickness. Black circles represent the mean composition of the larger particles formed in our pH 5 experiment. Error bars are standard deviations.

Even though the chemical compositions seemed similar, comparison of local atomic structures was more complex. In an earlier study, Bonneville, et al. (2009) identified the presence of vermiculite and ferrihydrite in the altered biotite layer. These observations were consistent with those of Murakami, et al. (2003) who, using high resolution TEM, observed these gradual mineralogical transformations in addition to the presence of

chlorite. On the other hand, other studies tended to show that the alteration layer formed on the mineral surface is amorphous. The mechanism proposed is no longer a gradual transformation associated with the preferential diffusion of selected ions, but a process of interfacial dissolution-reprecipitation (Hellmann, et al., 2003; Hellmann, et al., 2012; Hellmann, et al., 2015). The results obtained by Kawano and Tomita (2001) on an altered natural bytownite, which showed alteration of the amorphous layer, also support the latter process. In the case of an amorphous surface alteration layer, the nanominerals synthesized by our protocol could be good analogs of the surface processes of the minerals.

Concerning the second type of nanominerals (neoformed nanominerals in soils at a distance from the altered mineral surface), the nanominerals in our study may also be analogs of natural secondary nanomineral phases. Only a few authors have studied the composition and local atomic structure of such nanominerals. Dai, et al. (2014) observed the formation of nanoparticle aggregates after experimental alteration of bentonite by bacteria. SEM-EDX analyses showed that the nanoparticle aggregates were composed of Si, Na, Ca, Mg, Al, Fe, K. Wen, et al. (2014) also extracted nanominerals in a <450 nm fraction that exhibited Al, Si and Fe compositions and amorphous structures. These two studies demonstrate that not only Al and Fe, as classically described in literature, but also other elements such as Si, Na, K, Mg, and Ca may be involved in the formation of soil secondary nanominerals. It is therefore probable that the nanominerals that were synthesized in the present work are, at least in the case of the larger particles, representative of some nanominerals formed in soils.

4.5 Conclusion

This laboratory work simulated the successive processes of biotite alteration and the following neoformation of secondary phases from ions in solution. The nanominerals formed were amorphous phases that polymerized in two steps: (1) the initial growth phase formed 2 to 15 nm particles whose chemical composition closely resembled that of the alteration solution; (2) the maturation phase then resulted in 15 to 60 nm particles whose compositions are strongly controlled by the pH conditions. At pH 4.2 and pH 7, the structure of the nanominerals was dominated by Fe but its polymerization was hindered by the presence of Al, Si, Mg and K. Conversely, at pH 5, the polymerization of Fe was counteracted by the polymerization of high amounts of amorphous Si. Surprisingly, Al appeared to play a minor role in polymerization, regardless of the pH. However, thermodynamic and/or kinetic mechanisms that control the variations in the proportions of Fe and Si in the nanominerals as a function of pH remain to be explained. In comparison with previous alteration studies, the laboratory-synthetized phases of our study were estimated to be analogs of the nanominerals formed in natural biotite-bearing soils at varying distances from biotite surfaces.

The adsorption capacities of these nanominerals with respect to the OM should also be considered as a potential process of stabilization of the organic compounds by the mineral phases, enabling medium to long term sequestration of C in soils. Building on these first exploratory experiments and results, it will be interesting to examine the interactions between these Fe, Si, Al, Mg, K nanominerals and SOM. Like for the Fe or Al phases reported in the literature, we would expect coprecipitation processes leading to strong interference by OM with crystal growth and with the formation of smaller polymerized domains as well as differences in local atomic structures and reactivity.

4.6 Acknowledgements

This work was supported by Aix-Marseille University doctoral school ED251, ANR (NanoSoilC ANR-16-CE01-0012-02 project) and the *Institut Universitaire de France*. We would like to thank the European Synchrotron Radiation Facility (ESRF) (Grenoble, France) and ELETTRA synchrotron (Trieste, Italy) and their respective teams at the FAME and 11.1 beam lines for their kind and expert assistance during the EXAFS measurements. We thank Alain Plante who read the article and provided feedback.

5 Short range order mineral organic associations (sroMOAs) formed by weathering of primary minerals in soils: laboratory approach

5.1 Introduction

Organo-mineral interactions are recognized as a key factor in the stabilization of organic matter in soils (Kögel-Knabner, et al., 2008; Schmidt, et al., 2011; Kleber, et al., 2015). They contribute greatly to the soil C stock (2400 Gt, Stockmann, et al. (2013)) and thus play a key role in controlling the biogeochemical cycle of surface C (Le Quéré, et al., 2015). In some works, organo-mineral interactions are even considered as a lever for increasing the SOM pool in cases of land use change (Wissing, et al., 2013), of agro-ecological practices (Bolan, et al., 2012; Bolan, et al., 2013; Souza and Gomes, 2015) or of soil restoration (Silva, et al., 2015). Understanding the mechanisms governing the formation of organo-mineral complexes is therefore a major issue in view of increasing soil C stocks by 4 per 1000 (Paustian, et al., 2016; Minasny, et al., 2017).

Two types of localization of organo-mineral interactions can be distinguished in the soil matrix: pedogenic oxyhydroxides and mineral surfaces (see the exhaustive review by Kleber, et al. (2015).

- (1) Pedogenic oxyhydroxides are formed from soil solution by precipitation, due to changes in physicochemical conditions (pH, redox, concentrations, etc.). These variations may concern the solum, one or several horizons, or, on the contrary, be localized at micro-scale to nano-scale, in relation to porosity and / or biological activity. These are mainly precipitates of oxyhydroxides of Fe and Al (Kaiser and Guggenberger, 2000; Eusterhues, et al., 2005; Kleber, et al., 2005; Mikutta, et al., 2005; Rasmussen, et al., 2005; Matus, et al., 2008; Bruun, et al., 2010; Mikutta, 2011; Van De Vreken, et al., 2016). They would stabilize soil organic compounds rather by coprecipitation than by sorption processes (Wagai and Mayer, 2007; Eusterhues, et al., 2008; Mikutta, et al., 2014).

- (2) Soil mineral surfaces represent adsorption surfaces of OM. Organic compounds do not cover the entire surface of minerals but form disjoint patches (Lehmann, et al., 2007; Heister, et al., 2012; Remusat, et al., 2012; Vogel, et al., 2014). The adsorption mechanisms are explained by ligand exchanges, by interaction of charged organic compounds on a mineral surface with opposite charge, or by hydrophobic interactions (Lützow, et al., 2006; Kleber, et al., 2007; Keiluweit and Kleber, 2009). These interactions represent models of mechanisms that satisfy the theoretical concepts of physico-chemistry (Andersen, et al., 2016).

In the case of adsorption on mineral surfaces, models consider a perfect crystalline mineral structure, whereas soil clay minerals often have rather different properties compared to reference minerals (Churchman, 2010). Even less representative, the surface state of the mineral is not taken into account in these theoretical approaches. Alteration processes play a major role in the perturbation of mineral surfaces. It is shown (i) that soil minerals exhibit highly marked topographic nano-scale heterogeneities (Cheng, et al., 2008) and (ii) that the alteration creates, on the surface of the minerals, a layer with a thickness of some 10 to a few hundred nm with very different chemical and mineralogical characteristics compared to the pristine mineral. Either local surface mineral transformations (Bonneville, et al., 2009; Bonneville, et al., 2011), neoformed

phyllosilicates (Tazaki, 1986), gels or amorphous layers (Kawano and Tomita, 2001; Hellmann, et al., 2015; Wild, et al., 2016) have been observed on mineral surfaces according to minerals and alteration conditions. Whatever the phases formed, they represent at a local scale potentially very reactive zones with respect to OM. A recent conceptual model proposed to take into account these processes of alteration of the mineral surfaces in the organo-mineral interactions (Basile-Doelsch, et al., 2015). This model suggests that coprecipitation processes occur between mineral phases formed during weathering and soil organic compounds, likely contributing to stabilization of SOM.

Numerous batch synthesis experiments, coupled or not to incubation experiments, have been carried out to understand these OM stabilization mechanisms by coprecipitation with Fe and Al oxides (Masion, et al., 1994; Masion, et al., 2000; Jansen, et al., 2003; Colombo, et al., 2004; Xu, et al., 2010; Eusterhues, et al., 2011; Mikutta, et al., 2011; Henneberry, et al., 2012; Shimizu, et al., 2013; Eusterhues, et al., 2014b; Mikutta, et al., 2014). They show that, next to the formation of Fe and Al oxy-hydroxides, OM interaction with hydrolyzing metals results in insoluble metal–organic complexes. Considering the mineral phases, OM impairs the formation of Fe and Al oxy-hydroxides with higher crystalline order, and strongly alters their properties including particle size, metal coordination, and distortion of Fe/Al octahedra (Kleber, et al., 2015). On the other hand, considering the organic compounds, short-range order minerals (SRO) strongly stabilize OM against microbial degradation (e.g. Eusterhues, et al. (2014b) and reference therein).

These results can be paralleled with observations made in natural systems: the andosols (Levard and Basile-Doelsch, 2016). It has been shown that the presence of OM blocks the growth of secondary aluminosilicates (imogolite or allophane) at the protoimogolite stage (Levard, et al., 2012). On the other hand, the organic compounds are stabilized over very long periods (Torn, et al., 1997; Basile-Doelsch, et al., 2005). Thus, whatever the system (Al, Fe or Si + Al), co-precipitation induces two complementary effects: (1) organic compounds modify the mineral structure (particularly by limiting crystallization at short distances) and (2) the mineral phases complex OM protecting it from biodegradation.

In the present work, as in laboratory studies of Al and Fe (Masion, et al., 2000; Colombo, et al., 2004; Eusterhues, et al., 2011; Mikutta, et al., 2011; Shimizu, et al., 2013) our aim is to test if organo-mineral complexes can be formed by coprecipitation in the presence not only of Al and Fe, but also in presence of other elements resulting from the alteration of silicates. We rely on a preliminary work in which we synthesized amorphous nanophases from a solution resulting from the alteration of biotite (Tamrat, et al., submitted). In the present work, we characterize these short-range order Mineral-Organic Associations (sroMOAs) formed in the presence of OM at pH5 with increasing concentrations of organic compound (the metal to C ratio increasing from a No C state to 10, 1, 0.1 and 0.01). pH=5 was chosen to represent acidic soil pH states where these OM to mineral interactions are found to be the most efficient (Schwertmann and Murad, 1983; Voinot, et al., 2013). pH 5 is also in the mean of the range of measured pH inducing biotite weathering by mycorrhiza (Bonneville, et al., 2011).

5.2 Materials and Methods

5.2.1 Material

The studied biotite comes from Bancroft, Ontario Canada (Ward Science) (Turpault and

Trotignon (1994)):

$$K_{0.92}\left(Fe_{1.06}^{(2+)}Mg_{1.66}\right)\left(Fe_{0.094}^{(3+)}Ti_{0.12}Mn_{0.046}\right) \times [Si_3AlO_{10}](OH_{1.1}F_{0.9})$$

3,4-Dihydroxy-L-phenylalanine [$(HO)_2C_6H_3CH_2CH(NH_2)CO_2H$] (Sigma Aldrich) was used as a model for small molecules of SOM (Zimmerman, et al., 2004a). It presents the main functions known in organo-mineral stabilization processes: amine, carboxyl and a hydroquinone component (an aromatic ring with double hydroxyl phenol functional groups) (Mikutta, 2011; Kleber, et al., 2015) (Figure 45). At pH5, the amine group exists in NH^{3+} state, carboxyl group in COO^- state and phenol group in OH state. In literatures, the pK_a values for these three functional groups are not unambiguously defined (Dawson, et al., 1959; Kortum, et al., 1961; Clarke and Moffat, 1986; Martindale, et al., 1993). Some values found in literature and adopted for this work include 9.24 for the amine group, 2.58 for the carboxylic group and in the range between 8-10 for the hydroxyl groups. The nine C in this compound account for 9 C atoms in M:C atomic ratios.

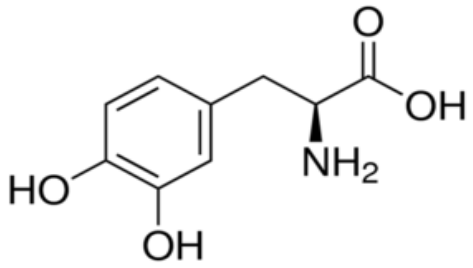

Figure 45: 3,4-Dihydroxy-L-phenylalanine

5.2.2 Experimental protocol

Biotite Weathering: Dissolution steps of biotite followed in this study were similar to ones detailed in Tamrat, et al. (submitted)(chapter 4). Briefly, the protocol involved reducing the biotite sheets to lower than 50 µm sizes, putting 33 g of this powder biotite in 1L weathering batches of pH=2 HNO_3 solution (solid:liquid ratio of 1:30) and then finally separating the truly dissolved species (leachate solution) from the bulk solution. These steps were done in 1L batches with 33 g of lower than 50 µm biotite particles. The leachate solution was retrieved using Tangential Filtration Flow (TFF) setup (Spectrum Labs) with a cutoff size of 10kD. Final leachate solution concentrations of 937 µM for Fe, 1006 µM for Si, 614 µM for Al, 883 µM for K and 1247 µM for Mg were recorded.

Synthesis of coprecipitates: Precipitation of sroMOAs was performed by increasing pH of 100ml leachate solution from a state of 2 to 5 in the presence of differing concentrations of OC. Ten fold increase of OC concentration in the initial solutions was adopted in our study giving molar Metal to C ratios (M:C) of 'No C', 10, 1, 0.1 and 0.01. Molar metal concentration stands for combined molar concentrations of Fe and Al. Other elements were excluded from the calculation to keep comparable ratios with previous works on Al and Fe coprecipitates reported in literatures (see review in Kleber, et al. (2015)). Titration to a pH value of 5 was achieved in 1.5, 1.5, 1.5, 2.0, and 5.4 hours for 'NoC', M/C=10, 1, 01, 001 respectively by adding 0.2N NaOH (Sigma Aldrich) at a constant rate of 70 µL/min (Figure 46).

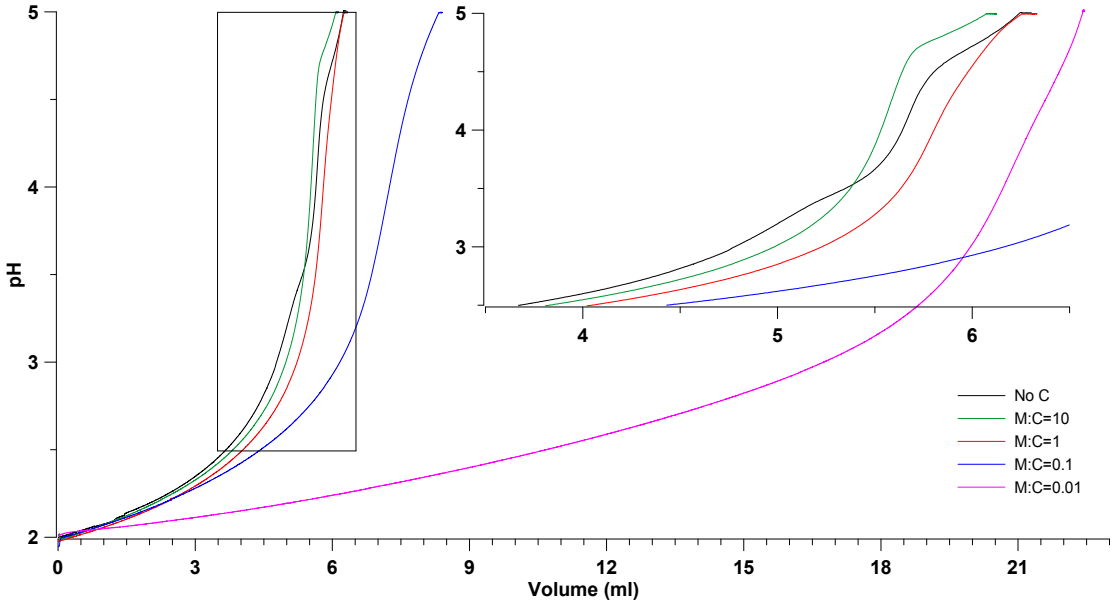

Figure 46: Titration curves during the precipitation of the sroMOA phases.

5.2.3 Physico-chemical characterization (ICP-AES, EXAFS and TEM)

Chemical composition of the leachate solution and concentrations of dissolved species were monitored with an inductively coupled plasma atomic emission spectrophotometer (ICP-AES, Horiba Jobin-Yvon "Ultima C", Longjumeau, France); with measurement uncertainty less than 10%. Extended X-ray Absorption Fine Structure (EXAFS) data was collected at ESRF synchrotron source on the FAME beam line (Grenoble, France) at the Fe K-edge. EXAFS data treatment was done using Athena software (Ravel and Newville, 2005) following data reduction steps of Manceau and Calas (1986). All radial distances in reference to the Radial Distribution Functions (RDF) in the result section are uncorrected for phase shift.

Imaging and nano chemical analysis of precipitates were performed using a JEOL JEM 2011 Transmission Electron Microscope (TEM) at CINaM/ Aix-Marseille University, France. Between 30 to 60 micrographs were taken for individual samples. Size analyses were done by measuring the size of a minimum of 10 data points (homogeneous clusters) per individual micrographs. Minimum and maximum sizes were considered to get size ranges of particles for each sample. Equipment and measurement details on chemical characterization tools can be found in chapter 4.

5.2.4 Reference standards selection for EXAFS analysis

The reference standards selected (Table 19 and Table 20 with Figure 47 in black) showed increasing levels of Fe octahedra polymerization in the order of Iron Citrate, Fe-C Colloids, Fe Dimers, Fe-SRO and 2L Ferrihydrite. Note: descriptions such as Fe-Fe are short designations for an Fe octahedra interacting with another Fe octahedra thus making Fe-O-Fe bonds. Similar designations will be used here after such as Fe-Si (for interactions with Si tetrahedra), Fe-Al (for an interaction with an Al octahedra unless specified otherwise) and Fe-C (for an interaction with a C based molecule thus giving Fe-O-C bonds).

2L Ferrihydrite: provided the highest Fe polymerization of all reference compounds in this study. It is characterized by 2.1 edge and 5 double corner interactions between Fe octahedra. Signals from these bonds are seen as upward convex signals at ~5.2 $Å^{-1}$ and

~7.5 $Å^{-1}$ on the EXAFS curve (Figure 47a) (Pokrovski, et al., 2003; Mikutta, et al., 2010; Mikutta, 2011). Also observed, in R-space, are a pair of peaks (or peak + shoulder combination) at radial distances of ~2.7 Å and ~3.0 Å corresponding to edge and double corner sharing interactions between Fe octahedra respectively (Figure 47b) (Rose, et al., 1997b).

Fe-SRO: by comparison, this standard is less crystalline than 2L Ferrihydrite. Going from 2L Ferrihydrite to Fe-SRO the edge interactions increase slightly to a coordination number of 2.6. But the double corner interactions greatly decrease, that is from 5 in 2L Ferrihydrite to 0.63 in Fe-SRO (Doelsch, et al., 2000).

Fe Dimers: in this standard, the edge sharing coordinations are reduced by more than half (i.e. from 2.6 in Fe-SRO to 1 in Fe Dimers). In addition, a 0.2 single corner coordination is recorded for this same standards (Rose, et al., 1996). This arrangement could be interpreted as either Fe octahedra forming dimers also forming single corner interactions at a coordination number of 0.2 or two separate clusters of Fe octahedra one sharing edges while the other sharing just single corners.

Fe-C Colloids are the least Fe polymerized standard. It additionally gives reference to organic matter complexing Fe. 1.9 C_1 atoms at 2.82Å and 1.5 C_2 atoms at 2.98Å account for the mono and bi-dentate Fe-O-C interactions respectively; while 0.4 Fe_3 atoms at 3.35Å and 0.7 Fe_4 atoms at 3.86Å account for double and single corner Fe-Fe octahedra interactions respectively (Rose, et al., 1998).

Iron citrate is the chelation of three carboxylic functional groups of a citrate anion with a central Fe atom produces a tridentate mononuclear complex (IUPAC, 2005). In transiting from the '2L Ferrihydrite, Fe-SRO and Fe Dimers' to 'Fe-C Colloids and Iron citrate' standards, the positive oscillations at ~5.2 $Å^{-1}$ and ~7.5 $Å^{-1}$ on the EXAFS curve lose intensity. In their place emerges a shoulder at ~5.7 $Å^{-1}$ which is characteristic of Fe-O-C bonds.

Table 19: Reference standards used in the LCF and other stages of the data treatment. Going down the list, they are placed in the order of decreasing Fe-C and increasing Fe-Fe interaction respectively.

Reference Standards	Description
Iron (III) Citrate	Iron citrate is a compound characterized by a central Fe^{3+} cation chelated to the three carboxylic groups of a citrate anion.
Fe-C Colloids	These Fe-C Colloids (FeZ32.Nsimi) are natural colloidal fraction (20-300KD) from the Nsimi river (South Cameron). Colloids in this standard contain poorly polymerized iron (small iron oligomers: i.e. dimers, trimers…) due to the complexation of Fe to carboxylic groups of OM. This reference standard is characterized by 1.9 and 1.5 C atoms at 2.82Å and 2.98Å distance respectively; and, 0.4 and 0.7 Fe atoms at 3.35Å and 3.86Å distances respectively (Rose, et al., 1998).
Fe Dimers	Iron dimers + PO_4 were synthetically produced by adding powder phosphoric acid into 1.5 M Iron(III) chloride solution. The solution was initially prepared from reagent grade $FeCl_3.6H_2O$ dissolved, in distilled water. Mix was adjusted to obtain P:Fe proportion of 0.5 at a hydrolysis ratio of R=1.5. This standard was selected because it consists of Iron dimers (Fe-Fe edge sharing) +PO_4 and can represent Fe-Fe dimer structure regardless and irrelevant of the PO_4 content. This reference standard is characterized by 1 and 0.2 Fe neighbors at a distance of 3.1 and 4.1 Å respectively (Rose, et al., 1996).
Fe-SRO	These polymers were synthetically produced by hydrolyzing Iron (III) Chloride in the presence of SiO_4 ligands at pH=5 at a resulting Si to Fe proportion of 4. For these conditions, no Fe-O-Si bonds were detected. Entities in this standard are characterized by strong inhibition of Fe-Fe edge sharing which is a characteristic of a two-dimensional growth scheme. This reference standard is characterized by 2, 0.6 and 0.63 Fe neighbors at a distance of 3.02, 3.14 and 3.49 Å respectively. That gives a trimer and a little bit of higher order Fe-Fe polymerization (Doelsch, et al., 2000).
2L Ferrihydrite	Ferrihydrite is a widespread hydrous ferric oxyhydroxide mineral at the earth's surface. 2L (i.e. two line) refers to the two X-Ray diffraction lines (peaks) which imply low level of crystallinity as compared to the 6L Ferrihydrite which is much more crystalline. It is a metastable nanomineral precursor to other minerals, e.g. hematite (Mindat.org, 2016). Sample was synthesized by hydrolyzing a ferric perchlorate solution up to pH=8. The precipitate was aged for three days in its mother solution at room temperature. Its Fe to Fe interactions are characterized by 2.1 and 5 Fe neighbors at radial distance of 3 and 3.43 Å respectively. (Drits, et al., 1993; Manceau and Drits, 1993).

Table 20: Tabular summary of bond types and proportions for reference standards

Reference Standards	Edge	Double Corner	Single Corner
Iron (III) Citrate	-	-	-
Fe-C Colloids	-	0.4	0.7
Fe Dimers	1	-	0.2
Fe-SRO	2.6	0.63	-
2L Ferrihydrite	2.1	5	-

5.3 Results

5.3.1 Titration experiment (co-precipitation stage)

The weathering stage for this study is identical to processes described in chapter 4. The pH monitoring of the mineral synthesis step (Figure 46) showed direct relation between abundance of C in the system and the NaOH consumption to reach the pH state of 5. Except for the No C case, all remaining curves followed similar trend but at a different OH^- consumption rate. In a 10 fold increase in the initial C content from M:C=10 to 1, a total of 0.22 ml (0.044 mmol of OH^-) additional NaOH was consumed to reach a final pH state of 5. In an additional 10 fold increase in C from M:C=1 to 0.1, 2.3ml (0.46 mmol of OH^-) additional NaOH was consumed. Last 10 fold increase in C from M:C=0.1 to 0.01, an additional 13.8ml NaOH (2.75 mmol of OH-) was consumed. That gives a 10.4 times more increase in OH^- consumption from the first to the second 10 fold C increment into the system. And an exact 6 times increase in OH^- consumption between the second and last 10 fold increase in C. Additionally, curve for the No C titration showed two more inflection points at pH states 3.5 and 4.5. With small amount of C presence (i.e. M:C=10) the additional inflection point was only restricted to pH~4.6. In any of the other samples (i.e. when C is more abundant than M:C=10) any of these distinct inflection points were totally absent giving smooth titration curves absent of inflection points from start to end pH state.

5.3.2 EXAFS – Iron local range order and extent of polymerization

5.3.2.1 Quantification of Fe polymerization: raw data analysis

EXAFS spectra and Radial Distribution Functions (RDFs) for the experimental samples are shown in Figure 47. In the RDF outputs, peaks between 1.2-2 Å correspond to the first coordination sphere of oxygen atoms (O, OH, or H_2O). Beyond this first shell region, Fe-Fe octahedra interactions markers (see 2.1.3.1) are observed with differing intensities.

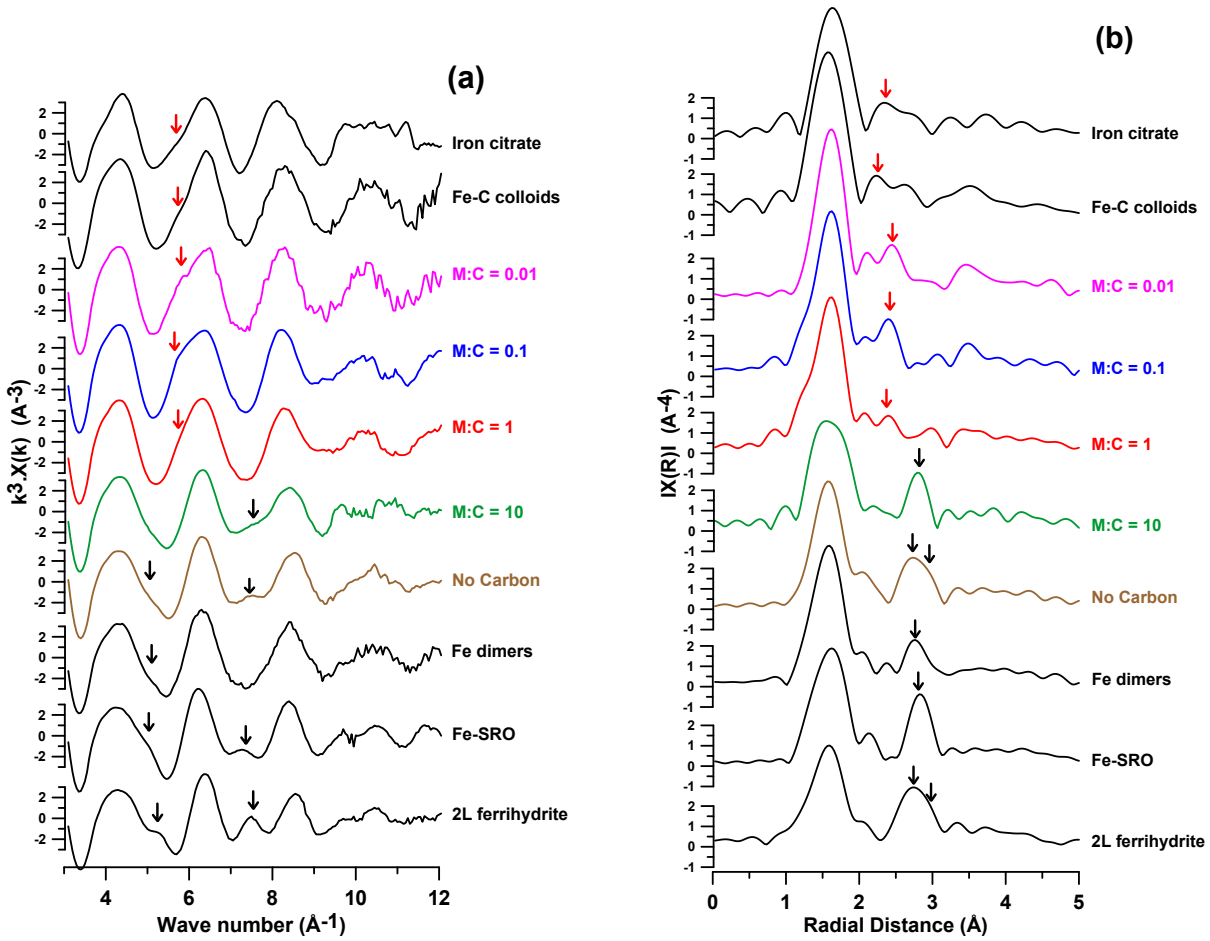

Figure 47: EXAFS and RDF plots. (a) k-space and (b) R-space 'pH=5' series. Black and red arrows on k-space spectra indicate parts of the oscillations specifically contributed from Fe-Fe and Fe-C interactions respectively. Same black and red arrows, in R-space, indicate radial distances corresponding to Fe-Fe and Fe-C interactions respectively.

Note: The No C sample mentioned in this result section is from a previous study (Tamrat, et al., submitted) reported in chapter 4 and reference to it in result figures and tables will not be repeated here after.

For the No C phases, in k-space, low intensity positive oscillation was recorded at ~7.5 $Å^{-1}$. Contribution at ~5.2 $Å^{-1}$ had a low intensity and appears as a shoulder. In R-space, a strong signal of a broad peak with a shoulder was observed between 2.4 Å to 3.2 Å. For M:C=10 phases similar signals appear in k-space but at reduced intensities. In R-space the signal around 2.9Å narrows into one single peak between 2.55 to 3.05 Å, without a shoulder. M:C=1 phases did not exhibit any of the signals from any of the reference standards representing neither Fe-Fe nor Fe-C interactions in both k and R-spaces. M:C=0.1 and M:C=0.01 phases showed similarity in their EXAFS signals. In both cases a shoulder at ~5.7 $Å^{-1}$ was observed. In R-space a 2nd shell peak at ~2.4 Å was detected. A noteworthy observation here was that this peak was at radial distance shorter than the Fe-Fe distance recorded for the 2nd shell of the low C samples (i.e. No C and M:C=10).

5.3.2.2 Quantification of Fe polymerization: LCF/comparison to reference standards

LCF results for all the samples are presented in Table 21. The EXAFS spectra to best fit fittings that led to the final results in Table 21 are shown in Figure 48 for visual

justification. Local structure of phases formed with No C showed significant resemblance to the moderately Fe-Fe polymerized '2L Ferrihydrite' at ~44%±15% and to a lesser extent to 'Fe-SRO' at ~25%±15% and 'Fe Dimers' at ~33%±15%.

Table 21: Linear Combination Fitting numbers.

	Iron Citrate	Fe-C Colloids	Fe Dimers	Fe SRO	2L Ferrihydrite	Sum	R-factor
	Fe-O-C	Fe-O-C + Fe-O-Fe	Fe-O-Fe				
No C			0.33	0.25	0.44	1.02	0.015
M:C=10	0.30			0.45	0.37	1.12	0.010
M:C=1	0.27	0.45		0.35		1.06	0.038
M:C=0.1	0.41	0.53		0.14		1.08	0.059
M:C=0.01	0.58	0.39		0.12		1.10	0.053

In the case of M:C=10 samples (compared to the No C samples) the collective contribution from purely Fe containing standards decreased from 102%±15% to 82%±15% (2L Ferrihydrite at 37%±15% and Fe-SRO at 45%±15%). Additionally, significant contributions to the fit were achieved to the M:C=10 phases from Iron citrate standard at 30%±15%. At a 10 fold increase in C (M:C=1), the contribution to fit from Iron citrate standard remained at 27%±15%. But this increase in C presence around Fe octahedra resulted in a shift from purely Fe standards (2L Ferrihydrite and Fe-SRO) to standards which are collectively dominantly comprised of Fe-O-C interactions (Fe-SRO at 35%±15% and Fe-C Colloids at 45%±15%). Further 10 fold increase in C presence (M:C=0.1) resulted in Fe-O-Fe contribution decrease from 35%±15% to 14%±15%. Whereas, Fe-O-C contributions (Iron Citrate and Fe-C Colloids) collectively increased from 72%±15% to 94%±15%. At maximum C content of M:C=0.01 small changes to the fit contributions were recorded (i.e. 3% increase in Fe-O-C and 2% decrease in Fe-O-Fe) but were well below the margin of error of 15% for LCF.

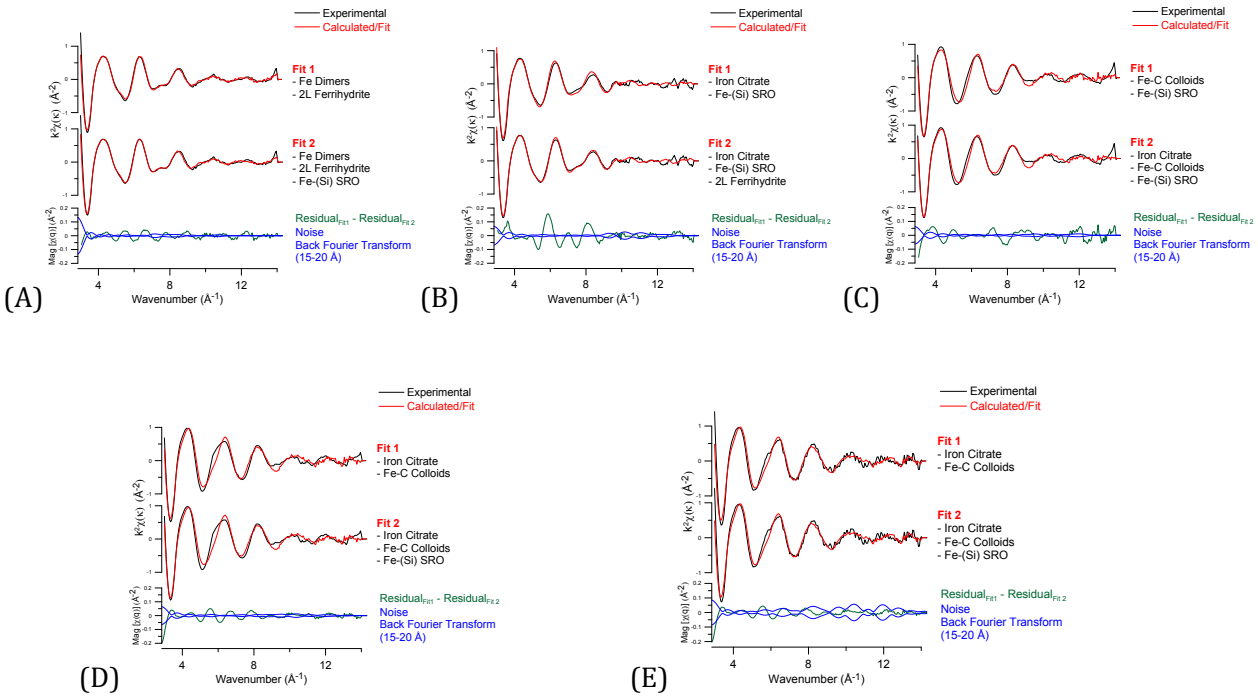

Figure 48: Linear Combination Fit of sample at No C (A), M:C=10 (B), M:C=1 (C), M:C=0.1 (D) and M:C=0.01 (E). Detail statistics that moved from best 2 standards fits to subsequently improved 3 standards fits can be found in Table 34 in Appendix 10.

5.3.3 TEM – Image Analysis/EDX: morphology, sizes of particles, chemical composition and state of crystallinity

TEM micrographs of sample series at the five M:C ratios are shown in Figure 49. Whatever the molar M:C ratio, particles were forming distinct clusters of smaller sized and larger sized particles. Size of the precipitated phases ranged from 2-50nm for the 'No C', 2-40nm for M:C=10, 5-200nm for M:C=1, 10-90nm for M:C=0.1 and 15-72nm for M:C=0.01 phases (Table 22). Regardless of carbon presence and also the sizes of the phases, electron diffraction analyzes showed a diffused pattern for all the samples.

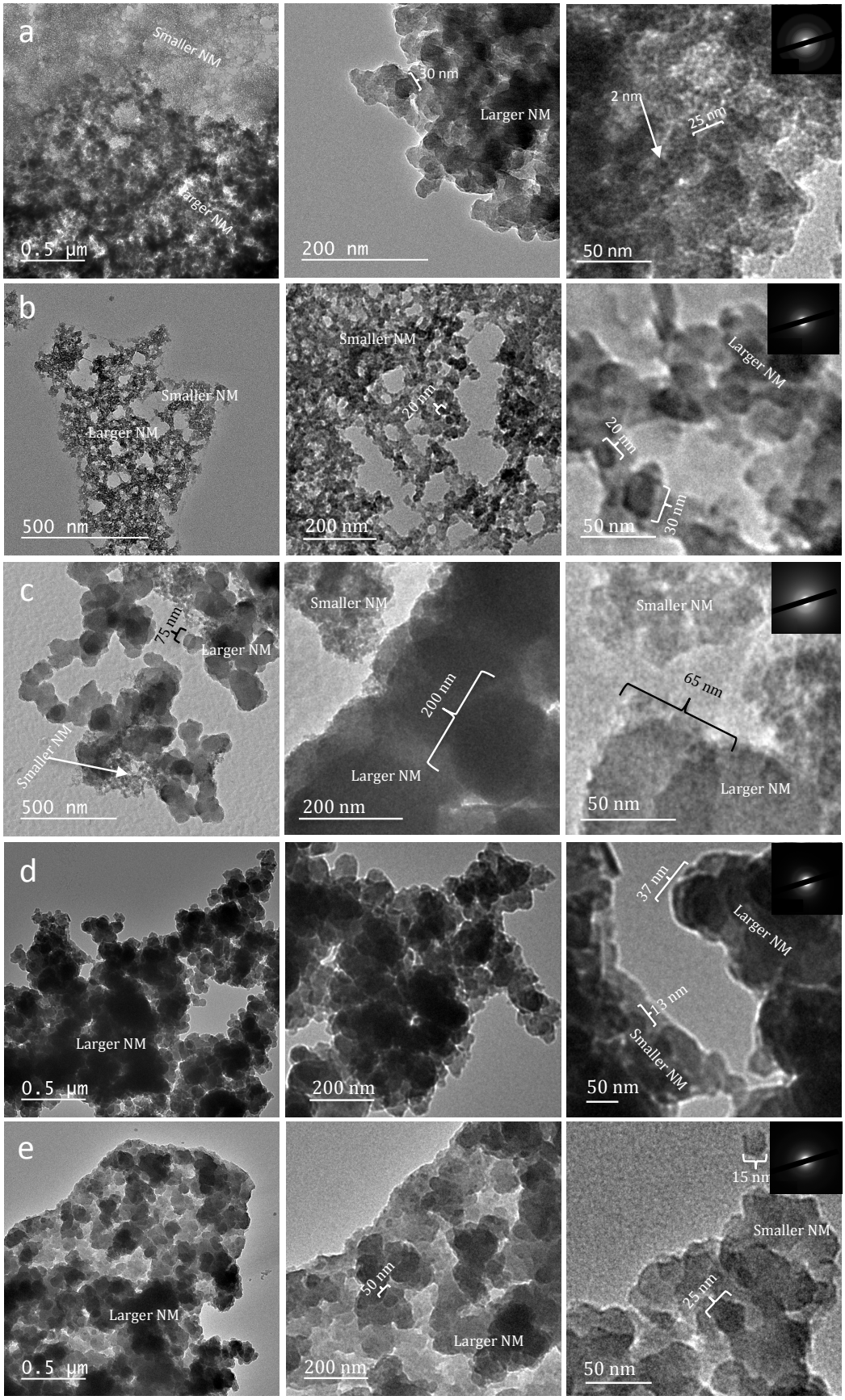

Figure 49: TEM electron micrographs of *sroMOAs – series at pH=5:* (a) 'No C', (b)M:C=10, (c) M:C=1, (d) M:C=0.1 & (e) M:C=0.01. In these phases, the diffused diffraction patterns indicate the lack of coherence in the scattering domains thus the amorphous nature of the co-precipitates. LP sroMOAs and SP sroMOAs stand for Larger Particle and Smaller Particles sroMOAs respectively.

TEM-EDX analyses of the particles are presented in the form of box plots in Figure 50 for Fe, Si, Al, K and Mg for each M:C ratio. The composition of the leachate at pH 2 provided by the weathering experiment represents the starting proportion of the dissolved cations. It is indicated in the results as 'Leachate Solution'.

Table 22: TEM images size analysis.

Size (nm)	No C	M:C=10	M:C=1	M:C=0.1	M:C=0.01
Smaller Particles	2 to 15	2 to 20	5 to 35	-	15 to 60
Larger Particles	10 to 50	10 to 40	55 to 200	10 to 90	35 to 72

The chemical composition of particles showed distinct variation within two major size ranges. Namely 'smaller nanoparticles' and 'larger nanoparticles' with sizes ranging between 2-60nm and 10-200nm respectively (Table 22). The sample M:C=0.1 is however an exception, because no smaller particles have been observed.

Chemical compositions of the smaller nanoparticles phases (Figure 41A) were in similar composition ranges. They were in close proximity to the concentration of the leachate solution with a slight enrichment in Fe, Si and Al and a significant depletion in K and Mg.

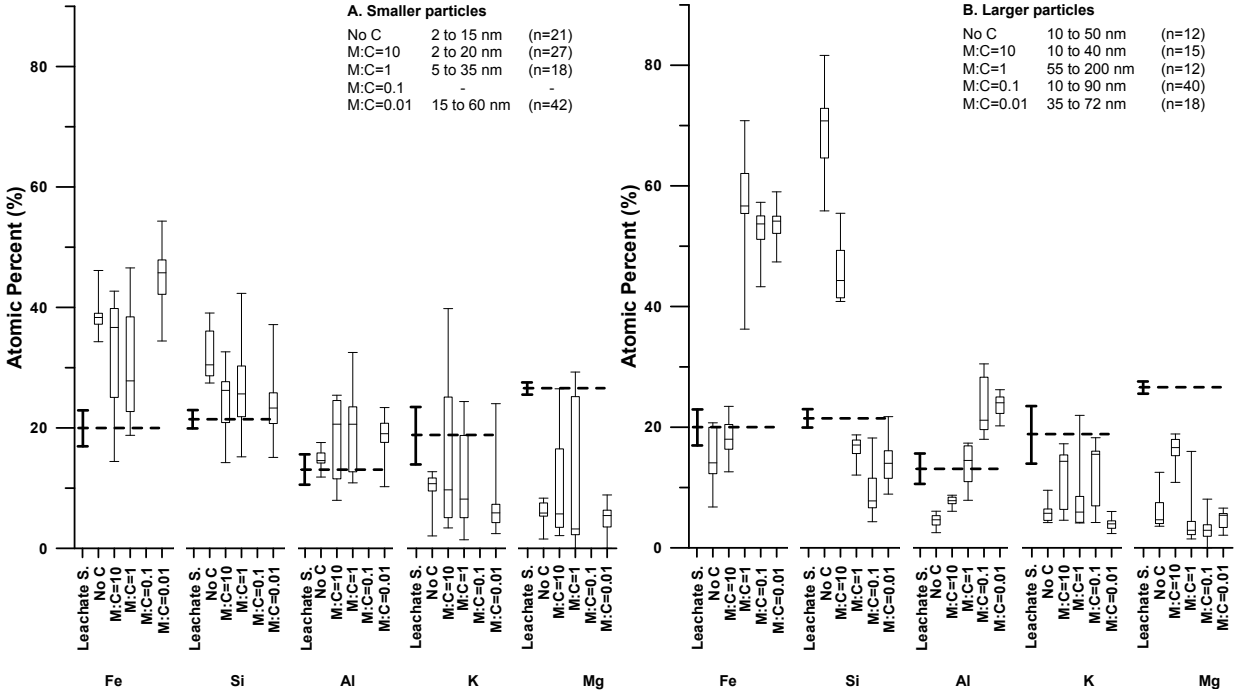

Figure 50: TEM-EDX chemical analysis of polymerized particles at the five molar M:C ratios. The "box-and-whisker" plots represent median values, the upper and lower quartiles, as well as the min and max of the data. Chemical composition of the leachate solution (Leachate S.) is also shown for comparison. A: chemical composition of the smaller nanoparticles; B: chemical composition of the larger nanoparticles. n: number of analyzed particles.

Larger nanoparticles, on the contrary, showed pattern dependent on C content for all elements except K and Mg. Si proved to be important at low C contents (No C and M:C=10) by showing enrichment compared to slight Fe and Al depleted concentrations. At higher C loading (M:C=1, 0.1 and 0.01) on the contrary, Fe contribution was important (and to a lesser extent also Al) and Si was observed to be depleted. Al contribution in these five phases, however, showed slight but distinct progressive increase with increasing OC

concentrations. With regard to K and Mg, both the smaller and larger nanoparticles showed depletion compared to the leachate solution. Generally we observe OC concentration at M:C=1 to be a turning point where deviations from this C concentration results in nano phases with opposing characteristics.

5.4 Discussion

5.4.1 Two stages of precipitation: growth and maturation

The formation of sroMOAs takes different routes in presence of significant amount of C (i.e. M:C≤1), as compared to low or no C samples (chapter 4). Locations on titration curves where pH shows reduced (or no) change mark conditions where secondary phases are forming at a higher rate (Figure 46). These lack of abrupt change in slope, observed for phases formed at M:C≤1, correlates with higher C presence in three batches. Therefore, the change in solubility of species (Fe, Al, etc.), which is often observed in a narrow pH range is masked by the higher concentration of C in the three batches formed at M:C≤1.

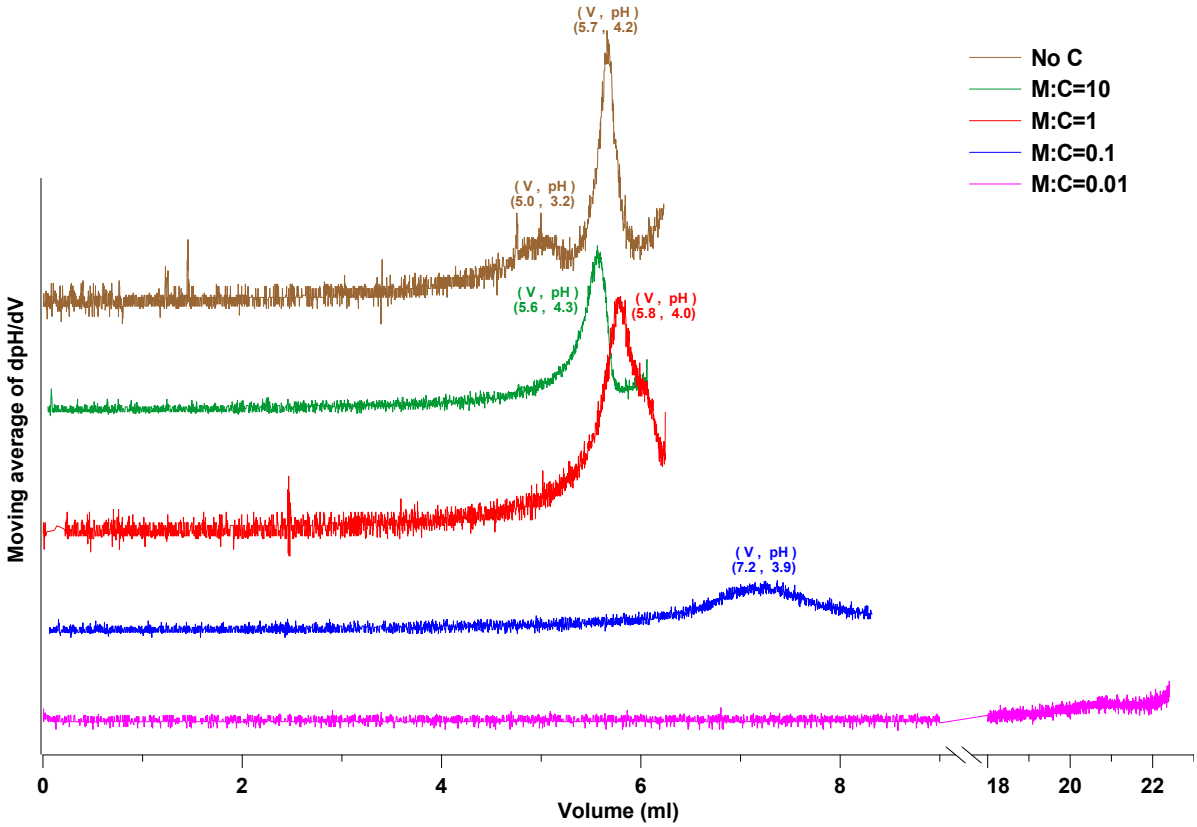

Figure 51: Moving average of the first derivative of the titration curves in Figure 46.

Figure 51 gives the first derivative of the titration curves in Figure 46. Locations in these derivative curves where the slope values reach a peak mark conditions where change in pH starts to decrease to a slower pace. Slower pH change means phases are precipitating at an increasing rate due to higher rate of OH^- consumption by the precipitates instead of the bulk solution. These values are marked as '5&5.7ml, '5.6ml,' '5.8ml' and '7.3ml' for M:C=NoC, 10, 1 and 0.1 batches respectively. Which in turn correlates to pH values approximately at 4.2 for all the four batches and at 3.2 at an initial stage of hydrolysis for the 'No C' batch. This result shows that, an average 5.7ml of 0.2N NaOH is required to reach pH ~ 4.2 when C is not present in abundance (M:C=1, 10 and No C). But at M:C=0.1

and 0.01 C competes with the inorganic species for the consumption of OH-. The earlier local precipitation conditions (pH=3.2 with 5ml of 0.2N NaOH) indicate that even small C concentrations disturb local precipitation of inorganic species at earlier stages of hydrolysis (i.e. pH<4.2). For M:C=0.01 where the OH- consumption rate does not change for the entire pH range due to the very high C concentration.

This C interference manifests directly on the size, chemical composition and structure of the phases formed (Kleber, et al., 2015). The differences in chemical composition as a function of size are illustrated in the form of a ternary diagram for Fe, Si and Al in Figure 52. The compactness of the data points indicates a homogenous chemistry between the different particles of the sroMOAs.

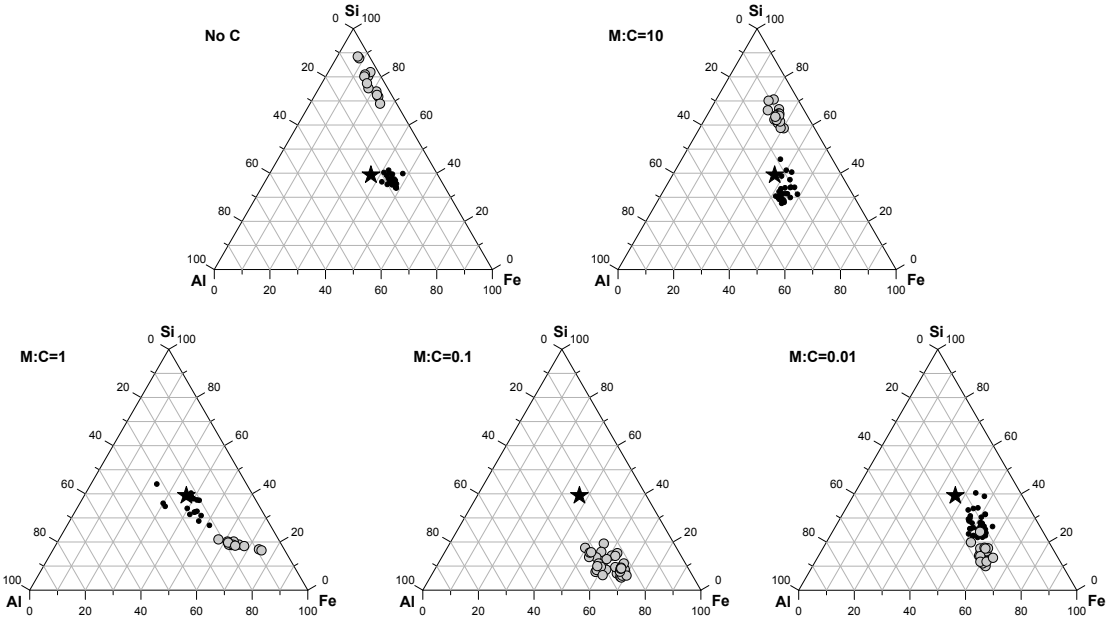

Figure 52: Ternary diagrams of Fe, Si and Al atomic proportions in the nanophases. The black star represents the initial composition of the leachate solution, the small black dots represent the composition of smaller nanominerals and the larger grey dots the composition of larger nanominerals.

In addition to difference in particle sizes these two sets of clusters show contrast in chemical composition and also in the way they interact with C. The smaller particles, whatever the added C content, have a chemical composition close to the initial leachate solution, with small Fe enrichment that signals an almost congruent precipitation process. This similarity proposes these smaller particles to probably be the initial nucleation and growth products similar to nanominerals precipitated in the absence of C (chapter 4). Organics do not seem to have an effect on the nucleation process in term of chemical composition.

Larger particles showed incongruent co-precipitation into different phases different in chemical composition from the smaller particles, from the leachate solution and also from each other at varying C concentrations. In our system we attempted OC to complex with monomeric states of inorganic cations. The difference in chemistry between these two size ranges in a single sample rules out the possibility of aggregation. Rather it is possible that these larger particles are forming while undergoing chemically altering growth phase (i.e. after the hydrolysis step), which is strongly affected by the abundance of C (An, et al., 2010).

In most natural systems, polyvalent inorganic cations act as ‘cation bridges’ between OC

and inorganic negatively charged surfaces (Kleber, et al., 2015). The theory behind the half side of the 'cation bridges' interaction (i.e. between the cations and the OC was used to explain the affinity of the different cations to OC. In these processes Al^{3+} and Fe^{3+} are far more effective in forming inner-sphere complexes in acidic soil states than cations of alkali and alkali earth metals (such as Ca^{2+} and Mg^{2+} which show predominance over transition metals in neutral and alkaline soils) (von Lützow, et al., 2006; Kleber, et al., 2015). This phenomenon explains Fe (and Al to a lesser extent) in our systems complexing with OC more efficiently than Si and far more efficiently than K and Mg when OC is present in high proportions (Mikutta, 2011). Same effect as Fe, more direct but with a lesser magnitude, is observed with Al (Figure 50). The trend shows clear increased enrichment of Al into the newly forming phases with increasing OC presence.

Figure 50b demonstrates two regimes of chemical composition. First one includes the No C and M:C=10 phases while the second includes the remaining three. Observed change when transiting from M:C=10 to 1 is proof of shift in the growth scheme of the nano phases when C proportion increases and reaches equality to that of the metals (Fe and Al). Data on Fe and Al also shows a higher increment in enrichment of these two trivalent cations when C proportion changes from M:C=10 to 1. Phases precipitated at M:C=0.1 and 0.01 show an almost identical chemical composition for all the cationic species. This could mean that there may not be unreacted cations remaining in solution to compete and complex with further addition of C (i.e. M:C<0.1).

5.4.2 Two mechanisms of sroMOAs growth

In the precipitation batches, relying on our LCF data, two mechanisms of growth were observed (Figure 53). Upon addition of OH^- we have on one hand the neutralization of dissolved cationic/metallic species in solution where by inorganic metal hydrolysis plus polymerization of minerals is promoted. The proportion of Fe interacting with Fe, Si and Al (to a lesser extent with Mg and K) (designated in Figure 53 as Fe-O-Fe curve) decreases from 100 to 12% with increasing C content. The second mechanism deals with Fe complexation with OC. Figure 53 clearly demonstrates DOPA interference with 'inorganic nucleation plus polymerization' increases with increase in its concentration.

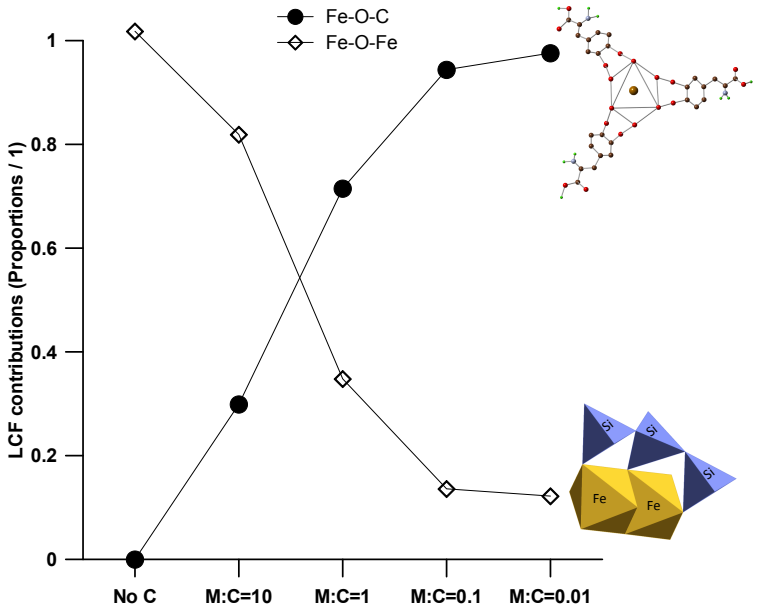

Figure 53: LCF contributions for Fe-O-C complexes and Fe-O-Fe interactions.

DOPA represents the functional groups that are abundantly present in natural organic matter. These functional groups, especially hydroxybenzoic acids and polycarboxylate, are active participants in organo-mineral interactions in the soil matrix (Kleber, et al., 2015). Fe-DOPA interaction is highly dependent on pH state. And the strength or extent of complexation is additionally dependent on DOPA abundance in the system.

DOPA with just its carboxylic functional group (pK_a=2.58) that is active at acidic soil pHs creates mono dentate mono nuclear complex. And in combination with other functional groups it may form bi or tri dentate complexes. The other functional groups, the double hydroxyls, are reported to be active at pH states as low as pH=5.5 regardless of their pK_a values (~8-10)(Kim, et al., 2015). Fe(III)-DOPA complex (Catecholate-type Fe(III) binding) which utilizes the double hydroxyls was repeatedly reported to give structural strength for mussel physical attachments to marine surfaces (Sever, et al., 2004; Hwang, et al., 2010). This interaction was unambiguously detected by Raman spectroscopy (Taylor, et al., 1996; Harrington, et al., 2010; Hwang, et al., 2010; Holten-Andersen, et al., 2011) and indirectly characterized via infrared spectroscopy (Pecoraro, et al., 1983; Sever, et al., 2004). Kim, et al. (2015) reported these interactions create a tris-bidentate Fe-catechol complex at higher pH states of 8.2 (at Fe:C=0.037) and the interaction reducing to bis-bidentate Fe-catechol complex at pH states of 5.5. They also reported that at low pH states (as low as pH 3) the di-hydroxyl functional groups cease to be active making impossible any complex formation via the double hydroxyls.

In a laboratory study by Mikutta (2011) single or double hydroxyl groups of hydroxybenzoic acid with or without the carboxylic functional groups were forming bidentate links with Fe. Mikutta (2011) additionally found higher interference to Fe polymerization from the catecholate-type rather than the carboxylate-type Fe(III) binding. Therefore, DOPA interference with inorganic polymerization is achieved via one or more of its functional groups.

Nevertheless, Fe^{3+} is not dominantly soluble at basic pH (Kleber, et al., 2015); but the bis- and tris- Fe(III)-DOPA complexes are known to be forming at ocean pH~8.2 (Hwang, et al., 2010). Therefore, Holten-Andersen, et al. (2011) argue a different angle that, conditions favorable to overcome this obstacle can only be found with in the mussel foot where by the byssus secretion creates a local acidic environment (pH~5-6) that allows Fe^{3+} and DOPA to complex. That is due to the higher affinity Fe^{3+} (compared to H^+) to O^-, regardless of the protonated state of the hydroxyl functional groups at acidic state (Kleber, et al., 2015). Afterwards the release into the ocean into a basic environment forces immediate agglomeration and creation of the bis- and tris- complexes (Holten-Andersen, et al., 2011).

Harrington, et al. (2010) report this interaction also utilizes other related transition metal cations. At acidic pH conditions (<4.7) the protonated state of the hydroxyl (OH) and also amine (NH_3^+) functional groups contribute to the organic-inorganic interactions by forming outer-sphere complexes (such as H-bonds) (Rodriguez, et al., 2015). This outer-sphere interaction could be expected to occur at slightly less than 50% capacity in our study of pH5 state.

Lee, et al. (2006) state that DOPA complexation with inorganic ions and surfaces is exclusively a high strength but reversible non-covalent interaction, which is not a hydrogen bond formation. The catecholate-type complex specifically has bond strength only modestly weaker than a covalent bond (Lee, et al., 2006; Holten-Andersen, et al., 2011). Regardless, this interaction has repeatedly been reported to be reversible with change in pH or in the presence of other OC with more affinity to Fe^{3+} (e.g. EDTA)

(Schwertmann and Murad, 1983).

Therefore, Figure 53 outlines that we have a shift between two competing mechanisms. This shift is affected by the proportion of C in the system at a transition M:C value of ~1 where both mechanisms are actively involved via the different possible interactions discussed above. But, to study the sustainability of the complexes formed, further incubation experiments are required to determine the enzymatic or bacterial degradation effects.

5.4.3 Optimal conditions of sroMOAs coprecipitation

In carbon stabilization studies optimal conditions for coprecipitates could be viewed from various angles. A couple of views include conditions that result in the most stable inorganic to organic interactions and/or conditions that result in the stabilization of the larger amount of organic material. Our study has progressed enough to test the latter view but not the former.

In a summary by Kleber, et al. (2015), OM coprecipitation with Fe and Al is expected to start at high C content as M:C~0.03. But the presence of OM is also expected to effectively impair the formation of higher crystalline order oxides and intensely alter properties such as particle size and metal coordination. In our proposed growth phase, C presence promotes size increase until a turning point in C proportion of M:C=1 (Figure 54). Higher presence of C (M:C<1) had a poisoning effect on growth, resulting in phases with reduced particle sizes. Other studies involving Ferrihydrite in MOAs have also reported similar associations of less aggregated structures and smaller crystals with lower M:C ratios (i.e. higher C content) (Kleber, et al., 2015). Therefore, our study suggests that equal metal (Fe+Al) to C molar proportions pose suitable conditions most favorable for growth. This option gives, if not chemical, at least efficient physical protection that is inherent in larger masses or aggregates.

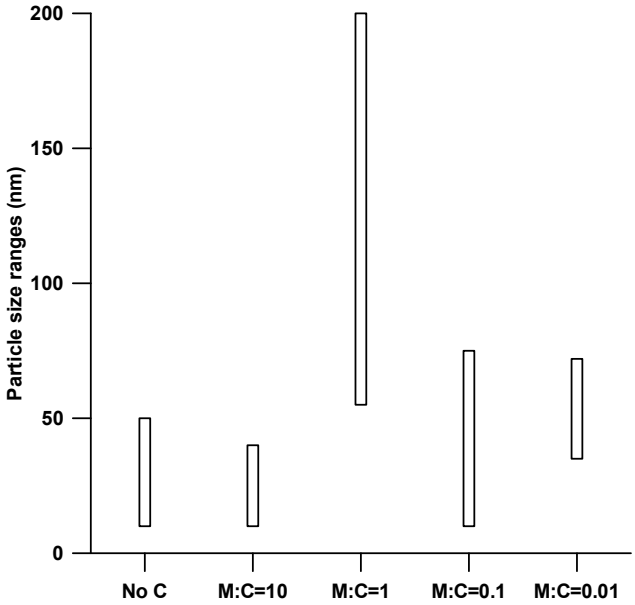

Figure 54: Particle size ranges, larger particles

5.4.4 Comparison with batch sroMOAs reported in the literature

What is distinct in our findings is that all formed phases are short range ordered. Factors contributing for the absence of crystallinity in our Fe polymers is the presence, in

abundance, of other inorganic cations (such as Si, Al, etc.) and C. Hindrance of crystallinity has been reported due to the presence of similar strongly complexing anions such as PO_4 (Rose, et al., 1996), SO_4 (Norton, et al., 1991) and SiO_4 (Doelsch, et al., 2000; Pokrovski, et al., 2003).

Most studies report similar outcomes of total absence of crystallinity but that is not always the case. Literatures also report traces of crystallinity, or full crystallinity but in small quantities, or less crystalline versions of a certain phases (e.g. 2L instead of 6L ferrihydrite), in the presence organic and inorganic cations (Doelsch, et al., 2000; Henneberry, et al., 2012). In our study, the EXAFS and LCF data show these interactions to be dominantly poorly polymerized Fe-O-Fe interactions. TEM diffraction analysis also showed no long-range order in the phases. For the phases formed at M:C=10 & 'No C' conditions, the complexes were not more advanced than edge sharing Fe-Fe_2 interactions. This was regardless of the low to no C contents respectively which ultimately resulted in Si enrichment and Fe depletion (Figure 50B).

The effect of Si species in the presence of Fe (oxyhydr)oxides is fairly studied. But some studies show residual crystallinity of the Fe species even in Si presence. Doelsch, et al. (2000) found crystalline akaganeite at low pH (<5) when hydrolyzing Iron (III) Chloride in the presence of SiO_4 ligands. Anderson and Benjamin (1985) demonstrated delay in the aging/crystallization of ferrihydrite from 24 hours to 1-2 weeks due to the presence of Si in the system. In an attempt to precipitate single phase α-FeOOH, Ristić, et al. (2015) showed CTAB presence (cetyltrimethylammonium bromide) produced less crystalline ferrihydrite like phase. They added gum arabic (GA) were able to stop α-FeOOH growth thereby facilitating the dissolution-recrystallization of α-Fe_2O_3 phases from α-FeOOH. These demonstrate that various organic and inorganic soil compositions have varying effect on the geochemical process that affect C stabilization.

In phases formed at M:C=1, 0.1 & 0.01, contrary to the significant Fe enrichment, no evidence of the expected Fe-O-Fe interactions were observed due to the high C content. This proves the preferential affinity of 'C in abundance' to Fe but at the same time its disruptive nature to polymerization of inorganic phases (Vilgé-Ritter, et al., 1999b). This phenomenon in co-precipitates was discussed by Kleber, et al. (2015) as metal oxides' tendency to embed in an organic matrix (Pédrot, et al., 2011; Mikutta, et al., 2014) in high C presence; and the resulting smaller subunits of the aggregates of MOAs (Vilgé-Ritter, et al., 1999b). Results in this study showed that this high C presence resulted in the inhibition of the strongly favored Fe to Fe coordination.

Nierop, et al. (2002) also considered metals other than Fe and Al in their experiments (Ca, Mg, Mn, Cu and Zn). These other cations lose significance for the same reason as K^+ and Mg^{2+} in our systems (i.e. having lower valence) unable to precipitate OM as significantly as Fe^{3+} and Al^{3+} (Evans, 1989; Stevenson, 1994). But most researches including Nierop, et al. (2002) neglect the significance of Si.

5.4.5 Are the sroMOAS produced representative of natural samples?

An obvious follow up step in this study would be to test the effectiveness of the organic-inorganic interaction we synthesized. To do so, we correlated the characteristic of the phases we synthesized to properties of natural soils in different parts of the world and different horizons of a soil profile. And extrapolated the organo mineral interactions and C turnover resistance to our synthetic samples.

Depending on the M:C ratio, our group of 5 samples gives characteristic resemblance to Andosols and Podzols. Andosols which are rich in allophanic phases (Si+Al) are organic rich because of the abundant oxide-organic interaction (Oades, 1988). Andosols are characterized by high Al+Si presence specifically in the 4Bw horizon (Basile-Doelsch, et al., 2005). This high Al+Si content is strongly dominated by poorly crystalline aluminosilicates (protoimogolite and proto-imogolite allophane phases). Basile-Doelsch, et al. (2005) argue the C stabilized by these phases to be "extraordinarily effective" but still with slow but evident turnover due to its dynamic equilibrium with the environment.

No C and M:C=10 samples are with major Si and minor Al composition. That closely resembles the 4Bw horizon in Andosols from most volcanic soils (Basile-Doelsch, et al., 2005). Basile-Doelsch, et al. (2007) additionally discuss that a wide range of the studied density fraction (1.9-2.3) was dominated by ITM (low polymerized imogolite type material). And the dominance of this specific phases resulted in the complexation of 53.8% of the total OC of the soil horizon when only ITM represented 39% of the bulk sample mass. This phenomenon is true with higher OC stabilization potential of poorly crystalline minerals in most volcanic soils (Torn, et al., 1997; Basile-Doelsch, et al., 2005). Therefore, these studies argue that the nature of the minerals to be a key factor in stabilizing OC. These ITMs are clearly an indicator that in volcanic soils low polymerized aluminosilicates are better chelators and stabilizers of C than iron oxides or crystalline phases (Basile-Doelsch, et al., 2007).

Also reported for 4Bw horizon of andosols is the very small proportions of OC that are bound to Fe oxides (Basile-Doelsch, et al., 2007; de Junet, et al., 2013) regardless of significant Fe presence (Fe:Si=2.1 for 4Bw horizon from the Reunion Island) (Basile-Doelsch, et al., 2005). Just like these soils, the minor Fe content in our No C and M:C=10 samples (Figure 52) has created poorly ordered Fe polymers unreacted with the OC (Figure 47) compared to Si+Al collectively.

But our results additionally showed silicon's significance in co-precipitating OM at low C concentrations. Similar hypothesis was proposed in chapter 4 with SRO phases precipitated in C free conditions. These observations give new insights, regardless of the lack of abundant literature on Si interaction with OM. That is due to the characteristic limited view of studies on preferred and higher probability of metal hydrolysis, which excludes Si. Research preferences are directed to Fe^{3+} and Al^{3+} due to their hydrolysis constant being below soil pH (Kleber, et al., 2015).

By contrast, in podzols' B horizon iron content seems to contribute most to OC stabilization. Eusterhues, et al. (2003) found this to be true with Fe oxides of high and low crystallinity for stabilized old SOM in the Bs horizon. They further argue that where the Fe content appears low, the stabilization of OC is aided by additional processes probably involving silicate species. This goes in accordance to the M:C=1, 0.1 and 0.01 samples in our study that are characterized by major Fe and minor Al content (Figure 52).

In typical podzol profiles, the B horizon is rich in Al, Fe and organic matter while overlying horizons are low in composition of same soil components (Jansen, et al., 2003). Jansen, et al. (2003) argue that enriched composition of these components is a key factor in their immobilization that is typical for the B horizon of these soils. In addition to the essential metal-C complexes, secondary Fe, Al and Al+Si oxides, oxyhydroxides and poorly crystalline phases (such as allophanes) are characteristic phases in these horizons (Karltun, et al., 2000; Levard, et al., 2012).

In podzols Karltun, et al. (2000) suggests the short-range ordered variable charge oxides (mostly Ferrihydrite) which contributes to the reactivity of the B horizon of podzols also contributes to the high surface area (Dzombak and Morel, 1990) that results in effective OC stabilization in the B horizon. Eusterhues, et al. (2007) also explain the preferential association of DOM (as the main sorbate in the Podzol) to be mainly associated with Fe oxides.

5.5 Conclusion

This synthesis experiment on MOAs successfully coprecipitated nanoparticles from dissolved species at varying C concentrations and at realistic soil pH 5 conditions. Formation of the new phases, undergone in two stages, resulted in (1) growth into smaller particles and (2) maturation into larger particles, both of which were structurally amorphous. From a chemistry stand point, the smaller particles (2-60nm) were not much differentiated from the leachate solution. While, the larger particles (10-200nm) were chemically far from the leachate solution. Fe, Al and Si phases, ones most likely to attain crystalline state, did not do so due to major interference from Fe, Si and C, and minor interference from Al, Mg and K. Surprisingly (and similar to cases observed in chapter 4), Al played only a minor role in the MOAs.

The formation of the smaller particles was not affected by varying C presence in the system. But with the larger particles low C presence (No C and M:C=10) meant major Si role in the MOAs, while high C presence (M:C=1, 0.1, 0.01) meant major Fe (and minor Al) role in the MOAs. When studying the role inorganic species play in stabilizing OM, Si is highly underemphasized while more emphasis is put on Fe and Al. Regardless of this narrative, our results demonstrate the importance of Si especially in conditions of low C presence.

Precipitates undergo much more advanced growth and maturation stages in higher C presence. Increase in C concentration to ratio of M:C=1 gave the optimal growth and maturation conditions which resulted in particles with sizes as large as 200 nm. Same increase to M:C=1 set conditions where carbon's complexing preference shifted from Si to Fe. More C in the system drastically retarded the same growth and maturation stages resulting in smaller particles.

This batch approach used in this protocol, although simplified compared to natural soil systems, it made possible the reproduction of physico-chemical conditions that are fairly realistic in mimicking soil processes. As a result, the coprecipitation process effectively reproduced nanominerals, which are analogues to particles in '4Bw horizon of Andosols with high Si presence' and particles in 'B horizon of podzols with high Fe presence'.

High Fe content at high C concentrations shows that if the C is not chemically bonded to the inorganic species, it is at least physically embedded in the matrix. This may mean, considering these thermodynamic conditions, the system is favoring stronger or longer storage/stabilization of carbon. But to go further with the long-term effects, the efficacy of the MOAs in withstanding enzymatic or bacterial attack should be studied via incubation experiments.

The lack of interest in co-precipitation studies with regard to Mg and K goes parallel to their depletion in the nanominerals formed in our study. But Si enrichment in our nanominerals prompts the need to include Si in co-precipitation studies.

6 Metal salt experiments

Duration for the previous biotite weathering batches took up to a month. And the precipitation stage that followed in some of the same preliminary experiments gave very small quantities of precipitates, not exceeding 20 mg. To remedy the latter shortcoming of quantity and also surpass the weathering stage; inorganic metal salts were used to duplicate the composition of the natural biotite leachate solution. The main question posed for this section was 'does artificially duplicating a leachate solution yield similar results as with materials produced with natural biotite?'

This subchapter will therefore describe steps followed in answering that question, duplicating the leachate solution and the results obtained with the produced precipitates (formation, structure, etc.). Even though the analysis was not advanced enough to describe the formation and structure of the precipitates, enough data will be presented to be compare with precipitates from natural biotite, the results for which were presented in previous sections of this manuscript (Chapters 4 and 5). Discussions and conclusions will also be presented as they pertain to the design of similar future works.

6.1 Material and methods

6.1.1 Materials

To artificially duplicate the biotite weathering leachate solution, five quantitatively major atoms (namely: Al, Fe, Si, K and Mg) were selected. For Si, silicium solution standard for ICP-MS from CHEM-LAB was used at an initial concentration of 1000 µg/ml. For the remaining four metals, following nitrate salts were utilized:

- Al - Aluminum nitrate nonahydrate (from SIGMA-ALDRICH)
- Fe - Iron(III) nitrate nonahydrate (from VWR)
- Mg - Magnesium nitrate hexahydrate (from SIGMA-ALDRICH)
- K - Potassium nitrate (from MERCK)

As in previous preliminary experiment, HNO_3 and NaOH were utilized at different stages of the study. The former was used to stabilize the pH at a value of 2 and the latter to raise it to higher values of 4.2, 5 and 7. The pH values were selected from a preliminary titration experiment, which yielded inflection points at those three pH values (Figure 37 in 4.2.1), similar to one used for the natural biotite weathering experiments. Additionally, studies have shown these pH values to represent pH range in acidic soil solutions, which are combination of conditions suitable for the precipitation of secondary minerals (Tietema, et al., 1993; Nierop, et al., 2002).

During the precipitation stages two OCs were used in coprecipitation and adsorption mineral formation modes. 3,4 Dihydroxy- L-phenylalanine (DOPA) is the first compound that was used as the primary OC. L-phenylalanine (missing the double hydroxyls from the phenol group compared to DOPA) was also utilized. These compounds are same as the OCs utilized in the preliminary experiments of section (Chapter 3) and are therefore not detailed further in this section.

6.1.2 Methods

The procedures in the experiments followed in achieving above mentioned objectives are as described below:

1. The metal salts had high tendency for absorbing moisture. Therefore, the salts were left in an oven at 40 ^{0}C overnight to remove over hydration.

Table 23: Calculations resulting in mass and volume of ingredients to add to make a pre-precipitation mix.

		Mg	Al	Si	K	Fe	Total
1	Cationic concentrations (µg/L) after 2 months of dissolution	12968.00	8002.42	35957.34	12077.69	26170.72	
2	Mass of cations (mg) in 100mL leachate solution at 2 months	1.30	0.80	3.60	1.21	2.62	**9.52**
3	Mass in 'row 2' X2 (mg) in 100mL leachate solution to approach the 60ppm saturation limit for Si in soils	2.59	1.60	7.19	2.42	5.23	**19.04**
4	Molecular formula of salts+hydration	$Mg(NO_3)_2.6H_2O$	$Al(NO_3)_3.9H_2O$	_	KNO_3	$Fe(NO_3)_3.9H_2O$	
5	Element/Molecule Molar mass (g/mol)	24.3/256.41	27/375.13	28.09/_	39.1/101.10	55.85/404.00	
6	Mass fraction of individual cations in their respective hydrated salts (1000 µg/mL Si solution)	0.09	0.07		0.39	0.14	
7	Mass of metal salts and Volume of "1000 µg/mL" Si solution to add	27.37 mg	22.24 mg	7.19 mg(mL)	6.25 mg	37.87 mg	**100.91 mg**

2. Row 7 of Table 23 gives the final quantity of the four metal salts and the 1000 µg/ml Si solution that were added to get a 100 ml solution. This would represent the leachate solution at 2 months of weathering.
   Conditions: In soils, natural Si concentrations are below 2 mM (56 ppm). Additionally, for good Fe detection with Fe edge EXAFS measurements, a minimum of 1 mg of Fe in the sample was required. Also to get as much mass for the final precipitate as possible initial elemental concentrations were also increased. Therefore, an increase was done but by still maintaining the elemental proportions in the leachate solution of the natural biotite weathering. Taking into account above three requirements, and expecting a final mass of ~19 mg, twice as much elemental masses (row 3) and in the form of the metal salt masses (row 7) were added into the mix.
3. For C addition, Metal to Carbon proportion of 'No C', 10, 1, 0.1 and 0.01 were adopted. Metal, in these calculations represented only contributions from Al and Fe. The higher affinity of trivalent metals, Fe and Al, to complex with organic ligands as compared to lower valence metals such as K, Ca, Mg, etc. validated the use of only Fe and Al in these 'metal to carbon' proportion calculations (Evans, 1989; Stevenson, 1994; Nierop, et al., 2002).
4. Individual salts and Si solution were consecutively added in a 100 ml glass beaker mounted on a magnetic stirrer in an initial 30 ml of ultra pure water. Volume was

adjusted to a final value of 100 ml at pH=2 by adding necessary volumes of dilute nitric acid (0.01 M) and/or ultra pure water. Solution was let to mix for ~10 minutes until all solutes added had dissolved. 1ml volume was taken from this mix for ICP-MS analysis and remaining volume was set up at an automatic titrator (785 DMP Titrino) for following precipitation stage of the experiment.

5. Precipitation was carried out by adding 0.01M NaOH solution at 70µL/min under vigorous stirring to avoid local super saturation of OH^- and rapid elevation of pH. Dosage rate in a similar range were used in Fe co-precipitation experiments in the presence of organic ligands by Mikutta (2011). The 100ml mix solution was titrated from pH 2 to 4.2, 5 and 7.
6. At the end, the post precipitation solutions were replaced into ultracentrifuge tubes and precipitates were settled in an ultra centrifuge at 80,000 rpm for a duration of 1 hour and 30 minutes. Settled portion was then replaced into glass vials by initially extracting the supernatant into a separate container. The settled portion was freeze-dried for subsequent EXAFS analysis.

Table 24: Scheme for the formation of coprecipitates at varying combinations of pH and OC proportions

	No C	M:C=10				M:C=1				M:C=0.1				M:C=0.01			
		DOPA		L-Ph		DOPA		L-Ph		DOPA		L-Ph		DOPA		L-Ph	
		Coprecipitation	Adsorption	Coprecipitation	Adsorption	Coprecipitation	Adsorption	Coprecipitation	Adsorption	Coprecipitation	Adsorption	Coprecipitation	Adsorption	Coprecipitation	Adsorption	Coprecipitation	Adsorption
pH 3										x							
pH 4.2	x	x				x				x							
pH 5	x	x				x				x				x			
pH 7	x	x				x				x							

Samples that were precipitated in the laboratory

x Samples that were analysed by EXAFS but not discussed in this section of the report

x Samples that were analysed by EXAFS and also discussed in this section of the report

6.1.2.1 EXAFS method

Extended X-ray Absorption Fine Structure (EXAFS) data was collected at the Fe K-edge on beam line 11.1 at the ELETTRA synchrotron (Trieste, Italy) and on FAME beam line at ESRF synchrotron source (Grenoble, France). Scan conditions are similar to the description given in section 4.2.4 and will not be repeated in this section. The data treatment was also done using Athena software (Ravel and Newville, 2005) in similar manner as previous chapters and detail can be found in section of chapter 4. Further details of the data reduction steps are similar to previous sections (4.2.4) and can also be inferred on Manceau and Calas (1986).

Note: Bonding between Fe and other species (e.g. Si, C, etc.) that would mean an iron from within an octahedron creating an Fe-O-Si, Fe-O-C, etc. interactions respectively

would, hereafter, be designated as Fe-Si, Fe-C, etc. for simplification purposes. Same usage will apply for other coordinations.

6.1.2.2 Reference standards

Structural information from the experimental spectra were compared with properly selected reference standards. For set of spectra from samples containing no C; goethite, 2L ferrihydrite, Fe-SRO and Fe dimers reference spectra were used. These set of spectra were selected for their gradually decreasing level of Fe polymerization. For set of spectra containing C; iron citrate, Fe-C colloids, Fe dimers, Fe-SRO and 2L ferrihydrite were used. These set also represented gradually decreasing Fe-C and increasing Fe-Fe interaction and in their structures. Details for these reference standards can be found in Appendix 8.

Note: In the context of the mix prepared for the precipitation of nanominerals in this section of the manuscript, the term "metal salts" will here after be used to refer to "the mix of the four metal salts + the Si solution standard".

6.2 Results

Data for all 16 nanominerals will not be presented here. But for this subsection, result only for two series (No C series and pH 5 series) (Figure 55 and Figure 56 respectively) will be presented.

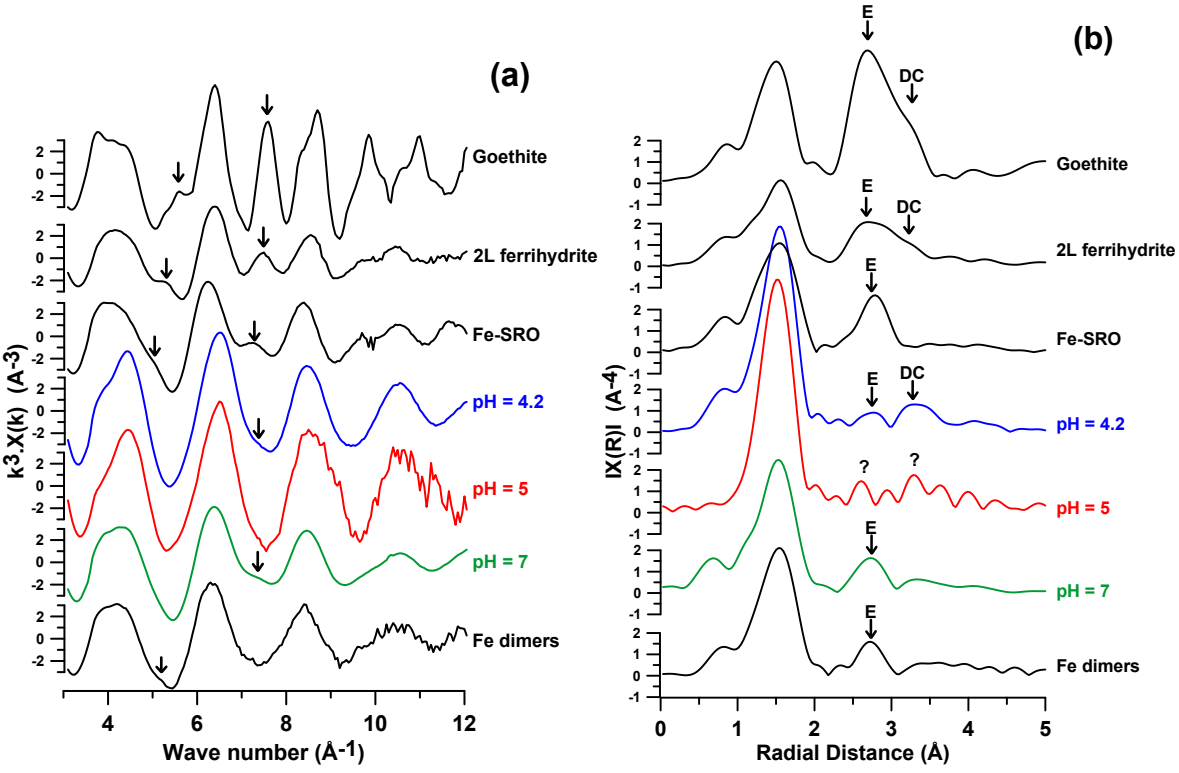

Figure 55: EXAFS analysis for nanominerals synthesized from metal salt mixes at three pH values in the absence of C. (a) k-space and (b) R-space. Spectra in black represent reference standards used to compare structural signals. Fe-Fe polymerization level for the four reference standards is know to decrease going from top to bottom. '?' indicates two possible Fe-Fe interactions in the pH 5 sample. 'E' and 'DC' show peak locations for edge and double corner sharing interactions respectively.

Compared to their reference standards, the three spectra in the No C series (Figure 55)

show faint or no Fe-Fe structural signal. Whereas, the five samples in the pH 5 series show two regimes (Figure 56) with regard to the structural information visible in the EXAFS spectra. First regime shows evidence of an interaction that is shorter than the shortest possible Fe-Fe_1 interaction (i.e. face sharing Fe octahedra, ~2.85 Å). This is consistently observed in M:C=0.01, 0.1 and 1 spectra as well as the reference standards Fe-C colloids and Iron citrate (Figure 56b). These spectra also show no peaks at radial distances where Fe-Fe interactions are expected to be seen (i.e. >~2.85 Å, not corrected for phase shift). Also observed was a faint positive oscillation (shoulder) in k-space between 5-7 $Å^{-1}$ similar to the reference standards containing Fe-C bonds (i.e. Fe-C colloids and Fe citrate).

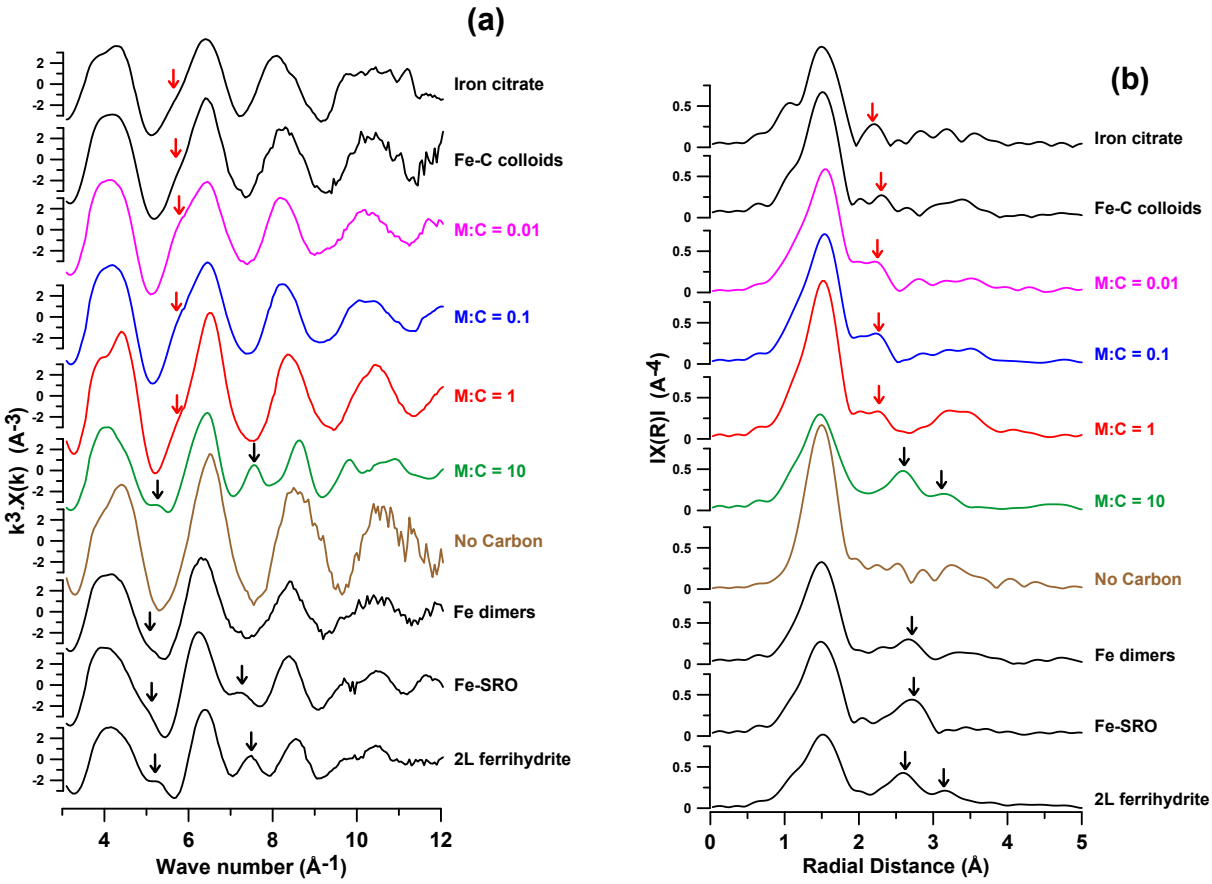

Figure 56: EXAFS analysis for nanominerals synthesized from metal salt mixes at five C concentrations at a fixed pH 5 state. (a) k-space and (b) R-space. Spectra in black represent reference standards used to compare structural signals. Fe-Fe polymerization level for the five reference standards is know to increase going from top to bottom. On the contrary, Fe-C interaction in the same reference standards decreases going from top to bottom. Black and red arrows on k-space spectra indicate parts of the oscillations specifically contributed from Fe-Fe and Fe-C interactions respectively. Same black and red arrows, in R-space, indicate radial distances corresponding to Fe-Fe and Fe-C interactions respectively.

Note: For the pH 5 series, for the sake of cleaning up noise of the No C spectrum, reducing the maximum limit for the spline clamps and also maximum limit for forward fourier transform (FFT) window to 12.15 $Å^{-1}$ was one possibility. Doing so gave a peak at 3.38 Å (uncorrected for phase shift) for the No C spectrum (see Figure 69 in Appendix 11). But to be able to compare all data/samples (i.e. this No C spectrum which is pH 5 in the 'No C series' with pH 4.2 and 7 spectra), similar data treatment parameters should be applied and were applied to all three. That included the FFT window max value of 12.15 $Å^{-1}$. This requirement cut out important structural data from pH 4.2 and 7 spectra. Additionally, Fe-Fe distance of 3.38 Å (uncorrected for phase shift) would correspond to

single corner interaction. This interaction, though highly unlikely to be achieved in this sample, is known to be the prerequisite for the transition from 2D to 3D growth schemes of Fe polymers that is observed in some crystalline iron oxides such as goethite and lepidocrocite (Rose, et al., 1996; Doelsch, et al., 2000). Specially considering the active insolubility of Si and Al species at pH 5 and thus their participation in the formation of new minerals. Thus larger FFT window between 1.80-14.23 $Å^{-1}$ was used for all five spectra (Figure 56).

6.3 Discussion

Using metal salts to surpass the dissolution stage of the experiment, simplified the protocol tremendously. The weathering process takes all but the last one day of the entire experimental duration. Due to the ease in the preparation of the artificial salt mix, and abundance of raw material, the duration for the entire experiment was reduced to a maximum of 2 days. That applied for all 16 combinations of nanoparticle formation as specified in Table 24.

Comparison of precipitated nanoparticles via the two mechanisms is given in Figure 57. First noticeable difference between the two formation mechanisms (i.e. using biotite leachate vs. mix from metal salts) is the absence (in k-space) or reduced intensity (in R-space) of Fe-Fe signals with the metal salt nanominerals. The one exception to that being M:C=10 sample. That is in the M:C=10 spectra, Fe-Fe signals were stronger for the metal salt nanominerals than for the precipitates from the biotite weathering. The Fe-Fe signals at ~5 $Å^{-1}$ that are often mildly expressed are completely absent in all the nanoparticles, again with one exception from M:C=10 sample of metal salts. In the case of the No C series (Figure 55a), in k-space window 4.5-5.5 $Å^{-1}$, spectra additionally indicate an almost 100% resemblance to k-space signal in the same range for Fe dimers reference standard. Signal in this k-space region, only observed in the presence of higher order Fe polymerization, indicates the elementary level of polymerization (maximum Fe dimers) achieved by the nanominerals from the salt mix. Comparison can be made with spectra in the same k-space region of higher order Fe-Fe interaction for 2L ferrihydrite and goethite (Figure 55a)).

The two precipitation mechanisms have one sample in common. That is 'pH 5 sample in the No C series' is the same as 'No C sample in the pH 5 series'. What can be observed in both spectra is noise in the data especially at higher k values. As a result, data treatment was unable to give clear peaks corresponding to any of the 'Fe with Fe' or 'Fe with the other metals' or 'Fe with Si' possible interactions. The state of insolubility of Si and Al (possibly also K and Mg) at this pH plays a major role in this phenomenon resulting in highly effective interference by Si and Al (possibly also by K and Mg) against Fe-Fe polymerization. Similar hindrance of Fe-Fe polymerization was evident in the 'pH 5 No C' batches precipitated from biotite weathering products but slightly less pronounced compared to its counterpart produced from the metal salts. As is discussed in detail in Chapter 4 this phenomenon is the result of the active state of insolubility of Si at pH 5.

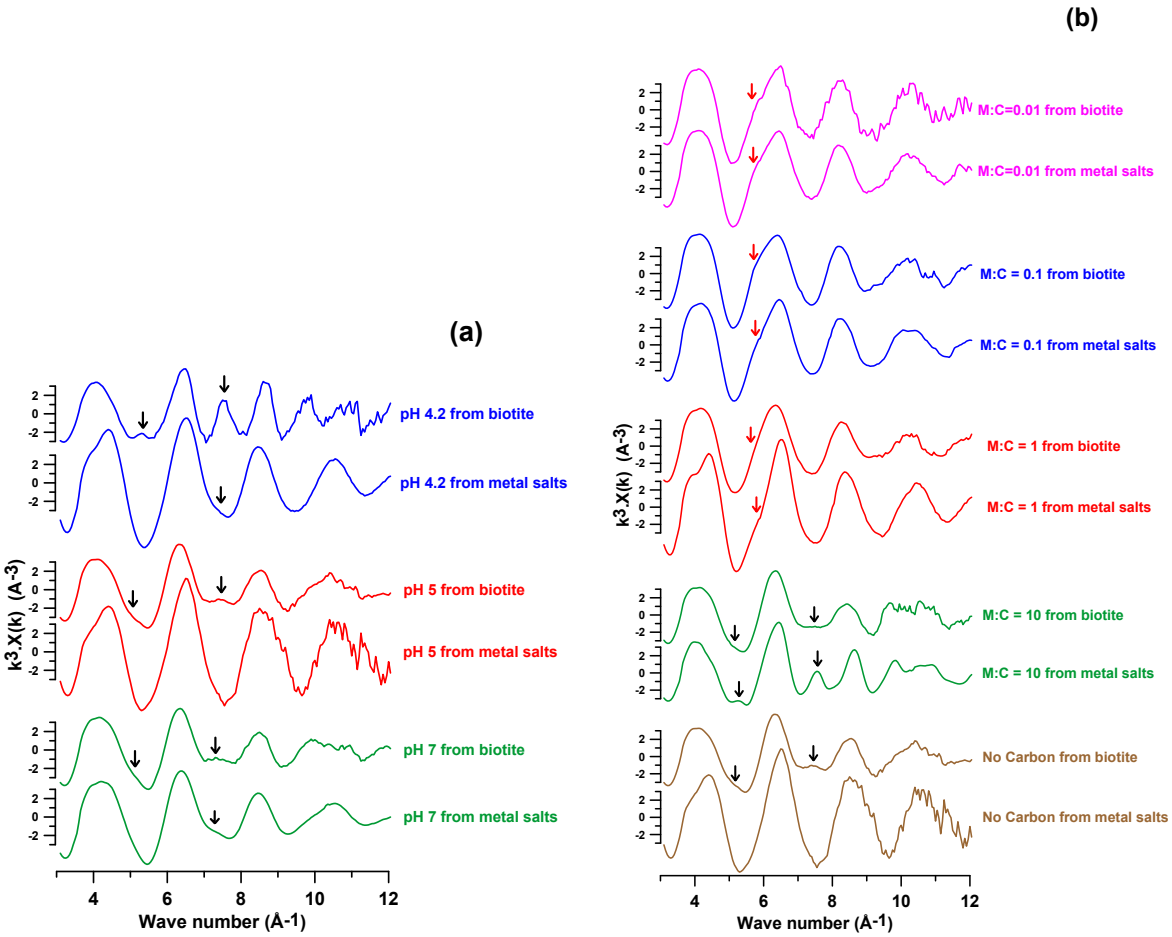

Figure 57: Fe k-edge EXAFS comparison of nanominerals formed using leachate solution from biotite weathering vs. mix solution from metal salts (and pure Si solution). (a) No C series and (b) pH 5 series. Black arrows show locations of Fe-Fe signals. Red arrows show location of Fe-C signals.

For the pH 5 sample (No C series, Figure 55b), the two peaks in R-space represented by "?" are located at radial distances possible for Fe-Fe interaction. These signals, though they stand out intensity wise, cannot unambiguously be labeled as Fe-Fe interactions since data treatment was unable to remove the harmonic oscillation from the background.

6.4 Conclusion

The metal salt mixes were basically an attempt to duplicate the leachate solution from the biotite batch weathering experiments. Though the effect may be small, an additional difference between these two solutions is the minor compositions in the leachate solution (e.g. Ti, Mn, Na, etc.), compositions that are otherwise absent in the metal salts mix. As a result, in some of the cases Fe octahedra were not able to polymerize with other Fe octahedra at all (e.g. pH 5, No C series). And in other cases there was not adequate enough polymerization but just enough small polymers such as dimers and may be trimers (e.g. pH 4.2 and 7, No C series). Nevertheless, one significant similarity between the two techniques is the lack of Fe-Fe signals at pH 5 for the 'No C series'. Though intensities of spectra were not of equivalent magnitude in the two techniques, Fe-Fe interactions were exceedingly hindered at pH 5 more than pH 4.2 and 7 in both natural leachate and metal salts cases.

Therefore, as a conclusion the results of this postliminary experiment tells us the extent

of Fe polymerization to be less advanced with metal salts nanominerals as compared to minerals precipitated from biotite weathering products. This difficulty to adequately duplicate natural processes makes these nanominerals precipitated from metal salts less representative of mineral formed in the soil matrix.

7 Conclusions and perspectives

7.1 General conclusions

In the course of this study, the general objective was to better understand natural SOM dynamics. As studied in their separate chapters, the sub-objectives entailed (1) answering questions related to understanding nCOMx synthesis in a controlled system at a laboratory scale and studying their dynamics. Additional question were also if the experimental protocol for the experiments yield nanominerals representative of natural systems.

First major step taken was simulating, in every aspect, the weathering of a primary mineral, biotite. Proportions of the weathering products indicated an incongruent dissolution process. Our results, therefore, support the understanding that different framework and interlayer cations get leached at a different rate. Irrespective of the incongruency of dissolution the primary objective of the weathering stage was to produce a solution mixed with truly dissolved species, which will be the primary building blocks in the synthesis of our new nanominerals (i.e. SRO and sroMOAs). To separate and collect these truly dissolved species, the choice of a 10 kD TFF membrane was valid regardless of the slower dissolution rate. Towards that end, our weathering protocol was able to produce leachate solution that was more representative of natural soil solutions compared to solutions utilized in other studies. Therefore, our leachate solution, recommended for synthesis experiments, was unique for the following critical reasons.

(1) Its variety with regard to elemental composition. Meaning it contained, therefore took into account, Si which is a major composition in natural soil systems. And also Mg and K whose contributions (though not directly pointed out in this study) are also significant.
(2) It abundance with regard to elemental composition. Which means using natural leachate solution allows abundant elemental composition to work with as opposed to most other studies that only use one or two metals to precipitate nCOMx.
(3) Pure chemical and physical (e.g. size) properties of the dissolved species (i.e. as opposed to mixed properties from undissolved colloidal particles).

Utilizing TFF membranes instead of dialysis membranes is an advantage and highly recommended for similar weathering studies because the prolonged exposure to acidity leaches the structure of the membrane and therefore compromises (1) the opening of the membranes thus the validity of the filtration cut off size and (2) also compromises the solution chemistry with unwanted contamination from C based compounds.

In the precipitation of just inorganic nanominerals, the objective was to study the pH effect on formation and structure of the synthesized phases. At all the natural soil pH conditions of formation adopted in our study, successful polymerization of even one dominant phase was obstructed, due to interference from the various composition of the starting material (leachate solution). Therefore, even though the inferior to 60 nm particle size at all pHs means our experiments are studying the very initial stages of formation, the synthesized phases in our study effectively mimic secondary minerals precipitated in nature. Specifically, the elemental compositions of the precipitates

uniquely being dominated by Fe at pH 4.2 and 7, and by Si at pH 5 demonstrates the complicated interaction that is consequence of our choice of a leachate solution that has minimum of five major compositions. This makes the nanomineral formation protocol adopted in this study, again, more close to natural processes than most other studies.

Our second set of synthesis experiments showed that it is possible to precipitate nanominerals in a laboratory context at acidic soil pH conditions where OM is most efficiently stabilized. The results showed that the protocol designed was effective, not only with inorganic species but also in the presence of OCs.

Similar to the experiments with just inorganic species, this section of the study also demonstrated that OM could be coprecipitated by not only Fe and Al species but also by alteration products from silicate minerals. Our protocol also effectively represented processes in natural systems where carbon abundance effectively and proportionally hinders polymerization of inorganic phases (and if conditions permit, final crystal formation). Additionally, it was shown that formation of secondary phases in abundance of dissolved species follows a complex path. This path in natural systems ultimately results in amorphous phases, which was also evident in our laboratory experiments due to interaction mainly between C, Fe and Si species. This study also demonstrated the much-deserved emphasis that needs to be given to Si in coprecipitation studies specifically in the presence of OM.

The <200nm particle size recorded in this study means the growth and maturation stages when OM is present are more advanced than when it is absent, but only to a limited proportion. This means, for effective stabilization of SOM in natural systems, an optimal balance is needed between proportions of the organic and inorganic reaction partners. Our study also demonstrates that under different environmental contexts this needed balance for optimal OM stabilization is variable (i.e. when composition of the soil systems are variable).

It is the conclusion of this study that the protocols followed for the production of these synthetic phases were effective in replicating in a wider range natural amorphous phases as well as precipitation processes. Therefore, this wider range allows us to finally assert that our study effectively represents wider array of natural soil systems (e.g. andosols, podzols, etc.).

7.2 Perspectives and future work

The protocol in this study was adequate with in the context of this PhD. But more can be done in better understanding SOM dynamics. Therefore, following observations and recommendations are necessary for similar work on SOM study for future studies.

1. It was instrumental to use state of the art equipment such as TEM and synchrotron based EXAFS analysis to characterize the nanominerals. But more could be done with regard to visually and chemically analyzing the surface alteration processes. That raises the set of experiments that were done with AFM imaging on biotite sheets. But studies were not advanced enough to be put in the main section of this report. Therefore, the preliminary work that was done with AFM and possible future perspective works can be found in Appendix 12.
2. It was with in the context of this PhD work to study soils such as andosols that contain aluminosilicate phases and other soils with pedogenic oxide content. There

was not enough time to pursue this future studies in this direction would aid in better understanding MOAs.

3. Iron based nanominerals reduce and organo-mineral interactions mineralize due to exposure to microbial activity. Since stabilization against reduction of the SROs and mineralization of the sroMOAs was beyond the scope of this study, these additional stages are left as a future perspective work that needs to be carried out to complete the cycle of results of this PhD.

APPENDICES

Appendix 1

Geochemical modeling using CHESS code

CHESS is a speciation model specifically developed to simulate the equilibrium state of complex aquatic systems, including oxides or minerals, organics, colloids and gases (van der Lee and De Windt 2002; De Windt, et al., 2005). CHESS stands for Chemical Equilibrium of Species and Surfaces and is actually used in many scientific areas (van der Lee and De Windt 2002; De Windt, et al., 2005).

The chemical reactions in aqueous solution (acid/base, complexation and redox) and the dissolution/precipitation of minerals can be calculated by CHESS either at thermodynamic equilibrium or under kinetic control. A kinetic approach would be the most relevant for modeling mineralogical transformations at 25 °C. However, a kinetic modeling requires to significantly increase the number of modeling parameters (e.g. nucleus surface, kinetic constant, pH catalysis or inhibition effect for every phase), of which many are characterized by strong uncertainties (or even not known). On the contrary, a thermodynamic equilibrium approach needs less data and the data are more accurately known. Though in this PhD work, CHESS calculations were performed only at thermodynamic equilibrium to provide first indications on minerals dissolution/precipitation.

In this phD work, the geochemical module CHESS of the HYTEC code (van der Lee et al., 2003), version 3.7, was used. The thermodynamic formation constants of the aqueous species and solid phases (minerals) were taken from the EQ3/6 thermodynamic database (Wolery, 1992) that contains high-temperature minerals (ex. Albite, Anorthite, Fayalite, Forsterite, etc.). The formation constants of the andesine and olivine phases were calculated by assuming an ideal solid solution between albite, anorthite and forsterite and fayalite phases, respectively. The end member fractions were estimated from the empirical formulae for andesine and olivine identified by X-ray diffraction.

$$ln\ K_f = \sum_i^p x_i\ \ln K_i + \sum_i^p x_i\ \ln x_i \qquad (1)$$

Equation (1) was further simplified into the following formula (equation (2)) for solid solution with only two end members (Chaurand, 2006).

$$\ln K_f = x \ln K_{BC} + (1-x) \ln K_{AC} + x \ln(x) + (1-x) \ln(1-x) \qquad (2)$$

A and B stand for the varying parts (towards AC and BC end members) of the empirical formula while C represents the elemental portion that always remains constant. The thermodynamic data for the solid phases considered in this study are reported in Table 25.

The formation constants were used to estimate the (under-) saturation state (SI) of the minerals with respect to an aqueous solution (leachate). Due to uncertainties, the leachate is assumed to be in thermodynamic equilibrium with respect to a given solid phase (mineral) if SI ranges between _0.5 and 0.5 log unit. A positive SI (supersaturated state) indicates that the given solid phase (mineral) may precipitate as a secondary phase. A negative SI (under-saturated state) indicates that the given solid phase

(mineral) is not stable with respect to the leachate and may dissolve.

Using thermodynamic calculation to determine the most appropriate experimental conditions: CHESS simulations

Initial system was simulated by adding the main basalt constituents in an aqueous solution at 25°C with respect to the S:L ratio, the mineral molecular weight and their proportion in basalt. For example to simulate the 1:30 ratio test, 0.09 mol/l of andesine, 0.045 mol/l of diopside, and 0.022 mol/l of olivine and ilmenite were added in 30 ml of aqueous solution. The dissolution/precipitation of minerals at equilibrium state was calculated in various physic-chemical conditions, i.e. with fixed pH ranging from 2 to 14.

Table 25: Thermodynamic constant calculations for three solid solutions. x=0.6 and 0.5 for andesine and x=0.36 for olivine were selected to yield solid solutions identified by the diffraction analysis.

		Andesine = $Na_{0.6}Ca_{0.4}Al_{1.4}Si_{2.6}O_8$		
A=NaSi, B=CaAl and C=$AlSi_2O_8$			x=0.6	
		Empirical Formula	log k (25°C)	ln k (25°C)
End member 1	AC	$NaAlSi_3O_8$ Albite	-2.76**	-6.37
End member 2	BC	$CaAl_2Si_2O_8$ Anorthite	-26.58**	-61.2
Solid Solution	$A_{1-x}B_xC$	$Na_{0.6}Ca_{0.4}Al_{1.4}Si_{2.6}O_8$	**-17.18***	**-39.56**
		Andesine = $Na_{0.5}Ca_{0.5}Al_{1.5}Si_{2.5}O_8$		
A=NaSi, B=CaAl and C=$AlSi_2O_8$			x=0.5	
		Empirical Formula	log k (25°C)	ln k (25°C)
End member 1	AC	$NaAlSi_3O_8$ Albite	-2.76**	-6.37
End member 2	BC	$CaAl_2Si_2O_8$ Anorthite	-26.58**	-61.2
Solid Solution	$A_{1-x}B_xC$	$Na_{0.5}Ca_{0.5}Al_{1.5}Si_{2.5}O_8$	**-14.80***	**-34.08**
		Olivine = $(Mg_{0.64}Fe_{0.36})_2SiO_4$		
A=Mg, B=Fe and C=SiO_4			x=0.36	
		Empirical Formula	log k (25°C)	ln k (25°C)
End member 1	AC	Mg_2SiO_4 Forsterite	-27.86**	-64.16
End member 2	BC	Fe_2SiO_4 Fayalite	-19.11**	-44.01
Solid Solution	$A_{1-x}B_xC$	$(Mg_{0.64}Fe_{0.36})_2SiO_4$	**-24.84***	**-57.19**

* Ideal solid solution model (Calculated)

** CHESS thermodynamic database

Experimental conditions deduced from CHESS simulations

CHESS outputs for the two minerals and three solid solutions are shown in Figure 58. These results suggest that a pH value lower than ~6, all minerals initially present in basalt are totally dissolved. An exception to that would be diaspore precipitating between pH X and Y as a secondary mineral in the cases of andesine dissolution, and rutile between pH X and Y in the case of ilmenite dissolution.

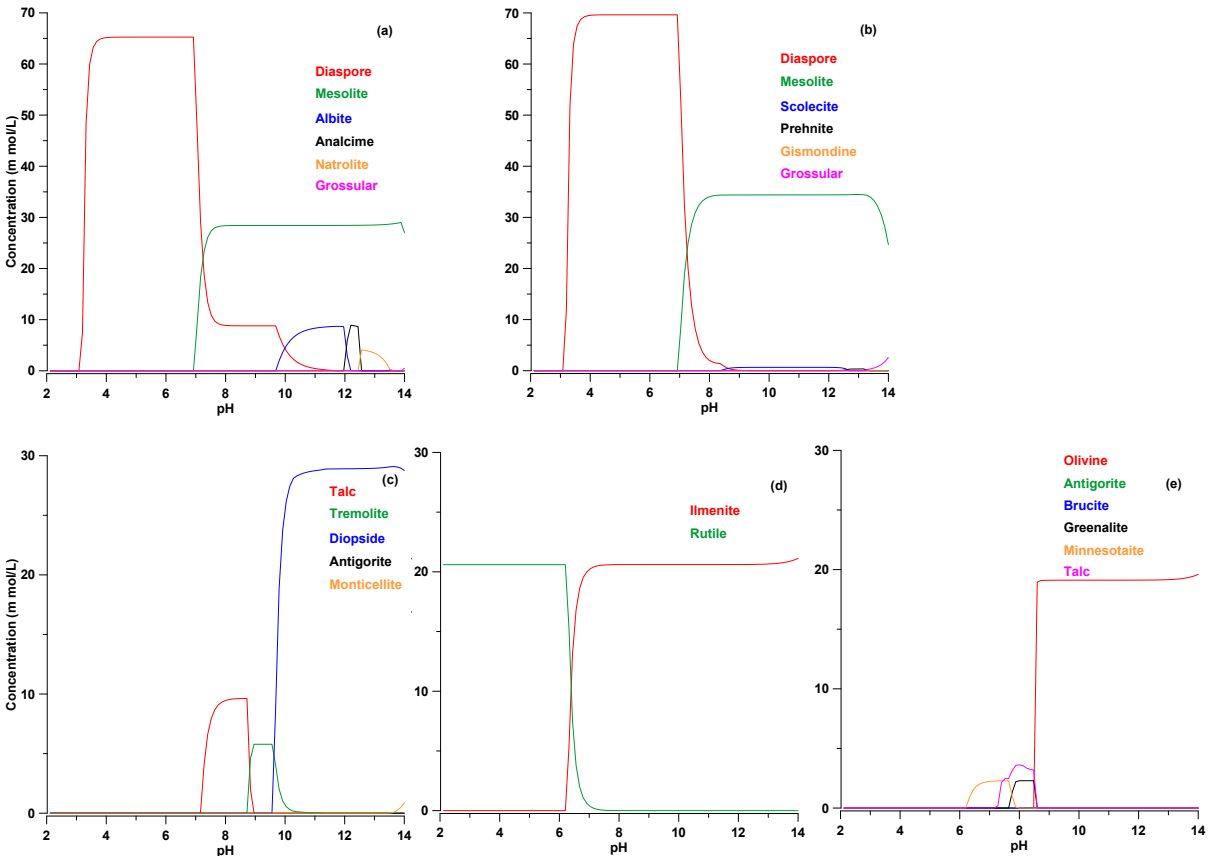

Figure 58: Basalt minerals in water. Individual figures represent thermodynamic equilibrium dissolution simulations for (a) Andesine ($Na_{0.6}Ca_{0.4}Al_{1.4}Si_{2.6}O_8$), (b) Andesine ($Na_{0.5}Ca_{0.5}Al_{1.5}Si_{2.5}O_8$) (c) Diopside, (d) Ilmenite and (e) Olivine $(Mg_{0.64}Fe_{0.36})_2SiO_4$.

But as mentioned previously, these geochemical CHESS simulations did not consider kinetic reactions. In an experiment by White (1983) of the dissolution of three glass rocks (Perlite, Obsidian and Pu Waa Waa glass) steady state conditions were reached after approximately 3 weeks of reaction at acidic conditions as low as pH 1.0 induced with HF. And at pH 6.2, steady state conditions were not reached even after 3 months.

Therefore, information from such above discussed studies complemented by CHESS data aided in determining suitable values for the two experimental conditions. Therefore, an extended experimental duration (2-4 weeks) and a fixed pH of 2 at 25°C were found suitable to begin the weathering/dissolution batch experiments.

Appendix 2

Table 26: Detailed result and discussion of preliminary experiments

	Objectives and Hypothesis	Methods and Resulting observations	Discussions and Recommendations
1st round experiments	The effect of washing the powdered biotite	> Not washing the powdered biotite resulted in unpredictable and random rises and drops of pH and conductivity measurements (Table 27 and Table 28).	> Washing would remove the very fine fraction (<50µm) and give better control and a steady evolution of pH and conductivity data.
2nd round experiments	Selecting suitable size ranges for better control	> Varying size ranges (100-200µm & 20-100µm) were weathered (Figure 59). > Of the two setups 20-100µm samples were the batches fine enough to effect significant dissolution with the weathering potential of 45ml HNO_3 with in a reasonable time window. > With an initial flawed understanding, due to release of cations to solution, electrical conductivity was expected to rise when weathering progressed.	> 20-100µm size range was the best alternative for these set of experiments. But since this range was slightly too wide, a narrower 50-100µm size range was recommended for subsequent experiments. > Further investigation was recommended to explain the dissolution vs. conductivity discrepancy as a function of time.
3rd round experiments	OM effect on weathering and probable simultaneous re-precipitation processes.	0.12g of L-phenylalanine was added to simulate 8% of OM presence as in natural systems. > OM addition gave an initial instantaneous drop in conductivity (Figure 60), which was followed by normal slower dissolution trends as observed in previous trial experiments. > Batches with OM reached stable state faster than batches with out. > In the experimental setup 'set 2' the dialysis membrane broke towards the end of the weathering process.	> The initial drop in conductivity was due to the instantaneous mass consumption of H^+ by the $-COO^-$ groups of the OC. > Sooner arrival to stability of batches containing OM was due to the reduced weathering capacity of 45ml HNO_3 due to competition of protons by the OM. > L-phenylalanine in this case did not aid in the rapid weathering contrary to observations with other OCs such as oxalate (Olsen and Donald Rimstidt, 2008). Therefore, control groups in upcoming batch experiments recommended.

	Objectives and Hypothesis	Methods and Resulting observations	Discussions and Recommendations
4th round experiments	> Understand the "weathering vs. conductivity with time discrepancy" via possible aggregation of particles (thus surface charge studies) > Chemical analysis towards understanding congruency of dissolution > Produce adsorbed and coprecipitated phases as well as ones produced in the absence of OC.	The decrease in pH in this experiment was allowed to decrease by replacing the same pH HNO_3 solution during sampling eluate (Figure 61). **Surface charge/Zeta potential analysis** > This analysis on batch 1 and 5 (Table 9 and Figure 62) puts peak 2 with in -13.36 to 2.89 mV zeta potential (close to neutral potential regions). But peak 1 value was between 2.64 to 19.04 mV zeta potentials. > Referring to Figure 63 (compilation of Table 29 and Table 30), population identified by peaks 1 and 2 will fall in the "Incipient instability" or "Rapid coagulation or flocculation" states respectively. **Congruency of dissolution** Difference in the concentrations vs. time values (Figure 64 and Figure 65) were barely above the error margins (especially to wards the end of weathering) but they are enough so to indicate shift in composition of the leachate solution with time. Data shows until a ~ 11 days cations' follow Fe > Mg > Si > K > Al > Mn > Ti release pattern while shifting to Si > Fe > Mg > K > Al > Mn > Ti release pattern after ~ 11 days. **Precipitation** > Adding 0.2N NaOH to raise the pH from 2 to 5 resulted in three phases namely a) FeSiAl PC phases (formed in the absence of OC) b) Adsorbed phases (8% OC added after pH5 was attained) and c) Coprecipitated phases (8% OC added starting from pH pH2); from **batches 1, 2 and 3** respectively. > Diffraction data for all three phases had no crystalline peaks but an extended hump between $2\theta=20^0$-50^0. These show complete lack of crystalline order.	**Surface charge/Zeta potential analysis** **Hypothesis 1:** Since both states promote slight and intense coagulation or flocculation respectively; the dissolved species, however small they are, will stick together. There by reducing charge mobility in the solution and thus lowering electrical conductivity. That means electrical conductivity readings will only be partially quantifying metal presence. Nevertheless, in aggregated state or not, charged or neutral, this dissolved metals will still be quantified by ICP-MS analysis. This hypothesis gives a reinforcing explanation to "Hypothesis 2" below, which is the more plausible explanation. **Hypothesis 2:** During weathering of minerals, the number of protons consumed for the release of a single structural cation equals the valence number of that cation (Weissbart and Rimstidt, 2000; Oelkers and Gislason, 2001). Therefore, when a mineral is being weathered a higher electrical conductivity potential is lost from solution where the effect is doubled, tripled or quadrupled equivalent to the valence number of the cation in consideration. Additionally, protons have higher electrical conductivity potential than any other cation (same for OH- compared to other anions) (microLAB, 2017). In consequence, the latter phenomenon alone could contribute to the over all decrease in conductivity despite the difference in H^+ to non-H^+ cation proportions. **Congruency of dissolution** According to the empirical formula in section 2.1.16 (assuming congruent dissolution) cation release pattern would follow Fe (0.38), Mg (0.55), Si (1), K (0.31), Al (0.33), Mn (0.02) and Ti (0.04). Values=molar ratio: [Cation]/ [Si]) An incongruent dissolution being the unambiguous conclusion here, the following additional observations were also made: 1. Three general release rate groups => a) The most leached cations (Si, Fe and Mg), b) the moderately leached cations (K and Al) and c)the least leached cations (Ti and Mn) (Figure 65). 2. The dominant leaching of Si after the ~ 11th day means the mineral (at least regions close to the interface) is losing its final structural integrity after this point in time. 3. This pattern is expected since Fe is an octahedral cation and more readily dissolved than the tetrahedral Si. Same goes for the other octahedral cations Mg, Ti and Mn. But [Fe]/[Si] in the unit cell amounts to 0.38. That being the case, the 1.3 to 0.9 [Fe]/[Si] in the leachate solution tells octahedral preferential dissolution from beginning to end of the experiment. For comparable experiments refer to Kalinowski and Schweda (1996) with short duration experiments and Hu and Jun (2012) with significant lapse of time.

Appendix 3

First round experiments

Table 27: pH readings of first round experiments. 1.5g of < 200µm biotite powder in 45 ml pH=2 HNO_3 solution.

pH	Total Elapsed Time (hr)	Samples							
		1	2	3	4	5	6	7	8
pH Initial	0	2	2	2	2	2	2	2	2
pH 2nd	24	2,95	5,55	3,01	2,87	4,41	5,83	5,06	6,08
pH 3rd	63	6,53	6,51	6,65	5,77	6,42	7,21	7,01	6,55

Table 28: Electrical conductivity readings of first round experiments. 1.5g of < 200µm biotite powder in 45 ml pH=2 HNO_3 solution.

Conductivity (microsimens)	Total Elapsed Time (hr)	Samples							
		1	2	3	4	5	6	7	8
Cond. Initial	0	1625	1625	1625	1625	1625	1625	1625	1625
Cond. 2nd	24	850	658	831	933	643	661	652	660
Cond. 3rd	63	699	720	720	580	700	826	707	725

Appendix 4

Second round experiments

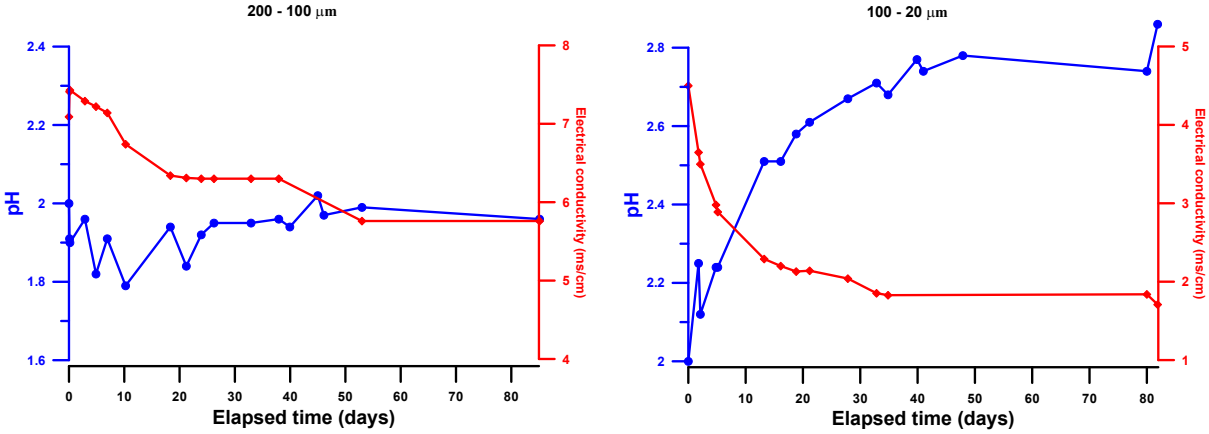

Figure 59: pH and Conductivity against time plots for two powder sample size ranges and biotite sheets

Appendix 5

Third round experiments

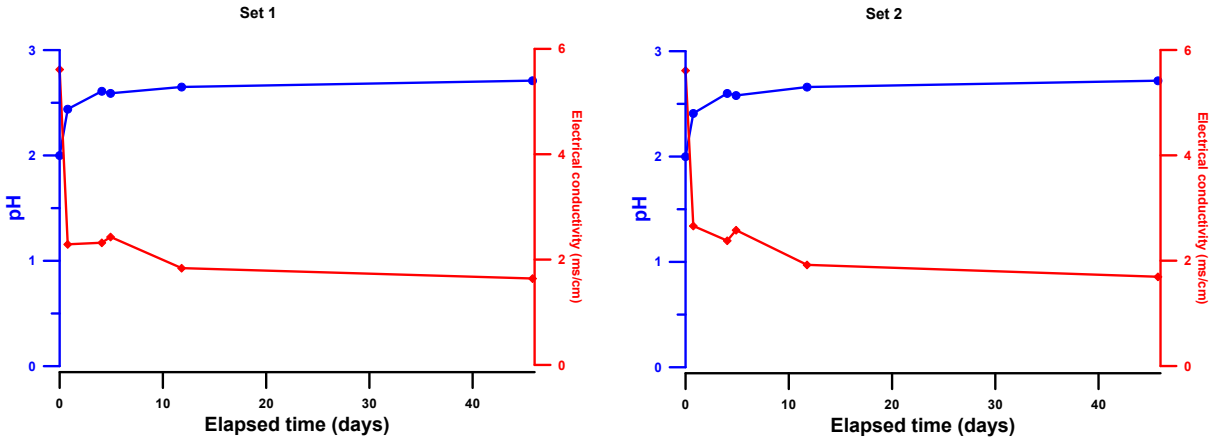

Figure 60: Dissolution of biotite in the presence of 8% L-phenylalanine. Duplicate batches.

Appendix 6

Fourth round experiments

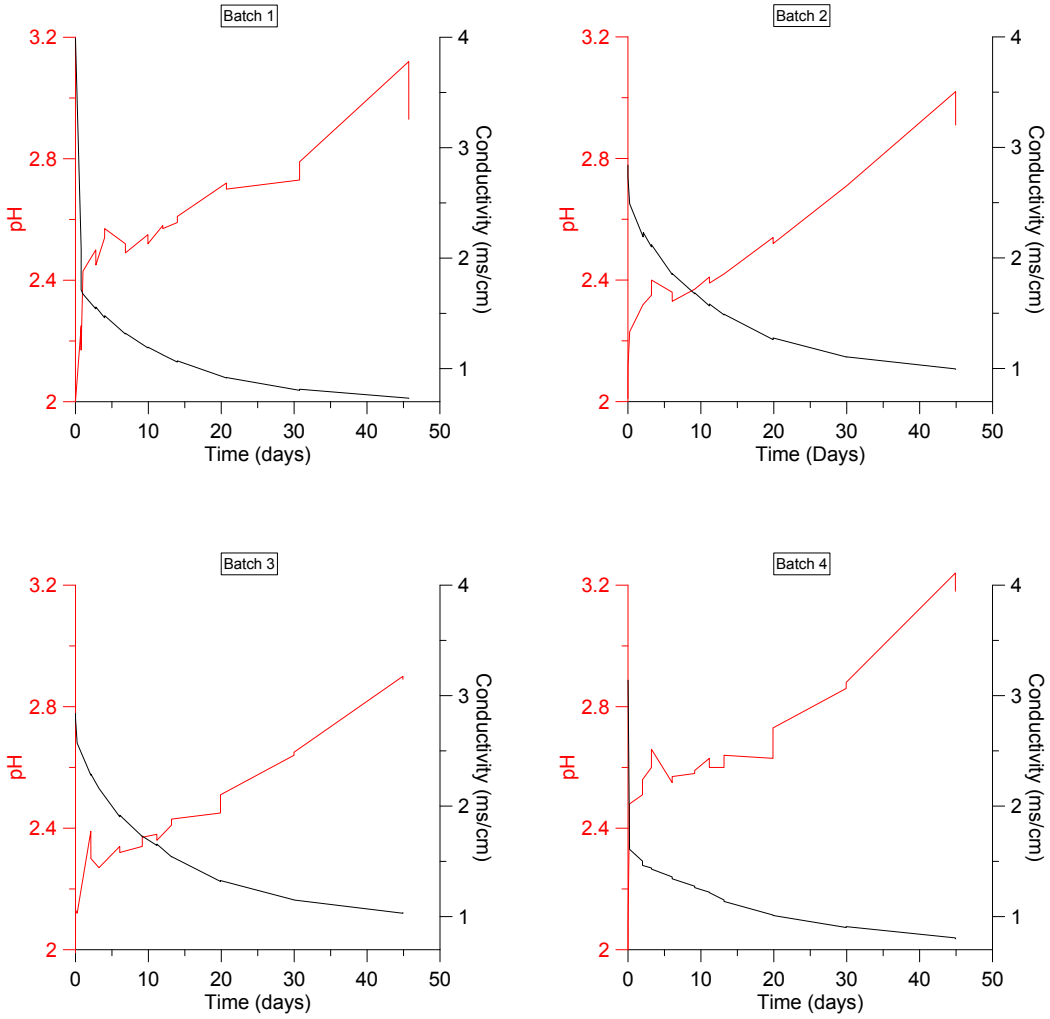

Figure 61: Solution evolution (pH and Conductivity) of experimental batches and a control group.

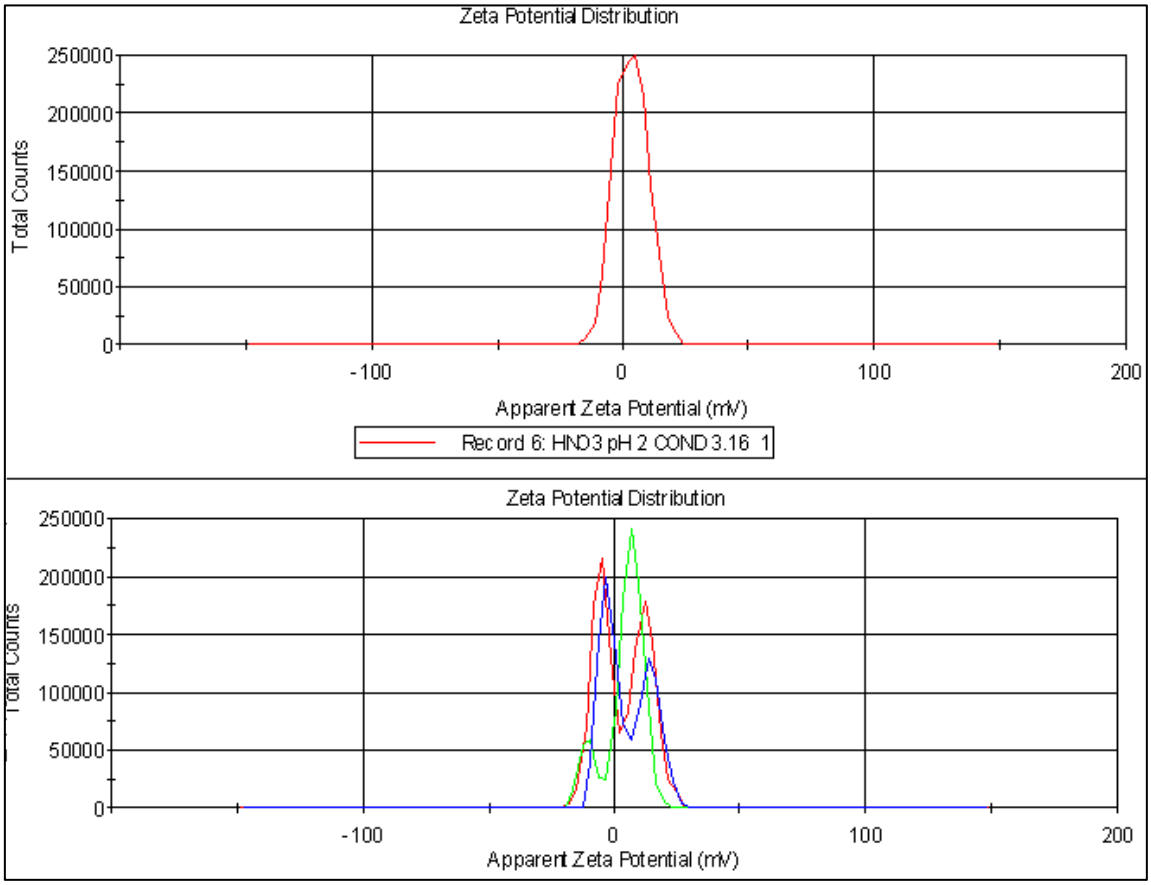

Figure 62: Zeta potential reading for negative control group batch 5 (top) and batch 1 (bottom)

Table 29: Zeta potential ± standard deviation. Supplementary data to Figure 62 above

Zeta P. (mv)	Red	Green	Blue
Peak 1	11.6 ± 5.33	7.09 ± 4.45	14.5±4.54
Peak 2	-4.93 ± 4.04	-9.54 ± 3.82	-1.5±4.39

Table 30: Zeta potential and subsequent stability behavior of the colloid. (Greenwood and Kendall, 1999; Hanaor, et al., 2012)

Zeta potential [mV]	Stability behavior of the colloid
From 0 to ±5,	Rapid coagulation or flocculation
From ±10 to ±30	Incipient instability
From ±30 to ±40	Moderate stability
From ±40 to ±60	Good stability
More than ±61	Excellent stability

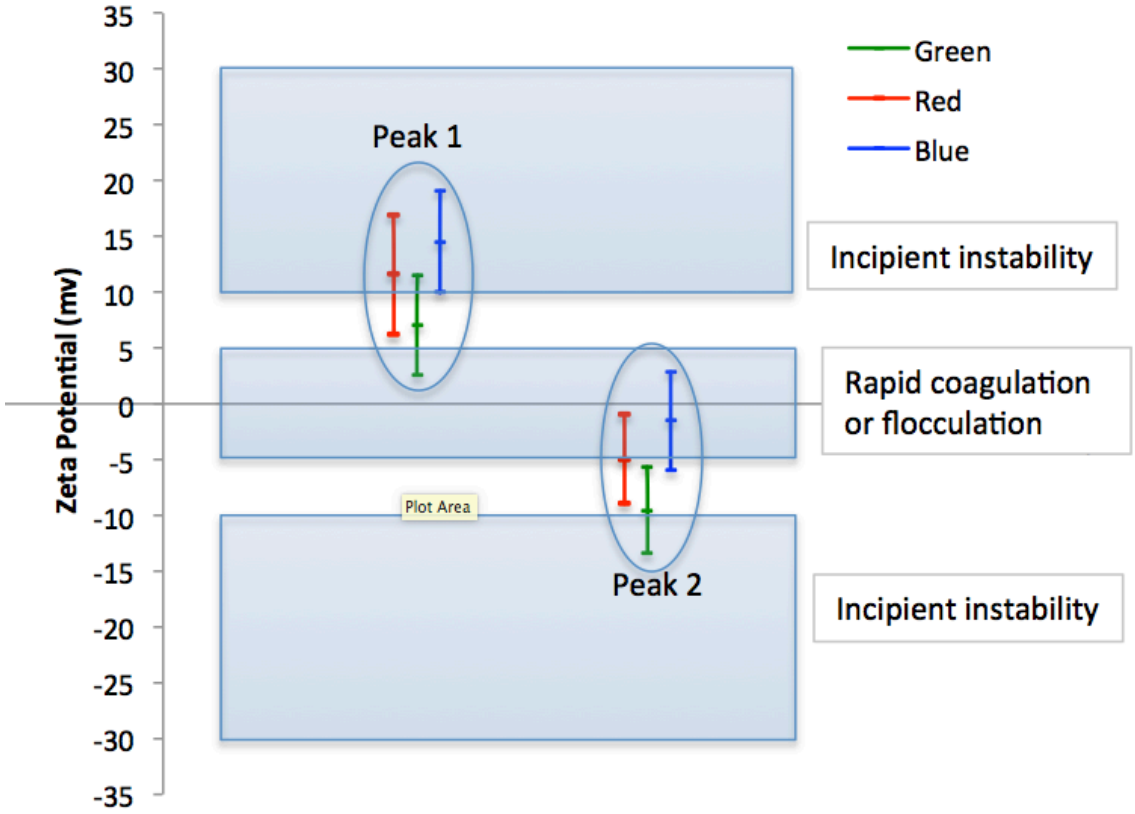

Figure 63: Data from Table 29 and Table 30 integrated

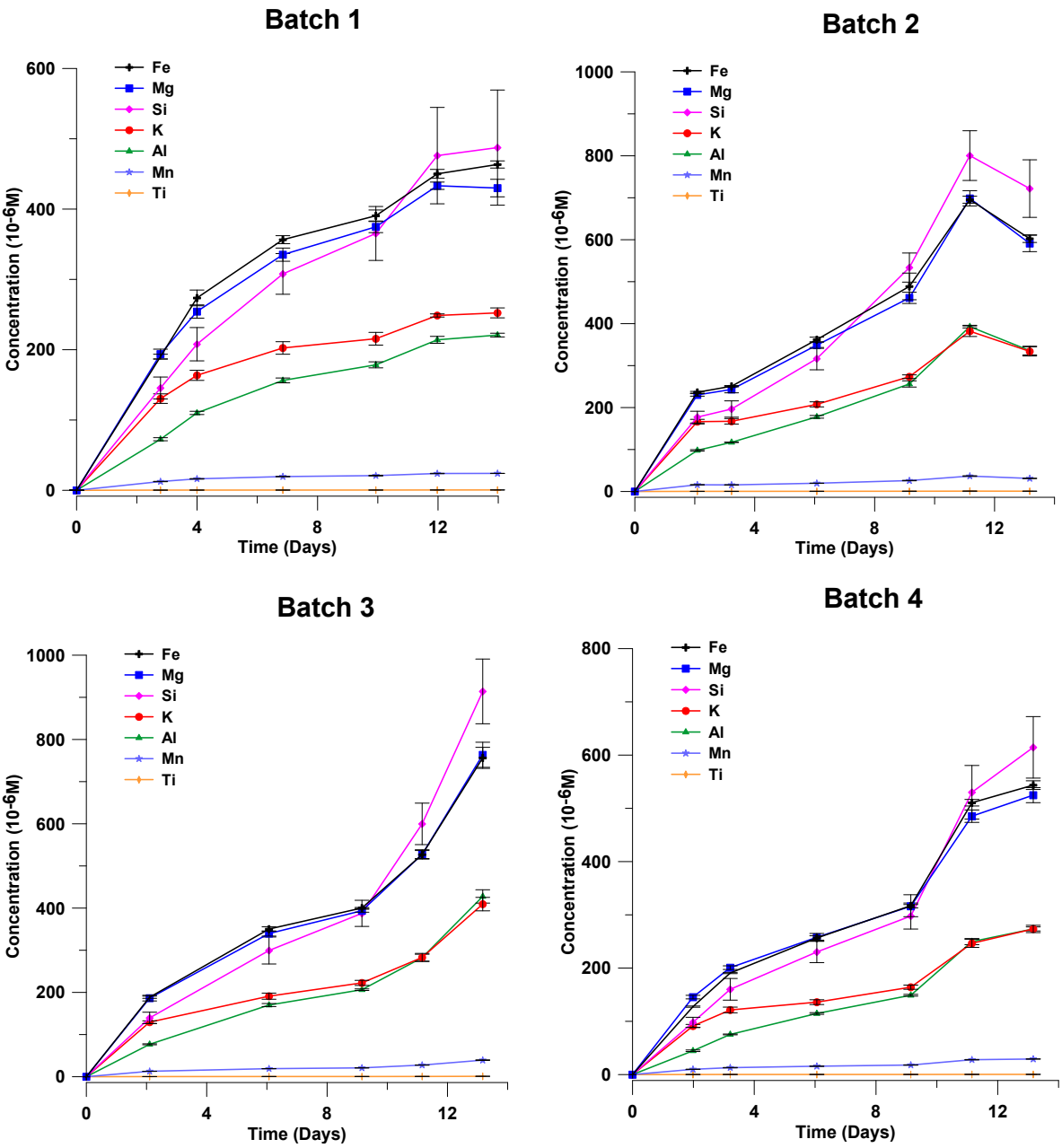

Figure 64: Compilation of cationic species concentrations against time with conductivity of solution plotted against time on a separate axis.

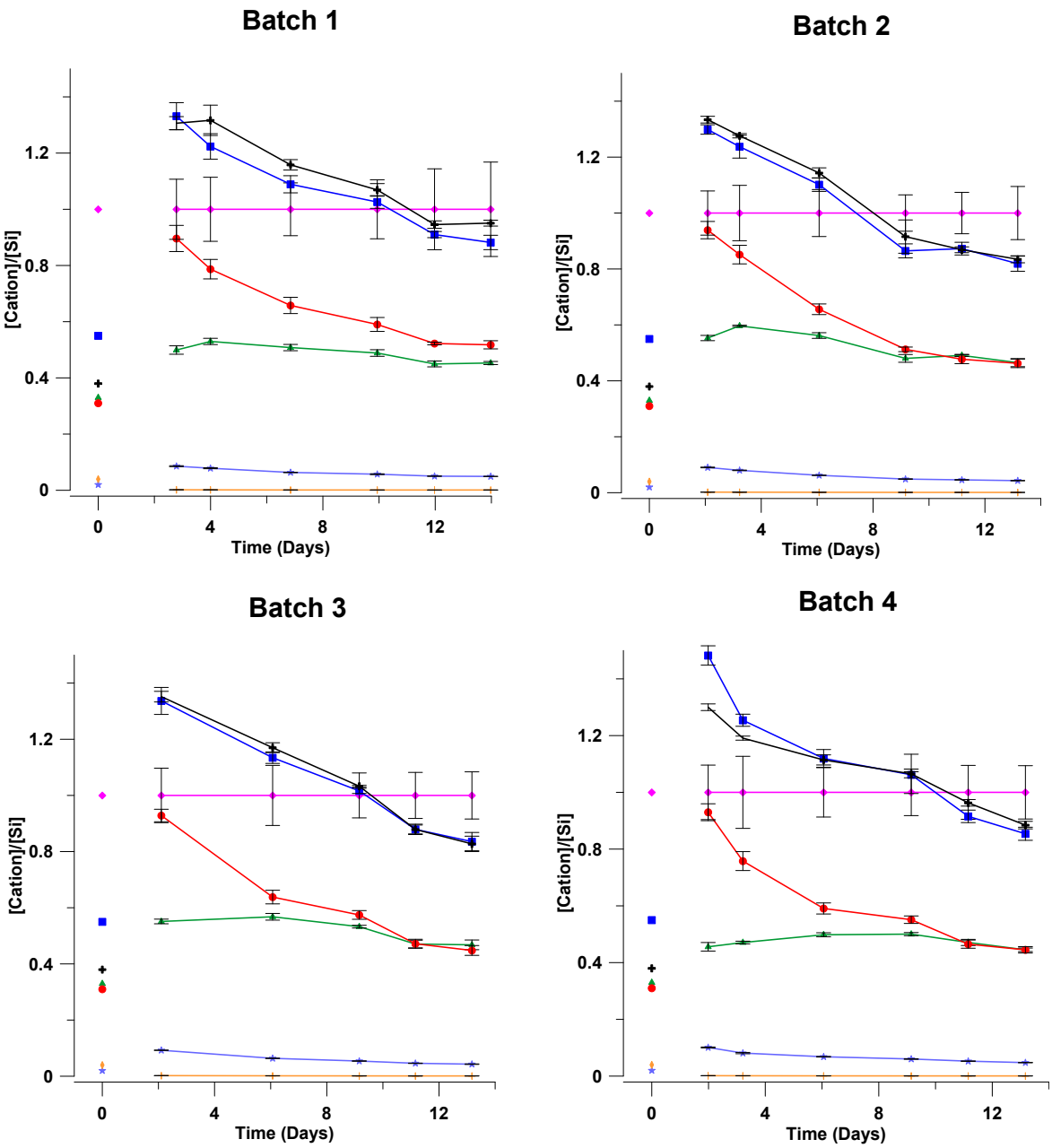

Figure 65: Cation concentrations (µM) normalized to the concentration of Si (µM) for ease of comparison.

Appendix 7

Table 31: Detail elemental release and biotite dissolution rate calculation including error values.

	Time (Days)	Mg Conc. (μM)	Mg Error (%)	Mg Error (μM)	Al Conc. (μM)	Al Error (%)	Al Error (μM)	Si Conc. (μM)	Si Error (%)	Si Error (μM)
	2.8	193.8	3.6	7.0	72.6	3.0	2.2	145.5	10.7	15.6
Concentration (μM)	14.0	429.9	2.9	12.5	220.8	1.2	2.6	487.5	16.8	81.9
	29.0	1246.7	1.9	23.2	613.6	5.0	30.5	1006.1	2.7	27.1

		Mg Release rate (μ mole/m2)	Mg Error (%)	Mg Error (μ mole/m2)	Al Release rate (μ mole/m2)	Al Error (%)	Al Error (μ mole/m2)	Si Release rate (μ mole/m2)	Si Error (%)	Si Error (μ mole/m2)
Elemental release	2.8	4.59	3.6	0.17	1.72	3.0	0.05	3.45	10.7	0.37
rate (μmol/m2)	14.0	10.19	2.9	0.30	5.23	1.2	0.06	11.55	16.8	1.94
	29.0	29.54	1.9	0.55	14.54	5.0	0.72	23.84	2.7	0.64

		Mg Dissolution rate (μ mole/m2/hr)	Mg Error (%)	Mg Error (μ mole/m2/hr)	Al Dissolution rate (μ mole/m2/hr)	Al Error (%)	Al Error (μ mole/m2/hr)	Si Dissolution rate (μ mole/m2/hr)	Si Error (%)	Si Error (μ mole/m2/hr)
Dissolution rate	2.8	0.069	3.6	0.002	0.026	3.0	0.001	0.052	10.7	0.006
(μ mole/m2/hr)	14.0	0.030	2.9	0.001	0.016	1.2	0.000	0.034	16.8	0.006
	29.0	0.042	1.9	0.001	0.021	5.0	0.001	0.034	2.7	0.001

		Mg Dissolution rate (10^{-8} mole/m2/hr)	Mg Error (%)	Mg Error (10^{-8} mole/m2/hr)	Al Dissolution rate (10^{-8} mole/m2/hr)	Al Error (%)	Al Error (10^{-8} mole/m2/hr)	Si Dissolution rate (10^{-8} mole/m2/hr)	Si Error (%)	Si Error (10^{-8} mole/m2/hr)
Dissolution rate	2.8	6.868	3.6	0.247	2.575	3.0	0.077	5.158	10.7	0.552
(10^{-8} mole/m2/hr)	14.0	3.038	2.9	0.088	1.560	1.2	0.019	3.444	16.8	0.579
	29.0	4.245	1.9	0.079	2.089	5.0	0.104	3.426	2.7	0.092

K Conc. (μM)	K Error (%)	K Error (μM)	Ti Conc. (μM)	Ti Error (%)	Ti Error (μM)	Mn Conc. (μM)	Mn Error (%)	Mn Error (μM)	Fe Conc. (μM)	Fe Error (%)	Fe Error (μM)
130.4	5.2	6.8	0.3	4.0	0.0	12.5	2.0	0.2	190.1	1.8	3.4
252.4	2.8	7.1	0.5	19.5	0.1	24.1	0.3	0.1	463.5	1.1	5.1
883.1	9.4	83.4							937.2	6.0	56.5

K Release rate (μ mole/m2)	K Error (%)	K Error (μ mole/m2)	Ti Release rate (μ mole/m2)	Ti Error (%)	Ti Error (μ mole/m2)	Mn Release rate (μ mole/m2)	Mn Error (%)	Mn Error (μ mole/m2)	Fe Release rate (μ mole/m2)	Fe Error (%)	Fe Error (μ mole/m2)
3.09	5.2	0.16	0.01	4.0	0.00	0.30	2.0	0.01	4.51	1.8	0.1
5.98	2.8	0.17	0.01	19.5	0.00	0.57	0.3	0.00	10.98	1.1	0.1
20.93	9.4	1.98							22.21	6.0	1.34

K Dissolution rate (μ mole/m2/hr)	K Error (%)	K Error (μ mole/m2/hr)	Ti Dissolution rate (μ mole/m2/hr)	Ti Error (%)	Ti Error (μ mole/m2/hr)	Mn Dissolution rate (μ mole/m2/hr)	Mn Error (%)	Mn Error (μ mole/m2/hr)	Fe Dissolution rate (μ mole/m2/hr)	Fe Error (%)	Fe Error (μ mole/m2/hr)
0.046	5.2	0.002	0.000	4.0	0.000	0.004	2.0	0.000	0.067	1.8	0.0
0.018	2.8	0.000	0.000	19.5	0.000	0.002	0.3	0.000	0.033	1.1	0.0
0.030	9.4	0.003							0.032	6.0	0.002

K Dissolution rate (10^{-8} mole/m2/hr)	K Error (%)	K Error (10^{-8} mole/m2/hr)	Ti Dissolution rate (10^{-8} mole/m2/hr)	Ti Error (%)	Ti Error (10^{-8} mole/m2/hr)	Mn Dissolution rate (10^{-8} mole/m2/hr)	Mn Error (%)	Mn Error (10^{-8} mole/m2/hr)	Fe Dissolution rate (10^{-8} mole/m2/hr)	Fe Error (%)	Fe Error (10^{-8} mole/m2/hr)
4.622	5.2	0.240	0.009	4.0	0.000	0.442	2.0	0.009	6.738	1.8	0.1
1.783	2.8	0.050	0.004	19.5	0.001	0.170	0.3	0.001	3.275	1.1	0.0
3.007	9.4	0.284							3.191	6.0	0.192

Appendix 8

Reference standards for EXAFS

1. Description of reference standards

Table 32: Description of reference standards. Going down the list, they are placed in the order of decreasing Fe-Fe interaction.

Reference Standards	Description
Goethite	Goethite is an iron bearing hydroxide mineral [α-FeO(OH)] and is found in soil and other low-temperature environments. Goethite is characterized by 2, 2 and 4 Fe neighbors at 3.01, 3.28 and 3.46 Å respectively (Szytula A., et al., 1968; Manceau and Combes, 1988; Manceau and Drits, 1993; Carvalho-e-Silva, et al., 2003). (Szytula A., et al., 1968; Manceau and Combes, 1988; Manceau and Drits, 1993; Carvalho-e-Silva, et al., 2003)(Szytula A., et al., 1968; Manceau and Combes, 1988; Manceau and Drits, 1993; Carvalho-e-Silva, et al., 2003)
2L ferrihydrite	Ferrihydrite is a widespread hydrous ferric oxyhydroxide mineral at the earth's surface. 2L (i.e. two line) refers to the two X-Ray diffraction lines (peaks) which imply low level of crystallinity as compared to the 6L ferrihydrite which is much more crystalline. It is a metastable nanomineral precursor to other minerals, e.g. hematite (Mindat.org, 2016)(Mindat.org, 2016)(Mindat.org, 2016). Sample was synthesized by hydrolyzing a ferric perchlorate solution up to pH=8. The precipitate was aged for three days in its mother solution at room temperature. Its Fe to Fe interactions are characterized by 2.1 and 5 Fe neighbors at radial distance of 3 and 3.43 Å respectively. This mineral is referred to as "Sample #A" in Manceau and Drits (1993) and additional details with regard to simulation of XRD curves can be referred in Drits, et al. (1993).
Fe-SRO	These Fe-SRO polymers were synthetically produced by hydrolyzing Iron (III) Chloride in the presence of SiO_4 ligands at pH=5 at a resulting Si to Fe proportion of 4. Entities in this standard are characterized by strong inhibition of Fe-Fe edge sharing which is a characteristic of a two-dimensional growth scheme. This reference standard is characterized by 2, 0.6 and 0.63 Fe neighbors at a distance of 3.02, 3.14 and 3.49 Å respectively. That gives a trimer due to the edge sharing interactions and a small composition of higher order Fe-Fe polymerization due to the corner interactions (Doelsch, et al., 2000).
Fe dimers	Iron dimers + PO_4 were synthetically produced by adding powder phosphoric acid into 1.5 M Iron(III) chloride solution. The solution was initially prepared from reagent grade $FeCl_3.6H_2O$ dissolved, in distilled water. Mix was adjusted to obtain P:Fe proportion of 0.5 at a hydrolysis ratio of R=1.5. This standard was selected because it consists of iron dimers (Fe-Fe edge sharing) +PO_4 and can represent Fe-Fe dimer structure regardless and irrelevance of the PO_4 content. This reference standard is characterized by 1 and 0.2 Fe neighbors at a distance of 3.1 and 4.1 Å respectively (Rose, et al., 1996).

2. Bond types and proportions

Table 33: Tabular summary of bond types and proportions for reference standards

Reference Standards	Edge	Double Corner	Single Corner
Goethite	4	4	0
2L ferrihydrite	2.1	5	0
Fe-SRO	2.6	0.6	0
Fe dimers	1	0	0.2

3. EXAFS of the reference standards

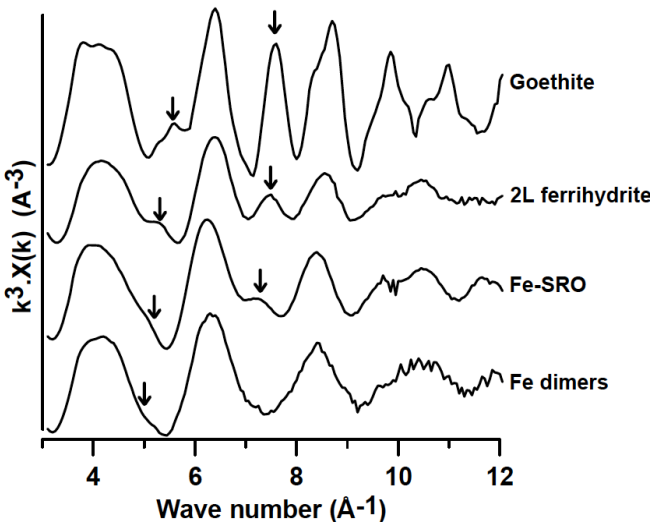

Figure 66: Reference standards in real space at k weight of 3. Spectra represent reference standards containing varying degree of Fe-Fe interactions.

Appendix 9

Additional data for EXAFS analysis

1. Linear combination fitting (LCF)

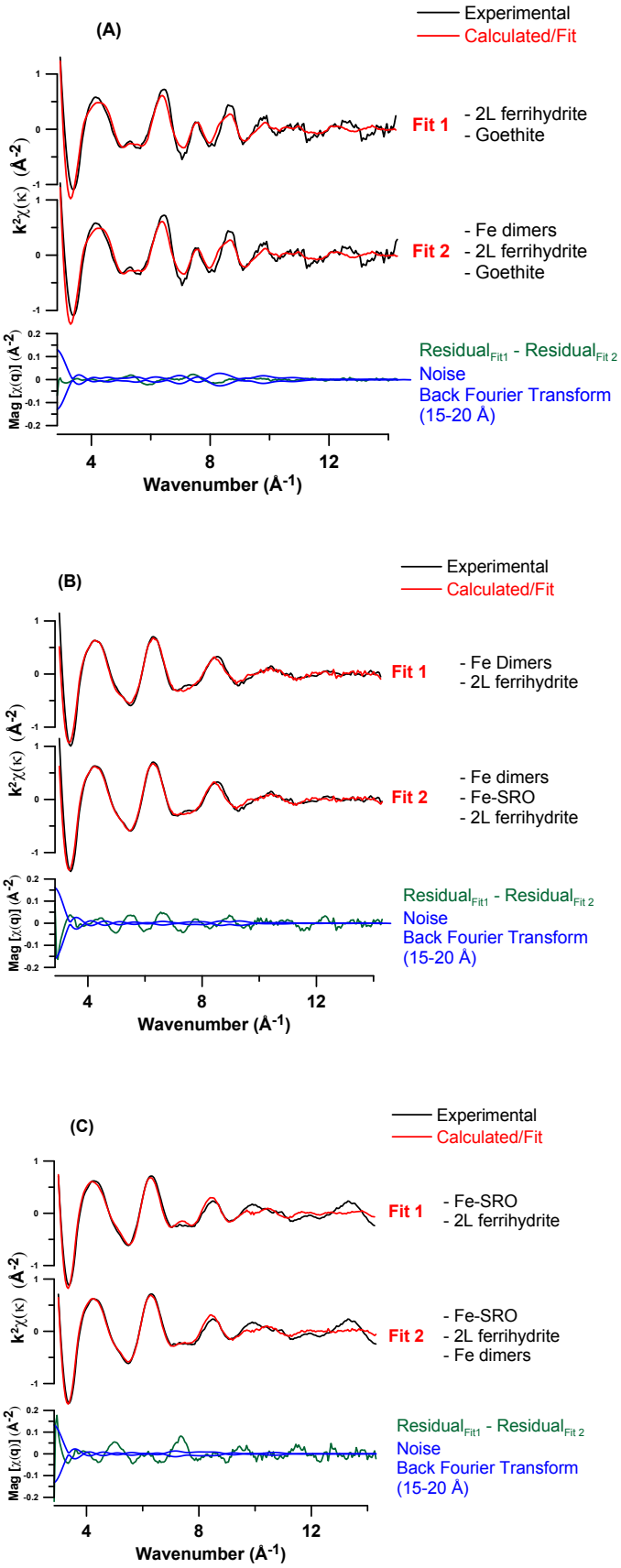

Figure 67: Linear Combination Fits of sample at (A) "pH=4.2 ", (B) "pH=5 " and (C) "pH=7 ". Noise data is depicted by two curves (in blue) representing an envelope of the noise signal.

2. Shell by shell fitting (SSF)

No C_ pH=4.2

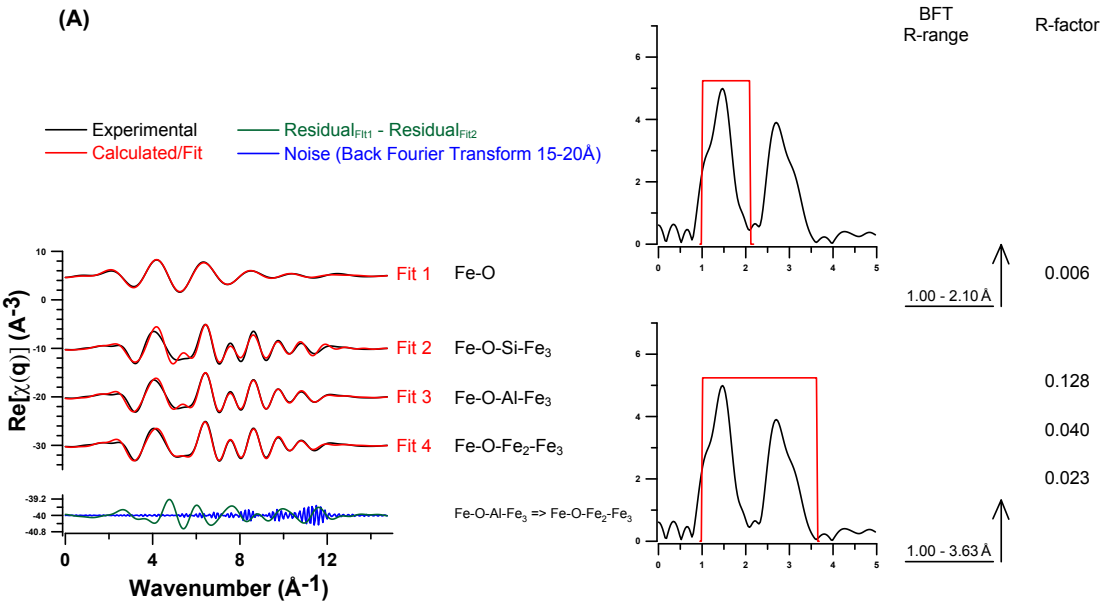

No C_ pH=5

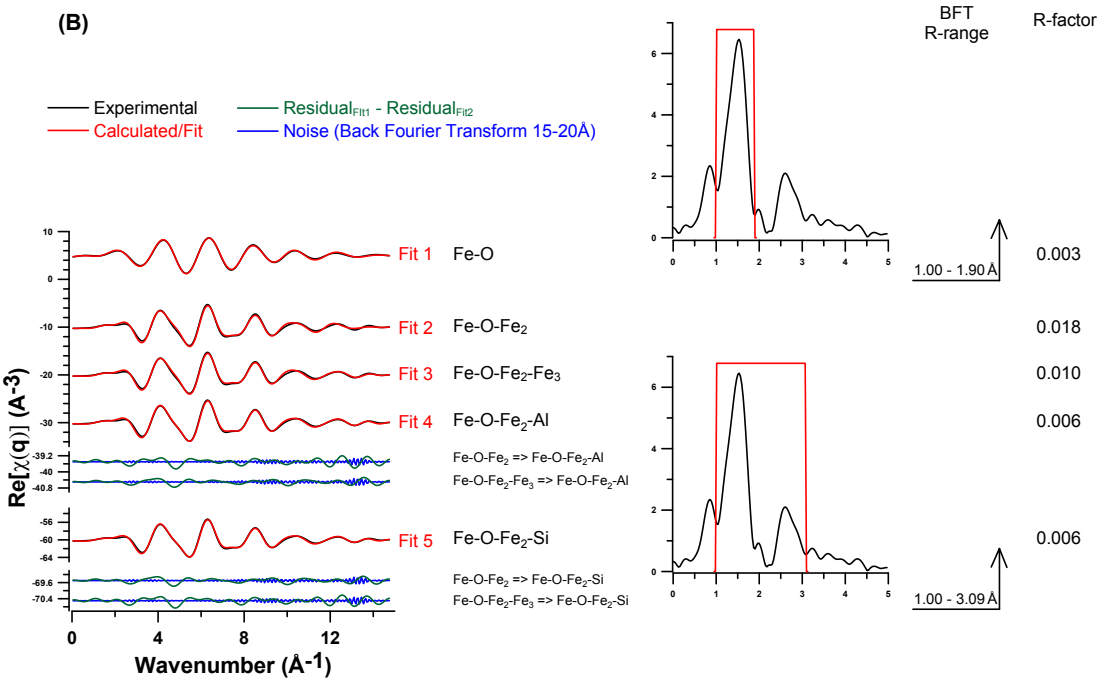

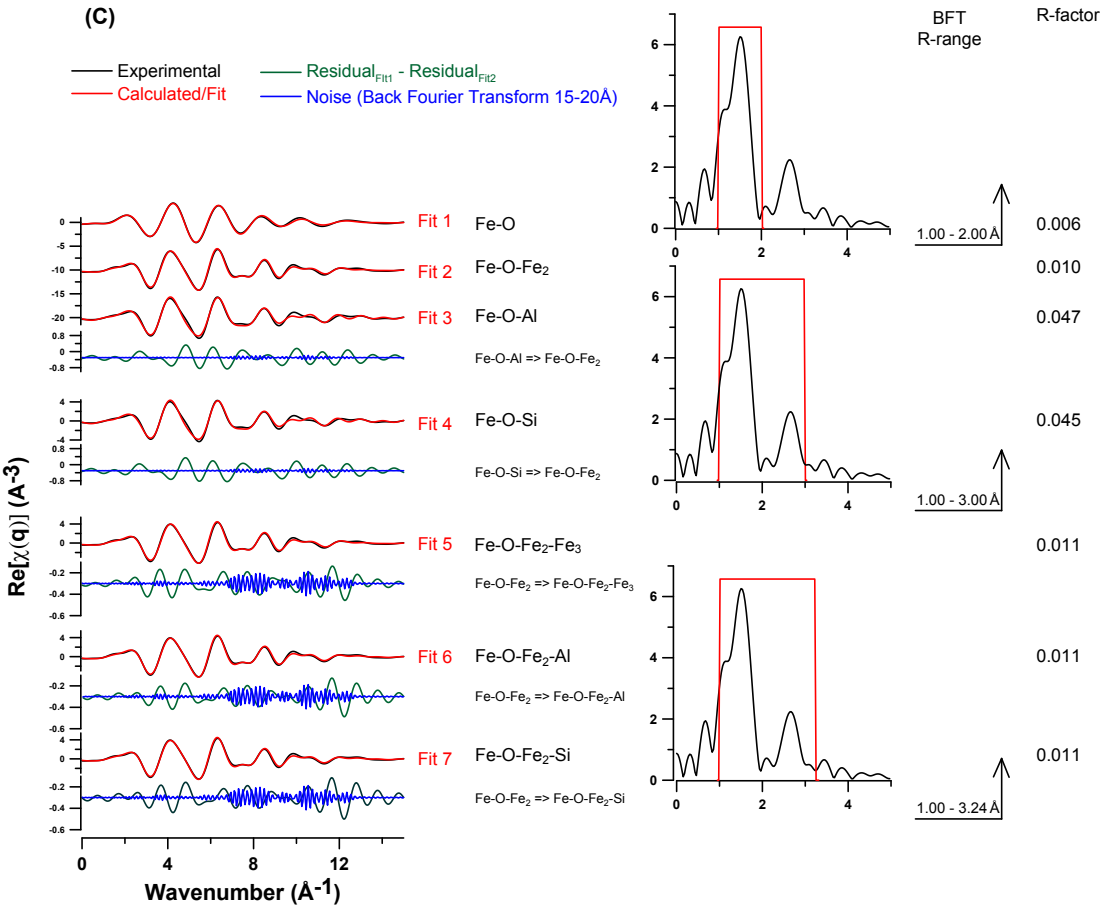

Plots for noise comparison:
For radial distances shorter than 3Å, 0.75 inches were allocated for 2 inches.
For radial distances longer than 3Å, 0.5 inches were allocated for 1 inch (that is equivalent to 2 units in 4 inches)..
That means the noise plots are magnified 5.33 times for distances after 3Å.
BFT R-range = Back fourier transfor Radial distance range

Figure 68: Shell-by-Shell fitting for sample (A) 'pH=4.2', (b) 'pH=5' and (C) 'pH=7' in the order of increasing radial distance from top to bottom. Scale for "Fit improvement vs. noise" comparisons is enlarged 5.33 times for radial distance fits larger than 3Å. BFT R-range = Back Fourier Transform Radial distance range.

Appendix 10

Table 34 details, 1st the best 2 standards fits then 3rd standards fits. Table is to aid in understanding the progression of the linear combination fitting.

Table 34: Detail LCF data for 2 and 3 standards fits

M:C ratio		Iron Citrate	Fe-C Colloids	Fe Dimers	Fe-SRO	2L Ferrihydrite	Sum	R-factor
0.01	2 Standards Fit	0.90	-	-	0.32	-	1.22	0.064
		0.75	-	0.43	-	-	1.19	0.062
		0.59	**0.47**	**-**	**-**	**-**	**1.07**	**0.055**
	3 Standards Fit	0.57	0.39	0.13	-	-	1.09	0.054
		0.58	**0.39**	**-**	**0.12**	**-**	**1.10**	**0.053**
0.1	2 Standards Fit	-	0.78	-	0.20	-	0.98	0.071
		-	0.68	0.30	-	-	0.98	0.071
		0.45	**0.60**	**-**	**-**	**-**	**1.05**	**0.612**
	3 Standards Fit	0.41	0.51	0.15	-	-	1.07	0.060
		0.41	**0.53**	**-**	**0.14**	**-**	**1.08**	**0.059**
1	2 Standards Fit	0.35	-	0.79	-	-	1.14	0.044
		-	0.61	-	0.39	-	1.00	0.043
		-	**0.41**	**0.60**	**-**	**-**	**1.01**	**0.040**
	3 Standards Fit	**0.27**	**0.45**	**-**	**0.35**	**-**	**1.06**	**0.038**
		0.21	0.32	0.53	-	-	1.06	0.037
10	2 Standards Fit	-	-	-	0.61	0.48	1.10	0.024
		0.38	-	-	0.70	-	1.08	0.022
		-	-	**0.66**	**-**	**0.39**	**1.05**	**0.020**
	3 Standards Fit	0.20	-	0.47	-	0.40	1.08	0.016
		0.30	**-**	**-**	**0.45**	**0.37**	**1.12**	**0.010**
No C	2 Standards Fit	-	-	-	0.51	0.53	1.04	0.019
		-	**-**	**0.54**	**-**	**0.46**	**1.00**	**0.017**
	3 Standards Fit	0.13	-	-	0.45	0.48	1.05	0.016
		-	**-**	**0.33**	**0.25**	**0.44**	**1.02**	**0.015**

Appendix 11

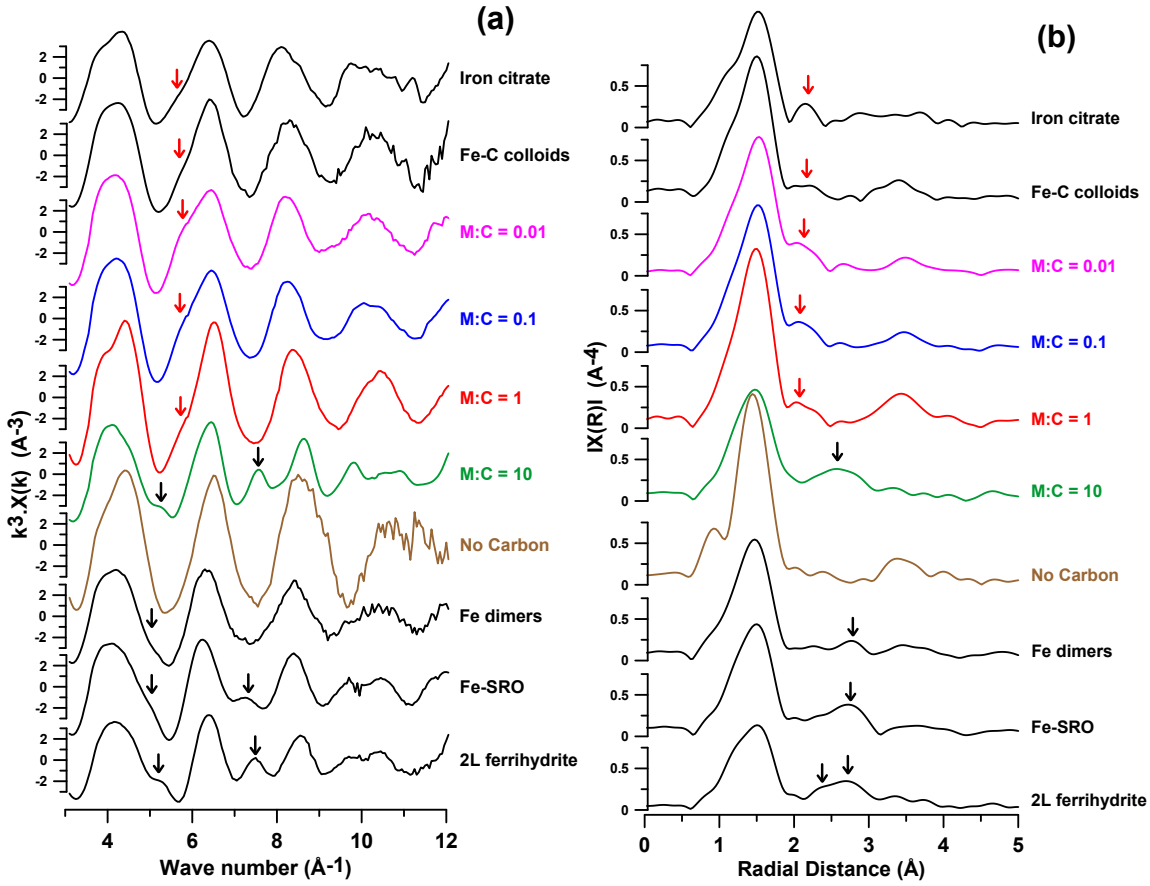

Figure 69: pH 5 series k window of 1.8 to 12.15 A^{-1}. Black and red arrows on k-space spectra indicate parts of the oscillations specifically contributed from Fe-Fe and Fe-C interactions respectively. Same black and red arrows, in R-space, indicate radial distances corresponding to Fe-Fe and Fe-C interactions respectively.

Appendix 12

AFM experiments: Preliminary dissolution and precipitation tests on biotite sheets

A minor section of the PhD work was dedicated to studying surface alteration of biotite sheets, and/or simultaneous reprecipitation of new phases. The AFM images in this study demonstrated slow natural weathering of minerals. These flat sheets were weathered to also give the starting materials (cationic species) for new mineral precipitates and also to act as support/stage for their nucleation and growth.

Surface alteration begins at structural discontinuities (edges, corners, etc.) where it is easy to dislocate structural components of the mineral. Surface dissolution progresses by preferentially and continuously attacking low energy sites thus resulting into pits. Like all precipitates, nCOMx often preferentially

form on mineral surfaces. And the pits will serve as a preferred precipitation sites (reduced formation energy) for these nano scale clusters during nucleation and growth.

Atomic Force Microscope (AFM)

Atomic Force Microscope (AFM) is a high-resolution type of scanning probe microscope, with demonstrated resolution on the order of fractions of a nanometer. The AFM consists of a cantilever with a sharp tip (probe) at its end that is used to scan the specimen surface. The cantilever is typically silicon or silicon nitride with a tip radius of curvature on the order of nanometers. When the tip is brought into proximity of a sample surface, forces between the tip and the sample lead to a deflection of the cantilever according to Hooke's law. Depending on the situation, forces that are measured in AFM include mechanical contact force, van der Waals forces, capillary forces, chemical bonding, electrostatic forces, magnetic forces, Casimir forces, solvation forces, etc (Bennig, 1988; Wikipedia, 2017).

AFM scans were performed with Innova Atomic Force Microscope from Bruker Corporation. Scans were done on Tapping Mode at a rate of 0.8 Hz on an area of 2 μm x 2 μm. HQ-NSC15/AlBS tapping mode tip/cantilever combination was used with tip height and radius of 15 μm and < 8nm respectively.

What is phase image?

According to Haugstad (2012) phase image is best defined as:

"The phase" is the time shift between the sinusoidal driving signal that vibrates the cantilever and the approximately sinusoidal motion of the tip as it oscillates near and far from the sample surface. This phase shift provides material contrast that may derive from different portions of each approach-retract cycle, whether the tip is sensing attractive forces far from contact (say due to a charged surface), or pushing into the surface, or breaking away, etc."

This image therefore utilizes the atomic force interaction between the tip and the material being scanned that is central to this technique as best described in the name AFM. We thus obtain information on weather or not there is variation detected in various mechanical/physical properties along the surface. Such changes include variations in material, hardness, elasticity, adhesion, friction, etc. properties.

Objective

Objective for this stage was to look for newly forming distinct surface alteration effects on the biotite surface (e.g. small-scale depressions/etch pits to demonstrate weathering, and bumps/precipitates to demonstrate precipitation) (Murakami, et al., 2003; Aldushin, et al., 2006; Pachana, et al., 2012).

Method

The experiment used of 5mm X 5mm biotite sheets. Unlike ground samples, unground minerals (specifically biotite in this study) have much reduced surface area to volume ratio. Consequently, one experimental objective that could be

disregarded would be the need for rapid reactions.

Note: Experimental steps in this section are a close duplicate of steps in the previous sections (powder biotite experiments). Therefore, details and supporting information from literatures will only be briefly repeated here and in depth descriptions can be referred in chapter 2.

Surface alteration experiments

Following sets of experimental batches demonstrate the dissolution of the biotite surface during different durations of time. Super flat surfaces were required to precipitate secondary minerals. To that end natural Biotite sheets were utilized. Scans were done on sizes of 5mm X 5mm sheet for all cases described here after.

All figures in this section (Figure 70 to Figure 73) and their AFM scan components are arranged as follows:

- Top left = Tapping Amplitude
- Top right = Tapping Phase
- Bottom left = Forward Topographic Scan
- Bottom right = Cross-sections (of locations indicated in above three images)

Analysis of control groups

To determine the surface smoothness of the starting material, AFM scans were started with acid cleaned Biotite sheets. Results show surface roughness (change in y direction) not exceeding an average depth value of 0.15nm (i.e. ±0.075nm) (Figure 70). Results were consistent with scans at other locations on the same samples.

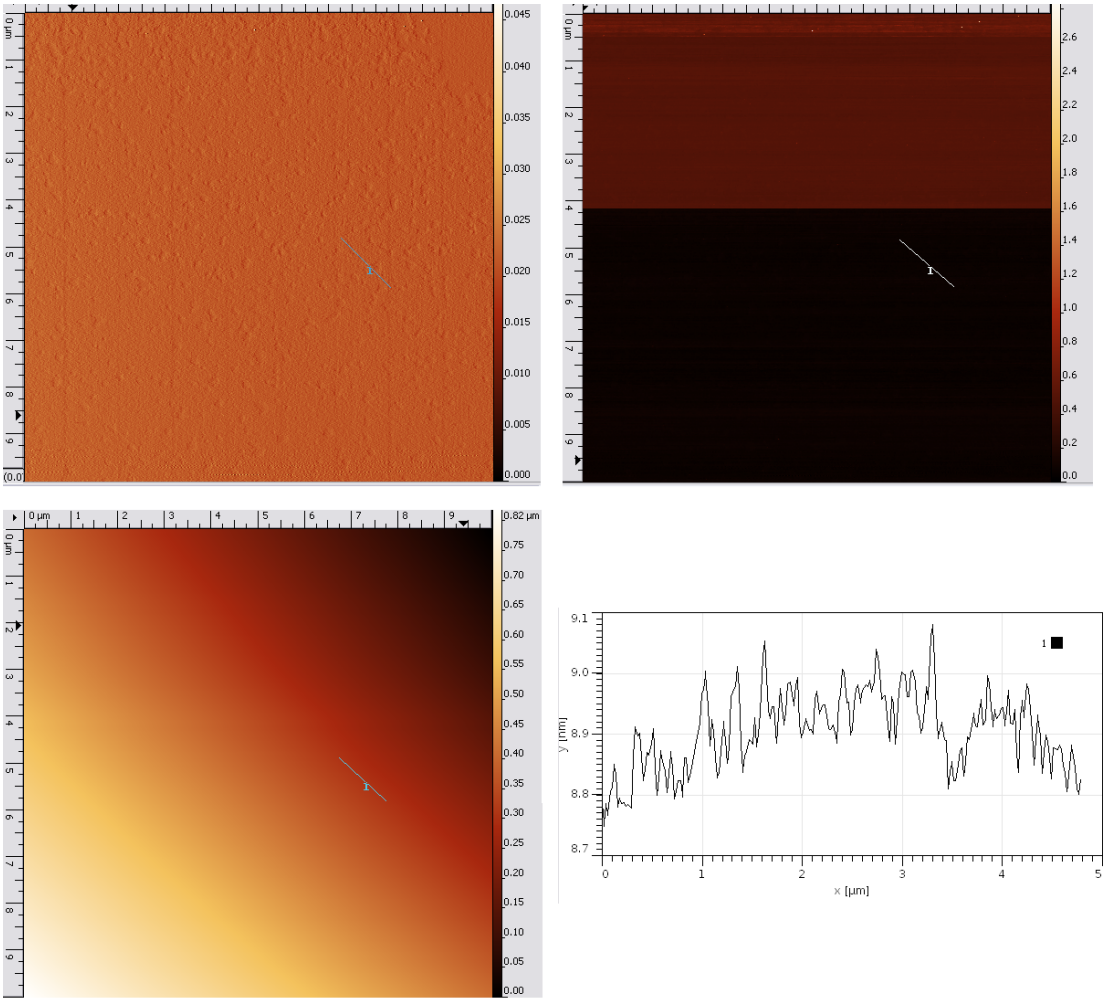

Figure 70: Acid cleaned raw biotite sheet. Note: Tapping phase image (top right), change in color is due to a computer glitch where change is irrelevant in this case.

1) Analysis with experimental groups

Following set of scans used sheets that were being weathered for increasing durations in time of 30, 45 and 308 days. At the end of exposure to acid solution, sheets were removed from solution and were put in a desiccator for air drying for a span of 24 hours.

i) Biotite Sheet: 30 days in Acid

Scans in Figure 71 show surface heterogeneities ranging in heights from few nanometers to hundreds of nanometers (section for latter height, not shown). In same figure scan was also able to show clear formation of 1nm and 3nm pits approximately corresponding to 1 and 3 TOT layers respectively. On the topographic image (bottom left) these pit formations are respectively observed as light brown (cross-section 3/green) and light black (cross-section 1/black) patches. This dissolution is accompanied by simultaneous or delayed precipitation of secondary minerals in the height range of few nano meters for un-aggregated cases. As can be seen from the "Phase image" the newly precipitated materials (owing to the lighter shade than the surrounding) suggest slightly stiffer (or more dense) material than the parent material (Haugstad, 2012). This effect demonstrates the immediate or delayed dissolution-

reprecipitation of secondary minerals at the mineral solution interface as demonstrated by Hellmann, et al. (2015).

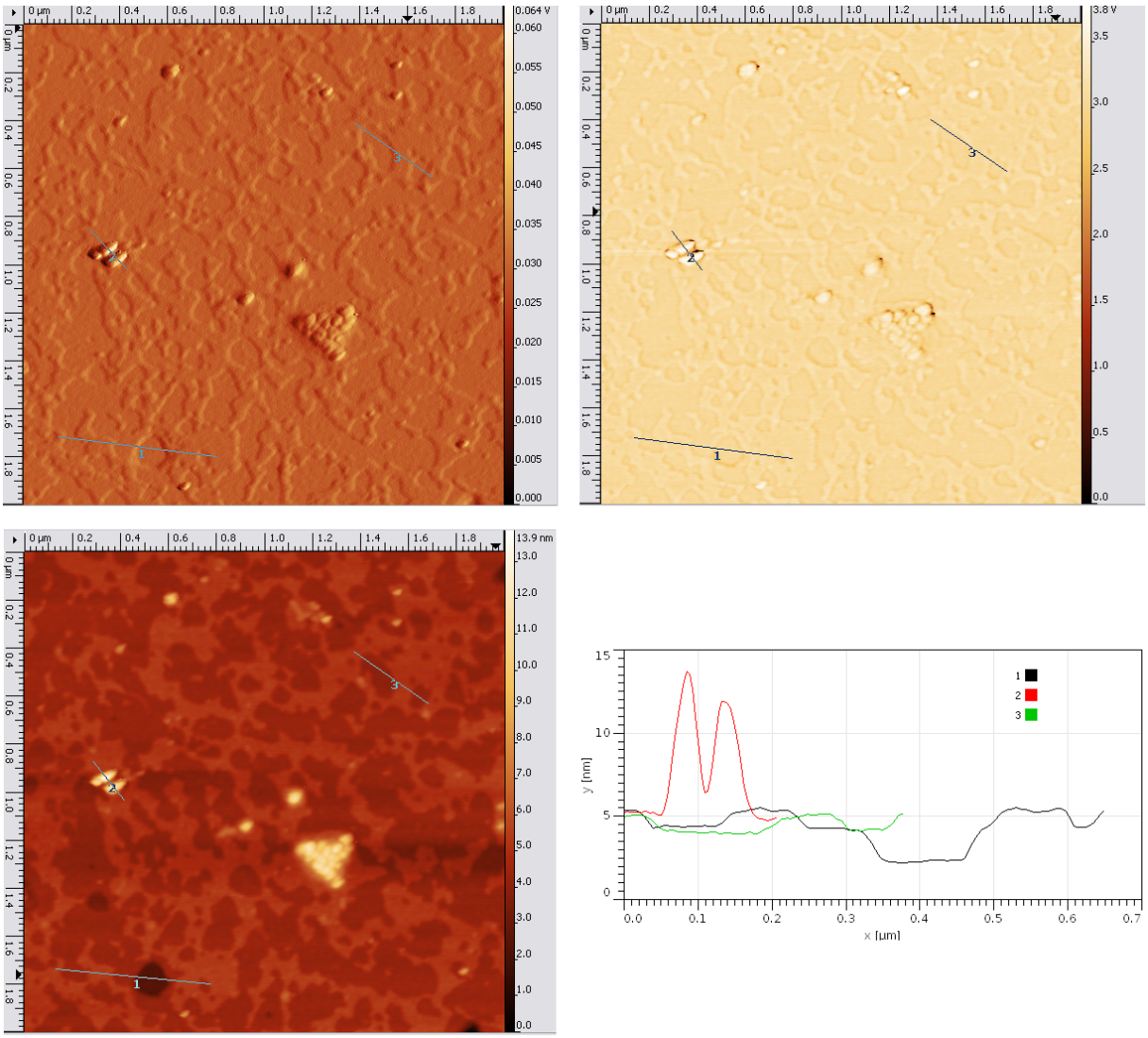

Figure 71: Biotite sheets 30 days in acid

ii) Biotite Sheet: 45 days in Acid: Before and after OM

Figure 72 below shows biotite sheets leached for 45 days. The tapping amplitude image shows minimal to none variation. That gives the data from tapping phase images greater credibility. Therefore, this means the changes observed in phase information all around the scanned surface were brought about partly by changes in material properties and partly by the variations in topography. The variations for the topographic data include the pits, re-precipitates (~9nm in height) and the really flat pristine surface. Locations of pit formation (cross-section 2/red) were not accompanied by change in phase data meaning the material with in the pits has similar material properties as the surrounding pristine surface. Locations of obvious new re-precipitates (cross-section 1/black) show minimal change in phase data except in occasional un-aggregated locations identified with brighter shades than the surrounding. These locations would represent new re-precipitates composed of material stiffer/denser than their surrounding.

For phase images to solely represent mechanical/physical properties topography and tapping amplitude data should show minimal to non variations. That is the case for the dark brown patches in the phase images (cross-section 3/green). These suggest a softer re-precipitate that seems to have blended in topographically with its surrounding.

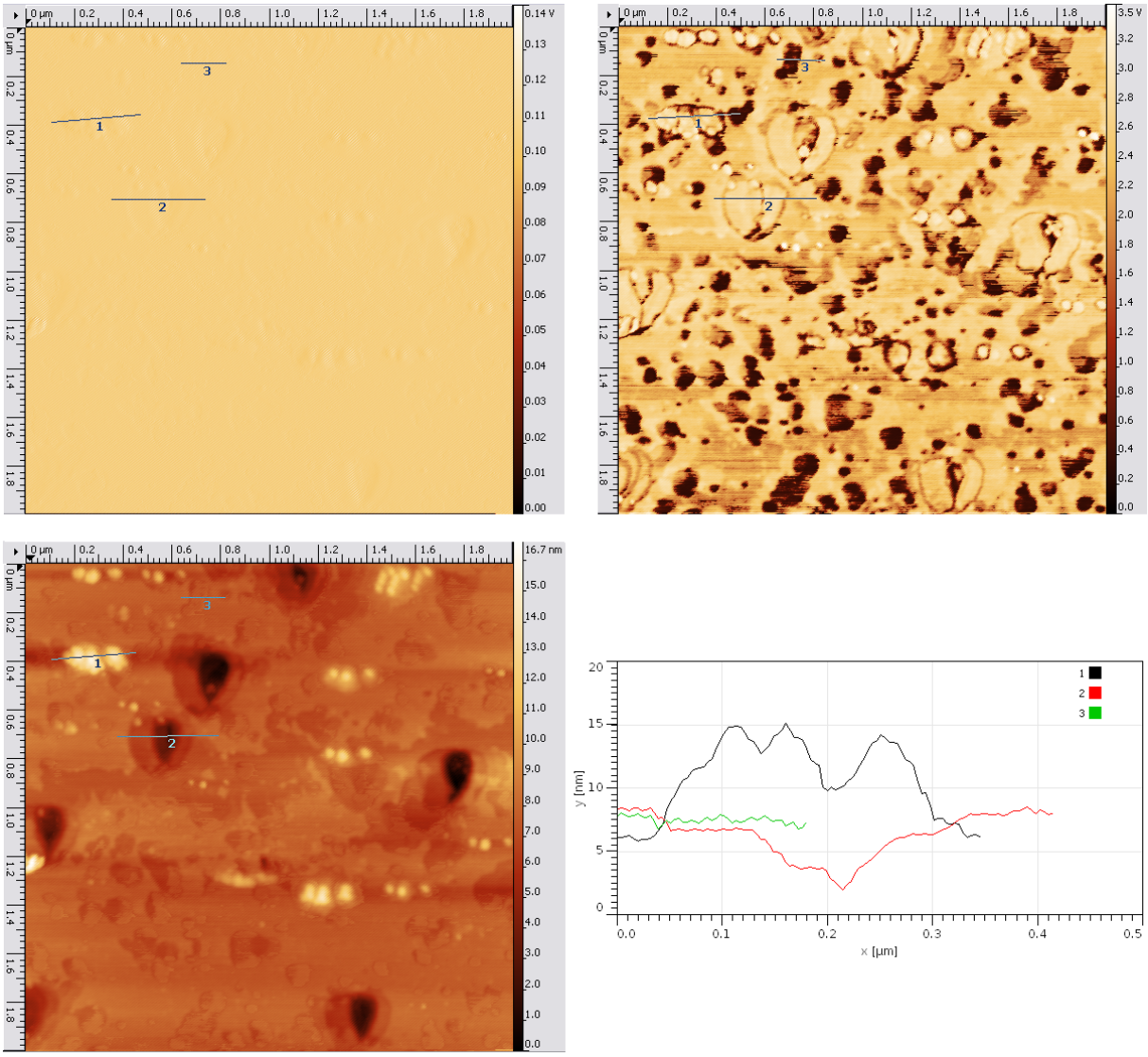

Figure 72: Biotite sheets 45 days in acid

iii) Biotite Sheet: 308 days in Acid

308 days was a prolonged exposure to acidic environment, therefore advanced weathering was expected. With the negligible variation in tapping amplitude, the three shades of colour in the phase image (bright white, light yellow, brown and dark brown) are variation contributed by either change in topography or material properties or both. The light yellow locations (see cross-sections 1/black and 2/red) in the phase image are correlated to pits that range in depth between 9 to18 nm. According to the colour these regions represent the stiffer pristine underlying biotite surface. The bright white data locations (cross-section 4/blue and left part of 3/green) in contrary are precipitates not exceeding 8 nm in height. Relatively speaking, these colours give the new precipitates a

stiffer/denser composition than the materials elsewhere in the scan, and ambiguously even stiffer than the pits. That is contrary to expectations for secondary phases relative to the pristine surface. The brown and dark brown shades represent surfaces in between locations of pits and precipitates. These locations are likely covered by new softer reprecipitates that are the result of 308 days of weathering. Or they represent an evenly leached out few nanometer deep softer liquid/solid interface/altered zone as discussed by most recent dissolution models (Frugier, et al., 2008; Geisler, et al., 2010; Hellmann, et al., 2015). For the latter case, processes may advance into the observed pits due to localized weathering (e.g. at locations requiring low energy for weathering such as edges, discontinuities, etc.) and locations of localized precipitation due to simultaneous dissolution re-precipitation processes (Hellmann, et al., 2015).

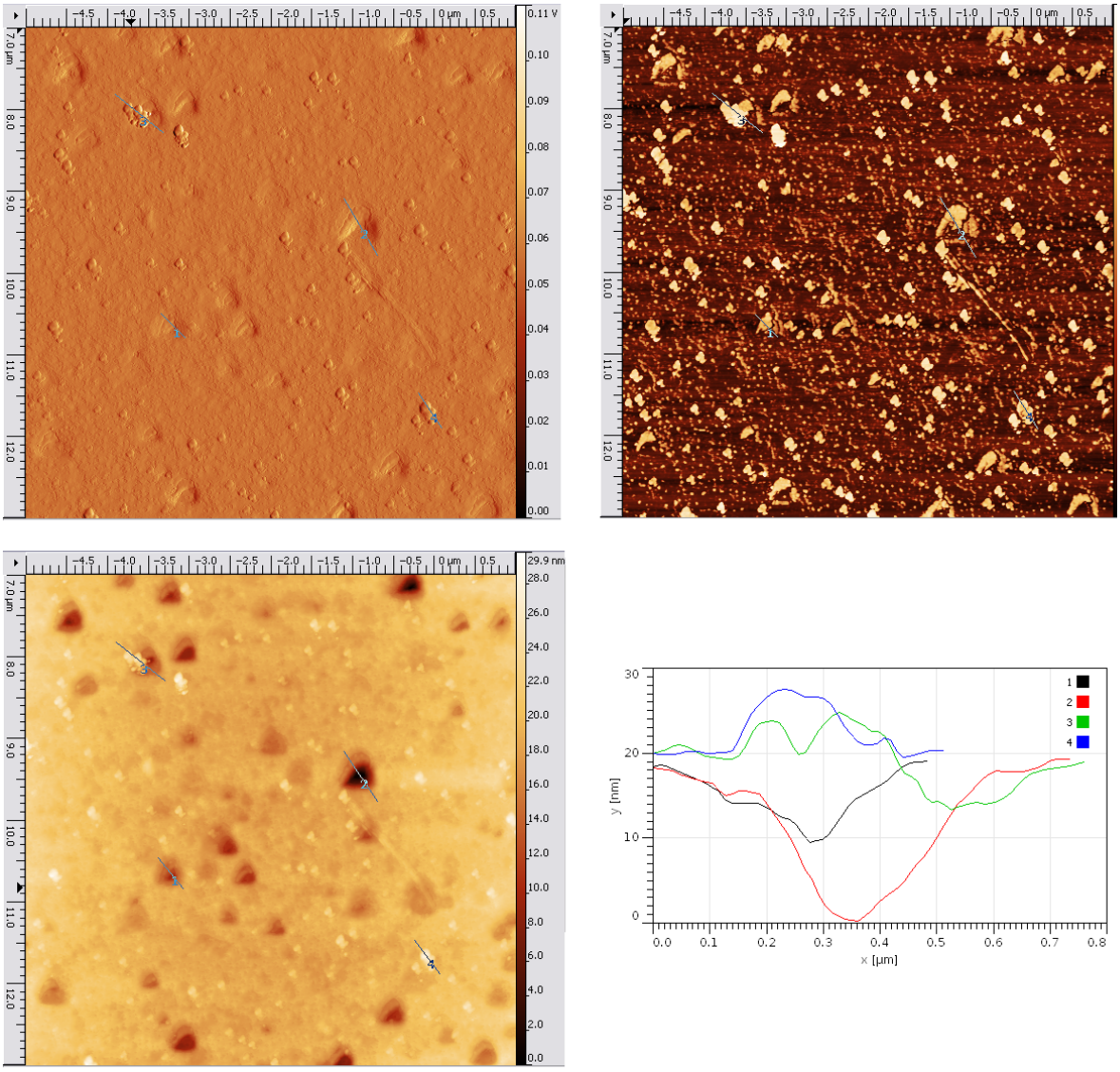

Figure 73: Biotite sheets 308 days in acid

2) Discussion

From this time dependent surface alteration experiments the major take away points were as detailed below.

- Exposure of biotite surface to acidic solution led to the weathering of the surface at localized low energy locations.
- Duration of exposure to acidity is proportional to extent of weathering, often prolonged exposure leading to formation of deeper pits (Figure 74).
- With prolonged weathering the reprecipitated phases will be more in abundance and less stiffer than the parent material with the exception of the samples in acid for 308 days (specifically with small sized precipitates). This prolonged experimental duration allowed more structural organization (such as aging) leading to what is observed as stiffer new materials than the parent material.

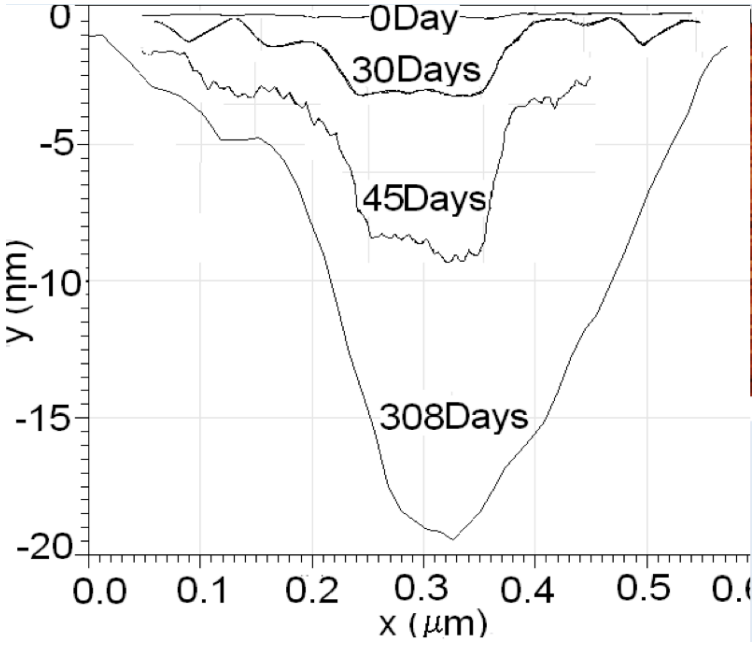

Figure 74: Superimposed cross-section views of variable duration of leaching. Note: location of pits in figure are not the same locations but pits at different location on different sheets.

3) Perspective

To make time based comparison of surface alteration it is best recommended to have pre and post weathering comparison to be made at the same location. More AFM experiments were designed that way but were not realized with in the time limit of this study. In achieving this objective, the 5mm X 5mm sheets were initially marked (laser ablated) before the dissolution commenced. Post dissolution re-precipitation effects would be analysed and conclusion can be drawn with 100% certainty.

Additionally, introducing an OC to the weathering process would give insight about possible ligand promoted dissolution and also coprecipitation of nCOMx at low energy sites. Finally, it should be noted that these sets of experiments were just preliminary/test experiments and the limits to this tool can be pushed much further. But that is left as a future work to be taken up by other individuals.

LIST OF REFERENCES

Acker, J. G. & Bricker, O. P. 1992. The influence of pH on biotite dissolution and alteration kinetics at low temperature. *Geochimica et Cosmochimica Acta,* 56**,** 3073-3092.

Akitt, J. W., Lester, L. & Kandelwal, F. H. J. 1972. *Journal of the Chemical Society* 26**,** 609-612.

Aldushin, K., Jordan, G. & Schmahl, W. W. 2006. Basal plane reactivity of phyllosilicates studied in situ by hydrothermal atomic force microscopy (HAFM). *Geochimica Et Cosmochimica Acta,* 70**,** 4380-4391.

Allison, F., Sherman, M. & Pinck, L. 1949. Maintenance of soil organic matter: I. Inorganic soil colloid as a factor in retention of carbon during formation of humus. *Soi Sci,* 68**,** 463–478.

Amelung, W., Brodowski, S., Sandhage-Hofmann, A. & Bol, R. 2008. Chapter 6 Combining Biomarker with Stable Isotope Analyses for Assessing the Transformation and Turnover of Soil Organic Matter. *In:* Donald, L. S. (ed.) *Advances in Agronomy.* Academic Press.

An, S., Mentler, A., Mayer, H. & Blum, W. E. H. 2010. Soil aggregation, aggregate stability, organic carbon and nitrogen in different soil aggregate fractions under forest and shrub vegetation on the Loess Plateau, China. *CATENA,* 81**,** 226-233.

Andersen, A., Reardon, P. N., Chacon, S. S., Qafoku, N. P., Washton, N. M. & Kleber, M. 2016. Protein–Mineral Interactions: Molecular Dynamics Simulations Capture Importance of Variations in Mineral Surface Composition and Structure. *Langmuir,* 32**,** 6194-6209.

Anderson, D. W. & Paul, E. A. 1984. Organo-Mineral Complexes and Their Study by Radiocarbon Dating1. *Soil Science Society of America Journal,* 48.

Anderson, D. W., Saggar, S., Bettany, J. R. & Stewart, J. W. B. 1981. Particle Size Fractions and Their Use in Studies of Soil Organic Matter: I. The Nature and Distribution of Forms of Carbon, Nitrogen, and Sulfur1. *Soil Science Society of America Journal,* 45.

Anderson, P. R. & Benjamin, M. M. 1985. EFFECTS OF SILICON ON THE CRYSTALLIZATION AND ADSORPTION PROPERTIES OF FERRIC OXIDES. *Environmental Science & Technology,* 19**,** 1048-1053.

Aradóttir, E. S. P., Sigfússon, B., Sonnenthal, E. L., Björnsson, G. & Jónsson, H. 2013. Dynamics of basaltic glass dissolution – Capturing microscopic effects in continuum scale models. *Geochimica et Cosmochimica Acta,* 121**,** 311-327.

Ares, J. & Ziechman, W. 1988. *Interactions of organic matter and aluminum ions in acid forest soil solutions: Metal complexation, flocculation, and precipitation*.

Arnarson, T. S. & Keil, R. G. 2000. Mechanisms of pore water organic matter adsorption to montmorillonite. *Marine Chemistry,* 71**,** 309-320.

Axelos, M., Tchoubar, D., Bottero, J. Y. & Fiessinger, F. 1985. Small-angle X-ray-

scattering of 2 aluminum hydroxide colloidal aggregates Al(OH)x, with x = 2.5 and 3 - Structure and power-law correlation of cluster aggregates. *Journal De Physique,* 46**,** 1587-1593.

Baldock, J. A. & Skjemstad, J. O. 2000. Role of the soil matrix and minerals in protecting natural organic materials against biological attack. *Organic Geochemistry,* 31**,** 697-710.

Basile-Doelsch, I., Amundson, R., Balesdent, J., Borschneck, D., Bottero, J.-Y., Colin, F., De Junet, A., Doelsch, E., Legros, S., Levard, C., Masion, A., Meunier, J.-D. & Rose, J. 2014. Andic soils: mineralogical effect onto organic matter dynamics, organic matter effects onto mineral dynamics, or both? *European Geosciences Union General Assembly.* Vienne (Autriche): Geophysical Research Abstracts.

Basile-Doelsch, I., Amundson, R., Stone, W. E. E., Borschneck, D., Bottero, J. Y., Moustier, S., Masin, F. & Colin, F. 2007. Mineral control of carbon pools in a volcanic soil horizon. *Geoderma,* 137**,** 477-489.

Basile-Doelsch, I., Amundson, R., Stone, W. E. E., Masiello, C. A., Bottero, J. Y., Colin, F., Masin, F., Borschneck, D. & Meunier, J. D. 2005. Mineralogical control of organic carbon dynamics in a volcanic ash soil on La Réunion. *European Journal of Soil Science,* 56**,** 689-703.

Basile-Doelsch, I., Balesdent, J. & Rose, J. 2015. Are Interactions between Organic Compounds and Nanoscale Weathering Minerals the Key Drivers of Carbon Storage in Soils? *Environmental Science & Technology,* 49**,** 3997-3998.

Basile-Doelsch, I., Brun, T., Borschneck, D., Masion, A., Marol, C. & Balesdent, J. 2009. Effect of landuse on organic matter stabilized in organomineral complexes: A study combining density fractionation, mineralogy and δ13C. *Geoderma,* 151**,** 77-86.

Batjes, N. H. 1996. Total carbon and nitrogen in the soils of the world. *European Journal of Soil Science,* 47**,** 151-163.

Belton, D. J., Deschaume, O. & Perry, C. C. 2012. FEBS Journal. *An overview of the fundamentals of the chemistry of silica with relevance to biosilicification and technological advances* 279**,** 1710-1720.

Bennett, P. C., Rogers, J. R., Choi, W. J. & Hiebert, F. K. 2001. Silicates, Silicate Weathering, and Microbial Ecology. *Geomicrobiology Journal,* 18**,** 3-19.

Bennig, G. K. 1988. Atomic force microscope and method for imaging surfaces with atomic resolution. Google Patents.

Berner, E. K. & Berner, R. A. 1996. *Global environment : water, air, and geochemical cycles*, Prentice Hall.

Berthonneau, J., Grauby, O., Ferrage, E., Vallet, J.-M., Bromblet, P., Dessandier, D., Chaudanson, D. & Baronnet, A. 2014. Impact of swelling clays on the spalling decay of building limestones: insights from X-ray diffraction profile modeling. *European Journal of Mineralogy*.

Bishop, A. N. & Philp, R. P. 1994. Potential for Amorphous Kerogen Formation via Adsorption of Organic Material at Mineral Surfaces. *Energy & Fuels,* 8**,**

1494-1497.

Blum, A. E. & Stillings, L. L. 1995. Feldspar dissolution kinetics. *Mineralogical Society of America,* 31**,** 291–351.

Bolan, N. S., Choppala, G., Kunhikrishnan, A., Park, J. & Naidu, R. 2013. Microbial Transformation of Trace Elements in Soils in Relation to Bioavailability and Remediation. *In:* Whitacre, D. M. (ed.) *Reviews of Environmental Contamination and Toxicology.* New York, NY: Springer New York.

Bolan, N. S., Kunhikrishnan, A., Choppala, G. K., Thangarajan, R. & Chung, J. W. 2012. Stabilization of carbon in composts and biochars in relation to carbon sequestration and soil fertility. *Science of The Total Environment,* 424**,** 264-270.

Bonan, G. B. H., M.D.; Parton W.J.; Wieder W.R. 2013. Evaluating litter decomposition in earth system models with long-term litterbag experiments: an example using the Community Land Model version 4 (CLM4). *Global Change Biology,* 19**,** 957–974.

Bonneville, S., Morgan, D. J., Schmalenberger, A., Bray, A., Brown, A., Banwart, S. A. & Benning, L. G. 2011. Tree-mycorrhiza symbiosis accelerate mineral weathering: Evidences from nanometer-scale elemental fluxes at the hypha–mineral interface. *Geochimica et Cosmochimica Acta,* 75**,** 6988-7005.

Bonneville, S., Smits, M. M., Brown, A., Harrington, J., Leake, J. R., Brydson, R. & Benning, L. G. 2009. Plant-driven fungal weathering: Early stages of mineral alteration at the nanometer scale. *Geology,* 37**,** 615-618.

Borer, P., Hug, S. J., Sulzberger, B., Kraemer, S. M. & Kretzschmar, R. 2009. ATR-FTIR spectroscopic study of the adsorption of desferrioxamine B and aerobactin to the surface of lepidocrocite (γ-FeOOH). *Geochimica et Cosmochimica Acta,* 73**,** 4661-4672.

Bottero, J. Y., Axelos, M. a. V., Tchoubar, D., Cases, J. M., Fripiat, J. J. & Fiessinger, F. 1987. Mechanism of formation of aluminum trihydroxide from keggin Al13 polymers. *Journal of Colloid Interface Science,* 117**,** 47-57.

Bottero, J. Y., Cases, J. M., Fiessinger, F. & Poirier, J. E. 1980. Studies of hydrolyzed aluminum chloride solutions. 1. Nature of aluminum species and composition of aqueous solutions. *The Journal of Physical Chemistry,* 84**,** 2933-2939.

Bottero, J. Y., Manceau, A., Villieras, F. & Tchoubar, D. 1994. Structure and Mechanisms of Formation of FeOOH(Cl)

Polymers. *American Chemical Society,* 10**,** 316–319.

Bottero, J. Y., Tchoubar, D., Cases, J. M. & Flessinger, F. 1982. Investigation of the hydrolysis of aqueous solutions of aluminum chloride. 2. Nature and structure by small-angle x-ray scattering. *Journal of Physical Chemistry,* 86**,** 3667-3673.

Boudot, J. P., Brahim, A. B. H., Steiman, R. & Seiglemurandi, F. 1989. Biodegradation of syn- thetic organo-metallic complexes of iron and aluminum with selected metal to carbon ratios. *Soil Biol. Biochem***,** 961–

966.

Bradley, S. M., Kydd, R. A. & Howe, R. F. 1993. The Structure of Al Gels Formed through the Base Hydrolysis of Al3+ Aqueous Solutions. *Journal of Colloid and Interface Science,* 159**,** 405-412.

Brantley, S. L. 2008. Kinetics of Mineral Dissolution. *In:* Brantley, S. L., Kubicki, J. D. & White, A. F. (eds.) *Kinetics of Water-Rock Interaction.* Springer New York.

Bray, A. W., Oelkers, E. H., Bonneville, S., Wolff-Boenisch, D., Potts, N. J., Fones, G. & Benning, L. G. 2015. The effect of pH, grain size, and organic ligands on biotite weathering rates. *Geochimica et Cosmochimica Acta,* 164**,** 127-145.

Brinker, C. J. & Scherer, G. W. 1990. Sol-gel science: the physics and chemistry of sol-gel processing. *Academic Press: San Diego***,** 908.

Brinkman, R. 1970. Ferrolysis, a hydromorphic soil forming process. *Geoderma,* 3**,** 199-206.

Broadley, K. J. 2010. The vascular effects of trace amines and amphetamines. *Pharmacology & Therapeutics,* 125**,** 363-375.

Brunauer, S., Emmett, P. H. & Teller, E. 1938. Adsorption of gases in multimolecular layers. *Journal of the American Chemical Society* 60**,** 309–319.

Bruun, T. B., Elberling, B. & Christensen, B. T. 2010. Lability of soil organic carbon in tropical soils with different clay minerals. *Soil Biology and Biochemistry,* 42**,** 888-895.

Buffle, J. & Van Leeuwen, H. P. 1992. Environmental particles.

Buffle, J. & Van Leeuwen, H. P. 1993. Sampling and Characterization of Environmental Particles. *Lewis Publishers: Chelsea,* **,** 554.

Burke, I., Yonker, C., Parton, W., Cole, C., Flach, K. & Schimel, D. 1989. Texture, climate and cultivation effects on soil organic matter content in U.S. grassland soils. *Soil Science Society of America Journal,* 53**,** 800–805.

Byrne, R. H., Luo, Y. R. & Young, R. W. 2000. Iron hydrolysis and solubility revisited: observations and comments on iron hydrolysis characterizations. *Marine Chemistry,* 70**,** 23-35.

Cabaniss, S. E. 1992. Synchronous Fluorescence Spectra of Metal-Fulvic Acid Complexes. *Environmental Science & Technology,* 26**,** 1133-1139.

Calabi-Floody, M., Bendall, J. S., Jara, A. A., Welland, M. E., Theng, B. K. G., Rumpel, C. & Mora, M. D. L. L. 2011. Nanoclays from an Andisol: Extraction, properties and carbon stabilization. *Geoderma,* 161**,** 159-167.

Calabi-Floody, M., Rumpel, C. & De La Luz Mora, M. Stability of soil organic matter in particle size fractions in top and subsoil of Chilean Andisols. Proceedings of the 20th World Congress of Soil Science (http://www.20wcss.org), 2014 Jeju, South Korea.

Cao, Y., Wei, X., Cai, P., Huang, Q., Rong, X. & Liang, W. 2011. Preferential adsorption of extracellular polymeric substances from bacteria on clay

minerals and iron oxide. *Colloids and Surfaces B: Biointerfaces,* 83**,** 122-127.

Cappelli, C., Van Driessche, A. E. S., Cama, J. & Huertas, F. J. 2013. In Situ Observation of Biotite Dissolution at pH 1 Using Advanced Optical Microscopy. *Crystal Growth & Design,* 13**,** 2880-2886.

Carvalho-E-Silva, M. L., Ramos, A. Y., Tolentino, H. C. N., Enzweiler, J., Netto, S. M. & Do Carmo Martins Alves, M. 2003. Incorporation of Ni into natural goethite: An investigation by X-ray absorption spectroscopy. *American Mineralogist,* 88**,** 876-882.

Catroux, G. & Schnitzer, M. 1987. Chemical, Spectroscopic, and Biological Characteristics of the Organic Matter in Particle Size Fractions Separated from an Aquoll1. *Soil Science Society of America Journal,* 51.

Chaurand, P. 2006. Contribution of the crystal chemistry and speciation of chromium and vanadium in modeling the alteration of artificial aggregates (by-products of steel)/Modélisation geochimique du comportement a la lixiviation des laitiers LAC.

Chen, L., Smith, P. & Yang, Y. 2015. How has soil carbon stock changed over recent decades? *Global Change Biology,* 21**,** 3197–3199.

Cheng, S., Bryant, R., Doerr, S., Rhodri, W. P. & Wright, C. 2008. Application of atomic force microscopy to the study of natural and model soil particles. *Journal of Microscopy,* 231**,** 384-94.

Chenu, C. & Plante, A. F. 2006. Clay-sized organo-mineral complexes in a cultivation chronosequence: revisiting the concept of the 'primary organo-mineral complex'

Complexes organo-minéraux < 2µm au sein d'une chronoséquence de mise en culture de sols: une réévaluation du concept de "complexe organo-minéral primare". *European Journal of Soil Science,* 57**,** 596-607.

Chevallier, T., Woignier, T., Toucet, J. & Blanchart, E. 2010. Organic carbon stabilization in the fractal pore structure of Andosols. *Geoderma,* 159**,** 182-188.

Chorover, J. 2011. Chapter 10. Impact of Soil Physicochemical and Biological Reactions on Transport of Nutrients and Pollutants in the Critical Zone. *Handbook of Soil Sciences: Resource Management and Environmental Impacts, Second Edition.* Second ed.: CRC Press.

Chorover, J., Amistadi, M. K. & Chadwick, O. A. 2004. Surface charge evolution of mineral-organic complexes during pedogenesis in Hawaiian basalt. *Geochimica et Cosmochimica Acta,* 68**,** 4859-4876.

Christensen, A. N., Lehmann, M. S. & Wright, A. 1982. A Small Angle Neutron Scattering Investigation on Aluminium Hydroxide. 36a**,** 779-781.

Christensen, A. N., Lehmann, M. S. & Wright, A. 1983. Kinetics of rust formation. A small angle neutron scattering investigation on iron (III) hyroxydes. *Acta Chemica Scandinavica,* A37**,** 63-69.

Christensen, B. T. 1992. Physical Fractionation of Soil and Organic Matter in

Primary Particle Size and Density Separates. *In:* Stewart, B. A. (ed.) *Advances in Soil Science.* New York, NY: Springer New York.

Christensen, B. T. 2001. Physical fractionation of soil and structural and functional complexity in organic matter turnover. *European Journal of Soil Science,* 52**,** 345-353.

Churchman, G. J. 2010. Is the geological concept of clay minerals appropriate for soil science? A literature-based and philosophical analysis. *Physics and Chemistry of the Earth, Parts A/B/C,* 35**,** 927-940.

Cismasu, A. C., Michel, F. M., Tcaciuc, A. P., Tyliszczak, T. & Brown, J. G. E. 2011. Composition and structural aspects of naturally occurring ferrihydrite. *Comptes Rendus Geoscience,* 343**,** 210-218.

Clarke, E. G. C. & Moffat, A. C. 1986. *Clarke's Isolation and Identification of Drugs,* London, GB, The Pharmaceutical Press.

Cliff, G. & Lorimer, G. W. 1975. The quantitative analysis of thin specimens. *Journal of Microscopy,* 103**,** 203–207.

Colombo, C., Ricciardella, M., Di Cerce, A., Maiuro, L. & Violante, A. 2004. Effect of tannate, pH, sample preparation, ageing and temperature on the formation and nature of Al oxyhydroxides. *Clays and Clay Minerals,* 52**,** 721–733.

Combes, J. M., Manceau, A. & Calas, G. 1990. Formation of ferric oxides from aqueous solutions: a polyhedral approach by X-ray absorption spectroscopy. II. Hematite formation from ferric gels. *Geochimica et Cosmochimica Acta,* 54**,** 1083–1091.

Combes, J. M., Manceau, A., G, C. & Bottero, J. Y. 1989. Formation of ferric oxides from aqueous solutions: A polyhedral approach by X-ray absorption spectroscopy: I. Hydrolysis and formation of ferric gels. *Geochimica et Cosmochimica Acta,* 53**,** 583-594.

Cop21. Report of the Conference of the Parties on its twenty-first session, held in Paris from 30 November to 13 December 2015. Sustainable Innovation Forum 2015, 2015 Paris. United Nations.

Cornell, R. M. & Schneider, W. 1989. Formation of goethite from ferrihydrite at physiological pH under the influence of cysteine. *Polyhedron,* 8**,** 149-155.

Cornell, R. M. & Schwertmann, U. 1979. Influence of organic anions on the crystallization of ferrihydrite. *Clays and Clay Minerals,* 27**,** 402-410.

Da Costa, G. M., De Grave, E., Bowen, L. H., De Bakker, P. M. A. & Vandenberghe, R. E. 1995. Temperature dependence of the hyperfine parameters of maghemite and al-substituted maghemites. *Physics and Chemistry of Minerals,* 22**,** 178-185.

Da Costa, G. M., De Grave, E., Bowen, L. H., Vandenberghe, R. E. & De Bakker, P. M. A. 1994. The center shift in Moessbauer spectra of maghemite and aluminum maghemites. *Clays and Clay Minerals,* 42**,** 628-633.

Da Costa, G. M., De Grave, E. & Vandenberghe, R. E. 1998. Mössbauer studies of magnetite and Al-substituted maghemites. *Hyperfine Interactions,* 117**,**

207-243.

Dahlgren, R., Shoji, S. & Nanzyo, M. 1993. Chapter 5 Mineralogical Characteristics of Volcanic Ash Soils. *In:* Sadao Shoji, M. N. & Randy, D. (eds.) *Developments in Soil Science.* Elsevier.

Dahlgren, R. A., Saigusa, M. & Ugolini, F. C. 2004. The Nature, Properties and Management of Volcanic Soils. *Advances in Agronomy.* Academic Press.

Dai, Q., Zhao, Y., Dong, F., Wang, B. & Huang, Y. 2014. Interaction between bentonite and Bacillus litoralis strain SWU9. *Applied Clay Science,* 100**,** 88-94.

Dawson, R. M., Elliott, D. C., Elliott, W. H. & Jones, K. M. 1959. *Data for Biochemical Research,* Oxford, Clarendon Press.

De Junet, A., Basile-Doelsch, I., Borschneck, D., Masion, A., Legros, S., Marol, C., Balesdent, J., Templier, J. & Derenne, S. 2013. Characterisation of organic matter from organo-mineral complexes in an Andosol from Reunion Island. *Journal of Analytical and Applied Pyrolysis,* 99**,** 92-100.

De Windt, L., Van Der Lee, J. & Schmitt, J.-M. 2005. Modélisation en géochimie des eaux Concepts et applications en environnement. *Techniques de l'ingénieur Chimie des milieux complexes,* base documentaire : TIB529DUO.

Dignac, M.-F., Derrien, D., Barré, P., Barot, S., Cécillon, L., Chenu, C., Chevallier, T., Freschet, G. T., Garnier, P., Guenet, B., Hedde, M., Klumpp, K., Lashermes, G., Maron, P.-A., Nunan, N., Roumet, C. & Basile-Doelsch, I. 2017. Increasing soil carbon storage: mechanisms, effects of agricultural practices and proxies. A review. *Agronomy for Sustainable Development,* 37**,** 14.

Doelsch, E., Deroche, B. & Van De Kerchove, V. 2006. Impact of sewage sludge spreading on heavy metal speciation in tropical soils (Réunion, Indian Ocean). *Chemosphere,* 65**,** 286-293.

Doelsch, E., Masion, A., Rose, J., Stone, W. E. E., Bottero, J. Y. & Bertsch, P. M. 2003. Chemistry and structure of colloids obtained by hydrolysis of Fe(III) in the presence of SiO4 ligands. *Colloids and Surfaces A: Physicochemical and Engineering Aspects,* 217**,** 121-128.

Doelsch, E., Moussard, G. & Macary, H. S. 2008. Fractionation of tropical soilborne heavy metals—Comparison of two sequential extraction procedures. *Geoderma,* 143**,** 168-179.

Doelsch, E., Rose, J., Masion, A., Bottero, J. Y., Nahon, D. & Bertsch, P. M. 2000. Speciation and Crystal Chemistry of Iron(III) Chloride Hydrolyzed in the Presence of SiO4 Ligands. 1. An Fe K-Edge EXAFS Study. *Langmuir,* 16**,** 4726-4731.

Doelsch, E., Rose, J., Masion, A., Bottero, J. Y., Nahon, D. & Bertsch, P. M. 2002. Hydrolysis of Iron(II) Chloride under Anoxic Conditions and Influence of SiO4 Ligands. *Langmuir,* 18**,** 4292-4299.

Doelsch, E., Stone, W. E. E., Petit, S., Masion, A., Rose, J., Bottero, J.-Y. & Nahon, D. 2001. Speciation and Crystal Chemistry of Fe(III) Chloride Hydrolyzed in the Presence of SiO4 Ligands. 2. Characterization of Si−Fe Aggregates by

FTIR and 29Si Solid-State NMR. *Langmuir,* 17**,** 1399-1405.

Dousma, J. & Debruyn, P. 1976. Hydrolysis-Precipitation Studies of Iron Solutions .1. Model for Hydrolysis and Precipitation from Fe(iii) Nitrate Solutions. *Journal of Colloid and Interface Science,* 56**,** 527–539.

Drits, V. A., Sakharov, B. A. & Manceau, A. 1993. Structure of feroxyhite as determined by simulation of X-ray diffraction curves. *Clay Minerals,* 28**,** 209-222.

Duan, J. & Gregory, J. 2003. Coagulation by hydrolysing metal salts. *Advances in Colloid and Interface Science,* 100 475–502.

Dzombak, D. A. & Morel, F. M. M. 1990. *Surface Complexation Modeling: Hydrous Ferric Oxide*, Wiley.

Elderfield, H. & Hem, J. D. 1973. The development of crystalline structure in aluminium hydroxide polymorphs on ageing. *Mineralogical Magazine,* 39**,** 89-96.

Essington, M. E. 2004. *Soil and Water Chemistry: An Integrative Approach, Second Edition,* Boca Raton, CRC Press.

Eusterhues, K., Hädrich, A., Neidhardt, J., Küsel, K., Keller, T. F., Jandt, K. D. & Totsche, K. U. 2014a. Reduction of ferrihydrite with adsorbed and coprecipitated organic matter: microbial reduction by Geobacter bremensis vs. abiotic reduction by Na-dithionite. *Biogeosciences,* 11**,** 4953-4966.

Eusterhues, K., Neidhardt, J., Hädrich, A., Küsel, K. & Totsche, K. 2014b. Biodegradation of ferrihydrite-associated organic matter. *Biogeochemistry,* 119**,** 45-50.

Eusterhues, K., Rennert, T., Knicker, H., Kögel-Knabner, I., Totsche, K. U. & Schwertmann, U. 2011. Fractionation of Organic Matter Due to Reaction with Ferrihydrite: Coprecipitation versus Adsorption. *Environmental Science & Technology,* 45**,** 527-533.

Eusterhues, K., Rumpel, C., Kleber, M. & Kögel-Knabner, I. 2003. Stabilisation of soil organic matter by interactions with minerals as revealed by mineral dissolution and oxidative degradation. *Organic Geochemistry,* 34**,** 1591-1600.

Eusterhues, K., Rumpel, C. & Kögel-Knabner, I. 2005. Organo-mineral associations in sandy acid forest soils: importance of specific surface area, iron oxides and micropores. *European Journal of Soil Science,* 56**,** 753-763.

Eusterhues, K., Rumpel, C. & Kögel-Knabner, I. 2007. Composition and radiocarbon age of HF-resistant soil organic matter in a Podzol and a Cambisol. *Organic Geochemistry,* 38**,** 1356-1372.

Eusterhues, K., Wagner, F. E., Häusler, W., Hanzlik, M., Knicker, H., Totsche, K. U., Kögel-Knabner, I. & Schwertmann, U. 2008. Characterization of Ferrihydrite-Soil Organic Matter Coprecipitates by X-ray Diffraction and Mössbauer Spectroscopy. *Environmental Science & Technology,* 42**,** 7891-7897.

Evans, L. J. 1989. Chemistry of metal retention by soils. *Environmental Science & Technology,* 23**,** 1046-1056.

Faimon, J. 2003. Formation of Colloidal Silica and Alumina During Experimental Granodiorite Weathering. *Aquatic Geochemistry,* 9**,** 305-341.

Fang, L., Cao, Y., Huang, Q., Walker, S. L. & Cai, P. 2012. Reactions between bacterial exopolymers and goethite: A combined macroscopic and spectroscopic investigation. *Water Research,* 46**,** 5613-5620.

Fao 2005. The importance of soil organic matter: Key to drought-resistant soil and sustained food production. *In:* Bot, A. & Benites, J. (eds.) *FAO SOILS BULLETIN.* Rome.

Fao 2014. Agriculture, Forestry and Other Land Use Emissions by Sources and Removals by Sinks. Climate, Energy and Tenure Division: FAO.

Fazle Rabbi, S. M., Lockwood, P. V. & Daniel, H. 2010. How do microaggregates stabilize soil organic matter? *19th World Congress of Soil Science, Soil Solutions for a Changing World.* Brisbane, Australia: IUSS.

Fontes, M. P. F. 1992. Iron oxide-clay mineral association in brazilian oxisols: A magnetic separation study. *Clays & Clay Minerals,* 40**,** 175-179.

Frugier, P., Gin, S., Minet, Y., Chave, T., Bonin, B., Godon, N., Lartigue, J. E., Jollivet, P., Ayral, A., De Windt, L. & Santarini, G. 2008. SON68 nuclear glass dissolution kinetics: Current state of knowledge and basis of the new GRAAL model. *Journal of Nuclear Materials,* 380**,** 8-21.

Galeska, I., Hickey, T., Moussy, F., Kreutzer, D. & Papadimitrakopoulos, F. 2001. Characterization and biocompatibility studies of novel humic acids based films as membrane material for an implantable glucose sensor. *Biomacromolecules,* 2**,** 1249–1255.

Gaur, A. & Shrivastava, B. D. 2015. Speciation using X-ray absorption fine structure (XAFS). *Review Journal of Chemistry,* 5**,** 361-398.

Gautier, Q., Berninger, U.-N., Schott, J. & Jordan, G. 2015. Influence of organic ligands on magnesite growth: A hydrothermal atomic force microscopy study. *Geochimica et Cosmochimica Acta,* 155**,** 68-85.

Gebauer, D., Kellermeier, M., Gale, J. D., Bergstrom, L. & Colfen, H. 2014. Pre-nucleation clusters as solute precursors in crystallisation. *Chemical Society Reviews,* 43**,** 2348-2371.

Geisler, T., Janssen, A., Scheiter, D., Stephan, T., Berndt, J. & Putnis, A. 2010. Aqueous corrosion of borosilicate glass under acidic conditions: A new corrosion mechanism. *Journal of Non-Crystalline Solids,* 356**,** 1458-1465.

Gislason, S. R. & Oelkers, E. H. 2003. Mechanism, rates, and consequences of basaltic glass dissolution: II. An experimental study of the dissolution rates of basaltic glass as a function of pH and temperature. *Geochimica et Cosmochimica Acta,* 67**,** 3817-3832.

Goh, K. M. 2004. Carbon sequestration and stabilization in soils: implications for soil productivity and climate change. *Soil Science & Plant Nutrition,* 50**,** 467–476.

Goldich, S. S. 1938. A Study in Rock-Weathering. *The Journal of Geology,* 46**,** 17-58.

Gonzalez Garcia, F., Ruiz Abrio, M. T. & Gonzalez Rodriguez, M. 1991. Effects of dry grinding on two kaolins of different degrees of crystallinity. *Clay Minerals,* 26**,** 549-565.

Greenwood, R. & Kendall, K. 1999. Selection of Suitable Dispersants for Aqueous Suspensions of Zirconia and Titania Powders using Acoustophoresis. *Journal of the European Ceramic Society,* 19**,** 479-488.

Guggenberger, G. & Kaiser, K. 2003. Dissolved organic matter in soil: challenging the paradigm of sorptive preservation. *Geoderma,* 113**,** 293-310.

Hanaor, D., Michelazzi, M., Leonelli, C. & Sorrell, C. C. 2012. The effects of carboxylic acids on the aqueous dispersion and electrophoretic deposition of ZrO2. *Journal of the European Ceramic Society,* 32**,** 235-244.

Harrington, M. J., Masic, A., Holten-Andersen, N., Waite, J. H. & Fratzl, P. 2010. Iron-Clad Fibers: A Metal-Based Biological Strategy for Hard Flexible Coatings. *Science (New York, N.Y.),* 328**,** 216-220.

Haugstad, G. 2012. *Atomic Force Microscopy: Understanding Basic Modes and Advanced Applications*, Wiley.

Hedges, J. I., Eglinton, G., Hatcher, P. G., Kirchman, D. L., Arnosti, C., Derenne, S., Evershed, R. P., Kögel-Knabner, I., De Leeuw, J. W., Littke, R., Michaelis, W. & Rullkötter, J. 2000. The molecularly-uncharacterized component of nonliving organic matter in natural environments. *Organic Geochemistry,* 31**,** 945-958.

Hedges, J. I. & Keil, R. G. 1999. Organic geochemical perspectives on estuarine processes: sorption reactions and consequences. *Marine Chemistry,* 65**,** 55-65.

Hedges, J. I. & Oades, J. M. 1997. Comparative organic geochemistries of soils and marine sediments. *Organic Geochemistry,* 27**,** 319-361.

Heister, K., Höschen, C., Pronk, G. J., Mueller, C. W. & Kögel-Knabner, I. 2012. NanoSIMS as a tool for characterizing soil model compounds and organomineral associations in artificial soils. *Journal of Soils and Sediments,* 12**,** 35-47.

Hellmann, R., Cotte, S., Cadel, E., Malladi, S., Karlsson, L. S., Lozano-Perez, S., Cabié, M. & Seyeux, A. 2015. Nanometre-scale evidence for interfacial dissolution–reprecipitation control of silicate glass corrosion. *Nat Mater,* 14**,** 307-311.

Hellmann, R., Penisson, J.-M., Hervig, R. L., Thomassin, J.-H. & Abrioux, M.-F. 2003. An EFTEM/HRTEM high-resolution study of the near surface of labradorite feldspar altered at acid pH: evidence for interfacial dissolution-reprecipitation. *Physics and Chemistry of Minerals,* 30**,** 192-197.

Hellmann, R., Wirth, R., Daval, D., Barnes, J.-P., Penisson, J.-M., Tisserand, D., Epicier, T., Florin, B. & Hervig, R. L. 2012. Unifying natural and laboratory chemical weathering with interfacial dissolution–reprecipitation: A study

based on the nanometer-scale chemistry of fluid–silicate interfaces. *Chemical Geology,* 294–295**,** 203-216.

Henneberry, Y. K., Kraus, T. E. C., Nico, P. S. & Horwath, W. R. 2012. Structural stability of coprecipitated natural organic matter and ferric iron under reducing conditions. *Organic Geochemistry,* 48**,** 81-89.

Henry, M., Jolivet, J. P. & Livage, J. 1992. Aqueous chemistry of metal cations: Hydrolysis, condensation and complexation. *In:* Reisfeld, R. & Jjørgensen, C. K. (eds.) *Chemistry, Spectroscopy and Applications of Sol-Gel Glasses.* Berlin, Heidelberg: Springer Berlin Heidelberg.

Hesterberg, D. 2010. Macroscale Chemical Properties and X-Ray Absorption Spectroscopy of Soil Phosphorus. *Developments in Soil Science,* 34**,** 313-356.

Higashi, T. 1983. Characterization of Al/Fe—humus complexes in dystrandepts through comparison with synthetic forms. *Geoderma,* 31**,** 277-288.

Hobson, R. P. & Page, H. J. 1932. Studies on the Carbon and Nitrogen Cycles in the Soil. VII. The Nature of the Organic Nitrogen Compounds of the Soil: "Humic" Nitrogen. *The Journal of Agricultural Science,* 22**,** 497-515.

Hochella, M. F. & Banfield, J. F. 1995. Chemical weathering of silicates in nature; a microscopic perspective with theoretical considerations. *Reviews in Mineralogy and Geochemistry,* 31**,** 353-406.

Hochella, M. F., Lower, S. K., Maurice, P. A., Penn, R. L., Sahai, N., Sparks, D. L. & Twining, B. S. 2008. Nanominerals, Mineral Nanoparticles, and Earth Systems. *Science,* 319**,** 1631-1635.

Holt, P. 2002. *Electrolytic Treatment of Wastewater in the Oil Industryf. Thesis (Ph. D.)- University of Sydney, Austrália.* PhD.

Holten-Andersen, N., Harrington, M. J., Birkedal, H., Lee, B. P., Messersmith, P. B., Lee, K. Y. C. & Waite, J. H. 2011. pH-induced metal-ligand cross-links inspired by mussel yield self-healing polymer networks with near-covalent elastic moduli. *Proceedings of the National Academy of Sciences of the United States of America,* 108**,** 2651-2655.

Houghton, R. A. 2003. Revised Estimates of the Annual Net Flux of Carbon to the Atmosphere from Changes in Land Use and Land Management 1850–2000. *Tellus B* 55**,** 378-390.

Hu, Y. & Jun, Y.-S. 2012. Biotite Dissolution in Brine at Varied Temperatures and CO2 Pressures: Its Activation Energy and Potential CO2 Intercalation. *Langmuir,* 28**,** 14633-14641.

Hu, Y. F., Xu, R. K., Dynes, J. J., Blyth, R. I. R., Yu, G., Kozak, L. M. & Huang, P. M. 2008. Coordination nature of aluminum (oxy)hydroxides formed under the influence of tannic acid studied by X-ray absorption spectroscopy. *Geochimica et Cosmochimica Acta,* 72**,** 1959-1969.

Huang, W. H. & Kiang, W. C. 1972. Laboratory dissolution of plagioclase feldspars in water and organic acids at room temperature. *American Mineralogist,* 57**,** 1849-1859.

Huang, Y.-T., Lowe, D. J., Churchman, G. J., Schipper, L. A., Cursons, R., Zhang, H., Chen, T.-Y. & Cooper, A. 2016. DNA adsorption by nanocrystalline allophane spherules and nanoaggregates, and implications for carbon sequestration in Andisols. *Applied Clay Science,* 120**,** 40-50.

Hwang, D. S., Zeng, H., Masic, A., Harrington, M. J., Israelachvili, J. N. & Waite, J. H. 2010. Protein- and Metal-dependent Interactions of a Prominent Protein in Mussel Adhesive Plaques. *Journal of Biological Chemistry,* 285**,** 25850-25858.

Iamarino, M. & Terribile, F. 2008. The importance of andic soils in mountain ecosystems: a pedological investigation in Italy. *European Journal of Soil Science,* 59**,** 1284-1292.

Icopini, G. A., Brantley, S. L. & Heaney, P. J. 2005. Kinetics of silica oligomerization and nanocolloid formation as a function of pH and ionic strength at 25°C. *Geochimica et Cosmochimica Acta,* 69**,** 293-303.

Ipcc 2013 *Climate Change 2013: The Physical Science Basis. Contribution of Working Group I to the Fifth Assessment Report of the Intergovernmental Panel on Climate Change,* Cambridge, United Kingdom and New York, NY, USA,, Cambridge University Press, .

Ipcc 2001. Climate Change 2001: The Scientific Basis. Summary for Policy Makers. IPCC (Intergovernment Panel on Climate Change). Cambridge, UK.

Ipcc, I. P. O. C. C. 2014. Climate Change 2014: Mitigation of Climate Change. *In:* Edenhofer, O., Pichs-Madruga, R., Sokona, Y., Minx, J. C., Farahani, E., Kadner, S., Seyboth, K., Adler, A., Baum, I., Brunner, S., Eickemeier, P., Kriemann, B., Savolainen, J., Schlömer, S., Von Stechow, C. & Zwickel, T. (eds.) *Working Group III Contribution to the Fifth Assessment Report of the Intergovernmental Panel on Climate Change.* Cambridge University Press.

Iupac 2005. *Nomenclature of Inorganic Chemistry*, The Royal Society of Chemistry.

Iyoda, F., Hayashi, S., Arakawa, S., John, B., Okamoto, M., Hayashi, H. & Yuan, G. 2012. Synthesis and adsorption characteristics of hollow spherical allophane nano-particles. *Applied Clay Science,* 56**,** 77-83.

Jahn, R., Zarei, M. & Stahr, K. 1992. Development of andic soil properties and of clay minerals in the semiarid climate of Lanzarote (Spain). *Mineralogica et Petrographica Acta, XXXV-A***,** 193–201.

Jain, A. K., West, T., Yang, X. & Post, W. 2005. Assessing the Impact of Changes in Climate and CO2 on Potential Carbon Sequestration in Agricultural Soils. *Geophysical Research Letters,* 32.

Jansen, B., Nierop, K. G. J. & Verstraten, J. M. 2003. Mobility of Fe(II), Fe(III) and Al in acidic forest soils mediated by dissolved organic matter: influence of solution pH and metal/organic carbon ratios. *Geoderma,* 113**,** 323-340.

Johansson, G. 1992. Structures of complexes in solution derived from x-ray diffraction measurements. *Advances in Inorganic Chemistry,* 39**,** 159–231.

Johnston, J. H. & Lewis, D. G. 1983. A detailed study of the transformation of

ferrihydrite to hematite in an aqueous medium at 92°C. *Geochimica et Cosmochimica Acta,* 47**,** 1823-1831.

Jolivet, J.-P. 2000. *Metal Oxide Chemistry and Synthesis: From Solution to Solid State*, John Wiley and Sons.

Jones, E. & Singh, B. 2014. Organo-mineral interactions in contrasting soils under natural vegetation. *Frontiers in Environmental Science,* 2**,** 2.

Jung, E. 1943. Zur Kenntnis der Ton-Humusbindung. *Bodenkunde und Pflanzenernährung,* 32**,** 325-336.

Kaiser, K., Eusterhues, K., Rumpel, C., Guggenberger, G. & Kögel-Knabner, I. 2002. Stabilization of organic matter by soil minerals — investigations of density and particle-size fractions from two acid forest soils. *Journal of Plant Nutrition and Soil Science,* 165**,** 451-459.

Kaiser, K. & Guggenberger, G. 2000. The role of DOM sorption to mineral surfaces in the preservation of organic matter in soils. *Organic Geochemistry,* 31**,** 711-725.

Kaiser, K. & Guggenberger, G. 2003. Mineral surfaces and soil organic matter. *European Journal of Soil Science,* 54**,** 219-236.

Kaiser, K. & Guggenberger, G. 2007. Sorptive stabilization of organic matter by microporous goethite: sorption into small pores vs. surface complexation. *European Journal of Soil Science,* 58**,** 45-59.

Kaiser, K., Guggenberger, G., Haumaier, L. & Zech, W. 1997. Dissolved organic matter sorption on sub soils and minerals studied by 13C-NMR and DRIFT spectroscopy. *European Journal of Soil Science,* 48**,** 301-310.

Kaiser, K. & Zech, W. 1996. DEFECTS IN ESTIMATION OF ALUMINUM IN HUMUS COMPLEXES OF PODZOLIC SOILS BY PYROPHOSPHATE EXTRACTION. *Soil Science,* 161**,** 452-458.

Kalinowski, B. E. & Schweda, P. 1996. Kinetics of muscovite, phlogopite, and biotite dissolution and alteration at pH 1–4, room temperature. *Geochimica et Cosmochimica Acta,* 60**,** 367-385.

Karlsson, T. & Persson, P. 2010. Coordination chemistry and hydrolysis of Fe(III) in a peat humic acid studied by X-ray absorption spectroscopy. *Geochimica et Cosmochimica Acta,* 74**,** 30-40.

Karlsson, T., Persson, P., Skyllberg, U., Mörth, C.-M. & Giesler, R. 2008. Characterization of Iron(III) in Organic Soils Using Extended X-ray Absorption Fine Structure Spectroscopy. *Environmental Science & Technology,* 42**,** 5449-5454.

Karltun, E., Bain, D. C., Gustafsson, J. P., Mannerkoski, H., Murad, E., Wagner, U., Fraser, A. R., Mchardy, W. J. & Starr, M. 2000. Surface reactivity of poorly-ordered minerals in podzol B horizons. *Geoderma,* 94**,** 265-288.

Kaviratna, H. & Pinnavaia, T. J. 1994. Acid hydrolysis of octahedral Mg (super 2+) sites in 2:1 layered silicates; an assessment of edge attack and gallery access mechanisms. *Clays and Clay Minerals,* 42**,** 717-723.

Kawano, M. & Tomita, K. 1995. Experimental study on the formation of clay

minerals from obsidian by interaction with acid solutions at 150 degrees and 200 degrees C. *Clays and Clay Minerals,* 43**,** 212-222.

Kawano, M. & Tomita, K. 2001. TEM-EDX study of weathered layers on the surface of volcanic glass, bytownite, and hypersthene in volcanic ash from Sakurajima volcano, Japan. *American Mineralogist,* 86**,** 284-292.

Keiluweit, M. & Kleber, M. 2009. Molecular-Level Interactions in Soils and Sediments: The Role of Aromatic π-Systems. *Environmental Science & Technology,* 43**,** 3421-3429.

Kim, B. J., Kim, S., Oh, D. X., Masic, A., Cha, H. J. & Hwang, D. S. 2015. Mussel-inspired adhesive protein-based electrospun nanofibers reinforced by Fe(iii)-DOPA complexation. *Journal of Materials Chemistry B,* 3**,** 112-118.

Kleber, M., Eusterhues, K., Keiluweit, M., Mikutta, C., Mikutta, R. & Nico, P. S. 2015. Mineral–Organic Associations: Formation, Properties, and Relevance in Soil Environments. *In:* Donald, L. S. (ed.) *Advances in Agronomy.* Academic Press.

Kleber, M., Mikutta, R., Torn, M. S. & Jahn, R. 2005. Poorly crystalline mineral phases protect organic matter in acid subsoil horizons. *European Journal of Soil Science,* 56**,** 717-725.

Kleber, M., Sollins, P. & Sutton, R. 2007. A conceptual model of organo-mineral interactions in soils: self-assembly of organic molecular fragments into zonal structures on mineral surfaces. *Biogeochemistry,* 85**,** 9-24.

Kögel-Knabner, I., Guggenberger, G., Kleber, M., Kandeler, E., Kalbitz, K., Scheu, S., Eusterhues, K. & Leinweber, P. 2008. Organo-mineral associations in temperate soils: Integrating biology, mineralogy, and organic matter chemistry. *Journal of Plant Nutrition and Soil Science,* 171**,** 61-82.

Kortum, G., Vogel, W. & Andrussow, K. 1961. *Kortum G et al; Dissociation Constants of Organic Acids in Aqueous Solution*, London : Butterworths.

Kraemer, S. M., Chiu, V. Q. & Hering, J. G. 1998. Influence of pH and Competitive Adsorption on the Kinetics of Ligand-Promoted Dissolution of Aluminum Oxide. *Environ. Sci. Technol.,* 32**,** 2876–2882.

Krull, E. S., Baldock, J. A. & Skjemstad, J. O. 2003. Importance of mechanisms and processes of the stabilisation of soil organic matter for modelling carbon turnover. *Functional Plant Biology,* 30**,** 207-222.

Kuwahara, Y. & Aoki, Y. 1995. Dissolution process of phlogopite in acid solutions. *Clays and Clay Minerals,* 43**,** 39-50.

Lagaly, G., Ogawa, M. & Dékány, I. 2013. Clay Mineral–Organic Interactions. *Developments in Clay Science,* 5**,** 435-505.

Lagzi, I., Mészáros, R., Gelybó, G. & Leelőssy, Á. 2013. Biogeochemical cycle of carbon. *Atmospheric Chemistry.* Eötvös Loránd University.

Lal, R. 1999. Soil management and restoration for C sequestration to mitigate the accelerated greenhouse effect. *Progress in Environmental Science,* 1**,** 307-326.

Lal, R. 2004. *Agricultural activities and the global carbon cycle*.

Lal, R. 2016. Beyond COP 21: potential and challenges of the “4 per Thousand” initiative. *Journal of Soil and Water Conservation,* 71**,** 20A–25A.

Lartiges, B. S., Bottero, J. Y., Derrendinger, L. S., Humbert, B., Tekely, P. & Suty, H. 1997. Flocculation of colloidal silica with hydrolyzed aluminum: An Al-27 solid state NMR investigation. *Langmuir,* 13**,** 147–152.

Lasaga, A. C. 1995. Fundamental approaches in describing mineral dissolution and precipitation rates. . *Reviews in Mineralogy and Geochemistry,* 31**,** 23-86.

Le Quéré, C., Moriarty, R., Andrew, R. M., Canadell, J. G., Sitch, S., Korsbakken, J. I., Friedlingstein, P., Peters, G. P., Andres, R. J., Boden, T. A., Houghton, R. A., House, J. I., Keeling, R. F., Tans, P., Arneth, A., Bakker, D. C. E., Barbero, L., Bopp, L., Chang, J., Chevallier, F., Chini, L. P., Ciais, P., Fader, M., Feely, R. A., Gkritzalis, T., Harris, I., Hauck, J., Ilyina, T., Jain, A. K., Kato, E., Kitidis, V., Klein Goldewijk, K., Koven, C., Landschützer, P., Lauvset, S. K., Lefèvre, N., Lenton, A., Lima, I. D., Metzl, N., Millero, F., Munro, D. R., Murata, A., Nabel, J. E. M. S., Nakaoka, S., Nojiri, Y., O'brien, K., Olsen, A., Ono, T., Pérez, F. F., Pfeil, B., Pierrot, D., Poulter, B., Rehder, G., Rödenbeck, C., Saito, S., Schuster, U., Schwinger, J., Séférian, R., Steinhoff, T., Stocker, B. D., Sutton, A. J., Takahashi, T., Tilbrook, B., Van Der Laan-Luijkx, I. T., Van Der Werf, G. R., Van Heuven, S., Vandemark, D., Viovy, N., Wiltshire, A., Zaehle, S. & Zeng, N. 2015. Global Carbon Budget 2015. *Earth Syst. Sci. Data,* 7**,** 349-396.

Lee, H., Scherer, N. F. & Messersmith, P. B. 2006. Single-molecule mechanics of mussel adhesion. *Proceedings of the National Academy of Sciences,* 103**,** 12999-13003.

Lehmann, J., Kinyangi, J. & Solomon, D. 2007. Organic matter stabilization in soil microaggregates: implications from spatial heterogeneity of organic carbon contents and carbon forms. *Biogeochemistry,* 85**,** 45-57.

Lehmann, J. & Kleber, M. 2015. The contentious nature of soil organic matter. *Nature,* 528**,** 60-68.

Leinweber, P. & Schulten, H. R. 1999. Advances in analytical pyrolysis of soil organic matter. *Journal of Analytical and Applied Pyrolysis,* 49**,** 359-383.

Levard, C. & Basile-Doelsch, I. 2016. Chapter 3 - Geology and Mineralogy of Imogolite-Type Materials. *In:* Yuan, P., Thill, A. & Bergaya, F. (eds.) *Developments in Clay Science.* Elsevier.

Levard, C., Doelsch, E., Basile-Doelsch, I., Abidin, Z., Miche, H., Masion, A., Rose, J., Borschneck, D. & Bottero, J. Y. 2012. Structure and distribution of allophanes, imogolite and proto-imogolite in volcanic soils. *Geoderma,* 183–184**,** 100-108.

Levard, C., Doelsch, E., Rose, J., Masion, A., Basile-Doelsch, I., Proux, O., Hazemann, J.-L., Borschneck, D. & Bottero, J.-Y. 2009. Role of natural nanoparticles on the speciation of Ni in andosols of la Reunion. *Geochimica et Cosmochimica Acta,* 73**,** 4750-4760.

Lind, M. D. 1967. Crystal structure of ferric chloride hexahydrate. *Journal of*

Chemical Physics 47**,** 990-993.

Lindemann, L. & Hoener, M. C. 2005. A renaissance in trace amines inspired by a novel GPCR family. *Trends in Pharmacological Sciences,* 26**,** 274-281.

Liu, C. & Huang, P. M. 2003. Kinetics of lead adsorption by iron oxides formed under the in- fluence of citrate. *Geochim. Cosmochim. Acta***,** 1045–1054.

Lorimer, G. W. & Cliff, G. 1976. Analytical electron microscopy of minerals. *In:* Wenk, H. R. (ed.) *Electron microscopy in mineralogy.* Berlin: Springer Verlag.

Lüttge, A., Bolton, E. & Lasaga, A. 1999. An interferometric study of the dissolution kinetics of anorthite: the role of reactive surface area. *American Journal of Science,* 299**,** 652-678.

Lützow, M. V., Kögel-Knabner, I., Ekschmitt, K., Matzner, E., Guggenberger, G., Marschner, B. & Flessa, H. 2006. Stabilization of organic matter in temperate soils: mechanisms and their relevance under different soil conditions – a review. *European Journal of Soil Science,* 57**,** 426-445.

Maccarthy, P. 2001. THE PRINCIPLES OF HUMIC SUBSTANCES. *Soil Science,* 166**,** 738-751.

Maillot, F., Morin, G., Wang, Y., Bonnin, D., Ildefonse, P., Chaneac, C. & Calas, G. 2011. New insight into the structure of nanocrystalline ferrihydrite: EXAFS evidence for tetrahedrally coordinated iron(III). *Geochimica et Cosmochimica Acta,* 75**,** 2708-2720.

Malmström, M. & Banwart, S. 1997. Biotite dissolution at 25°C: The pH dependence of dissolution rate and stoichiometry. *Geochimica et Cosmochimica Acta,* 61**,** 2779-2799.

Manceau, A. 1995. The mechanism of anion adsorption on iron oxides: Evidence for the bonding of arsenate tetrahedra on free Fe(O, OH)6 edges. *Geochimica et Cosmochimica Acta,* 59**,** 3647-3653.

Manceau, A. & Calas, G. 1986. Nickel-bearing clay minerals: II. Intracrystalline distribution of nickel: an X- ray absorption study. *Clay Miner,* 21**,** 341-360.

Manceau, A. & Charlet, L. 1994. The Mechanism of Selenate Adsorption on Goethite and Hydrous Ferric Oxide. *Journal of Colloid and Interface Science,* 168**,** 87-93.

Manceau, A. & Combes, J. M. 1988. Structure of Mn and Fe oxides and oxyhydroxides: A topological approach by EXAFS. *Physics and Chemistry of Minerals,* 15**,** 283–295.

Manceau, A. & Drits, V. A. 1993. Local structure of ferrihydrite and feroxyhite by EXAFS spectroscopy. *Clay Minerals,* 28.

Manceau, A., Ildefonse, P., Hazemann, J.-L., Flank, A.-M. & Gallup, D. 1995. Crystal Chemistry Of Hydrous Iron Silicate Scale Deposits at the Salton Sea Geothermal Field. *Clays and Clay Minerals,* 43**,** 304-317.

Manceau, A., Marcus, M. A. & Tamura, N. 2002. Quantitative Speciation of Heavy Metals in Soils and Sediments by Synchrotron X-ray Techniques. *In:* Fenter, P. A., Rivers, M. L., Sturchio, N. C. & Sutton, S. R. (eds.) *Applications*

of Synchrotron Radiation in Low-Temperature Geochemistry and Environmental Science. Washington, DC: Reviews in Mineralogy & Geochemistry.

Marschner, B., Brodowski, S., Dreves, A., Gleixner, G., Gude, A., Grootes, P. M., Hamer, U., Heim, A., Jandl, G., Ji, R., Kaiser, K., Kalbitz, K., Kramer, C., Leinweber, P., Rethemeyer, J., Schäffer, A., Schmidt, M. W. I., Schwark, L. & Wiesenberg, G. L. B. 2008. How relevant is recalcitrance for the stabilization of organic matter in soils? *Journal of Plant Nutrition and Soil Science,* 171**,** 91-110.

Martin, J. P. & Haider, K. 1986. Influence of mineral colloids on turnover rates of soil organic carbon. *Interactions of soil minerals with natural organics and microbes.* Madison: Huang|P.|M.

Martindale, W., Reynolds, J. E. F. & Parfitt, K. The Extra Pharmacopoeia. *In:* Reynolds, J. E. F., ed., 1993 London, England. The Pharmaceutical Press 466-472.

Masiello, C. A., Chadwick, O. A., Southon, J., Torn, M. S. & Harden, J. W. 2004. Weathering controls on mechanisms of carbon storage in grassland soils. *Global Biogeochemical Cycles,* 18**,** n/a-n/a.

Masion, A., Thomas, F., Tchoubar, D., Bottero, J. Y. & Tekely, P. 1994. Chemistry and Structure of Al(OH)/Organic Precipitates. A Small-Angle X-ray Scattering Study. 3. Depolymerization of the Al13 Polycation by Organic Ligands. *Langmuir,* 10**,** 4353-4356.

Masion, A., Vilgé-Ritter, A., Rose, J., Stone, W. E. E., Teppen, B. J., Rybacki, D. & Bottero, J.-Y. 2000. Coagulation-Flocculation of Natural Organic Matter with Al Salts: Speciation and Structure of the Aggregates. *Environmental Science & Technology,* 34**,** 3242-3246.

Matus, F., Garrido, E., Sepúlveda, N., Cárcamo, I., Panichini, M. & Zagal, E. 2008. Relationship between extractable Al and organic C in volcanic soils of Chile. *Geoderma,* 148**,** 180-188.

Matus, F., Rumpel, C., Neculman, R., Panichini, M. & Mora, M. L. 2014. Soil carbon storage and stabilisation in andic soils: a review. *Catena* 120**,** 102–110.

Mayer, L. M. 1994. Relationships between mineral surfaces and organic carbon concentrations in soils and sediments. *Chemical Geology,* 114**,** 347-363.

Mayer, L. M. 1999. Extent of coverage of mineral surfaces by organic matter in marine sediments. *Geochimica et Cosmochimica Acta,* 63**,** 207-215.

Mayer, L. M. & Xing, B. 2001. Organic Matter–Surface Area Relationships in Acid Soils. *Soil Science Society of America Journal,* 65**,** 250-258.

Mcbride, M. B. 1994. *Environmental Chemistry of Soils,* Oxford, Oxford University Press.

Mccarthy, J. E. & Zachara, J. M. 1989. Environmental Science & Technology (ACS Publications). *Environmental Science & Technology,* 23**,** 496-502.

Mccarthy, J. F., Ilavsky, J., Jastrow, J. D., Mayer, L. M., Perfect, E. & Zhuang, J. 2008. Protection of organic carbon in soil microaggregates via restructuring of

aggregate porosity and filling of pores with accumulating organic matter. *Geochimica et Cosmochimica Acta,* 72**,** 4725-4744.

Mcdaniel, P. A., Lowe, D. J., Arnalds, O. & Ping, C.-L. 2012. Andisols. *In:* Huang, P. M., Li, Y. & Sumner, M. E. (eds.) *Handbook of Soil Sciences, second edition Properties and Processes.* Boca Raton, FL: CRC Press.

Mee, I. 2009. *QUANTITATIVE CHEMICAL ANALYSIS* [Online]. Plymouth, MN, USA: Materials Evaluation and Engineering, Inc. Available: http://mee-inc.com/chemical-analysis.html [Accessed August 26 2014].

Mellini, M. & Menichini, R. 1985. Proportionality factors for thin film TEM/EDS microanalysis of silicate minerals. *Rendiconti della Societa Italiana di Mineralogia e Petrologia,* 40**,** 261–266.

Michel, F. M., Ehm, L., Antao, S. M., Lee, P. L., Chupas, P. J., Liu, G., Strongin, D. R., Schoonen, M. a. A., Phillips, B. L. & Parise, J. B. 2007. The Structure of Ferrihydrite, a Nanocrystalline Material. *Science,* 316**,** 1726-1729.

Microlab. 2017. *Conductivity Probe* [Online]. Bozeman, MT, USA: MicroLab, Inc. . Available: http://microlabinfo.com/equipment/sensors/conductivity_sensor/ [Accessed March 17, 2017].

Mikutta, C. 2011. X-ray absorption spectroscopy study on the effect of hydroxybenzoic acids on the formation and structure of ferrihydrite. *Geochimica et Cosmochimica Acta,* 75**,** 5122-5139.

Mikutta, C., Frommer, J., Voegelin, A., Kaegi, R. & Kretzschmar, R. 2010. Effect of citrate on the local Fe coordination in ferrihydrite, arsenate binding, and ternary arsenate complex formation. *Geochimica et Cosmochimica Acta,* 74**,** 5574-5592.

Mikutta, C. & Kretzschmar, R. 2008. Synthetic coprecipitates of exopolysaccharides and ferrihydrite. Part II: Siderophore-promoted dissolution. *Geochimica et Cosmochimica Acta,* 72**,** 1128-1142.

Mikutta, C., Mikutta, R., Bonneville, S., Wagner, F., Voegelin, A., Christl, I. & Kretzschmar, R. 2008. Synthetic coprecipitates of exopolysaccharides and ferrihydrite. Part I: Characterization. *Geochimica et Cosmochimica Acta,* 72**,** 1111-1127.

Mikutta, R., Kleber, M. & Jahn, R. 2005. Poorly crystalline minerals protect organic carbon in clay subfractions from acid subsoil horizons. *Geoderma,* 128**,** 106-115.

Mikutta, R., Lorenz, D., Guggenberger, G., Haumaier, L. & Freund, A. 2014. Properties and reactivity of Fe-organic matter associations formed by coprecipitation versus adsorption: Clues from arsenate batch adsorption. *Geochimica et Cosmochimica Acta,* 144**,** 258-276.

Mikutta, R., Zang, U., Chorover, J., Haumaier, L. & Kalbitz, K. 2011. Stabilization of extracellular polymeric substances (Bacillus subtilis) by adsorption to and coprecipitation with Al forms. *Geochimica et Cosmochimica Acta,* 75**,** 3135-3154.

Minasny, B., Malone, B. P., Mcbratney, A. B., Angers, D. A., Arrouays, D., Chambers,

A., Chaplot, V., Chen, Z.-S., Cheng, K., Das, B. S., Field, D. J., Gimona, A., Hedley, C. B., Hong, S. Y., Mandal, B., Marchant, B. P., Martin, M., Mcconkey, B. G., Mulder, V. L., O'rourke, S., Richer-De-Forges, A. C., Odeh, I., Padarian, J., Paustian, K., Pan, G., Poggio, L., Savin, I., Stolbovoy, V., Stockmann, U., Sulaeman, Y., Tsui, C.-C., Vågen, T.-G., Van Wesemael, B. & Winowiecki, L. 2017. Soil carbon 4 per mille. *Geoderma,* 292**,** 59-86.

Mindat.Org. 2016. *Ferrihydrite* [Online]. Hudson Institute of Mineralogy. Available: http://www.mindat.org/min-1493.html [Accessed May 18 2016].

Monger, H. C. & Gallegos, R. A. 2000. Biotic and abiotic processes and rates of pedogenic carbonate accumulation. *In:* Lal, R., Kimble, J. M., Eswaran, H. & Stewart, B. A. (eds.) *Global Climate Change and Pedogenic Carbonates.* Boca Raton, Florida: CRC Press.

Morris, A. L., Macarthur, M. W., Hutchinson, E. G. & Thornton, J. M. 1992. Stereochemical quality of protein structure coordinates. *Proteins,* 12**,** 345–364.

Murakami, T., Kogure, T., Kadohara, H. & Ohnuki, T. 1998. Formation of secondary minerals and its effect on anorthite dissolution. *American Mineralogist,* 83**,** 1209–1219.

Murakami, T., Utsunomiya, S., Yokoyama, T. & Kasama, T. 2003. Biotite dissolution processes and mechanisms in the laboratory and in nature: Early stage weathering environment and vermiculitization. *American Mineralogist,* 88**,** 377–386.

Nanzyo, M., Dahlgren, R. & Shoji, S. 1993. Chapter 6 Chemical Characteristics of Volcanic Ash Soils. *In:* Sadao Shoji, M. N. & Randy, D. (eds.) *Developments in Soil Science.* Elsevier.

Nesbitt, H. W. & Young, G. M. 1984. Prediction of some weathering trends of plutonic and volcanic rocks based on thermodynamic and kinetic considerations. *Geochimica et Cosmochimica Acta,* 48**,** 1523-1534.

Ng Kee Kwong, K. F. & Huang, P. M. 1981. Comparison of the influence of tannic acid and selected low-molecular-weight organic acids on precipitation products of aluminum. *Geoderma,* 26**,** 179-193.

Nichols, J. 1984. Relation of organic carbon to soil properties and climate in the southern great plains. *Soil Science Society of America Journal,* 48.

Nierop, K. G. J. J., Jansen, B. & Verstraten, J. M. 2002. Dissolved organic matter, aluminium and iron interactions: precipitation induced by metal/carbon ratio, pH and competition. *Science of The Total Environment,* 300**,** 201-211.

Ning, R. Y. 2003. Discussion of silica speciation, fouling, control and maximum reduction. *Desalination,* 151**,** 67-73.

Nordin, J. P., Sullivan, D. J., Phillips, B. L. & Casey, W. H. 1999. Mechanisms for fluoride-promoted dissolution of bayerite [β-Al(OH)3(s)] and boehmite [γ-AlOOH]: 19F-NMR spectroscopy and aqueous surface chemistry. *Geochimica et Cosmochimica Acta,* 63**,** 3513-3524.

Norén, K. & Persson, P. 2007. Adsorption of monocarboxylates at the water/goethite interface: The importance of hydrogen bonding. *Geochimica et Cosmochimica Acta,* 71**,** 5717-5730.

Norton, G. A., Richardson, R. G., Markuszewski, R. & Levine, A. D. 1991. Precipitation of jarosite compounds as a method for removing impurities from acidic wastes from chemical coal cleaning. *Environmental Science & Technology,* 25**,** 449-455.

O'day, P. A., Newville, M., Neuhoff, P. S., Sahai, N. & Carroll, S. A. 2000. X-Ray Absorption Spectroscopy of Strontium(II) Coordination. *J Colloid Interface Sci.,* 222**,** 184-197.

O'day, P. A., Rehr, J. J., Zabinsky, S. I. & Brown, G. E., Jr. 1994. Extended X-ray Absorption Fine Structure (EXAFS) Analysis of Disorder and Multiple-Scattering in Complex Crystalline Solids. *Journal of the American Chemical Society,* 116**,** 2938-2949.

O'loughlin, E., Gorski Ca, Scherer Mm, Boyanov Mi & Km, K. 2010. Effects of oxyanions, natural organic matter, and bacterial cell numbers on the bioreduction of lepidocrocite (gamma-FeOOH) and the formation of secondary mineralization products. *Environ Sci Technol.,* 44**,** 4570-6.

O'day, P. A., Rivera, N., Root, R. & Carroll, S. A. 2004. X-ray absorption spectroscopic study of Fe reference compounds for the analysis of natural sediments. *American Mineralogist,* 89**,** 572-585.

Oades, J. M. 1988. The retention of organic matter in soils. *Biogeochemistry,* 5**,** 35-70.

Oades, J. M. 1995. Kraznozems - organic matter. *Australian Journal of Soil Research,* 33**,** 43-57.

Oades, J. M., Gillman, G. P. & Uehara, G. 1989. Interactions of soil organic matter and variable-charge clays. *Dynamics of Soil Organic Matter in Tropical Ecosystems.* University of Hawaii, Niftal.

Oelkers, E. H. & Gislason, S. R. 2001. The mechanism, rates and consequences of basaltic glass dissolution: I. An experimental study of the dissolution rates of basaltic glass as a function of aqueous Al, Si and oxalic acid concentration at 25°C and pH = 3 and 11. *Geochimica et Cosmochimica Acta,* 65**,** 3671-3681.

Olsen, A. A. & Donald Rimstidt, J. 2008. Oxalate-promoted forsterite dissolution at low pH. *Geochimica et Cosmochimica Acta,* 72**,** 1758-1766.

Omoike, A. & Chorover, J. 2006. Adsorption to goethite of extracellular polymeric substances from Bacillus subtilis. *Geochimica et Cosmochimica Acta,* 70**,** 827-838.

Pachana, K., Zuddas, P. & Censi, P. 2012. Influence of pH and temperature on the early stage of mica alteration. *Applied Geochemistry,* 27**,** 1738-1744.

Pan, Y.-H., Vaughan, G., Brydson, R., Bleloch, A., Gass, M., Sader, K. & Brown, A. 2010. Electron-beam-induced reduction of Fe3+ in iron phosphate dihydrate, ferrihydrite, haemosiderin and ferritin as revealed by electron energy-loss spectroscopy. *Ultramicroscopy,* 110**,** 1020-1032.

Parfitt, R. L. 2009. Allophane and imogolite: role in soil biogeochemical processes. *Clay Mineralogy,* 44**,** 135–155.

Parfitt, R. L., Theng, B. K. G., Whitton, J. S. & Shepherd, T. G. 1997. Effects of clay minerals and land use on organic matter pools. *Geoderma,* 75**,** 1-12.

Parfitt, R. L. & Yuan, G. 2012. Does clay stabilise organic matter in New Zealand soils? *Soil Horizons,* 21.

Paustian, K., Lehmann, J., Ogle, S., Reay, D., Robertson, G. P. & Smith, P. 2016. Climate-smart soils. *Nature,* 532**,** 49-57.

Pecoraro, V. L., Harris, W. R., Wong, G. B., Carrano, C. J. & Raymond, K. N. 1983. Coordination chemistry of microbial iron transport compounds. 23. Fourier transform infrared spectroscopy of ferric catechoylamide analogues of enterobactin. *Journal of the American Chemical Society,* 105**,** 4623-4633.

Pédrot, M., Boudec, A. L., Davranche, M., Dia, A. & Henin, O. 2011. How does organic matter constrain the nature, size and availability of Fe nanoparticles for biological reduction? *Journal of Colloid and Interface Science,* 359**,** 75-85.

Percival, H. J., Parfitt, R. L. & Scott, N. A. 2000. Factors Controlling Soil Carbon Levels in New Zealand Grasslands Is Clay Content Important? *Soil Science Society of America Journal,* 64.

Persson, P. & Axe, K. 2005. Adsorption of oxalate and malonate at the water-goethite interface: molecular surface speciation from IR spectroscopy. *Geochimica et Cosmochimica Acta,* 69**,** 541–552.

Piccolo, A. 2001. The supramolecular structure of humic substances. *Soil Science Society of America Journal,* 166**,** 810-832.

Pokrovski, G. S., Schott, J., Farges, F. & Hazemann, J.-L. 2003. Iron (III)-silica interactions in aqueous solution: insights from X-ray absorption fine structure spectroscopy. *Geochimica et Cosmochimica Acta,* 67**,** 3559-3573.

Pokrovski, G. S., Schott, J., Hazemann, J.-L., Farges, F. & Pokrovsky, O. S. 2002. An X-ray absorption fine structure and nuclear magnetic resonance spectroscopy study of gallium–silica complexes in aqueous solution. *Geochimica et Cosmochimica Acta,* 66**,** 4203-4222.

Putnis, A. & Putnis, C. V. 2007. The mechanism of reequilibration of solids in the presence of a fluid phase. *Journal of Solid State Chemistry,* 180**,** 1783-1786.

Qafoku, N. P. 2010. Terrestrial Nanoparticles and Their Controls on Soil-/Geo-Processes and Reactions. *Advances in Agronomy,* 107**,** 33-91.

Rancourt, D. G., Thibault, P.-J., Mavrocordatos, D. & Lamarche, G. 2005. Hydrous ferric oxide precipitation in the presence of nonmetabolizing bacteria: Constraints on the mechanism of a biotic effect. *Geochimica et Cosmochimica Acta,* 69**,** 553-577.

Rasmussen, C., Torn, M. S. & Southard, R. J. 2005. Mineral Assemblage and Aggregates Control Carbon Dynamics in a California Conifer Forest. *Soil*

Science Society of America Journal, 69**,** 1711-1721.

Ravel, B. 2010. *EXAFS Modeling (Feffit / Artemis / SixPack)* [Online]. Available: http://cars9.uchicago.edu/ifeffit/FAQ/FeffitModeling - How_do_I_compare_different_fits.3F_R-factor.3F_Chi-square.3F [Accessed].

Ravel, B. & Newville, M. 2005. ATHENA, ARTEMIS, HEPHAESTUS: data analysis for X-ray absorption spectroscopy using IFEFFIT. *Journal of Synchrotron Radiation,* 12**,** 537-541.

Remusat, L., Rouzaud, J. N., Charon, E., Le Guillou, C., Guan, Y. & Eiler, J. M. 2012. D-depleted organic matter and graphite in the Abee enstatite chondrite. *Geochimica et Cosmochimica Acta,* 96**,** 319-335.

Rennert, T., Eusterhues, K., Hiradate, S., Breitzke, H., Buntkowsky, G., Totsche, K. U. & Mansfeldt, T. 2014. Characterisation of Andosols from Laacher See tephra by wet-chemical and spectroscopic techniques (FTIR, 27Al-, 29Si-NMR). *Chemical Geology,* 363**,** 13-21.

Rice, J. A. 2001. HUMIN. *Soil Science,* 166**,** 848-857.

Rickman, J. M. & Srolovitz, D. J. 1993. Defect interactions on solid surfaces. *Surface Science,* 284**,** 211-221.

Riedel, T., Biester, H. & Dittmar, T. 2012. Molecular Fractionation of Dissolved Organic Matter with Metal Salts. *Environmental Science & Technology,* 46**,** 4419-4426.

Riedel, T., Zak, D., Biester, H. & Dittmar, T. 2013. Iron traps terrestrially derived dissolved organic matter at redox interfaces. *Proceedings of the National Academy of Sciences,* 110**,** 10101-10105.

Ristić, M., Opačak, I., Štajdohar, J. & Musić, S. 2015. The influence of CTAB and gum arabic on the precipitation of α-FeOOH in a highly alkaline medium. *Journal of Molecular Structure,* 1090**,** 129-137.

Rodriguez, N. R. M., Das, S., Kaufman, Y., Israelachvili, J. N. & Waite, J. H. 2015. Interfacial pH during mussel adhesive plaque formation. *Biofouling,* 31**,** 221-227.

Rose, A. L. & Waite, T. D. 2003. Kinetics of Hydrolysis and Precipitation of Ferric Iron in Seawater. *Environmental Science & Technology,* 37**,** 3897-3903.

Rose, J., Flank, A.-M., Masion, A., Bottero, J.-Y. & Elmerich, P. 1997a. Nucleation and Growth Mechanisms of Fe Oxyhydroxide in the Presence of PO4 Ions. 2. P K-Edge EXAFS Study. *Langmuir,* 13**,** 1827-1834.

Rose, J., Manceau, A., Bottero, J.-Y., Masion, A. & Garcia, F. 1996. Nucleation and Growth Mechanisms of Fe Oxyhydroxide in the Presence of PO4 Ions. 1. Fe K-Edge EXAFS Study. *Langmuir,* 12**,** 6701-6707.

Rose, J., Manceau, A., Masion, A. & Bottero, J.-Y. 1997b. Structure and Mechanisms of Formation of FeOOH(NO3) Oligomers in the Early Stages of Hydrolysis. *Langmuir,* 13**,** 3240-3246.

Rose, J., Vilge, A., Olivie-Lauquet, G., Masion, A., Frechou, C. & Bottero, J.-Y. 1998. Iron speciation in natural organic matter colloids. *Colloids and Surfaces A:*

Physicochemical and Engineering Aspects, 136**,** 11-19.

Rufe, E. & Hochella, M. F. J. 1999. Quantitative assessment of reactive surface area of phlogopite during acid dissolution. *Science,* 285**,** 874–876.

Rytwo, G. 2004. Applying a Gouy–Chapman–Stern model for adsorption of organic cations to soils. *Applied Clay Science,* 24**,** 137-147.

Salgado, P., Melin, V., Contreras, D., Moreno, Y. & Mansilla, H. D. 2013. FENTON REACTION DRIVEN BY IRON LIGANDS. *Journal of the Chilean Chemical Society,* 58**,** 2096-2101.

Schaefer, D. W., Shelleman, R. A., Keefer, K. D. & Martin, J. E. 1986. Equilibrium structure and rigidity of alumina polymers. *Physica A: Statistical Mechanics and its Applications,* 140**,** 105-113.

Scheel, T., Dörfler, C. & Kalbitz, K. 2007. Precipitation of Dissolved Organic Matter by Aluminum Stabilizes Carbon in Acidic Forest Soils. *Soil Science Society of America Journal,* 71.

Scheel, T., Haumaier, L., Ellerbrock, R. H., Rühlmann, J. & Kalbitz, K. 2008. Properties of organic matter precipitated from acidic forest soil solutions. *Organic Geochemistry,* 39**,** 1439-1453.

Schmidt, C., Zimmermann, R. & Gaub, H. 1990. Multilayer adsorption of lysozyme on a hydrophobic substrate. *Biophysical Journal,* 57**,** 577–588.

Schmidt, M. W. I., Torn, M. S., Abiven, S., Dittmar, T., Guggenberger, G., Janssens, I. A., Kleber, M., Kogel-Knabner, I., Lehmann, J., Manning, D. a. C., Nannipieri, P., Rasse, D. P., Weiner, S. & Trumbore, S. E. 2011. Persistence of soil organic matter as an ecosystem property. *Nature,* 478**,** 49-56.

Schneider, W. 1984. Hydrolysis of Iron(ll1)...Chaotic Olation Versus Nucleation. *Inorganic Chemistry: A Journal of Critical Discussion of the Current Literature,* 3**,** 205-223.

Schnitzer, M. & Khan, S. U. 1972. *Humic Substances in the Environment,* New York, Marcel Dekker, Inc.

Schnitzer, M. & Kodama, H. 1992. Interactions between organic and inorganic components in particle-size fractions separated from four soils. *Soil Science Society of America Journal,* 56**,** 1099–1105.

Schott, J., Pokrovsky, O. S. & Oelkers, E. H. 2009. The Link Between mineral Dissolution/Precipitation Kinetics and Solution Chemistry. *Mineralogy & Geochemistry,* 70**,** 207-258.

Schweda, P. 1990. Kinetics and mechanisms of alkali feldspar dissolution at low

temperatures. Stockholm University.

Schwertmann, U. & Cornell, R. M. 2000. *Iron Oxides in the Laboratory. Preparation and Characterization*, Wiley-VCH Verlag GmbH.

Schwertmann, U. & Murad, E. 1983. Effect of pH on the formation of goethite and hematite from ferrihydrite. *Clays and Clay Minerals,* 31**,** 277-284.

Senesi, N. & Wilkinson, K. J. (eds.) 2008. *Analytical and Physical Chemistry of Environmental Systems*: John Wiley and Sons, Ltd, Publication.

Sever, M. J., Weisser, J. T., Monahan, J., Srinivasan, S. & Wilker, J. J. 2004. Metal-Mediated Cross-Linking in the Generation of a Marine-Mussel Adhesive. *Angewandte Chemie International Edition,* 43**,** 2986-2986.

Shi, Y., Baumann, F., Ma, Y., Song, C., Kühn, P., Scholten, T. & He, J. S. 2012. Organic and inorganic carbon in the topsoil of the Mongolian and Tibetan grasslands: pattern, control and implications. *Biogeosciences,* 9**,** 2287-2299.

Shimizu, M., Zhou, J., Schröder, C., Obst, M., Kappler, A. & Borch, T. 2013. Dissimilatory Reduction and Transformation of Ferrihydrite-Humic Acid Coprecipitates. *Environmental Science & Technology,* 47**,** 13375-13384.

Siéliéchi, J. M., Lartiges, B. S., Kayem, G. J., Hupont, S., Frochot, C., Thieme, J., Ghanbaja, J., D'espinose De La Caillerie, J. B., Barrès, O., Kamga, R., Levitz, P. & Michot, L. J. 2008. Changes in humic acid conformation during coagulation with ferric chloride: Implications for drinking water treatment. *Water Research,* 42**,** 2111-2123.

Sigg, L. & Stumm, W. 1991. *Aquatische Chemie: eine Einführung in die Chemie wässriger Lösungen und in die Chemie natürlicher Gewässer*, Verlag der Fachvereine.

Silva, L. C. R., Doane, T. A., Corrêa, R. S., Valverde, V., Pereira, E. I. P. & Horwath, W. R. 2015. Iron-mediated stabilization of soil carbon amplifies the benefits of ecological restoration in degraded lands. *Ecological Applications,* 25**,** 1226-1234.

Sollins, P., Homann, P. & Caldwell, B. A. 1996. Stabilization and destabilization of soil organic matter: mechanisms and controls. *Geoderma,* 74**,** 65-105.

Sollins, P., Kramer, M. G., Swanston, C., Lajtha, K., Filley, T., Aufdenkampe, A. K., Wagai, R. & Bowden, R. D. 2009. Sequential density fractionation across soils of contrasting mineralogy: evidence for both microbial- and mineral-controlled soil organic matter stabilization. *Biogeochemistry,* 96**,** 209-231.

Souza, G. D. S. E. & Gomes, E. G. 2015. Improving agricultural economic efficiency in Brazil. *International Transactions in Operational Research,* 22**,** 329-337.

Staff, S. S. 1999. *Soil Taxonomy — a basic system of soil classification for making and interpreting soil surveys, second edition.,* Washington, DC, U.S. Government Printing Office.

Staudt, C., Horn, H., Hempel, D. C. & Neu, T. R. 2004. Volumetric measurements of bacterial cells and extracellular polymeric substance glycoconjugates in biofilms. *Biotechnology and Bioengineering,* 88**,** 585-592.

Stevenson, F. J. 1994. *Humus chemistry. Genesis, composition, reactions,* New York, John Wiley.

Stillings, L. L. & Brantley, S. L. 1995. Feldspar dissolution at 25°C and pH 3: Reaction stoichiometry and the effect of cations. *Geochimica et Cosmochimica Acta,* 59**,** 1483-1496.

Stockmann, U., Adams, M. A., Crawford, J. W., Field, D. J., Henakaarchchi, N., Jenkins, M., Minasny, B., Mcbratney, A. B., Courcelles, V. D. R. D., Singh, K., Wheeler, I., Abbott, L., Angers, D. A., Baldock, J., Bird, M., Brookes, P. C.,

Chenu, C., Jastrow, J. D., Lal, R., Lehmann, J., O'donnell, A. G., Parton, W. J., Whitehead, D. & Zimmermann, M. 2013. The knowns, known unknowns and unknowns of sequestration of soil organic carbon. *Agriculture, Ecosystems & Environment,* 164**,** 80-99.

Sunda, W. G. & Kieber, D. J. 1994. Oxidation of humic substances by manganese oxides yields low-molecular-weight organic substrates. *Nature,* 367**,** 62-64.

Sutton, R. & Sposito, G. 2005. Molecular structure in soil humic substances: the new view. *Environmental Science & Technology,* 39**,** 9009-9015.

Swaby, R. J. & Ladd, J. N. Chemical nature, microbial resistance, and origin of soil humus. Transactions of Commissions IV and V of the International Society of Soil Science,, 1962 New Zealand. 3–8.

Szytula A., Burewicz A., Dimitrijevic Z., Krasnicki S., Rzany H., Todorovic J., Wanic A. & W., W. 1968. Neutron diffraction studies of α-FeOOH. *Physica Status Solidi,* 26**,** 429-434.

Takahashi, T. & Dahlgren, R. A. 2016. Nature, properties and function of aluminium–humus complexes in volcanic soils. 263**,** 110–121.

Tamrat, W. Z., Rose, J., Perrine, C., Clement, L. & Isabelle, B. D. submitted. Short range order mineral organic associations (sroMOAs) formed by weathering of primary minerals in soils: laboratory approach. *Geochimica et Cosmochimica Acta*.

Taylor, A. S., Blum, J. D., Lasaga, A. C. & Macinnis, I. N. 2000. Kinetics of dissolution and Sr release during biotite and phlogopite weathering. *Geochimica et Cosmochimica Acta,* 64**,** 1191-1208.

Taylor, S. W., Chase, D. B., Emptage, M. H., Nelson, M. J. & Waite, J. H. 1996. Ferric Ion Complexes of a DOPA-Containing Adhesive Protein from Mytilus edulis. *Inorganic Chemistry,* 35**,** 7572-7577.

Tazaki, K. 1986. Observation of primitive clay precursors during microcline weathering. *Contributions to Mineralogy and Petrology,* 92**,** 86-88.

Ten Have, R. & Teunissen, P. J. M. 2001. Oxidative Mechanisms Involved in Lignin Degradation by White-Rot Fungi. *Chemical Reviews,* 101**,** 3397-3414.

Theng, B. K. G. 2012. Chapter 12 - Humic Substances. *In:* Theng, B. K. G. (ed.) *Developments in Clay Science.* Elsevier.

Thieme, J. & Niemeyer, J. 1998. *Interaction of colloidal soil particles, humic substances and cationic detergents studied by X-ray microscopy,* Darmstadt, Steinkopff.

Tietema, A., Riemer, L., J.M., V., M.P., V. D. M., A.J., V. W. & I., V. V. 1993. Nitrogen cycling in acid forest soils subject to increased atmospheric nitrogen input. *Forest Ecology and Management* 57**,** 29-44.

Tipping, E. 1990. *Interactions of organic acids with inorganic and organic surfaces,* New York, Wiley.

Tonneijck, F. H., Jansen, B., Nierop, K. G. J., Verstraten, J. M., Sevink, J. & De Lange, L. 2010. Towards understanding of carbon stocks and stabilization in

volcanic ash soils in natural Andean ecosystems of northern Ecuador. *European Journal of Soil Science,* 61**,** 392-405.

Torn, M. S., Trumbore, S. E., Chadwick, O. A., Vitousek, P. M. & Hendricks, D. M. 1997. Mineral control of soil organic carbon storage and turnover. *Nature,* 389**,** 170-173.

Troeh, F. R. & Thompson, L. M. 2005. *Soils and Soil Fertility, 6th Edition*, Wiley-Blackwell Publishing

Tsomaia, N., Brantley, S. L., Hamilton, J. P., Pantano, C. G. & Mueller, K. T. 2003. NMR evidence for formation of octahedral and tetrahedral Al and repolymerization of the Si network during dissolution of aluminosilicate glass and crystal. *American Mineralogist,* 88**,** 54-67.

Turchenek, L. W. & Oades, J. M. 1979. Fractionation of organo-mineral complexes by sedimentation a density techniques soil samples. *Geoderma,* 21**,** 311-343.

Turpault, M. P. & Trotignon, L. 1994. The dissolution of biotite single crystals in dilute HNO3 at 24°C: Evidence of an anisotropic corrosion process of micas in acidic solutions. *Geochimica et Cosmochimica Acta,* 58**,** 2761-2775.

U.S.Doe. 2008. Carbon Cycling and Biosequestration. *Report from the March 2008 Workshop, DOE/SC-108.* U.S. Department of Energy Office of Science.

Urushadze, A. T., Chizhikova, N. P. & Urushadze, T. F. 2006. Mineralogical composition of the clay fraction in alluvial soils of eastern Georgia. *Mineralogy And Micromorphology Of Soils,* 39**,** 516-527.

Van Breemen, N., Mulder, J. & Driscoll, C. T. 1983. Acidification and alkalinization of soils *Plant and Soil* 75**,** 283-308.

Van De Vreken, P., Gobin, A., Baken, S., Van Holm, L., Verhasselt, A., Smolders, E. & Merckx, R. 2016. Crop residue management and oxalate-extractable iron and aluminium explain long-term soil organic carbon sequestration and dynamics. *European Journal of Soil Science,* 67**,** 332-340.

Van Der Lee, J. 2005. Reactive transport modelling with HYTEC. Users guide and tutorial. Fontainebleau, France: Ecole des Mines.

Van Der Lee, J. & De Windt , L. 2002. CHESS Tutorial and Cookbook. Updated for version 3.0. Users Manual Nr. LHM/RD/02/13. Fontainebleau, France: Ecole des Mines de Paris.

Van Veen, J. A. & Kuikman, P. J. 1990. Soil structural aspects of decomposition of organic matter by micro-organisms. *Biogeochemistry,* 11**,** 213-233.

Vilgé-Ritter, A., Masion, A., Boulangé, T., Rybacki, D. & Bottero, J.-Y. 1999a. Removal of Natural Organic Matter by Coagulation-Flocculation: A Pyrolysis-GC-MS Study. *Environmental Science & Technology,* 33**,** 3027-3032.

Vilgé-Ritter, A., Rose, J., Masion, A., Bottero, J. Y. & Lainé, J. M. 1999b. Chemistry and structure of aggregates formed with Fe-salts and natural organic matter. *Colloids and Surfaces A: Physicochemical and Engineering Aspects,*

147, 297-308.

Vogel, C., Heister, K., Buegger, F., Tanuwidjaja, I., Haug, S., Schloter, M. & Kögel-Knabner, I. 2015. *Clay mineral composition modifies decomposition and sequestration of organic carbon and nitrogen in fine soil fractions*.

Vogel, C., Mueller, C. W., Höschen, C., Buegger, F., Heister, K., Schulz, S., Schloter, M. & Kögel-Knabner, I. 2014. Submicron structures provide preferential spots for carbon and nitrogen sequestration in soils. 5, 2947.

Voinot, A., Lemarchand, D., Collignon, C., Granet, M., Chabaux, F. & Turpault, M. P. 2013. Experimental dissolution vs. transformation of micas under acidic soil conditions: Clues from boron isotopes. *Geochimica et Cosmochimica Acta,* 117, 144-160.

Von Lützow, M. V., Kögel-Knabner, I., Ekschmitt, K., Matzner, E., Guggenberger, G., Marschner, B. & Flessa, H. 2006. Stabilization of organic matter in temperate soils: mechanisms and their relevance under different soil conditions – a review. *European Journal of Soil Science,* 57, 426-445.

Wagai, R. & Mayer, L. M. 2007. Sorptive stabilization of organic matter in soils by hydrous iron oxides. *Geochimica et Cosmochimica Acta,* 71, 25-35.

Wagai, R., Mayer, L. M., Kitayama, K. & Shirato, Y. 2013. *Biogeochemistry* 112, 95-109.

Waksman, S. A. 1932. CONTRIBUTION TO OUR KNOWLEDGE OF THE CHEMICAL NATURE AND ORIGIN OF HUMUS: I. ON THE SYNTHESIS OF THE "HUMUS NUCLEUS". *Soil Science,* 34, 43-70.

Waksman, S. A. & Iyer, K. R. N. 1933. CONTRIBUTION TO OUR KNOWLEDGE OF THE CHEMICAL NATURE AND ORIGIN OF HUMUS: IV. FIXATION OF PROTEINS BY LIGNINS AND FORMATION OF COMPLEXES RESISTANT TO MICROBIAL DECOMPOSITION. *Soil Science,* 36, 69-82.

Wan, J., Tyliszczak, T. & Tokunaga, T. K. 2007. Organic carbon distribution, speciation, and elemental correlations within soil microaggregates: Applications of STXM and NEXAFS spectroscopy. *Geochimica et Cosmochimica Acta,* 71, 5439-5449.

Waychunas, G. A., Davis, J. A. & Fuller, C. C. 1995. Geometry of sorbed arsenate on ferrihydrite and crystalline FeOOH: Re-evaluation of EXAFS results and topological factors in predicting sorbate geometry, and evidence for monodentate complexes. *Geochimica et Cosmochimica Acta,* 59, 3655-3661.

Waychunas, G. A., Rea, B. A., Fuller, C. C. & Davis, J. A. 1993. Surface chemistry of ferrihydrite: Part 1. EXAFS studies of the geometry of coprecipitated and adsorbed arsenate. *Geochimica et Cosmochimica Acta,* 57, 2251-2269.

Weissbart, E. J. & Rimstidt, J. D. 2000. Wollastonite: Incongruent dissolution and leached layer formation. *Geochimica et Cosmochimica Acta,* 64, 4007-4016.

Wells, A. F. 1984. *Structural Inorganic Chemistry,* New York, Clarendon Press.

Wen, Y., Li, H., Xiao, J., Wang, C., Shen, Q., Ran, W., He, X., Zhou, Q. & Yu, G. 2014.

Insights into complexation of dissolved organic matter and Al(III) and nanominerals formation in soils under contrasting fertilizations using two-dimensional correlation spectroscopy and high resolution-transmission electron microscopy techniques. *Chemosphere,* 111**,** 441-449.

Weng, L., Van Riemsdijk, W. H. & Hiemstra, T. 2007. Adsorption of humic acids onto goethite: Effects of molar mass, pH and ionic strength. *Journal of Colloid and Interface Science,* 314**,** 107-118.

White, A. F. 1983. Surface chemistry and dissolution kinetics of glassy rocks at 25°C. *Geochimica et Cosmochimica Acta,* 47**,** 805-815.

White, A. F. & Brantley, S. L. 2003. The effect of time on the weathering of silicate minerals: why do weathering rates differ in the laboratory and field? *Chemical Geology,* 202**,** 479-506.

Whitehouse, D. J. 2011. Surface Geometry and Its Importance in Function. *Handbook of Surface and Nanometrology, Second Edition.* CRC Press.

Wikipedia. 2017. *Atomic force microscopy* [Online]. Wikimedia Foundation, Inc. Available: http://en.wikipedia.org/wiki/Atomic_force_microscopy [Accessed February 27 2017].

Wild, B., Daval, D., Guyot, F., Knauss, K. G., Pollet-Villard, M. & Imfeld, G. 2016. pH-dependent control of feldspar dissolution rate by altered surface layers. *Chemical Geology,* 442**,** 148-159.

Wissing, L., Kölbl, A., Häusler, W., Schad, P., Cao, Z.-H. & Kögel-Knabner, I. 2013. Management-induced organic carbon accumulation in paddy soils: The role of organo-mineral associations. *Soil and Tillage Research,* 126**,** 60-71.

Wolery, T. J. 1992. *EQ3/6, A Software Package for Geochemical Modeling of Aqueous Systems: Package Overview and Installation Guide (Version 7.0),* Livermore, California, Lawrence Livermore National Laboratory.

Xos. 2017. *Micro X-ray Fluorescence (μXRF)* [Online]. 15 Tech Valley Drive East Greenbush, NY 12061, USA: XOS. Available: https://www.xos.com/Micro-XRF [Accessed February 27 2017].

Xu, R. K., Hu, Y. F., Dynes, J. J., Zhao, A. Z., Blyth, R. I. R., Kozak, L. M. & Huang, P. M. 2010. Coordination nature of aluminum (oxy)hydroxides formed under the influence of low molecular weight organic acids and a soil humic acid studied by X-ray absorption spectroscopy. *Geochimica et Cosmochimica Acta,* 74**,** 6422-6435.

Yong, R. N. & Phadungchewit, Y. 1993. pH influence on selectivity and retention of heavy metals in some clay soils. *Canadian Geotechnical Journal,* 30**,** 821-833.

Yoon, T. H., Johnson, S. B., Musgrave, C. B. & Brown Jr, G. E. 2004. Adsorption of organic matter at mineral/water interfaces: I. ATR-FTIR spectroscopic and quantum chemical study of oxalate adsorbed at boehmite/water and corundum/water interfaces. *Geochimica et Cosmochimica Acta,* 68**,** 4505-4518.

Yu, G., Saha, U. K., Kozak, L. M. & Huang, P. M. 2006. Kinetics of cadmium

adsorption on aluminum precipitation products formed under the influence of tannate. *Geochimica et Cosmochimica Acta,* 70**,** 5134-5145.

Zänker, H., Hüttig, G., Arnold, T. & Nitsche, H. 2006. Formation of iron-containing colloids by the weatheringof phyllite. *Aquatic Geochemistry,* 12**,** 299.

Zhao, Z., Liu, H. & Qu, J. 2009. Effect of pH on the aluminum salts hydrolysis during coagulation process: Formation and decomposition of polymeric aluminum species. *Journal of Colloid Interface Science,* 330**,** 105–112.

Zimmerman, A. R., Chorover, J., Goyne, K. W. & Brantley, S. L. 2004a. Protection of Mesopore-Adsorbed Organic Matter from Enzymatic Degradation. *Environmental Science & Technology,* 38**,** 4542-4548.

Zimmerman, A. R., Goyne, K. W., Chorover, J., Komarneni, S. & Brantley, S. L. 2004b. Mineral mesopore effects on nitrogenous organic matter adsorption. *Organic Geochemistry,* 35**,** 355-375.

Žutić, V. & Stumm, W. 1984. Effect of organic acids and fluoride on the dissolution kinetics of hydrous alumina. A model study using the rotating disc electrode. *Geochimica et Cosmochimica Acta,* 48**,** 1493-1503.